

Characterisation of the Components in Cataclysmic Variables

Gabriel William Pratt

A thesis submitted in partial fulfilment
of the requirements for the degree of
Doctor of Philosophy.

Centre for Astrophysics
Department of Physics, Astronomy and Mathematics
University of Central Lancashire

December 1999

Declaration

The work presented in this thesis was carried out in the Department of Physics, Astronomy and Mathematics, University of Central Lancashire. Unless otherwise stated it is the original work of the author.

While registered for the degree of Doctor of Philosophy, the author has not been a registered candidate for another award of the University. This thesis has not been submitted in whole, or in part, for any other degree.

Gabriel William Pratt

December 1999

Abstract

This thesis presents new and archive X-ray, optical and ultraviolet observations of cataclysmic variables, and discusses the results obtained in the context of the relationship between the physical and spectral components visible. It concentrates on the eclipsing dwarf nova OY Carinae, which has been observed both in superoutburst and quiescence.

Optical 'wide *B*' band light curves were obtained at the end of the 1994 superoutburst and on the decline. Eclipse mapping of these light curves reveals an accretion disc with a considerable physical flare ($\sim 10^\circ$). These are the first maps of a disc in the superoutburst state that clearly show such flaring. Contemporaneous X-ray observations were obtained with the *ROSAT* HRI. No eclipse of the X-ray flux was detected, a similar result to that obtained from the *EXOSAT* observations of the 1985 superoutburst by Naylor et al. (1988), supporting the case for the existence of a coronal component source for the X-rays in high accretion rate systems.

Later *ROSAT* observations of OY Car in quiescence are presented. A 1994 PSPC observation allows constraints to be placed on the quiescent X-ray spectrum. OY Car returns similar values for the temperature of the emitting gas and the emission measure as its fellow eclipsing systems. It is difficult, however, to reconcile the column density inferred from the X-ray observation with that found from *HST* ultraviolet observations. A column density of $n_H \simeq 10^{22} \text{ cm}^{-2}$, found in the 'iron curtain' study by Horne et al. (1994), is not compatible with the X-ray spectrum.

New optical photometry, obtained during quiescence in 1998, is used to update the orbital ephemeris of the system. A further *ROSAT* HRI light curve, obtained in quiescence with good phase coverage, is presented. It displays an eclipse of the X-ray flux, detected at the 13σ level, which is coincident with the optical eclipse of the primary and suggests that the region of X-ray emission is comparable in size to the white dwarf. This confirms that the boundary layer region is visible in OY Car in quiescence, and, in common with similar systems, implies that the boundary layer is the source of the X-ray flux during periods of low mass accretion. The general picture of the X-ray emission from CVs, which has been built up from observations of different objects using different satellites, has thus been confirmed for the first time for the same object using the same satellite.

The fact that the quiescent boundary layer can be seen, and that the soft X-ray flux is not extinguished, together suggest that the 'iron curtain' may be variable and connected to the accretion. The thesis also explores for the first time the effect a 'warm absorber'

would have on the X-ray spectrum and the deduced column densities of high inclination CVs in quiescence.

The application of synthetic spectral analyses to ultraviolet observations of CVs is extensively reviewed, with particular emphasis on the spectral components observed. White dwarf model atmospheres and synthetic spectra are generated using TLUSTY and SYN-SPEC, and those *IUE* spectra of cataclysmic variables where the white dwarf can be seen are modelled using a χ^2 fitting routine. White dwarf synthetic spectra veiled by an 'iron curtain' are also calculated and applied to *IUE* archive observations of OY Car and similar systems. The resulting independently estimated white dwarf temperatures are compared with published values and with temperatures obtained from the application of different model atmosphere codes. The column density found by Horne et al. (1994) is confirmed. *IUE* archive observations of U Gem show a similar cooling time (~ 30 days) to more recent *HST* observations. It is shown that the major source of systematic error in estimating the white dwarf temperature from ultraviolet observations is uncertainty in the masses of the white dwarfs.

The final Chapter shows how scheduled (simultaneous) *HST* and *ASCA* observations of OY Car in quiescence will be used to place further constraints on the temperature of the emitting gas and the column density, and how the techniques developed for the ultraviolet modelling can be applied to the *HST* data. Future (accepted) *XMM* observations of UX UMa, to constrain spectral components in the high mass accretion rate regime, are also discussed.

Contents

1	Introduction	1
1.1	The Cataclysmic Variable Zoo	2
1.2	Accretion discs: energy considerations and X-ray production	4
1.3	Accretion discs: behaviour models	10
1.4	The ‘iron curtain’	17
1.5	Thesis Overview	19
2	Optical observations of the 1994 Feb superoutburst of OY Carinae	21
2.1	Introduction	21
2.2	Observations and data reduction	22
2.2.1	The light curves	22
2.3	Mapping the disc	26
2.3.1	Review of the eclipse mapping method	26
2.3.2	Mapping the 1994 Feb superoutburst disc	33
2.4	Discussion - flare angles and temperature distributions	39
2.5	Conclusions	42
3	ROSAT X-ray observations of the 1994 Feb superoutburst of OY Carinae	44
3.1	Introduction	44
3.2	The <i>ROSAT</i> Satellite	47
3.3	Observations and data reduction	49
3.4	The Superoutburst X-ray light curve	51
3.5	The Superoutburst Luminosity	51
3.6	Discussion	54
3.6.1	Comparison with VW Hyi	54
3.7	Conclusions	60

4	Optical and X-ray observations of OY Carinae in quiescence	63
4.1	Introduction	63
4.2	Observations and data reduction	66
4.2.1	PSPC X-ray and WFC EUV observations, 1994 July	66
4.2.2	Optical observations and HRI X-ray observations, 1998 Jan - Mar	67
4.3	The orbital ephemeris	70
4.3.1	Optical eclipse timing measurements	70
4.3.2	Method	74
4.4	The X-ray data	76
4.4.1	Spectral analysis of the 1994 July <i>ROSAT</i> PSPC observation	76
4.4.2	The 1998 Jan <i>ROSAT</i> HRI observation - an X-ray eclipse	81
4.5	Discussion	84
4.5.1	The quiescent X-ray spectrum	84
4.5.2	The quiescent luminosity, the eclipse and the absorption	85
4.6	Conclusions	89
5	Modelling of ultraviolet data in quiescence: critical review	91
5.1	Overview	91
5.2	<i>IUE</i> : the satellite and data archive	92
5.3	Non-magnetic CVs in the ultraviolet	96
5.3.1	Observational characteristics	96
5.3.2	Boundary layer temperatures from ultraviolet observations of CV winds	99
5.4	The white dwarf primary	102
5.4.1	Detection	103
5.4.2	Temperature determination of the primary	104
5.4.3	Other measurable primary parameters	108
5.4.4	Summary	110
5.5	Spectrum dearchival and initial development of the fitting process	110
5.6	Model construction using TLUSTY and SYNSPEC	119
5.6.1	The basics of TLUSTY	121
5.6.2	Calculating the model atmospheres and synthetic spectra	123
5.7	Spectral Modelling	128
5.7.1	Overview — and some caveats	128
5.7.2	Some synthetic spectral analyses	129

5.8	Discussion	143
5.9	Summary and conclusions	149
6	Conclusions and Further work	151
6.1	Summary of results and conclusions	151
6.2	Further work	154
6.2.1	Forthcoming observations with <i>ASCA</i> and the <i>HST</i>	154
6.2.2	Future observations	159
	Appendices	164
A	The Zanstra method applied to CV winds	164
B	Overview of the basic equations used in model stellar atmosphere generation	166
C	Details of TLUSTY and SYNSPEC input and output files	171
D	Acronyms used	175
	References	177

Acknowledgements

I offer great thanks and appreciation to my supervisor, Barbara Hassall, for her support and encouragement, instruction, guidance and useful advice. And for her patience when faced with multiple drafts of this work. Thanks are also extended to Gordon Bromage, for his invaluable assistance and encouragement in his rôle as second supervisor.

Thanks to Tim Naylor, Janet Wood and Koji Mukai, with whom I have had many fruitful collaborations and stimulating discussions during days at Keele and elsewhere. Constance la Dous extended outstanding hospitality and provided valuable insights into ultraviolet observations during a visit to Sonneberg Observatory. Very helpful conversations pertaining to the work in this thesis were had with Ed Sion while in Sonneberg and with the staff at the University Observatory, Göttingen: Klaus Beuermann, Rick Hessman, Boris Gänsicke and Klaus Reinsch. Martin Barstow kindly got me started on TLUSTY and SYNSPEC, and Ivan Hubeny provided essential files and very useful recommendations for using his programs. I am grateful to the staff at SAAO, particularly Fred Marang and Dave Buckley, for help with the telescope and the data reduction, respectively. I thank the *ROSAT* scheduler, Jakob Engelhauser, for flexibility as to the choice of time slots I wanted in 1998 Jan-Feb. My thanks to the observers of the Variable Star Section of the Royal Astronomical Society of New Zealand, and especially Frank Bateson, who supplied the data on OY Car. Matt Burleigh helped with the access to my data from the 1998 *ROSAT* run. I thank Andy Adamson and Pete Newman for providing essential computing support as STARLINK Managers. I acknowledge the use of facilities provided by the PPARC STARLINK project, and I acknowledge the financial support of a research studentship from the University of Central Lancashire.

I am very grateful to my friends and colleagues at the University of Central Lancashire and elsewhere, who have helped no end in making the last few years more bearable with the benefit of shared experience. It is a long list, but you know who you are. Many thanks, too, to my friends in Ireland, who have supported me and kept in contact through all this and over the years since we all left (and in some cases didn't leave, or left and returned to) Ballyhaunis.

Finally, I wish to give special thanks to my parents and family for all they have done for me, for their faith in me, for their support and for their encouragement. It is something of a cliché to refer to formative experiences in acknowledgements such as this, but I feel I must point out that the night sky in the West of Ireland can be breathtaking. I am forever grateful to my parents for bringing me up in such a way as to enable me to appreciate this fact.

This thesis is dedicated to the memory of my brother, Adam, and to the memory of my dear friend, Anne Marie O'Loughlin.

Chapter 1

Introduction

This thesis is concerned with observations of dwarf novae, a subclass of non-magnetic cataclysmic variable binary star, and in particular with one example, OY Carinae. Multiwavelength data are used to probe various aspects of this intriguing system in both the superoutburst and quiescent states. Further simultaneous time on the *Hubble Space Telescope* (*HST*) and the *Advanced Satellite for Cosmology and Astrophysics* (*ASCA*) has been awarded, and is scheduled for 2000 Mar, giving coverage of the system in high resolution X-ray and ultraviolet wavelengths. In this connection, a critical review of the modelling techniques for ultraviolet spectra has been undertaken and is also presented. The review utilises archive data of many cataclysmic variable systems from the now defunct *International Ultraviolet Explorer* (*IUE*) satellite and from the *HST* archive itself.

OY Car is a well studied system because of two attributes in particular: its inclination and its short orbital period. It is a deeply eclipsing cataclysmic variable, with an inclination of $i = 83^\circ$, a value which allows the identification of the physical components of the system through timing observations throughout its ~ 91 min orbit. As such it is a member of a relatively select group of cataclysmic variables. Moreover, the quality of modern spectroscopic observations, across wavelengths ranging from infrared to X-ray, has allowed the identification of spectral components which can be directly related to the energy process taking place, and so to the physical components themselves. While theory has been successful in explaining much of the observed behaviour, there are still many interesting problems which can be addressed with further observations. Interpretation of data from eclipsing systems like OY Car offers a further challenge chiefly because of inclination effects.

The optical, X-ray and ultraviolet observations presented here address some of the outstanding problems, such as the effect of the ‘iron curtain’ seen in high inclination sys-

tems. The results are discussed in the context of similar observations of lower inclination, non-eclipsing systems.

The remainder of this Chapter describes the different types of cataclysmic variable, their respective physical components, and how the physical processes give rise to the emissions studied in this thesis. Note that, in keeping with the conventions of the cataclysmic variable community, cgs or solar units are used throughout.

1.1 The Cataclysmic Variable Zoo

Up to 70% of all stars may be members of binary or multiple systems. This thesis deals with the cataclysmic variables (CVs), which are close binary stars consisting of a white dwarf (the primary) accreting matter from a late-type, quasi-main sequence star (the secondary). CVs are, as a class, characterised by variations in all wavelengths on a wide variety of timescales, all connected to the accretion process. In many cases this accretion is in bursts, resulting in large releases of energy, hence ‘cataclysmic’. Within the standard white dwarf/main sequence star paradigm, however, a very wide variety of behaviour is displayed. The classification scheme has subclasses and subclasses of subclasses¹.

The most basic classification scheme is drawn from the way in which matter is accreted from the secondary star onto the white dwarf. While magnetic fields undoubtedly play a large role in all CVs, the magnetic field of the primary can control the accretion flow only if the field strength is $\gtrsim 10^5$ G.

CVs with a relatively weak magnetic field ($\lesssim 10^5$ G) are characterised by the fact that the transferred material forms an accretion disc around the primary star. Such non-magnetic CVs (a relative term) are the subject of this thesis, and all have this binary and accretion disc structure. The physical purpose of the disc is to enable the transfer of mass inwards, to be accreted onto the white dwarf, and the transfer of angular momentum outwards. The point of impact of the mass transfer stream from the secondary star with the edge of the accretion disc is called the bright spot.

The physical components of a typical nonmagnetic CV, and their characteristic energy ranges are: the secondary (infrared - optical), the white dwarf (optical - ultraviolet), the accretion disc (infrared - extreme ultraviolet [EUV]), the bright spot (optical - ultraviolet) and the boundary layer between the accretion disc and the surface of the white dwarf (EUV - X-ray).

¹Once memorably described as “over Balkanisation” by Patterson et al. (1997b; as they defined yet another subclass).

The non-magnetic CVs are subclassified into several categories according to their respective long-term photometric behaviour, which is directly a result of the mode of accretion onto the white dwarf. These categories are (organised after Warner's comprehensive review 1995):

- **Classical novae**, which have had only one observed eruption. The range from pre-nova brightness to maximum is from 6 to 19 magnitudes. The largest amplitude eruptions with shortest duration are in the very fast novae (days); the lowest amplitude, are in the slow novae, with durations that may last for years. The mechanism for the eruptions is thermonuclear runaway of the accreted material on the surface of the white dwarf.
- **Recurrent novae** are previously recognised novae that have repeated. The main spectroscopic distinction between these types and the following dwarf novae is that classical and recurrent novae are observed to eject a substantial shell of material.
- **Dwarf novae**, which are subject to smaller amplitude quasi-periodic outbursts ($\sim 3 - 5$ magnitudes) on timescales ranging from tens of days to tens of years. The outbursts are due to a release of gravitational energy after a sudden increase in the rate of mass transfer through the accretion disc. Dwarf novae are further subclassified after their respective prototypes as follows:

Z Cam stars show standstills ~ 0.7 magnitudes below maximum, during which outbursts proper can cease for tens of days to years;

SU UMa stars are subject to occasional superoutbursts (on timescales of hundreds of days) in addition to normal dwarf nova outbursts, rising to ~ 0.7 magnitudes above normal outburst maximum and lasting ~ 5 times as long. There is a further subclass of extreme SU UMas, designated *ER UMa stars*, which have unusually high mass transfer rates and show extremely short intervals between superoutbursts (19 - 44 d) and a very short normal outburst interval (3 - 4 d);

U Gem stars include all other dwarf novae.

- **Novalike variables**, which are thought to be pre-novae, post novae, and Z Cam stars that are in permanent standstill. They are observed as such because the observational baseline available to us (~ 100 years) is too short to reveal a change in their state. This class includes the *VY Scl stars*, which are observed to undergo occasional reductions from approximately constant magnitude, thought to be due to a temporary reduction of the mass transfer rate.

In those CVs where the primary has a large magnetic field ($> 10^5$ G), the gas stream material retains its identity only until the magnetic field of the primary is able to control the flow. At this point the stream material locks onto the magnetic field lines and is accreted along them, to impact onto the surface of the primary in an accretion column. In those systems where the magnetic field strength of the primary is sufficient to cause synchronisation of the rotation period of the white dwarf and the orbital period, accretion is along the field lines and the system is a **polar** or *AM Her* star. With less powerful magnetic fields, synchronism cannot be achieved. If the magnetic moment of the white dwarf is small, an accretion disc can form but this is truncated at the inner edge, and subsequent accretion is along field lines. These are the **intermediate polars**, which, as a class, display a wide variety of periodic phenomena.

But non-magnetic CVs, more specifically the dwarf novae, are the subject of this work. Understanding of such systems is intimately connected to the behaviour of the accretion disc, on which there is a vast amount of work — both observational and theoretical — in the literature.

1.2 Accretion discs: energy considerations and X-ray production

This Section covers the underlying energy considerations of accretion, and deals with the production of X-rays from CVs. The observations presented in this thesis cover different outburst states in a wide range of wavelengths. The aim of this Section is thus to provide the theoretical context for these observations.

See e.g. Frank et al. (1992) for a review of the theory of accretion onto compact objects, which presents a derivation from first principles.

Energy considerations

In CVs, the shape of the secondary is distorted due to the gravitational influence of the white dwarf (the white dwarf radius is small enough to make it immune to the reciprocal effect). Tidal interaction on the secondary causes it to rotate synchronously with the orbital revolution and removes any orbital eccentricity.

The shape of the distorted secondary can be obtained from the Roche approximation (an exact representation requires a knowledge of the star's density distribution), which assumes that the stars are point masses at their respective centres of gravity and thus that the gravitational field due to each star is undistorted.

In the orbital plane of a binary system, the total potential at any point, consisting of the sum of the gravitational potentials of the two stars and the effective potential of the centrifugal force is (Krusewski 1966; Pringle 1985; Frank et al. 1992):

$$\Phi(r) = -\frac{GM_{wd}}{|r - r_{wd}|} - \frac{GM_s}{|r - r_s|} - \frac{1}{2}|\Omega \times r|^2 \quad (1.1)$$

where r , r_{wd} and r_s are the position vectors of m , M_{wd} (white dwarf mass), and M_s (secondary star mass) from the centre of mass, and Ω is the orbital angular velocity.

Roche equipotential surfaces are described when $\Phi(r) = \text{const}$, and close to each star they are almost spherical. In a binary system, their shapes are governed entirely by the mass ratio, $q = M_s/M_{wd}$, and their scale is determined by the binary separation, a . The topology of the equipotential surfaces is determined by the Lagrange points, at which a test particle will remain stationary because there are no forces acting on it (effectively saddle points in $\Phi[r]$).

In a binary system, the Roche lobe is the critical equipotential surface of each star that passes through the inner Lagrange (L_1) point. The combined effect of each star and the rotation of the binary causes distortion of the Roche lobes, such that in three dimensions the critical surface resembles two perfect teardrop shapes joined point to point at L_1 . In CVs, the secondary star has filled its Roche lobe and the unbalanced gas pressure at L_1 , where the net gravity vanishes, causes the material to be pushed out over the saddle point and into the potential well of the white dwarf.

The gravitational potential energy, ΔE_{acc} , released by a mass m , by its accretion from infinity onto the surface of a primary of radius R_{wd} , mass M_{wd} , is:

$$\Delta E_{acc} = GM_{wd}m/R_{wd} \quad (1.2)$$

As luminosity is equal to the rate of energy liberation, and if 100% of the gravitational potential energy is converted into radiation, then the accretion luminosity is:

$$L_{acc} = GM_{wd}\dot{M}/R_{wd} \quad (1.3)$$

where \dot{M} is the mass transfer rate.

The binding energy of a gas element of mass m in the Keplerian orbit nearest the surface of the primary star is $\frac{1}{2}GM_{wd}m/R_{wd}$. The gas elements start at large distances from the primary with negligible binding energy, so the total accretion disc luminosity in a steady state must be:

$$L_{disc} = \frac{GM_{wd}\dot{M}}{2R_{wd}} = \frac{1}{2}L_{acc} \quad (1.4)$$

From these simple energy considerations, it can be seen that half the accretion energy is liberated via gravitational energy in the accretion disc itself, as the material spirals down through the disc to the surface of the white dwarf. This energy is released by the accretion disc primarily as ultraviolet and optical radiation (typical temperatures of 10,000 - 40,000 K in the main body of the disc); observations of CVs in the ultraviolet are discussed further in Chapter 5.

The rest of the accretion energy is still contained in the kinetic energy of the matter. Except where the primary star is spinning fast, frictional interactions in the transition region between the disc and the white dwarf (the boundary layer) will allow the dissipation of this remaining accretion energy. This is achieved when the material of the disc is decelerated to match the rotational velocity of the primary. The boundary layer luminosity is given by

$$L_{BL} = L_{disc} \left(1 - \frac{\Omega_{wd}}{\Omega_K(R_{wd})} \right)^2 \quad (1.5)$$

where Ω_{wd} is the angular rotation velocity of the white dwarf and $\Omega_K(R_{wd})$ is the Keplerian angular velocity at the stellar surface (R_{wd}). This formulation for the boundary layer luminosity is from the Appendix of Kley (1991); this derivation, unlike previous efforts, takes into account the transfer of angular momentum (and therefore energy) onto the primary star.

The emitting area of the boundary layer is small compared to that of the rest of the disc. Numerical simulations by Popham & Narayan (1995) indicate that the radial width of the boundary layer region is only $\sim 5\%$ - 15% of the white dwarf radius. As such, it should be a source of high energy radiation. Observations of nonmagnetic CVs in the X-ray, some of which are detailed in Chapters 3 and 4, confirm that, in the limit of present detector sensitivity, the boundary layer is the only *observable* source of X-rays from such systems. The theoretical justification for this is discussed in the next Section.

Newer, more sensitive satellites may enable the detection of other sources of X-rays, the most probable of which is coronal emission from the secondary. In single and binary M-dwarfs, dynamo action and magnetic activity increase with rotation rate. In CVs, the secondary stars are synchronously rotating with the binary orbit and since these orbital periods are so short, this implies they have rapid rotation rates. These secondaries are at and beyond the upper extremes of the rotation rates seen in field and binary M-dwarfs.

X-ray emission versus stellar rotation rate is a well-studied signature of magnetic activity. The X-ray flux increases as a function of rotation rate up to a saturation level for the most rapidly rotating stars (i.e. periods of several hours). For the rotation period of

the secondary star in any eclipsing CV the expected X-ray flux can be calculated. For the rotation period of the M-dwarf in UX UMa, for example, the saturation regime is in effect and, if it shows a normal level of activity, an X-ray luminosity of $\sim 2 \times 10^{28} - 2 \times 10^{29}$ ergs s^{-1} can be expected, with a spectrum showing a hard (2 – 3keV) and soft ($\sim 0.3 - 0.8$ keV) component (cf. Singh et al. 1999, Gizis 1998). Additionally, magnetically-driven flares might also be seen, which have luminosities up to $\sim 10^{32}$ erg s^{-1} .

X-rays from the boundary layer

It was suggested that the boundary layer region could be a source of X-rays from CVs with accretion discs by Shakura & Sunyaev (1973), Lynden-Bell & Pringle (1974) and Bath et al. (1974). Early satellite observations of CVs allowed Pringle (1977) and Pringle & Savonije (1979) to build on this and to propose that the boundary layer was in fact the prime source of the X-rays from nonmagnetic CVs. Further, they found that the optical thickness of the boundary layer region is a crucial determinant of the energy of the emitted radiation, and that the optical thickness is in turn dependent on the mass accretion rate. Pringle & Savonije (1979) argued that for low accretion rates ($\dot{M} \lesssim 10^{16}$ gs^{-1} , or $\sim 1.6 \times 10^{-10} M_{\odot} yr^{-1}$), the boundary layer region is optically thin and the emission is in hard X-rays with a characteristic temperature $kT \sim 20$ keV. In contrast, for higher accretion rates the boundary layer region becomes optically thick, the hard X-ray emission is suppressed, and most of the radiation is emitted as soft X-rays at $kT \lesssim 1$ keV. The boundary layer X-rays themselves are probably produced by either strong shocks (Pringle & Savonije 1979) or turbulent viscosity (Tylenda 1981a). Thus, for instance, dwarf novae in quiescence will emit hard X-rays, but in outburst they will emit softer X-rays.

A theoretical consideration of typical boundary layer temperatures, depending on the mass accretion rate, is found in Frank et al. (1992 — see also Warner 1995). A brief summary follows.

If the region is optically thick, the luminosity must diffuse through a distance $\sim H$ (the scale height of the disc) before emerging over an area $\sim 2\pi R_{wd}2H$. The effective temperature of the boundary layer with a nonrotating white dwarf is then (e.g., Warner 1995)

$$4\pi R_{wd}H\sigma T_{BL}^4 \approx \frac{1}{2} \frac{GM_{wd}\dot{M}_d}{R_{wd}} \quad (1.6)$$

$$T_{BL} \approx 2.9 \times 10^5 M_{wd}^{1/3} (M_{\odot}) R_9^{-7/9} \dot{M}_{18}^{2/9} \text{ K} \quad (1.7)$$

where R_9 is the radius of the white dwarf measured in units of 10^9 cm and \dot{M}_{18} is the mass

flux rate through the disc measured in units of 10^{18} g s^{-1} , respectively. A temperature of $3 \times 10^5 \text{ K}$ is equivalent to $\sim 0.03 \text{ keV}$.

If, however, the boundary layer is optically thin, radiation escapes directly from the shockfront that forms where the gas hits the surface of the primary. The low density and optical depth of the region mean that the material cools very inefficiently, and must be heated to high temperatures in order to radiate the energy away. For a perfect gas, the temperature of the post-shock is (e.g., Frank et al. 1992; Warner 1995)

$$T_{sh} = \frac{3}{16} \frac{\mu_m m_H}{k} v_p^2 \quad (1.8)$$

where v_p is the pre-shock velocity, μ_m and m_H are the mean molecular weight and the mass of the H atom, and k is the Boltzmann constant, respectively. The shock temperature of the gas arriving at the primary is then

$$T_{sh} = \frac{3}{16} \frac{\mu_m m_H}{k} \frac{GM_{wd}}{R_{wd}} \quad (1.9)$$

$$= 1.85 \times 10^8 M_{wd}(M_\odot) R_9^{-1} \text{ K} \quad (1.10)$$

where R_9 is the radius of the white dwarf measured in units of 10^9 cm , and the mass of the white dwarf is expressed in solar masses. A temperature of $2 \times 10^8 \text{ K}$ is equivalent to $\sim 18 \text{ keV}$. Thus it can be seen that there is a difference of many orders of magnitude in the expected temperature of the boundary layer depending on the outburst state of the system. Aspects of these characteristic temperatures will be investigated observationally in the following Chapters.

The cooling timescale of the gas, which is dependent on the mass accretion rate, governs how the radiation will be emitted. At temperatures of $\sim 10^8 \text{ K}$, the cooling of the optically thin gas occurs through the relatively inefficient process of free-free emission (thermal bremsstrahlung). During outburst, the accretion rate rises and the whole boundary layer region becomes optically thick. In this case, the distance the shocked gas flows before cooling is less than the disc thickness, so that the hard X-rays emitted downstream of the shock will have to diffuse through the (also optically thick) disc material. Thermalised, soft X-rays are emitted from the blackbody source.

Patterson & Raymond (1985a, b) modelled the boundary layer region and confirmed the predictions described above. They additionally found that at *any* accretion rate, there is always some gas accreting near the top of the disc where the optical depth is low. The luminosity due to this hot, optically thin ‘atmosphere’ on the otherwise cool boundary layer will emerge as hard X-rays. Figure 1.1, taken from Patterson & Raymond (1985a), illustrates the different areas of X-ray emission depending on the accretion rate.

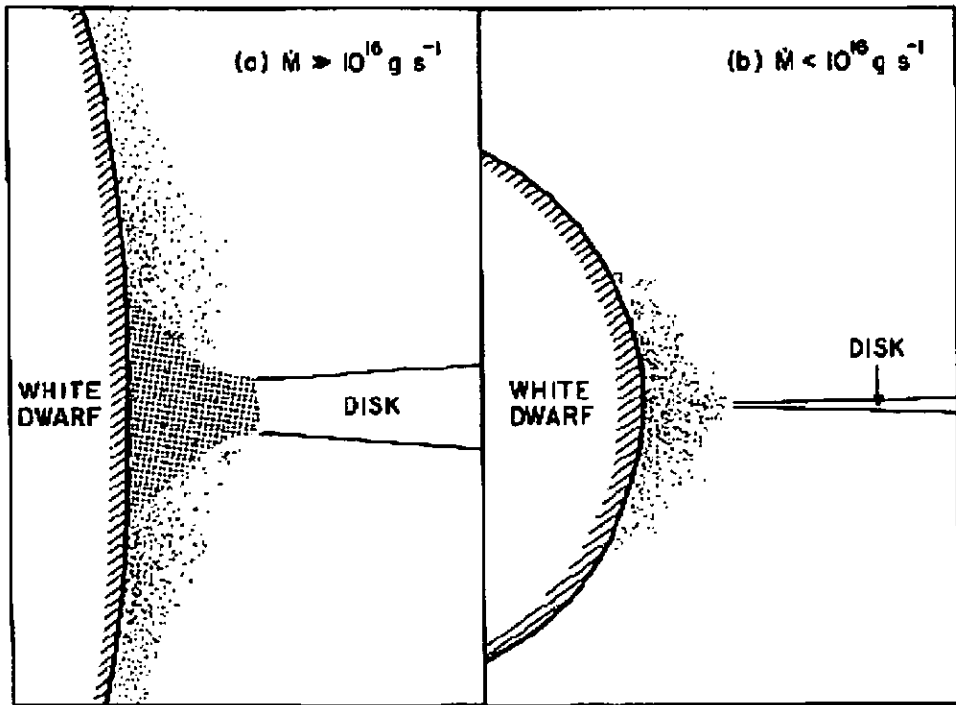


Figure 1.1: The picture of the boundary layer region for (a) high accretion rates and (b) low accretion rates, according to Patterson & Raymond (1985a). The dotted region is optically thin and radiates the bremsstrahlung component at $T \sim 10^8$ K; the shaded region is optically thick and radiates a blackbody component at $T \sim 3 \times 10^5$ K. From Patterson & Raymond (1985a).

Recent numerical models by Narayan & Popham (1993) and Popham & Narayan (1995) have added more details to the standard picture. Popham and Narayan distinguish between the “dynamical boundary layer” very near the surface of the primary star, where the angular velocity is found to deviate significantly from Keplerian as the material switches from rotational to pressure support, and the more extended “thermal boundary layer”, where the luminosity is radiated. The radial widths are $\sim 1\% - 3\%$ and $\sim 5\% - 15\%$ of the white dwarf radius, respectively. Narayan and Popham find that the structure of the boundary layer and the nature of the resulting spectrum depends not only on the mass accretion rate, but also on the mass and rotation velocity of the white dwarf: for typical CV white dwarf masses of $M_{wd} \sim 0.6 - 1.0M_{\odot}$, the peak temperatures are $kT \approx 17 - 30$ keV, a value which reduces if $v_{wd}/v_{break} \gtrsim 0.1$. Here v_{wd} is the rotation velocity of the white dwarf, and v_{break} is the breakup rotation velocity.

Satellite observations of CVs in X-rays have broadly confirmed the theoretical predictions outlined above. For reviews, see, e.g., Córdova & Mason (1984a; *Einstein*), Eracleous et al. (1991a, b; *Einstein*), Mukai & Shiokawa (1993, *EXOSAT*), van Teeseling & Verbunt (1994; *ROSAT*), Richman (1996; *ROSAT*), van Teeseling et al. (1996; *ROSAT*), or Verbunt et al. (1997; *ROSAT*). Further discussion on locating the X-ray source from observation, including data obtained for this thesis, can be found in Chapters 3 and 4.

From the above discussion it should be clear that the boundary layer luminosity in X-rays should be comparable to the disc luminosity in the optical and ultraviolet, provided the white dwarf is not rotating too rapidly. Intimate knowledge of the intrinsic boundary layer and accretion disc spectra is not yet within our grasp. However, it has become increasingly clear through observation that the boundary layer luminosities of, especially, high mass transfer rate CVs are considerably lower than that predicted by current theory (see e.g., Belloni et al. 1991, van Teeseling et al. 1996). This effect is often termed the ‘missing boundary layer problem’. There are myriad possible explanations for the ‘missing boundary layer problem’, some of which are discussed in the context of the data used for this thesis in Chapters 3 and 4.

1.3 Accretion discs: behaviour models

The quasi-periodic behaviour of dwarf nova outbursts is currently most successfully explained by the disc instability model of Osaki (1974). In this model, matter is stored in the disc and then rapidly accreted via some, at that time unknown, instability mechanism. Current theoretical work (see the review by Osaki 1996, and references therein) makes use

of the fact that accretion discs are predicted to be subject to two separate instabilities, operating on three timescales, all of which are inherent to both the disc material and to the physical conditions in force at a particular time. Fundamentally, the model predicts that the disc undergoes limit-cycle behaviour in the instabilities as dictated by the different timescales.

Disc timescales

The three timescales of importance in accretion discs are:

- (i) The **dynamical timescale**, t_{dyn} , usually taken to be either the rotation timescale, $t_\phi = R/v_\phi = \Omega^{-1}$, or the time taken to establish vertical equilibrium, $t_z = H/c_s$. Here v_ϕ is the Keplerian velocity at R , H is the disc half-thickness and c_s is the sound speed. In any case, if thin disc approximations are used,² $t_\phi \simeq t_z$.
- (ii) The **thermal timescale**, $t_{th} = \frac{\text{Heat content per unit area}}{\text{Local dissipation rate}}$. It can be shown that $t_{th} \geq t_{dyn}$.
- (iii) The **viscous timescale**, $t_\nu \simeq (R/H)^2 \gg t_{th}$ for a thin disc.

The latter two timescales are most important in disc instability theory.

Disc instabilities

The two instabilities thought to contribute to dwarf nova outbursts are:

- (i) The **thermal instability**, which is caused by the fact that the local heating rate Q^+ and the local cooling rate Q^- are not always in equilibrium. Because $t_{th} \ll t_\nu$, the surface density of the disc $\Sigma(\dot{M})$ is fixed on the thermal timescale. This implies that it is the disc thickness H , and not the surface density Σ , which changes in response to heating or cooling. The criterion for a thermal instability is if

$$\frac{d \log Q^+}{d \log T_c} > \frac{d \log Q^-}{d \log T_c} \quad (1.11)$$

where $T_c = T(z = 0)$ is the central temperature.

- (ii) The **viscous instability**. Since all variations at radius R are determined by $\Sigma(R, t)$, and $t_\nu \gg t_{th}, t_z$, this implies that hydrostatic and thermal equilibria are maintained

²This is useful as the disc can then be regarded as a two dimensional gas flow. Assumes (a) an axisymmetric gravitational potential, (b) that the disc self-gravity is negligible, (c) that the material is in circular orbits and (d) that the disc is thin, such that $H \ll R$. See Frank et al. (1992).

during slow viscous changes and also that the viscosity, $\nu = \nu(\Sigma, R)$. If a change of variables is made such that $\mu = \nu\Sigma$, it can eventually be shown (see e.g., Frank et al. 1992) that there is a viscous instability if

$$\frac{\partial\mu}{\partial\Sigma} < 0 \tag{1.12}$$

The disc instability model

For a review of the development of the disc instability model see Warner (1995) or Osaki's (1996) PASP review.

According to Warner (1995), a breakthrough in the discovery of the mechanism for the disc instability was made when Hoshi (1979) noted that the opacity, $\kappa(\rho, T)$, for a typical stellar composition, has a strong temperature dependence due to the partial ionization of H and He at $T \sim 10^4$ K. Crucially, $\partial\mu/\partial\Sigma < 0$ at this temperature, leading to a viscous instability. Warner notes that Hoshi's work went largely unremarked until the Sixth North American Workshop on Cataclysmic Variables, at Santa Cruz in 1981.

In general, $\mu(\Sigma, \dot{M}_d)$, where \dot{M}_d is the mass flux through the disc, is multivalued. It is dependent on the vertical energy transport of the disc and, to a large extent, governs the state of the material. Like in stars, if T_{eff} is high, the material is fully ionized and energy transport is purely radiative; conversely if T_{eff} is low, only zones of partial ionization will occur in the disc material and energy transport can take place by convection.

It can be shown (e.g., Frank et al. 1992) that for the optically thick regime, $\mu \propto \Sigma^{7/5}$, while for the optically thin regime, $\mu \propto \Sigma$, i.e., $\partial\mu/\partial\Sigma > 0$ for both regimes and as such they are viscously stable. However, at an optical depth of $\tau \sim 1$, $\mu \propto \Sigma^{-2/5}$, i.e., $\partial\mu/\partial\Sigma < 0$, producing a thermally and viscously unstable situation. There are thus two different regimes of $\partial\mu/\partial\Sigma$. More detailed modelling of the situation (e.g., Meyer & Meyer-Hofmeister 1983) has established that the curve on the $\log \mu - \log \Sigma$ plane is a smooth S-curve. The physical description of the behaviour of the disc is that it is cool and convective for low \dot{M} , hot and radiative for high \dot{M} , with an unstable transition zone.

The disc is thought to display limit cycle behaviour on the $\log \mu - \log \Sigma$ plane (e.g., Meyer & Meyer-Hofmeister 1981). Let $\mu_s \approx \dot{M}/3\pi$ be the steady disc value (arising from a steady state treatment of the accretion onto a slowly-rotating non-magnetic white dwarf), and let this lie on the stable branch of the $\log \mu - \log \Sigma$ plane. Now suppose that, in a given disc annulus, $\mu \neq \mu_s$. The disc will evolve along the curve towards the stable state on the (slower) viscous timescale, trying to achieve equilibrium.

Conversely, if $\mu \neq \mu_s$, and this value now lies on the *unstable* branch, the disc evolves away from μ_s and towards the viscously stable branch on the (faster) thermal timescale.

As $t_{th} \ll t_\nu$, the evolution is vertically away from the viscously unstable branch, not along it. This behaviour describes an hysteresis curve in the $\dot{M} - \Sigma$ plane, which is shown schematically in Figure 1.2.

It is generally agreed that the instability in an annulus produces a sharp discontinuity in the viscosity and other parameters, causing the outburst to propagate like a combustion front in both directions (e.g., Meyer 1984). There is qualitative agreement with observations, and the model itself is flexible enough to explain a wide variety of observed behaviour.

The disc instability model predicts that the outer radius of the accretion disc should vary over time. In the high viscosity state, the mass flux through the disc, \dot{M}_d , increases. This implies that angular momentum is transported outwards at a higher rate and the disc radius grows. However, in the low viscosity state, the mass transfer stream adds relatively low angular momentum material to the outer edge of the disc, and the disc radius shrinks.

The model can account for the outburst properties of most of the various types of CV. Novalike variables have a mean \dot{M} above the unstable regime, and so have no outbursts. U Gem stars and SU UMa stars have a mean \dot{M} in the unstable regime and so have semi-regular outbursts. Z Cam stars are thought to have their mean \dot{M} in the transition zone between the stable and unstable regimes. In this case, a slight increase in \dot{M} pushes them up into the stable regime, where they behave like novalikes and have no outbursts (corresponding to a standstill), while a slight decrease in the \dot{M} drops them into the unstable region, leading to outburst behavior.

It is worthwhile to note an alternative model proposed by Bath (1969, 1975), building on work by Paczyński et al. (1969). The *mass transfer instability* model has currently fallen out of favour but variations on its theme are periodically revived as a possible explanation for the superoutburst phenomenon. It is based on the premise that mass transfer through the L_1 point is unstable. The most-invoked cause for the instability is variations in the mass transfer rate from the secondary, most often attributed to irradiation (e.g., Meyer & Meyer-Hofmeister 1983; Osaki 1985).

Accretion discs are a universal phenomenon, playing a fundamental part in everything from the formation of planets around stars to the energy production at the cores of quasars. Those in dwarf novae are among the best studied because of their relative simplicity. Many of the principles of the disc instability model discussed here are used in similar approaches to the postulated accretion discs in active galactic nuclei (e.g., Mineshige & Shields 1990).

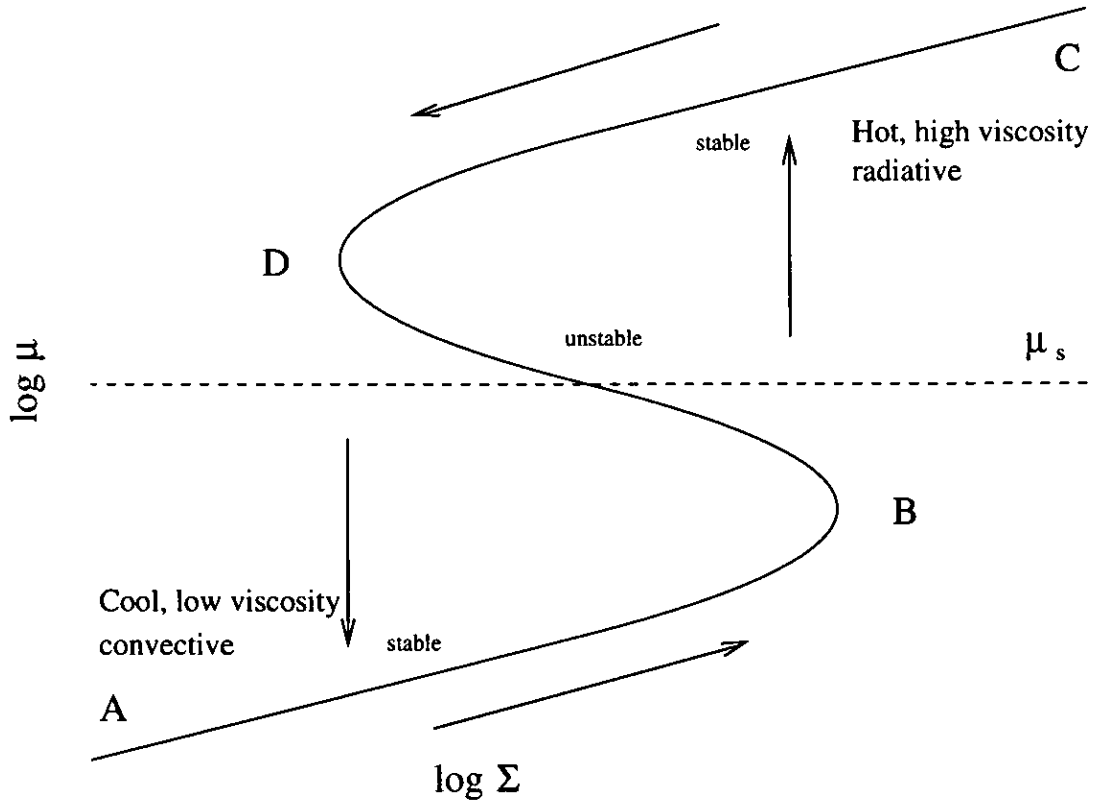


Figure 1.2: A schematic illustration of the S-curve in the $\mu - \Sigma$ plane. In dwarf novae, the steady state mass flux rate is on the unstable branch of the curve, leading to limit cycle behaviour. $A \rightarrow B$: μ increases steadily on viscous timescale. $B \rightarrow C$: μ jumps to upper branch on the thermal timescale. $C \rightarrow D$: μ decreases steadily on the viscous timescale. Finally, $D \rightarrow A$: μ jumps to lower branch on thermal timescale. In novalike variables, the steady state mass flux rate is on the hot, stable branch of the curve, while in Z Cam stars, the steady state mass flux rate is in the transition zone between the unstable and the stable regimes. See text for further details.

The superoutburst mechanism and the tidal resonance model

SU UMa dwarf novae undergo less frequent superoutbursts interspersed in the normal outburst cycle. These are brighter and longer in duration than normal outbursts. A second defining characteristic of SU UMa dwarf novae are the so-called superhumps, which manifest themselves as humps in the orbital light curve during superoutburst, and which drift in phase with a period $\sim 3\%$ longer than the orbital period of the system. Superhumps appear irrespective of inclination. The light curves of OY Car presented in Chapter 2 show very clear superhumps. Because the superhump period drifts through the orbital period at a well known rate ($\simeq 3\%$), the orbital periods of even face-on systems can be derived relatively accurately.

The currently accepted explanation for superoutbursts and associated superhumps was provided observationally by Vogt (1982), and theoretically by Whitehurst (1988a, b), Osaki (1989b) and Whitehurst & King (1991). It consists principally of a precessing, elliptical disc caused by asymmetric perturbation by the secondary star, leading to a tidal resonance phenomenon; this is known as the *tidal resonance model*. SU UMa systems typically have orbital periods $P_{orb} \leq 3\text{h}$ and mass ratios $q \leq 0.3$, and it is these factors that are thought to have a significant role in the production and growth of the tidal phenomena. These tidal instabilities are thought to provide a mechanism for the actual production of superoutbursts and superhumps.

Whitehurst (1988a, b), and Whitehurst & King (1991), using detailed numerical simulations of the eclipsing dwarf nova Z Cha (which has a mass ratio, $q = M_2/M_1 = 0.15$), found that tidal resonance caused a ring of higher density material to form, initially the outer edge of the disc, and which was subsequently converted into a precessing elliptical ring over the duration of the superoutburst. Optical observations of OY Car presented in Chapter 2 may show evidence for such an elliptical ring, or disc.

Superoutbursts are similar to normal dwarf nova outbursts in their rise and fall, so the central question to be addressed regards the extension of their duration. Osaki (1989b) explains that during a normal outburst (subsequent to a superoutburst) the disc radius is less than the tidal radius ($R_{disc} < R_{tidal}$), so little angular momentum is removed by tidal interactions, and not all of the excess mass is accreted. Through a series of normal outbursts, the disc will grow secularly in mass and radius until the disc radius is greater than the radius at which tidal resonance occurs ($R_{disc} > R_{tidal}$). Only in this case can the tidal effects produce an asymmetric disc, enhancing tidal torques and maintaining the disc in the high viscosity state, enabling the loss of accumulated angular momentum. This

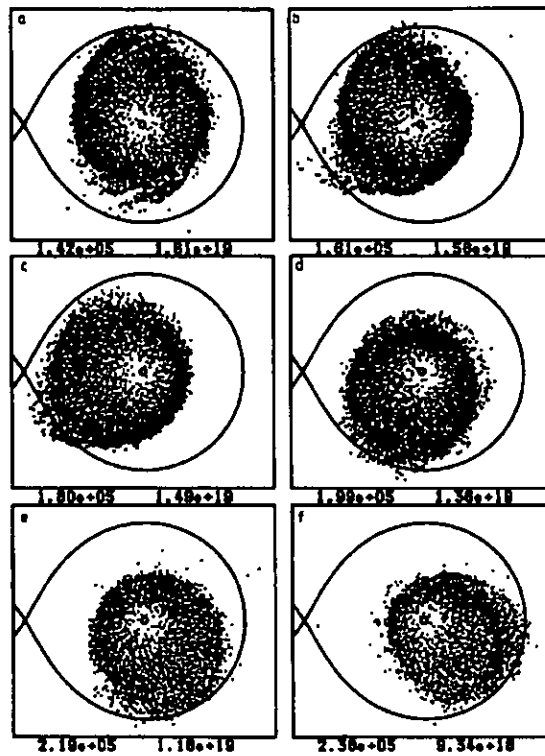


Figure 1.3: An illustration of the effects of tidal resonance from accretion disc simulations of a system with $q = 0.12$. The images are three orbital periods apart. From Whitehurst (1998a).

prolongs the outburst by allowing most of the gas to move to smaller radii and accrete onto the primary star. Warner (1995, and references therein) states that typically $\sim 10\%$ of the disc mass is accreted during a normal outburst, and $\sim 50\%$ during a superoutburst.

The superhumps themselves are thought to be connected to the disc. Observations of Z Cha and OY Car in the ultraviolet (Harlaftis et al. 1992a; Billington et al. 1996) show dips in the ultraviolet flux at times of optical superhump maxima. An increased vertical height at the disc edge, likely connected to the tidal resonance phenomenon, appears to be obscuring the central regions. This has the effect of reducing the ultraviolet flux, but subsequent reprocessing of this intercepted flux enhances the optical flux, producing the superhumps.

The presence or absence of superhumps has profound implications for the eclipse mapping process. This is discussed further in the context of the optical light curves presented in Chapter 2, some of which exhibit superhumps. Additionally, as these observations were obtained on the decline from superoutburst, superhump evolution is seen, and is also discussed.

1.4 The ‘iron curtain’

One final observational discovery needs introduction, mainly because of its bearing on later Chapters; this is the so-called ‘iron curtain’, which has been detected in the ultraviolet spectra of some high inclination dwarf novae in quiescence, and in some novalike variable spectra.

The ultraviolet spectra of dwarf novae in quiescence are composed of flux contributions from the white dwarf, accretion disc and bright spot, the strength of the latter two components dictated by the mass transfer rate through the disc. The ‘iron curtain’ phenomenon was first described in detail in an *HST* spectroscopic study of OY Car by Horne et al (1994). After decomposing the quiescent *HST* spectrum of OY Car into its constituent parts, Horne et al. encountered serious difficulties in fitting the spectrum of the white dwarf with the accepted solar abundance models because of a forest of FeII features centred around $\lambda \sim 1600 \text{ \AA}$ and $\lambda \sim 2500 \text{ \AA}$. The cause of the spectroscopic feature has been dubbed the ‘iron curtain’ for this reason and for the similarity of these features to those found in the spectra of early-type stars. The term was first coined — in the context of early-type stars — by Shore (1992).

During fitting of the white dwarf spectrum, Horne et al. found that raising the abundance of Fe to three times solar levels improved the quality of the fit somewhat, but implied a physically implausible situation — by what process can the photosphere of a CV white dwarf come to have three times the solar abundance of FeII? Horne et al. then began to investigate the possibility that a region other than the white dwarf photosphere may produce the features seen in the spectrum. The spectrum was thus modelled as a solar abundance white dwarf as absorbed by a veiling gas at $T_{\text{gas}} \sim 10^4 \text{ K}$, also of solar abundance. This improved the fit significantly, and the addition of a Mach ~ 6 velocity dispersion ($\Delta V \simeq 60 \text{ km s}^{-1}$ for $T \sim 10^4 \text{ K}$) subsequently optimised the fit.

While the veiling gas must be connected in some way to the disc (what else could produce the observed effect, once the white dwarf itself has been ruled out?), its actual location was still somewhat uncertain. When Horne et al. modelled the velocity dispersion as being due to the Keplerian velocity field of the disc, they found that the absorbing gas had to be distributed with $\Delta R/R = (R/12R_{\text{wd}})^{3/2}$, where ΔR is the thickness of the FeII curtain. Their best fit model puts the gas in the inner accretion disc with $R/R_{\text{wd}} \simeq 5$ and $\Delta R/R \simeq 0.3$, suggesting that the lower hemisphere of the white dwarf is simply obscured by the inner disc, not inconceivable considering OY Car’s inclination of 83° (Wood et al. 1989). However, this model leaves the upper hemisphere of the white dwarf in clear view,

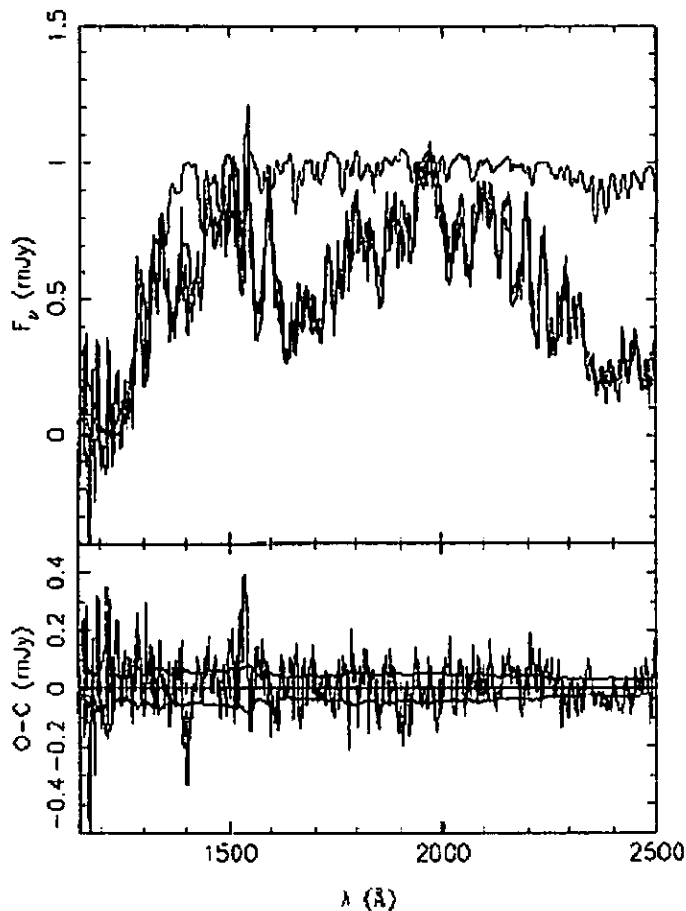


Figure 1.4: The ‘iron curtain’ detected in the *HST* ultraviolet spectrum of OY Car by Horne et al. (1994). The upper panel shows, the observed spectrum of OY Car and the best-fit solar abundance white dwarf spectrum viewed through a solar abundance veiling gas. An unveiled solar abundance white dwarf is shown for comparison. Lower panel shows residuals. From Horne et al. (1994).

whereas some of the absorption features are over 80% deep.

An alternative is that outer disc material is the source of the veiling gas. In order for the veiling gas to be associated with the outer disc region, though, the region must have supersonic ($\text{Mach} \simeq 6$) but sub-Keplerian ($\Delta V/V \simeq 0.07$) velocity disturbances. One hypothesis emerges from the fact that the bright spot could provide a conceivable mechanism to elevate the gas to $z/R \sim 0.12$ (needed to produce this effect for OY Car’s inclination). This gas would then require several Kepler periods to establish hydrostatic equilibrium; the same gas at 10^4 K, which produces the deep absorptions in the ultraviolet, has sufficient optical depth to produce the Balmer continuum and line emission characteristic of quiescent CV optical spectra.

However, follow-up observations of other high inclination systems by Catalán et al. (1998), including more observations of OY Car, show that the ‘iron curtain’ features are present around the orbit, lending weight to the suggestion that the absorbing gas originates

in the upper atmosphere of the disc and may not necessarily be linked to the impact region of the gas stream.

Perhaps the most startling finding of the Horne et al. (1994) study was the conclusion that the veiling gas had a column density of $N_H \simeq 10^{22} \text{ cm}^{-2}$, a value which is potentially difficult to reconcile with X-ray observations as at that column density the soft X-ray flux should be extinguished (Naylor & la Dous 1997). Note that in the X-ray regime, the absorption is measured as the equivalent hydrogen column density of a solar abundance gas; hydrogen itself ceases to be an absorber and that the metals absorb the X-rays.

Since the initial detection of an ‘iron curtain’ of OY Car, a raft of other systems have subsequently been discovered to show evidence for gas veiling the white dwarf spectrum. Archive *IUE* spectra of Z Cha and OY Car were retrospectively shown to display an ‘iron curtain’ overlying the white dwarf spectrum (Wade et al. 1994a). Similar spectral features have now been found in *HST* spectroscopic studies of AL Com (Szkody et al. 1998) and, very weakly, in WZ Sge and V2051 Oph (Catalán et al. 1998). There have been no detections thus far of veiling gas in low inclination systems.

1.5 Thesis Overview

Multiwavelength observations presented in this thesis investigate conditions in the accretion disc and boundary layer regions of OY Car in both quiescence and superoutburst. The results are discussed in terms of previous observations of OY Car itself and of similar systems, and in the context of the various spectral and physical components visible. The first three Chapters are concerned with this intriguing system.

The next Chapter branches out and considers systems other than OY Car. Because simultaneous *HST* and *ASCA* time has been scheduled but the data not yet obtained, a critical review of the modelling of ultraviolet spectra of various dwarf novae in quiescence (including OY Car), is also presented. The discussion is again in the context of the physical and spectral components visible.

The Chapters are organised as follows. Chapter 2 details optical observations of the 1994 Feb superoutburst of OY Car, and uses the eclipse mapping technique to derive some of the characteristics of the accretion disc during this high mass accretion episode. In Chapter 3 contemporaneous *ROSAT* X-ray observations are described, which reveal insights about the highest energy process taking place during this superoutburst.

Chapter 4 details further optical and X-ray observations of OY Car, this time in quiescence. An updated ephemeris is derived for the system from the optical data, and

this is subsequently used to phase the *ROSAT* X-ray light curve.

Chapter 5 anticipates the further simultaneous ultraviolet/X-ray observations from *HST* and *ASCA* by critically reviewing techniques for modelling the ultraviolet spectrum in quiescence using synthetic spectra. The techniques learned in the course of this Chapter are expected to contribute significantly to the analysis of the forthcoming data. Some of these techniques are tested on archive *IUE* and *HST* observations of similar systems, and the results compared with those in the literature.

Finally, Chapter 6 presents the conclusions of the thesis and details what results might be expected from the simultaneous data, including a discussion of the anticipated *ASCA* spectrum, and details of how the *HST* spectrum will be decomposed and modelled. Lastly, unanswered questions about OY Car and other systems, which will provide the basis for future work, are discussed.

Chapter 2

Optical observations of the 1994 Feb superoutburst of OY Carinae

2.1 Introduction

This Chapter concerns the eclipse mapping of ‘broad B ’ band optical data of OY Car, acquired at the end of the system’s 1994 Feb superoutburst as part of an X-ray/optical observing campaign. The aim of these observations, contemporaneous with the X-ray data presented in Chapter 3, was to investigate the extent of the thickening of the disc during superoutburst and on the decline. The X-ray observations, because of the inclination of the system, in principle allow constraints to be placed on the location of the X-ray source.

The eclipse mapping technique, first introduced by Horne in 1985, has established itself as one of the most important methods for studying and deducing the properties of the accretion discs of many different types of CV. One of the basic assumptions of the original method is that the disc lies flat in the orbital plane. Over the years, however, there has been mounting evidence, in all wavelengths, for substantial vertical structure in the discs of dwarf novae in outburst and superoutburst, and in the discs of novalike variables (see e.g., Naylor et al. 1987, 1988; Naylor 1989; Harlaftis et al. 1992a, b; Wood et al. 1995b; Robinson et al. 1995; Billington et al. 1996; Mason et al. 1997).

While the data presented here are not the first data set of this type (similar data sets are discussed in Krezeminski & Vogt 1985, Schoembs 1986, Naylor et al. 1987, and Hessman et al. 1992), this is the first time light curves obtained from OY Car, or any similar system, in superoutburst or on the superoutburst decline, have been explicitly mapped

with a flared disc. This in principle allows the derived flare angles to be compared with those obtained from normal outburst data sets.

The observations are described in Section 2.2. Section 2.3 describes the disc mapping process and includes a review of the eclipse mapping method. The results are described in Section 2.4, where they are compared with recently published results from observations of Z Cha in outburst, and with older observations of OY Car itself in outburst. Conclusions are presented in Section 2.5.

2.2 Observations and data reduction

Monitoring observations made by the Variable Star Section of the Royal Astronomical Society of New Zealand (VSS RAS NZ) confirm that OY Car underwent a superoutburst on 1994 February 1, stayed at maximum for 7 days, and returned to quiescence over a subsequent 13 day period. The present optical observations were obtained at the end of the superoutburst plateau and on the decline. There is one contemporaneous optical/X-ray observation (1994 Feb 8); the X-ray data cover the period leading up to these optical observations and, as will be seen in Chapter 3, support the conclusions arrived at from the eclipse mapping in this Chapter.

Figure 2.1 shows the magnitude of OY Car before, during and after the 1994 Feb superoutburst, and uses data both from the VSS RAS NZ and the present observations by way of illustration.

High time resolution optical photometric light curves were obtained nightly from 1994 Feb 8 to Feb 15 by Prof. J. Patterson on the 1m telescope at CTIO, Chile. The dates and times of each observation are shown in Table 2.1, the journal of observations. The Automated Single-Channel Aperture Photometer (ASCAP) was used in conjunction with a Hamamatsu R943-02 photomultiplier tube. All observations were taken using an integration time of 5 sec through a CuSO_4 filter. This filter has a wide bandpass (3300-5700 Å) which gives a broad *B* response, but includes a substantial amount of *U* (3000 – 4200 Å, approx). The counts per 5 sec were corrected for atmospheric extinction and converted to milli-Janskys, and phased with the orbital period using the updated ephemeris derived in Chapter 4.

2.2.1 The light curves

The overall behaviour of the system over the eight days of observations is shown in Figure 2.2. The decline in flux is marked over the period of the observations, as expected

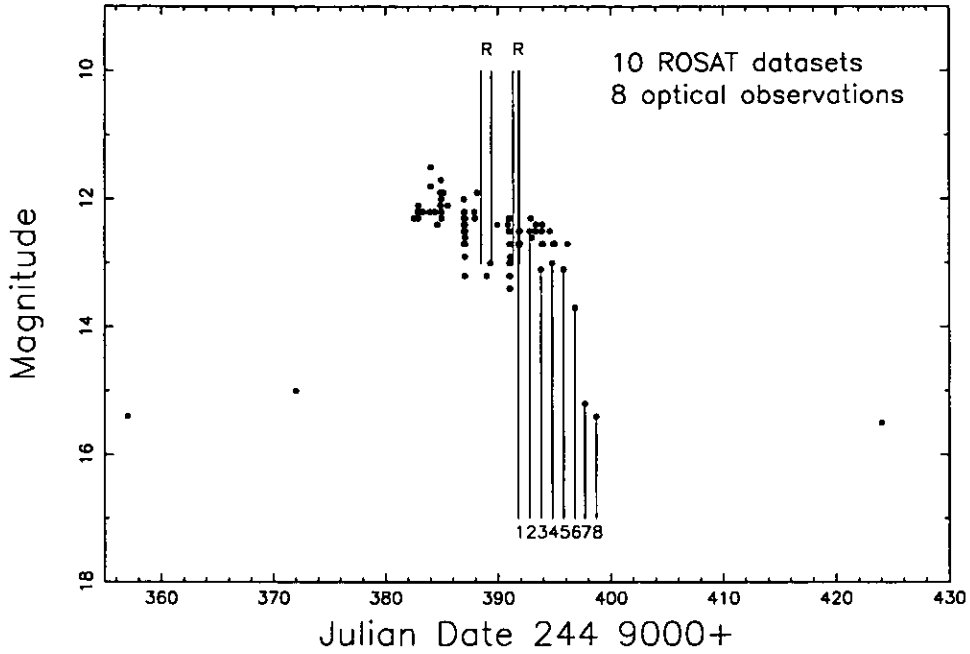


Figure 2.1: The light curve of OY Car during the 1994 Jan superoutburst, from observations supplied by the VSS RAS NZ. The X-ray observations are presented in Chapter 3. The optical data discussed in this Chapter, obtained on the decline, are also shown. The mean, out-of-eclipse flux from these data have been converted to Oke AB magnitudes using $AB = -2.5 \log f_\nu - 48.60$ (Oke 1974), to illustrate the decline in brightness over the course of the observations.

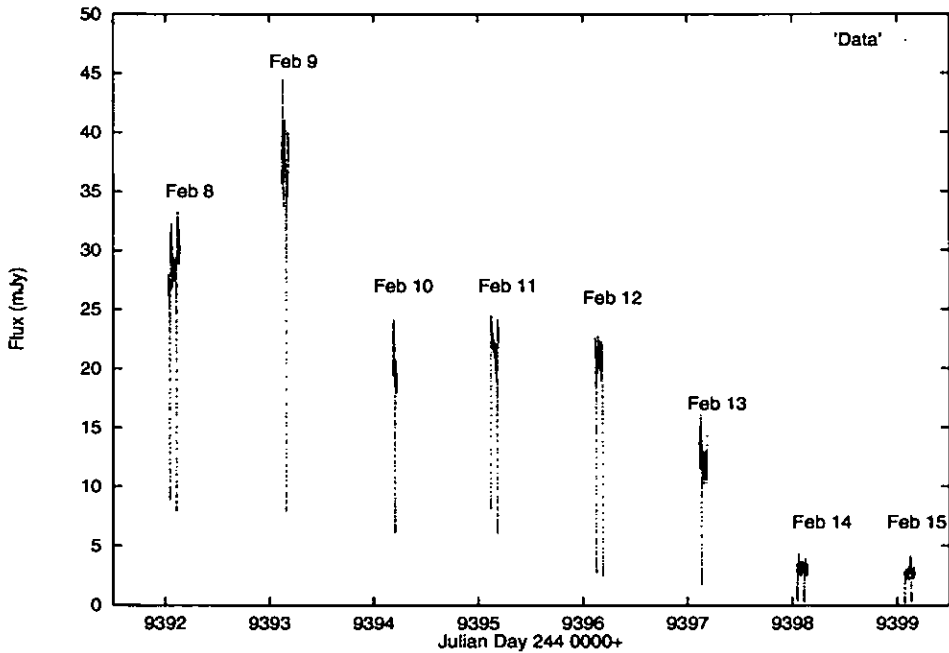


Figure 2.2: All the optical light curves of OY Car obtained at the end of the superoutburst of Feb 1994. The decline in flux over the period in question is clearly seen. Each eclipse covered is also clearly seen; expanded plots of each observation are shown in Figures 2.3 and 2.4. The observations taken on 1994 Feb 14 and 15 are virtually at the quiescent level.

Table 2.1: Journal of photometric observations obtained by Prof. J. Patterson at CTIO, Chile, during superoutburst and on the decline.

UT Date	UT start	HJED start 2449300+	Duration (sec)
1994 Feb 8	06:21:22	91.764 84	9452
1994 Feb 9	07:26:04	92.810 99	5647
1994 Feb 10	08:12:09	93.843 03	3606
1994 Feb 11	07:24:47	94.810 17	6358
1994 Feb 12	07:26:03	95.811 09	6324
1994 Feb 13	07:22:58	96.807 62	6521
1994 Feb 14	06:32:42	97.774 11	8641
1994 Feb 15	06:48:22	98.785 03	8427

from a glance at Figure 2.1, with an especially sharp drop (~ 28 per cent) between Feb 13 and Feb 14. Figures 2.3 and 2.4 show the individual optical light curves obtained over the period from 1994 Feb 8 to 1994 Feb 15, phased onto the orbital period of OY Car using the ephemeris derived in Chapter 4 (eqn. 4.1).

The apparent rise in flux between the observations of 1994 Feb 8 and 1994 Feb 9 is real. Much of the excess flux in the light curve of Feb 9 appears to come from the large superhump feature, which covers almost 0.5 in orbital phase. Orbital coverage is such that it is difficult to find a ‘continuum’ level from which to make a quantitative estimate of the flux rise, but if the flux immediately after eclipse is taken as a ‘continuum’ level, then the rise in flux above the average flux level of the previous day is ~ 20 per cent.

The early eclipses appear to be roughly symmetric, but become increasingly asymmetric as the decline progresses. On Feb 14, the superhump is at $\phi \sim 0.2$, and the eclipse shape is strikingly similar to that for quiescence; however, by Feb 15, the superhump is at $\phi \sim 0.8$, and the feature previously identified as the bright spot egress gives way again to a more round-bottomed eclipse. For the ‘most quiescent’ light curve, that of Feb 14, the method of Wood et al. (1985; of which more in Section 4.3.1) was used to measure the half-flux points of the eclipse, which in quiescence correspond to mid-ingress and egress of the white dwarf. A value of 255 ± 5 s was found for the eclipse width, slightly longer than that of the white dwarf eclipse in quiescence (231s; Wood et al. 1989), and a value that probably results from an over-estimation due to the superhump feature that is near the eclipse.

A close examination of the light curves of Feb 8 and 11 (Figure 2.3), where two eclipses are covered, shows that there are variations in the eclipse depths. In both cases, the superhump is moving away from the eclipse phase so that the superhump is further away

from the eclipse in the second eclipse. The increase in the depth of the second eclipse can be attributed solely to the fact that the superhump has moved.

The superhumps themselves show marked variations. On Feb 8 and Feb 9, the superhump is ~ 0.25 mag; it becomes less distinct on Feb 11 and Feb 12, but again becomes visible from Feb 13. Also visible are dips arising from self-absorption, similar to those seen in *HST* observations of OY Car in superoutburst by Billington et al. (1996). They can be attributed to obscuration of the central parts of the disc by the superhump material itself, explained by Billington et al. (1996) as time dependent changes in the thickness of the disc at the outer edge. This azimuthal asymmetry is distinct from the wholesale physical flaring of the disc. The best example of the dip phenomenon is in the light curve of Feb 8, where it can be seen to occur in the superhump over two consecutive orbital periods. The dips come and go over the course of the observations, being visible in the light curves of Feb 8, 9, 13, and 15, but not visible in the light curves of Feb 10, 11, 12 and 14. The superhump peaks are difficult to define when the dips are significant, but an approximate ephemeris is given by (uncertainties in parenthesis)

$$\text{HJED}_{sh} = 2449391.76597 + 0.06495(442)E_{sh} \quad (2.1)$$

A comparison with the updated orbital ephemeris of the system calculated in Chapter 4 shows that the superhump period is 2.9% longer than the orbital period, practically the same as the canonical value of 3%. Calculations using this approximate superhump ephemeris reveal that the superhumps visible in the light curves of Feb 14 and Feb 15 are late superhumps, shifted in phase from the normal superhumps by 180° . Both the late superhump ($\phi \sim 0.25$) and a faint quiescent orbital hump ($\phi \sim 0.85$) can be seen in the light curve of Feb 14. The late superhump visible in the Feb 15 light curve is enhanced in intensity due to a coincidence with the quiescent orbital hump.

The light curves of 1994 Feb 10, 13, 14 and 15 show clearly that the orbital phase at which the hot spot is first eclipsed (i.e., the hot spot ingress) changes on a nightly basis. This effect has been seen in similar observations of OY Car by Schoembs (1986) and Hessman et al. (1992), and has been interpreted as being due to the eclipse of the hot spot on the edge of a precessing, non-circular disc. Hessman et al. (1992) use the phase information of a large number of eclipses (20, including their own and those of Schoembs 1986) to compile a set of disc radii at various times which correspond to different positions in a rotating frame defined by the disc beat period¹. Local disc radii are the

¹The beat period is defined as $P_b = P_s P_{orb} / (P_s - P_{orb})$ where P_s and P_{orb} are the superhump period and orbital period, respectively. OY Car has a well defined beat period of 2.6 days (Warner 1995, and references therein).

only explanation for the observed changes in the eclipse times of the hot spot, given a well defined secondary shadow and a constant gas stream trajectory. The result (illustrated in a “difficult diagram” - Hessman et al. 1992), after determining the geometry of the hot spot eclipses, measuring the eclipse phases, and calculation of the relevant quantities (including the stream trajectory and the shadow of the secondary) is a distinctly non-circular disc. Unfortunately, a similar analysis of the light curves presented here would produce too few points for a quantitative analysis.

2.3 Mapping the disc

2.3.1 Review of the eclipse mapping method

The eclipse mapping method developed by Horne (1985a) is used here to investigate the surface brightness distribution of the disc during the superoutburst. This technique is established as one of the most important methods for studying accretion discs in many types of CV. The method for recovery of the surface brightness of the disc from photometric data is based on the theory of image entropy, originally introduced in Gull & Daniel (1978), and the development of an optimised Maximum Entropy (ME) algorithm, by Bryan & Skilling (1980) and Skilling & Bryan (1984). The Maximum Entropy Method (MEM) is applied to the problem of deconvolving the eclipse profile. For reviews of the method see e.g. Wood (1994) and Warner (1995).

Fundamentally, the method involves synthesising eclipse light curves and then using the MEM procedure to find the positive disc image that is consistent with the data and which maximises the image ‘entropy’, subject to certain criteria.

Light curve synthesis

In order to calculate a synthetic eclipse light curve, it is assumed that the tidally distorted surface of the secondary star is given by the corresponding critical surface of the Roche potential:

$$\Psi = \frac{1}{1-q} \cdot \frac{1}{R_{wd}} + \frac{q}{1+q} \cdot \frac{1}{R_s} - \frac{S^2}{2} \quad (2.2)$$

where R_{wd} and R_s are distances from the white dwarf and red-dwarf centres of mass (in units of the binary separation a), S is the distance to the axis of rotation, and $q = M_s/M_{wd}$ is the binary mass ratio. This is an alternative formulation of eqn. 1.1.

With the further assumptions that

- (i) The accretion disc lies flat in the orbital plane,

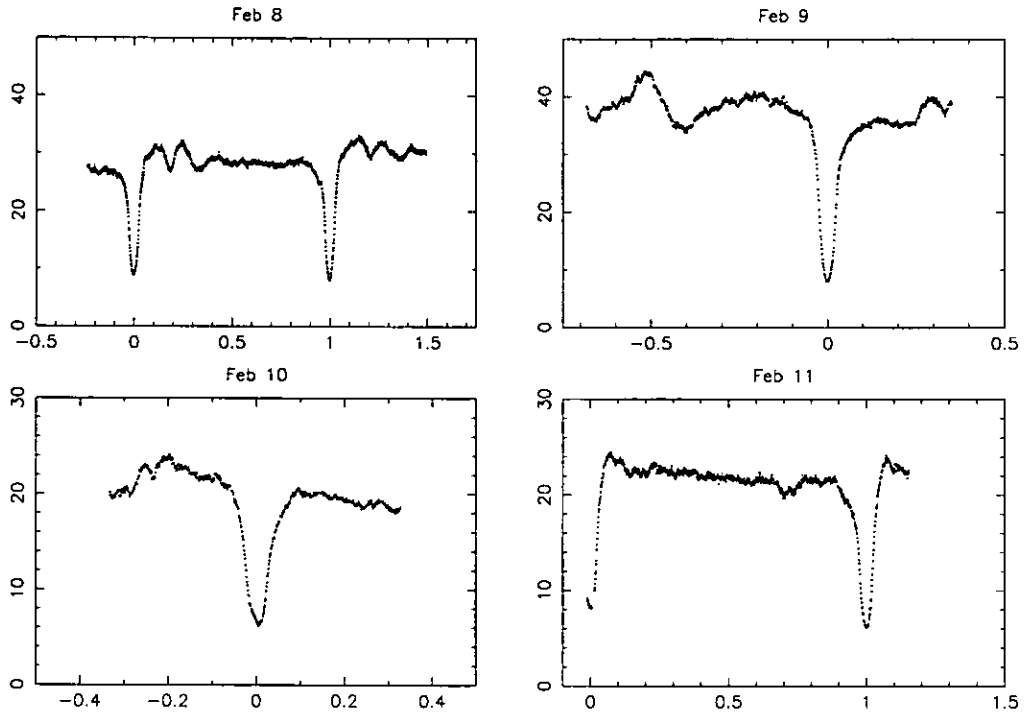


Figure 2.3: Four optical light curves of OY Car in superoutburst. The x-axis is orbital phase, the y-axis mJy. Note that the scale of the y-axis changes from Feb 9 to Feb 10.

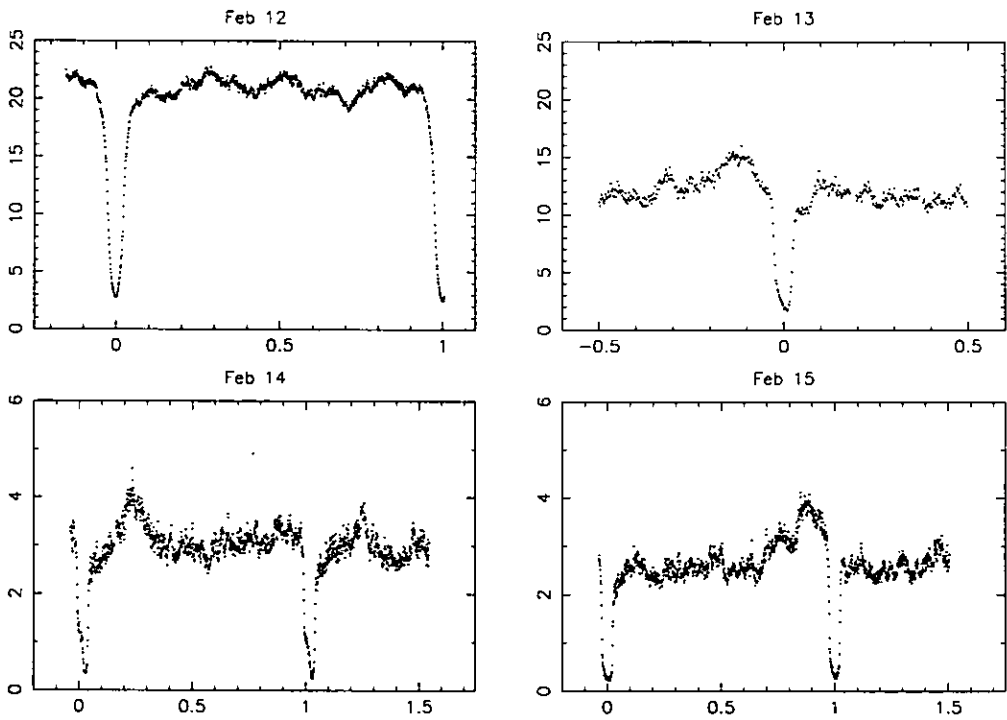


Figure 2.4: Four more optical light curves of OY Car on the decline from superoutburst. The x-and y-axes are as for figure 2.3. Note that the scale of the y-axis has changed.

- (ii) The only changes in flux are due to the eclipse by the secondary star, and
- (iii) That the emitted radiation is independent of orbital phase (i.e., the observed surface brightness distribution of the disc remains fixed with respect to the binary); this disallows time-dependent changes on the orbital period, thus superhumps cannot be mapped,

a light curve can be calculated from a disc *image* as detailed below. The flat disc approximation fails if the disc edge intercepts the line of sight, i.e. if $90 - i > \alpha/2$, where α is the disc opening angle ($= 0$ if a flat disc is assumed). For this Section and the remainder of the Chapter, α will be used to denote the opening angle of the disc. Thus $\alpha/2$ is the flare half-angle.

For convenience when discussing their alternative approaches, the following notation is taken from the concise summary of the eclipse mapping method in Baptista & Steiner (1993). The surface of the disc is divided into a Cartesian grid comprised of N^2 elements that cover a square region of side length λR_{L1} , centred on the white dwarf and bisected along one edge by the L_1 point. The significance of using the L_1 point is illustrated in Horne (1985a), where it is shown that the Roche-lobe occupied by the primary is nearly independent of the mass ratio q , provided distances are measured in units of R_{L1} , the distance from the centre of the white dwarf to the L_1 point (see Figure 1 of Horne 1985a). Thus by varying the values of λ and N , different fractions of the primary lobe area can be covered at different spatial resolutions.

The spatially integrated disc flux at binary phase ϕ is calculated by summing the contributions of all visible surface elements:

$$m_\phi = \theta^2 \sum_{j=1}^N I_j V_{j\phi}, \quad (2.3)$$

where I_j is the intensity along the line-of-sight to surface element j , and $V_{j\phi}$ (called either the occultation function or the visibility function) is the fraction of the element j that is visible at phase ϕ . The visibility function is dependent on the intrinsic geometry of the eclipse (i, q), and the chosen image matrix (λ, N). The solid angle of each pixel as seen from Earth is

$$\theta^2 = \left[\frac{(\lambda R_{L1})^2}{Nd^2} \right] \cos i \quad (2.4)$$

where i is the inclination of the system, and d is its distance from the Earth.

The geometry of the eclipse can then be specified accurately using only three parameters:

- the mass ratio, q , which controls the size of the Roche lobes;
- the phase of conjunction, phase zero, ϕ_0 ; and
- the phase width of the eclipse, $\Delta\phi$, at the centre of the disk, which, once q has been given, determines the inclination, i .

A light curve can now be calculated by specifying values for the above parameters. The MEM technique can subsequently be used to optimise the fitting of the synthetic light curve, given by m_ϕ , to the data, given by d_ϕ .

Image reconstruction using Maximum Entropy Methods

Maximum Entropy images are found “by maximising a scalar function in image space, the image ‘entropy’, subject to the constraint that the predicted data associated with the image are consistent with the observed data” - Horne (1985a). The code used for the constrained maximisation of the entropy was developed by Skilling. The algorithm is described in Skilling & Bryan (1984), and the FORTRAN implementation, MEMSYS, is described in Burch et al. (1983). MEMSYS is available on the UK STARLINK network.

The entropy function is defined with respect to a default image D :

$$S = - \sum_{j=1}^N p_j \ln \left(\frac{p_j}{q_j} \right) \quad (2.5)$$

where

$$p_j = \frac{I_j}{\sum_k I_k} \quad q_j = \frac{D_j}{\sum_k D_k} \quad (2.6)$$

where I_j is the image value at pixel j and D_j is the corresponding value for the default image. The above equations include *a priori* information in the default image D :

$$D_j = \frac{\sum_k \omega_{jk} I_{jk}}{\sum_k \omega_{jk}} \quad \omega_{jk} = \exp \left[-\frac{(R_j - R_k)^2}{2\Delta^2} \right] \quad (2.7)$$

where ω_{jk} is a weighting and R_j and R_k are the distances of the pixels j and k from the centre of the disc. The definition above, called the “radial profile default” (Horne 1985a), sets D_j as the axisymmetric average of the image I_j , suppressing azimuthal information in the default image and maintaining the radial structure of I_j on scales greater than Δ . Δ is called, in Baptista & Steiner (1993), the “radial blur width”. It sets the extension of the influence of the entropy in the radial direction through the default image D_j .

The input data d_ϕ are phase-binned eclipse profiles, modelled with simulated light curve fluxes as values of m_ϕ . If the number of phase bins in the input data is M , and

the uncertainties associated with the lightcurve are given by σ_ϕ , then these uncertainties give information as to how well determined the eclipse profile is. The data constraints (how well the simulated light curve matches the observed light curve) are imposed by the familiar reduced χ^2 -statistic:

$$\chi^2 = \frac{1}{M} \sum_{\phi=1}^M \frac{(m_\phi - d_\phi)^2}{\sigma_\phi^2} = \frac{1}{M} \sum_{\phi=1}^M r_\phi^2 \quad (2.8)$$

By maximising the entropy, S , of the image map relative to the default map, subject to the constraint that the predicted light curve fits the data with a specific value of χ^2 , a balance is achieved between the entropy and the data. As described in Horne (1985a), “When the data strongly constrain the image, the entropy has little effect. When the data is very noisy, the image is determined primarily by the entropy”.

In practice, the default map is specified by the user and is usually assumed to have azimuthal symmetry, thus forcing the resulting disc map to be as azimuthally symmetric as is possible given the data. This approach has been used in the following analysis. In a more complicated default map, the user risks losing global information at the expense of specifics, although even with the azimuthally symmetric default map, specific information emerges (see Section 2.4). An initial image evolves through iterated adjustments by MEMSYS towards the ME image. MEMSYS tries first to reduce the value of χ^2 until the (user defined) target value, CAIM, is reached. Subsequently, $\chi^2 = \text{CAIM}$ is maintained while the entropy is increased. As a result, discussions of the quality of the fit in terms of the absolute value of χ^2 are not generally undertaken, as in the case of eclipse mapping, a specific value of χ^2 is being *aimed for*, whilst in other implementations a specific value *is arrived at*.

Alternative approaches and recent developments

A review of some of the recent developments in the eclipse mapping field can be found in Wood (1994).

The alternative approach of Baptista & Steiner (1991, 1993), especially useful for eclipse mapping of low signal to noise data, involves the introduction of two further constraint functions to be used in conjunction with the χ^2 statistic. These were developed to avoid the overfitting of parts of the light curve, a common problem that occurs when the χ^2 statistic alone is used, and which naturally results in spurious features appearing on the resulting disc map. Baptista & Steiner first define the T' -statistic, given by:

$$T' = \frac{1}{M} \sum_{\phi=1}^M \frac{(m_\phi - d_\phi)}{m_\phi \sigma_\phi} = \frac{1}{M} \sum_{\phi=1}^M \frac{r_\phi}{m_\phi} \quad (2.9)$$

The residuals in the overfitted parts of the light curve tend to be of the same sign, thus the T' -statistic was developed to reduce the bias in the residuals that occurs when the χ^2 -statistic is used. In effect, this constraint function measures the correlation between the residuals and the inverse of the fluxes at each phase. In practice, the T' -statistic is used in conjunction with the χ^2 -statistic. Tests on light curves of the novalike variable V4140 Sgr, maximising the entropy S such that the fit to the data had a specific χ^2 and T' , improved the quality of the fit in low signal to noise light curves (Baptista & Steiner 1991).

A quantitative assessment of the improvement in the fit (to a synthetic data set) was provided by a quality parameter Q , a complex function composed of a combination of yet another χ^2 indicator of the goodness of the reconstruction, a T -statistic defined in Reiter & Pfeiderer (1986) to evaluate the presence of correlated residuals, and a granulation indicator to measure the presence of transposed noise from the light curve to the reconstruction.

On the basis of the findings from reconstructions using the $\chi^2 + T'$ -statistic, Baptista & Steiner (1993) decided that the T' statistic is, like the χ^2 statistic, flux-dependent, which means that it does not act equally across the range of the light curve in question. Baptista & Steiner (1993) therefore introduced the R -statistic, given by:

$$R = \frac{1}{\sqrt{M-1}} \sum_{\phi=1}^{M-1} r_{\phi} \cdot r_{\phi+1} \quad (2.10)$$

The advantage of this expression is that for uncorrelated residuals each term has an equal chance of being positive or negative: neighbouring residuals with the same sign contribute a positive term to the R -statistic, while the converse is true if they are negative. Early results suggest, on the basis of the quality parameter Q , that the $\chi^2 + R$ statistic produces better reconstructions than those of the $\chi^2 + T'$ or the χ^2 alone. These alternative approaches to the original method are still not implemented generally — note that results presented throughout the rest of this Chapter were obtained using the original χ^2 constraint only.

Another major development to the standard eclipse mapping technique concerns adaptation of the light curve synthesis code to take into account the physical flaring of the disc, i.e., one that increases in thickness outward from the centre, but is not concave. The method was first introduced in Wood (1994), and application of the method to data of Z Cha in outburst followed in Robinson et al. (1995). The modification effectively changes the visibility function of each pixel to take into account the disc flare.

As with the original definition of the visibility function, this can only be valid when the edge of the disc does not obscure the line of sight to the disc centre, i.e. when $\alpha/2 \leq 90 - i$.

This implementation is used in the analysis throughout the rest of this Chapter.

Rutten (1998) has recently developed a 3D eclipse mapping method, which allows modelling of a three dimensional disc in conjunction with the surface of a Roche lobe filling secondary star. This flexible geometry allows information to be extracted from the entire light curve, and not just the eclipse phases as in the standard method.

What differentiates Rutten's method from those described previously is the 3D element, and the ability to parameterise the contribution of the secondary star. The grid used is a new development, consisting of a large number of triangular tiles which describe the surface of the disc and the secondary star. As with previous methods, the disc surface is built on a Cartesian grid centred on the primary star. However, a third orthogonal coordinate is added to each point in the plane to define the 3D shape of the disc. As the grid now possesses a top and bottom surface, the disc rim can be accurately represented. Many different options are available: "optically thin" elements can be defined; the inner hemisphere of the secondary can be irradiated; etc. Rutten (1998) anticipates that this method will be most useful when applied to light curves where both the secondary star and the accretion disc contribute substantially.

Optimisation of the light curve fitting is achieved, as before, using MEM techniques. However, different light sources can have similar effects on the light curve, so as Rutten (1998) states "Even more so than in the case of standard eclipse mapping, with 3D light curve fitting, results must always be treated with caution ...". Apart from the versatile geometry, similar constraints apply to the 3D mapping technique as to the standard technique. At the time of writing, Rutten's method has not been used on anything but synthetic data sets.

Finally, there is Physical Parameter eclipse mapping (PPEM; Vrielmann et al. 1999). Only very recently introduced, the method reconstructs spatially resolved maps of physical parameters such as temperatures and even surface densities. This is achieved by fitting eclipse light curves at several wavelengths simultaneously with the aid of a model which describes the dependence of the disc spectrum on the physical parameters. The main difference between this method and the classical method is the replacement of the intensity distributions that are the normal outcome of the fitting process with distributions in physical parameters. As such, the method requires the explicit choice of a model describing the intensity of the disc as a function of the physical parameters to be mapped. The choice of model is crucial and requires a knowledge of the systematic effects introduced by the use of a certain model in order to estimate the reliability of the reconstructed parameters. The model may be as simple as a blackbody spectrum or as complicated as the model

atmospheres described in Chapter 5. It must be said that the method is rather complicated and as Vrielmann et al. (1999) state “Only when we know the behaviour of the parameters can the resulting maps be interpreted with confidence . . . the PPEM method cannot give us more information about the accretion disc than the used model allows”.

2.3.2 Mapping the 1994 Feb superoutburst disc

The eclipse mapping program used in this analysis is the extension of Horne’s original code that allows a flared disc. The implementation was written by Dr. J.H. Wood. That the line of sight must intercept the disc surface constrains the allowed flare angles to $\alpha/2 < 90 - i$, which, given the $83^\circ.3$ inclination of OY Car (Wood et al. 1989), constrains $\alpha/2 \lesssim 6^\circ$ if realistic results are to be obtained.

Method

The disc dominates the flux at the optical bandpass used; thus the contribution from the secondary will be negligible. In choosing which light curves to map, those in which eclipses were contaminated with superhump light were avoided, as the presence of this excess light can affect the disc light distribution and cause spurious artifacts, especially if near phase zero (see e.g., Warner & O’Donoghue 1988); this excess light is anyway precluded by the assumptions of the eclipse mapping process. For this data set, it is clear that the light curves of 1994 Feb 8, 10, 11, 13, and 15 exhibit signs of superhump light contamination of the eclipse phase. These light curves also show dips, discussed above; these would render the eclipse mapping program invalid, as in this case $\alpha/2 > 90 - i$. The light curves of 1994 Feb 9 and 12 were thus chosen for mapping. An attempt was made to map the light curve of 1994 Feb 15, but the poor signal to noise of the observation made this difficult and introduced too much uncertainty for a realistic disc map.

The February 9 and February 12 data were each divided into 40 bins for orbital phase $-0.2 \leq \phi \leq 0.2$. It was found that simple Poissonian statistics produced uncertainties that were small when compared to the intrinsic flickering of the data, so a constant percentage error derived from the ratio of the flickering to the average flux out of eclipse was adopted, thus giving a more realistic measure of the intrinsic scatter of the data. This constant percentage error was different for each data set, as the mean out of eclipse flux has dropped by a factor ~ 40 percent in the 3 day period between the light curves. A mass ratio $q = 0.102$, a distance $d = 82$ pc, and inclination $i = 83.3^\circ$ were used as standard parameters, all from Wood et al. (1989), and a Cartesian grid of 69×69 pixels, with the white dwarf at the centre, was used to cover the accretion disc plane.

A flat disc was assumed for initial mapping purposes. This produced maps with pronounced artifacts (such as front-back asymmetries or bright rings at the outer edge) and a high value of χ^2 , as would be expected if the flare had been ignored (Wood 1994). A constant flux was subtracted from the light curve of Feb 12 and the result was mapped with a flat disc; however, artifacts were still present (cf. Robinson et al. 1995). A flared disc was then adopted, with the value of the disc opening angle, α , being gradually incremented from the flat case. This produced an immediate improvement in the front-back asymmetry and reduced the value of χ^2 . Acceptable fits to each light curve were subsequently obtained by using a combination of the front-back asymmetry and χ^2 diagnostics. The corresponding disc opening angles were $\alpha = 11^\circ \pm 1^\circ$ for the 1994 Feb 9 light curve, and $\alpha = 10^\circ \pm 1^\circ$ for the Feb 12 light curve, respectively, where the errors have been estimated from the best fit judged on χ^2 -values. The resulting contour maps from the discs of February 9 and February 12 can be seen in Figures 2.5, 2.7.

The radial temperature distribution of a disc in a steady state is predicted to be (e.g., Frank et al. 1992):

$$T^4 = \frac{3GM_{wd}\dot{M}}{8\pi\sigma r^3} \left[1 - \left(\frac{R_{wd}}{r} \right)^{1/2} \right] \quad (2.11)$$

where T is the temperature at radius r . This can be compared with the blackbody temperature calculated from the reconstructed disc, as shown in Figures 2.6 and 2.8.

For comparison, the disc map and temperature distribution obtained when the light curve of Feb 12 is fitted with a flat disc are shown in Figures 2.9 and 2.10. Figure 2.11 shows the light curves calculated from the flat and flared disc maps, plotted with the actual data. It is obvious that the flared disc (reduced $\chi^2 = 0.5$) is a far better fit than a flat disc (reduced $\chi^2 = 5.1$).

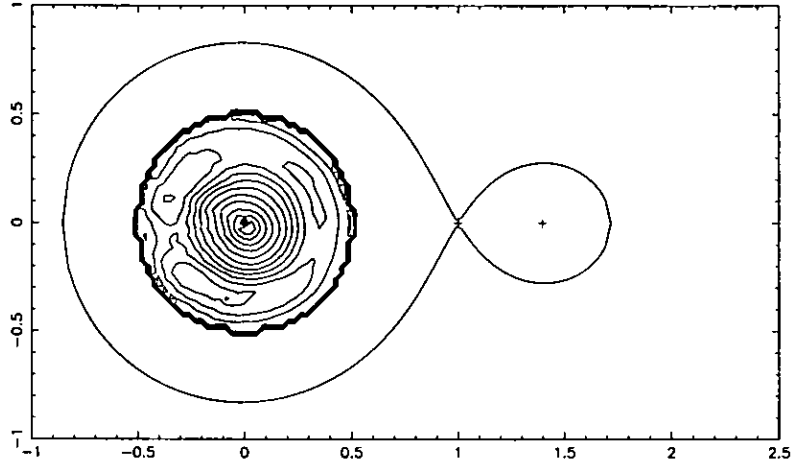


Figure 2.5: The reconstructed surface brightness in the disc of February 9. The flare angle is $\alpha = 11^\circ$. The contour scale is logarithmic, with a contour interval of 0.2 decades. The x- and y-axes are in Roche lobe units.

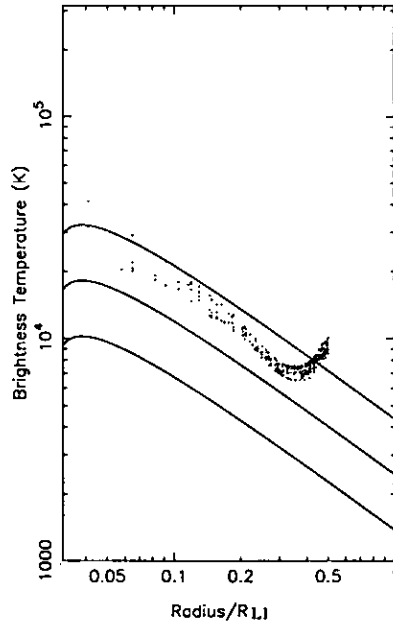


Figure 2.6: The brightness temperature distribution in the Feb 9 disc. Models of steady state optically thick discs for, from top to bottom: $\dot{M} = 10^{-9}$, 10^{-10} , and $10^{-11} M_\odot \text{ yr}^{-1}$, are also shown. The x-axis is distance in units of R_{L1} .

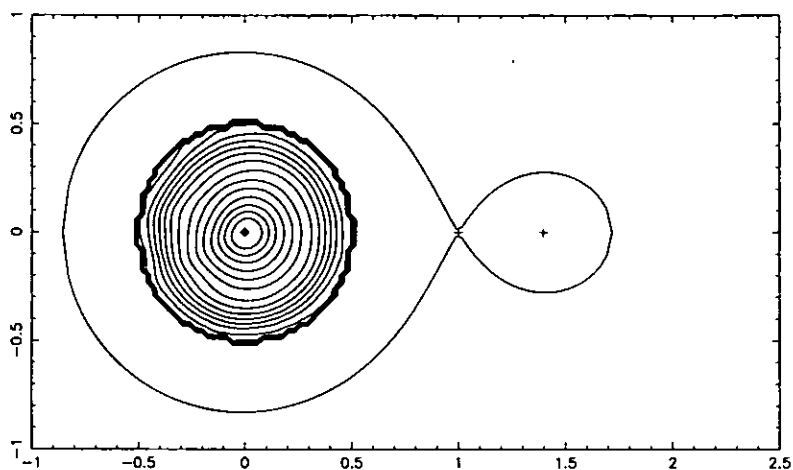


Figure 2.7: The reconstructed surface brightness in the disc of February 12. The flare angle is $\alpha = 10^\circ$. The contour scale is logarithmic, with a contour interval of 0.2 decades. The x- and y-axes are in Roche lobe units.

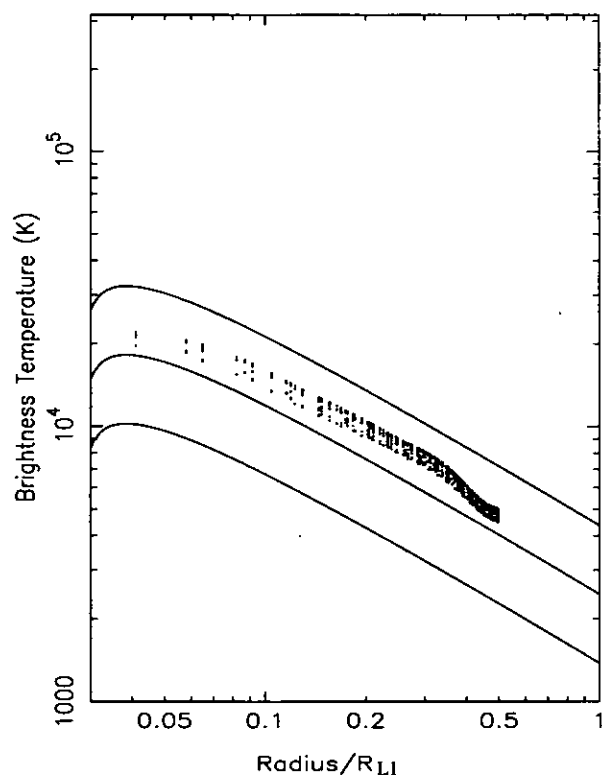


Figure 2.8: The brightness temperature distribution in the Feb 12 disc. Models of steady state optically thick discs for, from top to bottom: $\dot{M} = 10^{-9}$, 10^{-10} , and $10^{-11} M_\odot \text{ yr}^{-1}$, are also shown. The x-axis is distance in units of R_{L1} .

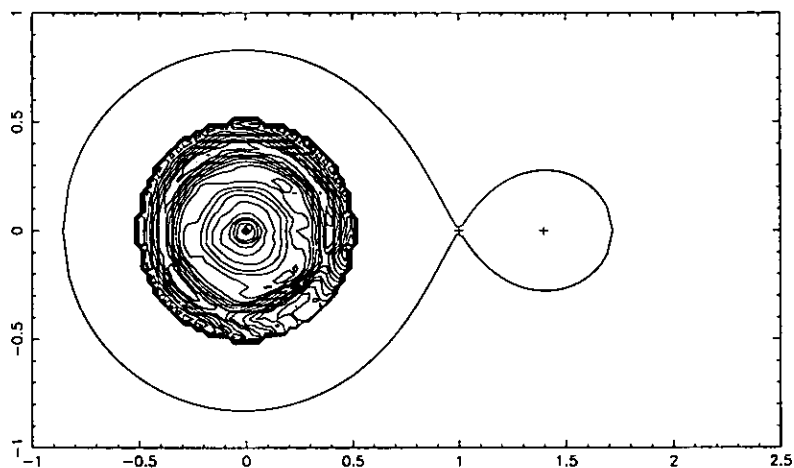


Figure 2.9: For comparison with Figure 2.7, this is the reconstructed surface brightness in the disc of February 12 using a flat disc model. The contour scale is logarithmic, with a contour interval of 0.2 decades. The x- and y-axes are in Roche lobe units.

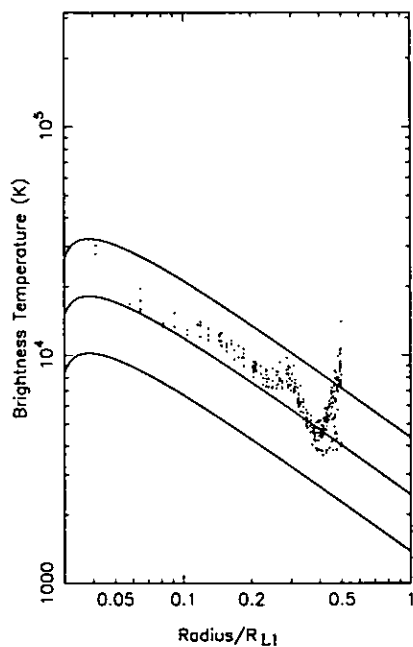


Figure 2.10: The corresponding brightness temperature distribution in the Feb 12 disc when fitted with a flat disc model. Models of steady state optically thick discs for, from top to bottom: $\dot{M} = 10^{-9}$, 10^{-10} , and $10^{-11} M_{\odot} \text{ yr}^{-1}$, are also shown. The x-axis is distance in units of R_{L1} .

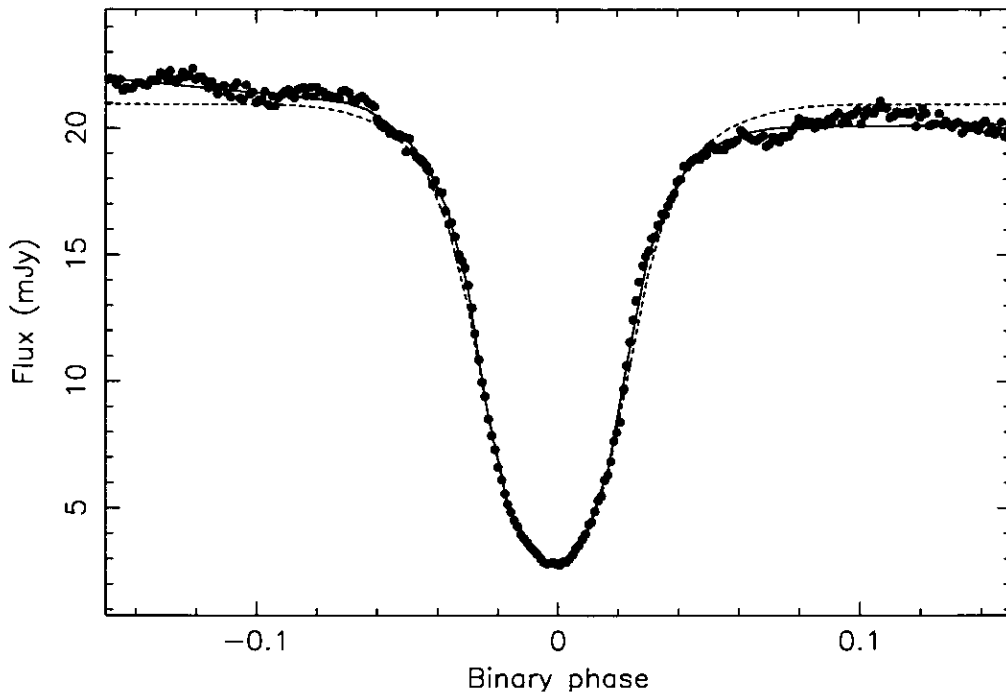


Figure 2.11: A comparison of the light curves calculated from the reconstructed disc map of Feb 12 when modelled with a flat disc (dashed) and a flared disc of opening half-angle $\alpha/2 = 5^\circ$ (solid). The reduced χ^2 of the fit is 5.1 for the flat disc, but 0.5 for the flared disc.

2.4 Discussion - flare angles and temperature distributions

In the context of accretion disc mapping, the motivation for considering flared discs has arisen from the poor fitting, and the occurrence of spurious structure, that have resulted from flat disc model fits to outburst and superoutburst light curves. During outbursts of Z Cha (Warner & O'Donoghue 1988; Robinson et al. 1995) and OY Car (Rutten et al. 1992b), bright rings around the outer edge of the disc and/or front-back asymmetries were present in the reconstructed disc when the light curve was mapped with a flat disc. There are two interpretations for this phenomenon: either the observed features are due to an uneclipsed light source (e.g., the secondary star, or a large disc), or the disc is exhibiting a physical flare. See the review by Wood (1994) for further discussion.

Mapping light curves with flared discs has been attempted by previous authors at normal outburst maximum for both OY Car and Z Cha. Rutten et al. (1992a) briefly considered a flared disc in their optical examination of OY Car at normal outburst peak. They used small opening angles and did obtain a satisfactory fit to the light curve, but this caused a front-back asymmetry to develop. Rutten et al. (1992a) prefer the uneclipsed light source interpretation, finally eliminating the spurious features by subtracting 15 per cent of the flux before mapping.

However, the *HST* light curve of Z Cha at normal outburst maximum was mapped with a disc of opening angle $\alpha = 16^\circ$ by Robinson et al. (1995; this is an acceptable opening angle because the inclination of Z Cha is less than that of OY Car). The map was very symmetric and there was no evidence for an uneclipsed light source. The fact that by mid-decline, the light curve could be modelled by an axisymmetric flat disc, lends weight to the interpretation of the Robinson et al. data at outburst maximum as being due to a flared disc.

It has been demonstrated in Section 2.3.2 that a disc with a substantial flare exists in OY Car three days into the decline from superoutburst. These are the first maps of a disc in the superoutburst state that clearly show such flaring. The symmetry of the disc maps suggests that there is no uneclipsed light source in these light curves, as does the asymmetry in the map of the flux-subtracted light curve. It may be possible that transient uneclipsed light sources (due, presumably, to the disc) develop and disappear over the course of an outburst or superoutburst, and that these have previously been observed and mapped.

One effect of this method should perhaps be noted here. The inclination of Z Cha ($81.^\circ 8$) is lower than that of OY Car and yet the derived opening angle of the disc in Z

Cha is larger. The method (and code) used was identical. The method needs to be applied to more systems before it can be definitively said whether the effect is systematic.

Flare angles

A comparison between calculated theoretical flare angles and those obtained from eclipse mapping can be undertaken by way of illustrating the differences between observations and theory.

The *steady state* theoretical flare angle is given by (Shakura & Sunyaev 1973; Frank et al. 1992)

$$\frac{h_d}{r_d} = 1.72 \times 10^{-2} \alpha_\nu^{-\frac{1}{10}} M_{wd}^{\frac{3}{8}} (r_d \times 6.9)^{\frac{1}{8}} \left(\frac{\dot{M}}{1.587 \times 10^{-10}} \right)^{\frac{3}{20}} \left\{ 1 - \left[\frac{R_{wd}}{r_d} \right]^{\frac{1}{2}} \right\}^{\frac{3}{5}} \quad (2.12)$$

Here the equation is normalised to solar values, and α_ν is the viscosity. Assuming that the disc radius is approximately equal to the tidal radius ($r_d \sim r_t$), r_t is approximated by

$$r_t = r_d = \frac{0.6a}{1+q} \quad (2.13)$$

(Warner 1995; after Paczyński 1977), where a is the binary separation and q is the mass ratio. Using the binary parameters from Wood et al. (1989), and assuming $\alpha_\nu \sim 1.0$, a *steady state* disc flare angle of $\alpha \simeq 2.6^\circ$ is found.

Alternatively, if the disc is assumed to be in a *non-steady state*, and that the disc includes radiative and convective zones, then

$$\frac{h_d}{r_d} \sim 0.038 \left(\frac{\dot{M}}{1.587 \times 10^{-10}} \right)^{\frac{3}{20}} \quad (2.14)$$

(adapted from Smak 1992). Adopting $\dot{M} \sim 4 \times 10^{-10} M_\odot \text{ yr}^{-1}$ (from Figure 2.8), gives $\alpha \simeq 5^\circ$.

Thus the observed disc opening angle of OY Car on the decline from superoutburst ($\alpha \simeq 10^\circ$) is considerably larger than that predicted by either steady state or non-steady state theory.

The recent observational discovery of spiral shocks in the accretion discs of IP Peg and U Gem in outburst (Steehns et al. 1996, 1997; Neustroev & Borisov 1998; Harlaftis et al. 1999; Morales-Rueda et al. 1999) may provide a feasible mechanism for the production of these opening angles. In the case of IP Peg, Harlaftis et al. (1999) find an upper limit of $\alpha = 30^\circ$ for the opening angle of the disc. More pertinent to this work, perhaps, Morales-Rueda et al. (1999) find $\alpha \approx 11^\circ$ in IP Peg just before the system enters optical decline. It is possible that the disc flare seen in the eclipse maps presented here is a

manifestation of these spiral shocks, smeared across the whole surface of the disc as a result of the disc mapping process. It may also be that increased vertical structure at the disc edge is contributing to the resulting disc opening angle if this interpretation is correct. Note, however, that theoretical work by e.g., Murray (1996, 1998) favours the existence of stationary spiral shocks in longer period, less extreme mass ratio systems than OY Car. Both U Gem and IP Peg fulfil these criteria.

It should be noted that limb darkening has not been taken into account in the calculation of the disc opening angles. The first steps towards including limb darkening in eclipse mapping have recently been taken by Robinson and collaborators (Robinson et al. 1999), using the *HST* light curve of Z Cha previously mapped with a flared disc of opening angle $\alpha/2 = 8^\circ$ (Robinson et al. 1995). The net result of including the limb darkening in their analysis of their ultraviolet data set is to reduce the opening angle of the disc to $\alpha/2 = 6^\circ$, a value that is still between 2° and 3° larger than that given by disc model atmospheres (Robinson et al. 1999). The temperature distribution became steeper as a result of including limb darkening, but the use of optically thick disc model atmospheres flattened the distribution again, so that the net effect was virtually no change in the temperature distribution. The inclusion of limb darkening and the use of realistic disc model atmospheres to convert the surface brightness to temperature (rather than the blackbody spectra normally used) has closed the gulf between the theory and observation of steady-state, optically thick discs, but problems still remain. Robinson et al. (1999) suggest the inclusion of a concave disc geometry and disc irradiation will close the gap still further. Disc irradiation has been shown to be an important effect in outburst by e.g., King (1997, 1998). Note that limb darkening will have less of an effect on the *B* band optical data presented here than it did on the Robinson et al. (1995) ultraviolet data.

The contour maps in Figures 2.5 and 2.7 are fully compatible with the data. There is no obvious superhump activity in the Feb 12 light curve and the disc image is very azimuthally symmetric. Conversely, there is a large superhump feature in the light curve of Feb 9, and the reconstructed disc image is asymmetric.

Figure 2.6 shows that the slope of the disc temperature distribution on Feb 9 appears only approximately compatible with the theoretical steady state solutions (given by eqn. 2.12). The overall rate of mass flow is slightly larger than that for the disc of Feb 12.

The turn-up at the edge of the brightness temperature distribution on Feb 9 is similar to that seen in disc maps of Z Cha (Warner & O'Donoghue 1988), and may suggest the presence of a ring at the outer edge. Numerical simulations of superoutburst discs by Whitehurst (1988a, 1988b) and Whitehurst & King (1991) suggest that a ring exists at

the outer edges of the disc in superoutburst, and indeed, precessing rings are a possible explanation for the superhump phenomenon. Unfortunately, due to the inherent limitations of the eclipse mapping method, it cannot be said definitively whether the ring is real or an artifact from the modelling process.

In contrast, the observed slope of the disc brightness temperature distribution on Feb 12 (Figure 2.8) is quite compatible with the overplotted theoretical curves of optically thick, steady state discs. This result shows that on the superoutburst decline, at least, the disc is close to the optically thick, steady state expected. Such discs have also been seen in Z Cha in outburst (e.g. Warner & O’Donoghue 1988; Horne & Cook 1985, but *not* in the *HST* observations of Robinson et al. 1995) and novalike variables e.g. EW Tri, UX UMa and V363 Aur (Rutten et al. 1992a). The average rate of mass flow through the disc at this stage in the decline appears to be $\sim 4 \times 10^{-10} M_{\odot} \text{ yr}^{-1}$. There is no evidence for a ring at the outer edge of the disc at this stage in the superoutburst decline.

This can be compared with a normal outburst peak mass flow rate of $\sim 1 \times 10^{-9} M_{\odot} \text{ yr}^{-1}$ for OY Car, again with a relatively good fit to steady state theoretical disc curves (Rutten et al. 1992a). The fact that the disc mass flow rate found here is lower than that found at normal outburst maximum is noted. However, the data presented here were obtained well into the decline from superoutburst — the flux from the system is virtually at the quiescent level two days after the acquisition of these data.

2.5 Conclusions

The optical data presented here show for the first time the flaring of the disc of OY Car up to three days into the superoutburst decline. The following conclusions may be drawn:

1. The disc of OY Car is flared 3 days into the superoutburst decline, having an opening angle of $\sim 10^{\circ} \pm 1^{\circ}$. Although it is difficult to quantify the formal uncertainties, there is marginal evidence for a decrease in the opening angle between one day into the decline, when the opening angle is $\sim 11^{\circ} \pm 1^{\circ}$, and two days later. These values for the opening angle allowed the best agreement between the model light curve and the actual data, based on the fact that the lowest value of χ^2 could be aimed for in each case.
2. There is a decrease in the mass flow rate between one day into the decline, and three days after.
3. There is a possible change in the radial temperature distribution. One day into the

decline the disc may not be in a steady state, whereas the agreement with a steady state disc is very good three days later.

It is not difficult to envisage even larger opening angles during superoutburst maximum, but it is unclear whether the disc is thickened at the edge, or nearer the centre. Could the disc be concave, rather than the smooth wedge-shape in cross-section implicit in this analysis? Is the flaring a global phenomenon, or is it a localised (in azimuth) but large scale feature that is unavoidably smoothed and smeared due to the disc mapping process (cf. Billington et al. 1996; this work)? Is the flaring a manifestation of the spiral shocks that have been observed in IP Peg and U Gem, again smoothed across the whole disc surface by the mapping process? What is seen in these results may be a combination of all these effects.

If the flaring is wholesale and affects the whole disc, then perhaps the most perturbing aspect is the large differences between theoretical opening angles and those observed. Perhaps the inclusion of disc concavity and irradiation of the outer disc would resolve the discrepancies. Failing that, the lack of a simple mechanism to support this structure becomes a problem, perhaps solvable by invoking disc magnetic fields.

Chapter 3 presents contemporaneous X-ray observations that suggest that the central regions are being obscured, most likely by the edge of the flared disc suggested in this analysis.

Chapter 3

ROSAT X-ray observations of the 1994 Feb superoutburst of OY Carinae

3.1 Introduction

This Chapter contains details of *ROSAT* X-ray observations of OY Car in superoutburst, obtained contemporaneously with the optical observations presented in Chapter 2.

The basic theory of the origin of the X-ray emission from dwarf novae is covered in Chapter 1; however, three fundamental points should perhaps be reiterated at this stage. These are:

- the boundary layer is expected to be the source of the bulk of the X-ray emission from dwarf novae, provided the primary is not spinning fast;
- in quiescence the boundary layer region is thought to be optically thin, radiating in hard X-rays ($\sim 2 - 20$ keV); and
- in outburst, the X-ray emitting region should become optically thick, emitting softer ($\lesssim 1.0$ keV) X-rays.

By the time of these observations, experimental tests of all these theoretical predictions had been undertaken. Extensive observations of many dwarf novae in both the high and low mass accretion rate regimes, by X-ray satellites such as *Einstein* and *EXOSAT*, had broadly confirmed the theory that the optical thickness of the boundary layer region depended on the outburst state of the system in question.

Satellite observations of dwarf novae in outburst or superoutburst are difficult due to their inherent unpredictability and the timescales involved. Satellite response times are frequently very slow, while, perversely, normal outburst durations in particular are often very short. Continuous monitoring is impractical whereas Target of Opportunity (TOO) observations typically take two days to come into effect. Systems with a relatively well determined and frequent outburst recurrence cycle, such as VW Hyi, have been extensively observed using TOO observations, despite the difficulties involved. Those systems which are not so predictable, which include the three well-known eclipsing SU UMa dwarf novae OY Car, Z Cha and HT Cas, have not been so well observed. Nevertheless, one previous observation of OY Car itself served as a stimulus for much of our present knowledge of the origin of X-ray emission from dwarf novae in the high mass accretion rate regime. This was the *EXOSAT* observation by Naylor et al. (1988), in which, for the first time, timing observations of an eclipsing system were used to try and locate the source of the X-rays.

This observation provided quite a shock. Up to this point, it had always been assumed that the X-rays from dwarf novae in outburst originated, like in quiescence, from the boundary layer. Since optical observations confirm that the white dwarf and boundary layer are eclipsed in outburst, it seemed natural to assume that the boundary layer region would also be eclipsed, leading to an eclipse of the X-ray flux. In fact, Naylor et al. (1988) found no evidence for an X-ray eclipse of OY Car during the 1985 May superoutburst. Naylor et al. concluded instead that the source of the X-rays from OY Car in superoutburst was an extended region which they thought most likely to be an optically thin corona.

Given the difficulties involved in achieving successful TOO observations of eclipsing dwarf novae in outburst or superoutburst, it was not long before a similar timing analysis was applied to an eclipsing novalike variable instead. These systems, fixed in the high mass accretion rate regime, have been likened to dwarf novae in a state of permanent outburst. The *ROSAT* timing observation of UX UMa by Wood et al. (1995b) also failed to show an eclipse of the X-rays, again indicating an extended region as the X-ray source. In addition, the spectrum was extremely soft and consistent with a blackbody (although only marginally so), while the overall X-ray luminosity was a factor of 10 lower than expected when compared to other, lower inclination novalike variables. If it is assumed that the novalike variable is accreting at the canonical value of $\dot{M} \sim 10^{-9} M_{\odot} \text{ yr}^{-1}$, then the X-ray luminosity of UX UMa was a factor of 1000 lower than expected. The lack of X-ray eclipse and the low luminosity imply that the boundary layer is hidden from view at all orbital phases.

The most recent pertinent observation is that of OY Car in superoutburst by Mauche

(1997b). No eclipses of the EUV flux were observed, again implying an extended emission region.

The picture that has been built up from the results of these three observations indicates, fundamentally, that the X-ray source observed in eclipsing systems during high mass accretion rate episodes (or in systems in a permanent high mass accretion state) is not the boundary layer, but is instead a considerably more extended region. The X-rays from the boundary layer are obscured, most likely by the outer edge of the accretion disc; this obscuration also explains the low observed X-ray luminosities. The spectra are softer than in quiescence. The extended source of the X-rays detected may either be a static accretion disc corona, or a wind.

The specific aim of the X-ray observations reported here was to confirm the lack of eclipse (observed with *EXOSAT* by Naylor et al. 1988) in the *ROSAT* passband. These observations recognise the fact that the greater sensitivity of *ROSAT* could give better temporal resolution, and that different X-ray instruments, with differing passbands, may detect different spectral components (or even physical components, a theme returned to in Chapter 6). In addition, a proposal to observe OY Car in quiescence had been accepted following the previous Announcement of Opportunity, although this observation was held over and was eventually acquired after the observations detailed in this Chapter. Those quiescent observations are detailed in Chapter 4. Thus OY Car was observed with the same satellite in superoutburst and quiescence, potentially allowing comparisons to be made between different accretion regimes.

The optical observations were obtained in an attempt to pin down the location of the absorbing material that was obscuring the X-ray eclipse in Naylor et al.'s observations, using optical disc maps. In Chapter 2, eclipse mapping of optical observations of the 1994 Feb superoutburst of OY Car showed that the accretion disc is flared to a considerable extent ($\alpha \sim 10^\circ$) even three days into the superoutburst decline, suggesting that absorption in the edge of a disc with this extent of flaring could obscure the boundary layer regions.

This Chapter, then, contains results from a pointed *ROSAT* X-ray observation obtained immediately prior to the optical observations. There is one simultaneous observation. Section 3.2 describes the *ROSAT* satellite, while in Section 3.3 the observations and data reduction are described. Sections 3.4 and 3.5 deal with the X-ray light curve and luminosity, while in Section 3.6 the results are discussed and compared with results from the similar, but non-eclipsing system VW Hyi. The results strongly support the hypothesis that it is obscuration by disc material that causes the boundary layer to be invisible during the high mass accretion rate regime.

3.2 The *ROSAT* Satellite

As both this Chapter and Chapter 4 deal with data obtained with the *ROSAT* X-ray satellite, this Section gives a brief introduction to the satellite itself, its instruments and its detectors.

The German-US-UK satellite Röntgen Satellite (*ROSAT*; Briel et al. 1996) was launched on 1990 June 1, equipped with what was at that time the largest ever imaging X-ray telescope. The telescope was operated from, and schedules were drawn up at, the German Science Operations Centre (GSOC) situated in Weilheim, Germany. Since GSOC was the only ground station involved in satellite operations, ground contacts were very short (6 to 8 minutes) and occurred only in six (out of a total of 15) consecutive orbits per day. As a consequence, *ROSAT* had to operate in a highly automatic fashion, and extensive on-board data storage was required.

The *ROSAT* mission was governed by two scientific objectives. The first consisted of an all-sky survey with the imaging X-ray and EUV telescopes, the second a detailed study of selected X-ray and EUV sources. The primary objective lasted 6 months and discovered $\sim 60\,000$ objects; the satellite then proceeded to provide more detailed observations of selected sources, including many that were discovered as a result of the highly-successful all-sky survey phase. References include: Pounds et al. (1993; the WFC all-sky survey), Fleming et al. (1996; catalogue of white dwarfs found in the all-sky survey) and Voges et al. (1999; the bright source catalogue).

ROSAT carried a main payload that consisted of a large X-ray telescope (XRT; see Briel et al. 1996), at the time the most powerful ever built, designed for measurement of soft X-rays in the energy range 0.1 - 2.5 keV. The telescope design was a Wolter type I mirror assembly, which focussed the incoming X-rays by means of four nested confocal parabolic-hyperbolic mirror pairs, made of the glass ceramic material Zerodur. As detectors, the focal plane assembly of the XRT carried two Position Sensitive Proportional Counters (PSPC; see e.g., Briel & Pfeffermann 1995) and one High Resolution Imager (HRI; David et al. 1991), which were mounted on a turret for alternate positioning in the focus. The turret also contained the detector preamplifiers and a gas supply system to provide a continuous flow of detector gas (60% Ar, 20% Xe, 20% CH₄) to the PSPCs. The data acquisition and control electronics were arranged on a fixed platform around the turret housing. A schematic cross-section of the X-ray telescope assembly is shown in Figure 3.1.

The PSPCs were multiwire proportional counters, consisting of two separate counters.

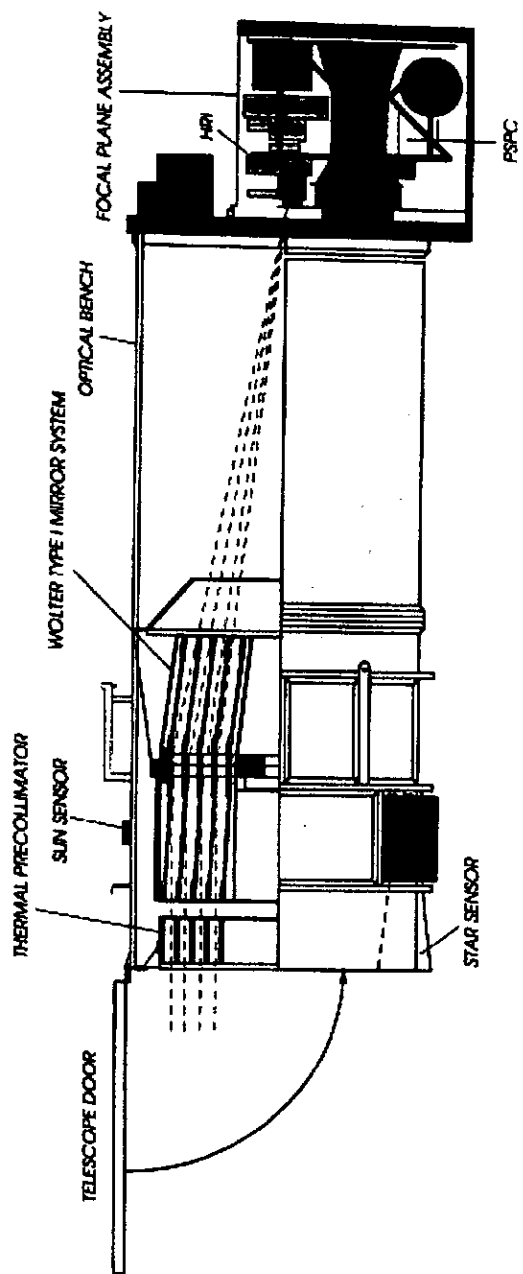


Figure 3.1: A schematic diagram of the layout of the *ROSAT* XRT. The X-ray detectors, the PSPC and the HRI, lie in the focal plane assembly. Taken from the *ROSAT* webpage (<http://www.xray.mpe.mpg.de/rosat>).

One was the position sensitive X-ray detector, the other was used as an anti-coincidence detector. The HRI was a two-dimensional position sensitive microchannel plate (MCP) based detector.

The secondary *ROSAT* payload consisted of the Wide Field Camera (WFC; Sims et al. 1990), which extended the measuring range to the extreme ultraviolet (EUV) region, and was capable of detecting photons with energies in the range 0.04 keV - 0.2 keV. The WFC comprised three nested aluminium mirrors to focus the EUV radiation onto an MCP X-ray detector. A focal plane turret assembly was used to select one of two identical detector assemblies.

Near the end of the all-sky survey phase (late 1990), a failure of the on-board electronics caused the satellite to spin out of control and the XRT was accidentally pointed at the sun. Control was quickly re-established, but one of the PSPCs was blinded. The second PSPC was operated for a further four years until depletion of the gas supply forced it to be switched off. It was used for one final 10-day observing campaign in 1998 December. By this time there were numerous malfunctions and the satellite had again been accidentally pointed at the sun. Nonetheless, *ROSAT* successfully completed its very last observations before being switched off on 1999 Feb 12. The legacy of nearly a decade of X-ray observations can now be found in the *ROSAT* archive, mirrored in the UK at the Leicester Database and Archive Service (LEDAS - <http://ledas-www.star.le.ac.uk>).

3.3 Observations and data reduction

The X-ray observations detailed here were obtained during the 1994 Feb superoutburst of OY Car, the peak of which lasted from 1994 Feb 1 - 7 (from VSS RAS NZ observations — the exact dates are given in Chapter 2, Section 2.2). These observations, obtained with the *ROSAT* HRI, were acquired between Feb 4 and Feb 8, and so were taken at the height of the superoutburst. The Principal Investigator (PI) was Dr. B.J.M. Hassall; the data are public and available at LEDAS. The data set additionally includes some simultaneous WFC coverage. There is one contemporaneous optical/X-ray observation (1994 Feb 8).

Figure 2.1 (in Chapter 2) shows the optical magnitude of OY Car before, during and after the 1994 Feb superoutburst, and uses data both from the VSS RAS NZ and the optical observations detailed in that Chapter for illustration. The same Figure also shows the timing of the X-ray observations relative to the optical observations. For the remainder of this Chapter, to avoid confusion (and because there is a one-day gap in these data), ‘observation’ will be used to describe the actual n -day baseline over which the individual

Table 3.1: Journal of superoutburst *ROSAT* HRI X-ray observations.

Observation ID	Date	HJED start (244 9300+)	Phase covered	Duration (seconds)	Source count rate ^a (counts s ⁻¹ × 10 ⁻²)
ror300392	1994 Feb 4	88.492	0.885–0.916	160	4.8 ± 1.7
.	.	88.499	0.997–0.224	1240	3.7 ± 0.5
.	1994 Feb 5	89.419	0.579–0.600	112	−0.4 ± 0.6
.	.	89.427	0.709–0.945	1288	3.0 ± 0.5
.	1994 Feb 7	91.352	0.197–0.433	1288	2.5 ± 0.4
.	1994 Feb 8	91.799	0.277–0.599	1624	2.5 ± 0.4
.	.	91.870	0.405–0.428	80	3.0 ± 2.0
.	.	91.879	0.549–0.716	904	2.2 ± 0.5
.	.	91.891	0.745–0.839	512	1.7 ± 0.6
.	.	91.930	0.353–0.404	280	3.9 ± 1.2

^aThis is the time-averaged count rate from the source after background subtraction. The errors quoted are Poissonian – calculated as $\sqrt{\text{counts}}/\text{duration}$. Note that the errors may be a slight underestimate as the (small) contribution from the background is ignored. Dataset 3 has a negative average count rate and the errors are unreliable.

‘datasets’ were obtained.

The start time of the HRI observation was 1994 February 4 23:43:33 UT (HJED 244 9388.489 639), and the overall time on target was 7.4 kiloseconds. No special scheduling was carried out, so that no specific range of phases (such as the eclipse phase) was covered. The dates, times, phases covered and durations of the individual X-ray observation datasets are given in the journal of X-ray observations, Table 3.1.

The data were reduced using ASTERIX software (Allan & Vallance 1995). Source counts were extracted from a circular region of radius 150 arcsec. The background annulus, centred on the source, had inner and outer radii of 200 arcsec and 600 arcsec respectively. These dimensions were chosen for compatibility with those used in the comprehensive compilation of *ROSAT* CV observations by van Teeseling et al. (1996). Source data and background data were binned into 1s bins and background subtracted. The background-subtracted total flux light curve was then corrected for vignetting, dead time, and scattering. Lastly, all times were converted to (Heliocentric Julian Ephemeris Date) HJED.

The extracted background data were scaled to the dimensions of the source extraction circle, and a background light curve created in the same way.

The *ROSAT* WFC observed OY Car for 26.6 kiloseconds on 1994 February 5 and 5.9 kiloseconds on 1994 February 7, with the S1a filter, which is sensitive to the spectral range 90 - 206 eV. The data were extracted using ASTERIX and WFCPACK (Denby & McGale 1995) software. There was no detection. Using a source radius of 5' and a background annulus, centred on the source, of inner and outer radii 10' and 20', respectively, the estimated 3σ

upper limit to the superoutburst count rate is 1.2×10^{-3} counts s^{-1} .

3.4 The Superoutburst X-ray light curve

The total superoutburst light curve was obtained by folding all the datasets into 24 bins on the orbital period of OY Car using the updated ephemeris calculated in Chapter 4 (eqn. 4.1). The duration of each bin was marginally smaller, at 227.2 s, than the totality of the white dwarf eclipse as given in Wood et al. (1989), of 231 s. The starting point of the binning was chosen so that one phase bin was exactly centred on phase zero. The effective exposure time of each of the 24 bins is illustrated in Figure 3.2. The phase coverage in the data was such that ~ 97 per cent of the orbit was covered, including one eclipse. The resulting phase-folded superoutburst light curve can be seen in Figure 3.3. The large error bars on the bin centred on phase $\phi = 0.95$ are due to the poor coverage in this bin; this lack of coverage extends ~ 25 per cent into the white dwarf eclipse phase bin at phase $\phi = 0.0$.

The mean out-of-eclipse flux is $(2.8 \pm 0.2) \times 10^{-2}$ counts s^{-1} , while the flux in white dwarf eclipse is $(3.8 \pm 1.7) \times 10^{-2}$ counts s^{-1} . The background count rate in the white dwarf eclipse bin is $(2.3 \pm 1.3) \times 10^{-2}$ counts s^{-1} . If the null hypothesis is such that there is an eclipse, but that background fluctuations produce the observed in-eclipse flux, there is no total eclipse of the X-rays in the vicinity of the white dwarf at the $3.8/1.3 = 2.9\sigma$ level.

Instead taking only the first four datasets, which cover the eclipse phase, and applying the above analysis, then there is no eclipse of the X-ray flux at the 2.3σ level.

3.5 The Superoutburst Luminosity

As the default data products from the *ROSAT* HRI give no spectral resolution¹, the total time-averaged count rate was used in order to make a very rough estimate of the intrinsic luminosity of the system in superoutburst.

ROSAT observations of VW Hydri suggest that there is no evidence for a spectral change during outburst (Wheatley et al. 1996), at least at the *ROSAT* PSPC wavelength range. We believe that this may apply equally to OY Car in superoutburst. While there is a soft blackbody component producing the majority of the flux in this state, we believe

¹The HRI actually has a very limited (two band) spectral response. Unfortunately, the software for the reduction of these data was not available at UCLan STARLINK node, and time constraints did not allow the reduction of the data at another site (although this was investigated). These data may allow a better estimate of the superoutburst luminosity.

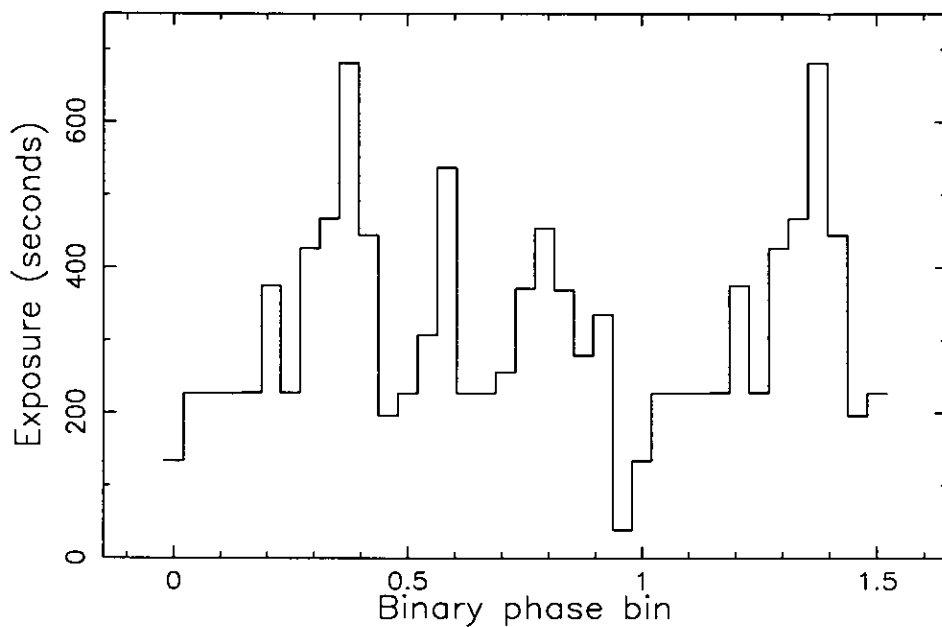


Figure 3.2: The effective exposure times of each of the 24 phase bins used in the generation of the superoutburst X-ray light curve.

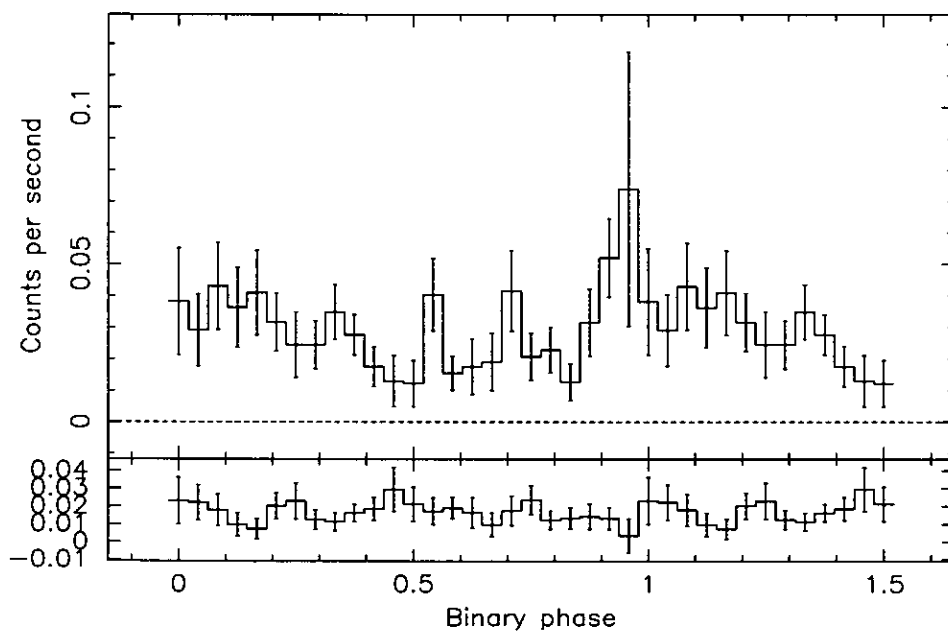


Figure 3.3: The upper panel shows the *ROSAT* HRI superoutburst X-ray light curve folded, in 24 bins, on the orbital period of OY Car. The lower panel shows the background light curve scaled to the dimensions of the source extraction circle. All error bars are Poissonian.

that this component is not visible when OY Car is observed by *ROSAT* because of an unfortunate coincidence of the spectral response of the satellite, with the fact that the disc is flared, and the inclination of the system, discussed further in Section 3.6. If this is the case, then the weaker ‘coronal’ component will be visible as it was during the *EXOSAT* observation of OY Car in Naylor et al. (1988), and the observation of UX UMA by Wood et al. (1995b), and will be the dominant contributor to the flux in the *ROSAT* passband.

The temperature found in the *EXOSAT* study of OY Car in superoutburst by Naylor et al. (1988) was ill-constrained but was found to be $T > 10^6$ K (i.e., $kT > 0.09$ keV). The temperature of the coronal source found in the Wood et al. (1995b) study of UX UMA was better constrained to be $kT = 0.18 - 0.41$ keV, depending on whether the source was Bremsstrahlung or a Raymond-Smith plasma.

The estimation of an X-ray luminosity for OY Car in superoutburst involved generating simulated spectra within XSPEC (Arnaud 1996). A range of underlying Bremsstrahlung and Raymond-Smith plasma model temperatures were used in conjunction with a neutral absorption model. Values of $N_H = 10^{20}$ and 10^{21} cm⁻² were used. The average N_H in the region of the sky occupied by OY Car is 10^{21} cm⁻², and a lower absorption was included for comparison (however, see caveats below).

The spectra were all normalised to the observed mean count rate of the superoutburst observation presented here, and the exposure time of each spectrum was taken to be 7400 s, identical to the total exposure time of the observation. Removal of the intervening absorption allowed a rough estimate of the ‘intrinsic’ flux. In calculating the luminosity, a distance of 82 pc was used (Wood et al. 1989).

The results, for three different underlying Bremsstrahlung and Raymond-Smith plasma temperatures, are shown in Table 3.2.

It can be seen that the intrinsic luminosity is sensitive to both the temperature of the underlying source and to the N_H of the absorber, for the temperatures and absorptions under discussion here. *Assuming* that the N_H of the interstellar absorber is $\sim 10^{21}$ cm⁻², as suggested from the GETNH program (Marshall & Clark 1984), then the spread in values for the ‘intrinsic’ X-ray luminosity as measured from this observation is $L_X \sim 10^{30} - 10^{33}$ erg s⁻¹. This range is very dependent on the assumptions used in the choosing of the model values, as discussed further below. Note also that the Marshall & Clark (1984) work is an estimate of the total line of sight in the Galaxy on a very coarse grid, and is primarily of use to extragalactic astronomy. A column density of $N_H = 10^{21}$ cm⁻² is more an upper limit in this case, as the distance of OY Car is very much less than the distance of the path through the Galaxy. Indeed, if the canonical value of 1 atom cm⁻³ is

Table 3.2: The ‘intrinsic’ 0.1 - 2.5 keV luminosities for several underlying Bremsstrahlung temperatures, normalised to the flux and count rate of the HRI observation of OY Car in superoutburst presented in this Chapter. For clarity all values are quoted to two significant figures but note that these are based on observed count rates which have an uncertainty of $\sim 7\%$.

kT (keV)	N_H ($\times 10^{22}$ cm $^{-2}$)	ECF flux ($\times 10^{-12}$ erg cm $^{-2}$ s $^{-1}$)	Intrinsic flux ($\times 10^{-12}$ erg cm $^{-2}$ s $^{-1}$)	Luminosity ($\times 10^{30}$ erg s $^{-1}$)
Bremsstrahlung				
0.1	0.01	7.0	25.0	20.0
.	0.10	160.0	6300.0	5100.0
0.3	0.01	5.1	9.1	7.4
.	0.10	21.0	130.0	100.0
0.5	0.01	4.5	6.8	5.5
.	0.10	12.0	42.0	33.0
Raymond-Smith				
0.1	0.01	4.1	9.2	7.4
.	0.10	77.0	1200.0	980.0
0.3	0.01	3.7	4.4	3.6
.	0.10	7.2	1.6	13.0
0.5	0.01	2.6	3.1	2.5
.	0.10	3.8	6.9	5.6

^aFlux calculated from the mean HRI count rate using the energy-to-count conversion factors, for the respective spectra, in the HRI calibration report (David et al. 1997).

^bFlux of simulated spectrum, after normalisation to count rate of the X-ray observation presented here, and removal of intervening absorption, in the 0.1 - 2.5 keV passband.

adopted, then at the distance of OY Car, the interstellar absorption can be estimated at $N_H \sim 3 \times 10^{20}$ cm $^{-2}$. Furthermore, there is some evidence that the interstellar absorption is low around the Sun out to around 50 - 100 pc. This is the so-called ‘Local Bubble’; see e.g., Sfeir et al. (1999) for a recent determination of its extent using *Hipparcos* data. The dominant absorber of the X-rays in OY Car is thus expected to be intrinsic to the system. This local absorption in OY Car is discussed in greater detail in Section 3.6.1.

3.6 Discussion

3.6.1 Comparison with VW Hyi

Comparison of the outburst/superoutburst X-ray spectrum of OY Car with that of VW Hyi is instructive in many ways. VW Hyi may well be regarded as the canonical low-inclination dwarf nova. The system is bright in the optical ($m_v[\text{max}] \sim 9.5$, $m_v[\text{min}] \sim 13.3$), and is observed to undergo regular outbursts ($T_n \sim 30\text{d}$; Ritter & Kolb 1998), and superoutbursts ($T_s \sim 180\text{d}$; Ritter & Kolb 1998). Its apparent brightness is to some extent due to the exceptionally low interstellar absorption to the system ($N_H \sim 6 \times 10^{17}$ cm $^{-2}$): it has thus been well studied in all wavelengths, including in X-rays.

Summary of observations to date

EUV data VW Hyi has been detected in outburst with the *ROSAT* WFC during the all-sky survey phase (see, e.g., Wheatley et al. 1996). Additionally, VW Hyi was detected in superoutburst with the *EUVE*. Mauche's (1996) observation showed different count rates depending on the spectrometer, with the count rate highly variable for the duration of the observation across all three detectors (see Table 3.3). The corresponding EUV spectrum of VW Hyi is shown to peak longward of 200 Å, and does not extend shortward of 100 Å.

In Section 3.3 it was shown that OY Car was not detected by the *ROSAT* WFC during the 1994 Jan superoutburst. However, OY Car has been detected in superoutburst by *EUVE*. Mauche (1997b) observed 13 eclipse phases during a continuous observation of the 1997 Mar superoutburst of OY Car. No eclipses of the EUV flux occurred, suggesting, in common with the *EXOSAT* result of Naylor et al. (1988), the existence of an extended soft X-ray/EUV source in the high accretion rate regime.

Table 3.3 summarises the EUV observations of OY Car and VW Hyi to date.

X-ray data OY Car and VW Hyi have been observed in an outburst state by both *EXOSAT* and *ROSAT*, although in the case of OY Car a normal outburst has never been caught. There is an increase in the soft X-ray flux from both systems during superoutburst (e.g., van der Woerd et al. 1986; Naylor et al. 1988), but the actual scale of the increase differs — the increase is a factor of ~ 100 for VW Hyi, whereas for OY Car it rises only by a factor ~ 3 . Naylor et al. (1988) find a range of superoutburst X-ray luminosities of $L_x = 10^{31} - 10^{32}$ erg s $^{-1}$; Warner (1995, and references therein) quotes an average superoutburst X-ray luminosity for VW Hyi of $L_x = 10^{34}$ erg s $^{-1}$.

X-ray components in the spectrum of VW Hyi

VW Hyi was observed in superoutburst several times by *EXOSAT*. According to van Teeseling et al. (1993), the superoutburst X-ray spectrum of VW Hyi can be modelled in terms of either

- A single component optically thin spectrum with 8.6×10^{-3} keV $\leq kT \leq 8.6 \times 10^{-2}$ keV (i.e. $10^5 - 10^6$ K), or,
- A combination of a hot, optically thin component at $kT > 8.6 \times 10^{-2}$ keV (which they tentatively identify with the 2.17 keV quiescent spectrum found by Belloni et

Table 3.3: Comparison of the EUV observations of OY Car and VW Hyi.

	OY Car	VW Hyi
<i>ROSAT</i> WFC		
Quiescence	No detection ^a	18.7 ± 2.7 cts s ⁻¹
Outburst	Unobserved	0.08 ± 0.04 cts s ⁻¹
Superoutburst	No detection ^b	Unobserved
<i>EUVE</i>		
Quiescence	Unobserved	No detection
Outburst	Unobserved	~ 0.09 cts s ^{-1c}
Superoutburst	$0.68/0.81$ cts s ^{-1d}	~ 1.0 cts s ⁻¹ (SW) ^e . ~ 4.0 cts s ⁻¹ (MW) ~ 2.0 cts s ⁻¹ (LW)

^a 1.5×10^{-3} cts s⁻¹ upper limit

^b 1.2×10^{-3} cts s⁻¹ upper limit

^cIn the Al/Ti/C detector during the all-sky survey phase

^dFrom Mauche (1996). The detector is the Deep Survey spectrometer.

^eEstimated by the present author from Mauche (1997b)

al. 1991; see Chapter 4) and a cooler, optically thick component at 6.9×10^{-3} keV $< kT < 8.6 \times 10^{-3}$ keV (i.e., $8 \times 10^4 - 10^5$ K).

Wheatley et al. (1996) prefer the optically thin plus blackbody component interpretation for the spectrum of VW Hyi in both outburst and superoutburst. They suggest the superoutburst spectrum is a result of a drop of a factor $\sim 3 - 4$ in the hot optically thin component and the rise of a very soft blackbody component that is easily detected by the *EXOSAT* filters but not by the *ROSAT* instruments. In other words, the quiescent and outburst spectra can both be explained in the context of a variation in the relative strengths of just the two components. They find no evidence for spectral change (from thermal Bremsstrahlung to blackbody, for example) during outburst observations².

Naylor et al.'s (1988) spectral analysis of the OY Car observation suggested that the coronal X-ray source was relatively hot ($T \gtrsim 10^6$ K) and optically thin, with a temperature of $kT \sim 8.6 \times 10^{-2}$ keV.

²Although see Hartmann et al. (1999), in which BeppoSAX observations of VW Hyi during and after outburst show clear evidence of spectral evolution. There is also a decrease in the X-ray flux over the course of the observation (the *ROSAT* PSPC observation detailed in Wheatley et al. (1996) displayed a constant flux). Hartmann et al. argue that the explanation could lie in differing outburst behaviour, i.e., the outbursts had different characteristics.

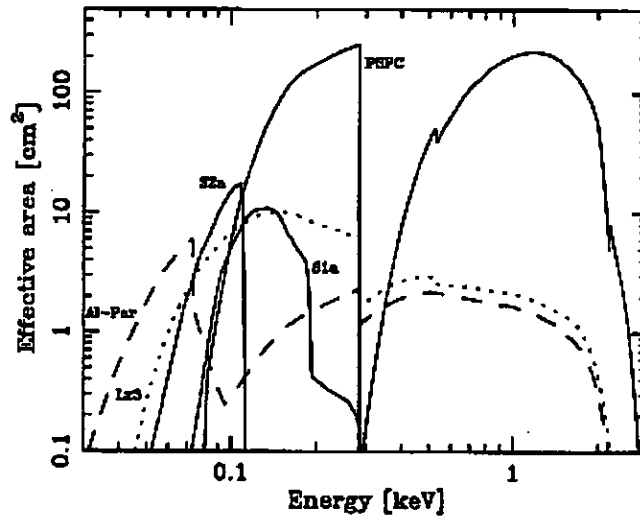


Figure 3.4: Figure 9 of Wheatley et al. (1996), showing the respective spectral responses and effective areas of the instruments on *EXOSAT* and *ROSAT*.

So, how similar are OY Car and VW Hyi?

Interpretation of the X-ray data from these two systems requires consideration of several important interconnected factors:

- Firstly, the effects of the different spectral responses of various X-ray instruments must be taken into account. Table 3.4 summarises the instruments (and their respective spectral ranges) on EUV/X-ray satellites relevant to this discussion, viz, *EUVE*, *EXOSAT*, *ROSAT*, and *GINGA*. A comparative illustration of the effective areas and spectral responses of the instruments on *EXOSAT* and *ROSAT* can be found in Figure 3.4.
- OY Car is an eclipsing system, whilst VW Hyi is not,
- The absorption of the X-ray source, which is to an unknown extent dependent on the inclination. The absorption can have up to three possible components:
 - (i) *interstellar absorption*, which is very low for VW Hyi but which is still uncertain for OY Car;
 - (ii) the *local absorption* which in the case of OY Car in quiescence is due to the presence of the ‘iron curtain’ of material which veils the white dwarf in quiescence (Horne et al. 1994). This effect has not been observed in any non-eclipsing dwarf nova, suggesting that the ‘iron curtain’ is connected with the effect of the disc in high inclination systems;

(iii) *disc edge absorption*, which occurs in high inclination systems in superoutburst and is a consequence of the disc edge obscuring the central regions while flared. This effect can be seen manifested as dips at superhump maximum in the optical superoutburst light curves in Chapter 2 (most effectively in the light curve of Feb 8 [Figure 2.3], when the superhump itself is very obvious, and is very obviously affected by dips), while Billington et al. (1996) find similar dips in *HST* light curves of OY Car in superoutburst. There is no known way of disentangling the effects of absorption due to the material of an ‘iron curtain’ from that due to a disc seen nearly edge-on; or indeed, it is not yet known whether they are one and the same effect.

Wrapped up in this is the question of the X-ray luminosity — similar systems would be expected to have similar X-ray luminosities. According to Warner (1995, and references therein), the average X-ray luminosity of VW Hyi in superoutburst, as measured by *EXOSAT*, is $L_x \sim 10^{34}$ erg s⁻¹. In contrast, Naylor et al. (1988), also using *EXOSAT* find a considerably lower X-ray luminosity for OY Car in superoutburst ($L_x \sim 10^{31} - 10^{32}$ erg s⁻¹). A still lower limit value is found for the *ROSAT* observations presented here ($L_x \sim 10^{30}$ erg s⁻¹), although this value is very model-dependent. Moreover, Wood et al. (1995b) also find a surprisingly low X-ray luminosity for UX UMa ($L_x \sim 10^{30}$ erg s⁻¹), using *ROSAT*.

A qualitative explanation for the lower X-ray luminosity can be arrived at if the satellite spectral responses and the absorption/ inclination are considered.

Satellite spectral responses can and do confuse the issue. Wheatley et al. (1996) describe the evolution of the X-ray spectrum of VW Hyi from quiescence to outburst as the appearance of a very soft blackbody component accompanied by a change in the relative strengths of the optically thin component. In quiescence, the optically thin component dominates, while in outburst, the very soft blackbody component rises to contribute most of the flux, but this flux is outside the *ROSAT* bandpass. This component has disappeared by the end of the outburst.

In the absence of evidence to the contrary, at present it seems plausible to assume that the same components occur in the outburst X-ray spectrum of OY Car. Assuming that this is the case, then only the optically thin components can contribute in this observation of OY Car in the *ROSAT* bandpass. This suggests that the total high-energy output of OY Car is underestimated because neither the *ROSAT* HRI nor the PSPC is sufficiently sensitive to the lower energy ranges.

Table 3.4: Instruments, filters, and spectral energy ranges (90% response energy limits) of recent EUV and X-ray satellites.

Satellite	Instrument name	Range (keV)
<i>EUVE</i>	Lex/B scanner	0.07 - 0.25
	Al/Ti/C scanner	0.05 - 0.08
	SW spectrometer	0.07 - 0.18
	MW spectrometer	0.03 - 0.09
	LW spectrometer	0.02 - 0.04
<i>EXOSAT</i>	Low Energy (LE)	
	3000-Lexan	0.05 - 1.77
	4000-Lexan	0.07 - 1.77
	Al-Par	0.04 - 1.77
	Medium energy (ME)	1 - 20 5 - 50
<i>ROSAT</i>	WFC	
	S1a	0.09 - 0.21
	S2a	0.06 - 0.11
	PSPC/HRI	0.1 - 2.5
<i>GINGA</i>	Large Area Counter	2 - 30

The inclination of the system is crucial, and contributes to the general confusion regarding the absorption to the X-ray source. The inclination of VW Hyi ($i \sim 60^\circ$) simply allows more of the soft X-ray and EUV emitting boundary layer to be seen directly. For OY Car however, although the boundary layer can be seen in quiescence (see Chapter 4), during outburst/superoutburst there is no direct line of sight because the disc has flared up as shown in Chapter 2, and the inclination is such that the flared disc blocks the view of the central regions. This is also the case with UX UMa (Wood et al. 1995b). Because of inclination effects, instead of the dominant, and very luminous, soft blackbody component seen in VW Hyi during superoutburst, in OY Car and UX UMa a weaker, optically thin coronal source is seen.

The picture is thus as follows:

- *Quiescence*: Single component, the optically thin boundary layer, independent of inclination (Belloni et al. 1991; Wheatley et al. 1996; this work, Chapter 4).
- *Superoutburst*: High inclination: single, optically thin coronal component (Naylor et al. 1988; Wood et al. 1995b; this work). Low inclination: optically thin, presumably coronal component (it is unlikely that this component is connected to the quiescent

component above, as previously suggested by van Teeseling et al. 1993), plus dominant, very soft, optically thick blackbody component. The latter is not seen in high inclination systems because of the effect of the disc.

In Section 3.5 an ‘intrinsic’ superoutburst X-ray luminosity for OY Car is estimated. If the above factors were truly accounted for, OY Car would likely have a similar X-ray luminosity to VW Hyi. Similarly, UX UMa would have a similar X-ray luminosity to fellow low inclination novalike variables. What is frustrating here is the fact that there are no observations, with latter-day X-ray satellites, of eclipsing systems in outburst, so the change in the absorption between quiescence and outburst due to material local to the system is not known.

Further discussion

This discussion does not suggest that the L_X/L_{opt+UV} ratio problem (or ‘missing boundary layer problem’) has been solved. Even in quiescence, many systems (including VW Hyi and OY Car itself — see Chapter 4) display a low boundary layer luminosity compared to disc luminosity; typically the quiescent X-ray luminosity is a tenth of the optical+UV luminosity. In outburst, the X-ray luminosity can differ by a factor of a hundred from the optical+UV luminosity. One possible explanation for the exacerbation of the problem during outburst is given by Long et al. (1993), who suggest that the surface layers of the white dwarf spin up during outburst, storing part of the outburst energy in these layers for slow release at a later time. The timescale for the release of the stored energy is still not fully understood, but it is known that the rate of energy release will be dependent on the effective viscosity of the differentially rotating white dwarf photosphere.

The X-rays from OY Car in the high accretion rate regime must be emitted from an extended source. Similarly for UX UMa. A quantitative measurement of the change in the local absorption when an outburst or superoutburst occurs in an eclipsing or high inclination system, as compared to quiescence, is now urgently needed, as is a quantitative assessment of the spectral changes between outburst and quiescence.

In conclusion, it is not yet possible to disentangle the effect of the satellite bandpasses from the effect of the disc/ increased absorption on the estimated luminosity of OY Car.

3.7 Conclusions

A self-consistent picture of OY Car under conditions of high mass accretion emerges with the X-ray and optical data obtained during the 1994 Feb superoutburst.

The X-ray data presented here comprise only the third X-ray observation of an eclipsing CV in the high accretion rate regime. When the data are folded on the orbital period of the system, there is no eclipse of the X-ray flux. This is in agreement with the previous X-ray observation of OY Car in superoutburst, and also with the *ROSAT* observation of the novalike variable UX UMa by Wood et al. (1995b). It suggests that the source of the X-rays in superoutburst in high inclination systems is not the boundary layer per se.

In Chapter 2, optical observations obtained during the decline of the 1994 Feb superoutburst reveal a disc with substantial vertical structure: a disc with an opening angle of $\alpha \sim 10^\circ$ on the optical decline. The X-ray luminosity is ill-constrained, but taking into account count rates from the data presented here and previous observations, OY Car is definitely less luminous in X-rays than the non-eclipsing system VW Hyi, as measured from *EXOSAT* observations, by at least a factor of ten. Naylor et al. (1987, 1988) used contemporaneous observations in wavelengths other than X-rays to suggest that the disc of OY Car had considerable vertical structure during the 1985 May superoutburst, and that the increased local absorption that resulted had the effect of shielding the boundary layer from view at all orbital phases. The optical observations presented in Chapter 2, imply a flared disc and support this suggestion.

The *ROSAT* superoutburst observation of OY Car presented here has a count rate comparable to the quiescent *ROSAT* count rate (see Chapter 4), taking into account the fact that different detectors were used. This suggests that the *ROSAT* instruments are detecting a greater part of the optically thin component than the corresponding detectors on *EXOSAT*, which in turn did not detect the hardest X-rays observed by *ROSAT*. It is thus probable that the derived X-ray luminosity of OY Car in superoutburst is an underestimate because of a combination of:

- obscuration of the boundary layer regions, which are still emitting soft X-rays, by the edge of a flared disc and other local absorption above the plane of the disc, and,
- different satellite bandpasses, and enhanced sensitivities to different regions of the high energy spectrum.

These two factors acting together result in a decrease in the observed X-ray flux from OY Car as compared to VW Hyi, leading to potentially false conclusions being drawn regarding the X-ray luminosity of the system and a very low L_X/L_{opt+UV} ratio. The inclination of the system is likely the main factor.

Any wish-list for the X-ray observations presented in this Chapter would have included an X-ray spectrum. While the extraction of an HRI spectrum is possible, the fact that

there are only two channels would not allow any constraints to be placed on the superoutburst spectrum of OY Car, other than whether the spectrum is generically 'hard' or 'soft'. The author is willing to guess that the spectrum will be relatively hard compared to that of a low inclination system. What is now needed is a high-quality outburst spectrum of OY Car (or any other eclipsing system for that matter), sufficient to determine if there are soft and hard X-ray components analogous to those observed in the outburst spectrum of VW Hyi. *XMM* will be the satellite to resolve this question, of which more in Chapter 6.

The fact that X-rays are being detected supports the wind/corona model for the source of the X-rays in the high mass accretion rate regime. Whether this source is static (corona) or moving (wind) is yet to be determined. Again, *XMM*, with greater sensitivity and higher throughput, should help resolve this issue. See Chapter 6 for further discussion.

Chapter 4

Optical and X-ray observations of OY Carinae in quiescence

4.1 Introduction

This Chapter contains details of observations of OY Car in quiescence during 1994 and 1998.

The basic theory of the origin of the X-ray emission from dwarf novae is covered in Chapter 1; in summary, observations of similar systems and theoretical considerations lead one to expect that during the course of the observations presented here, hard X-rays ($\sim 2 - 20$ keV) were being produced in an optically thin boundary layer region; furthermore, timing observations of an eclipsing system are the best way of locating the source of the X-rays.

It was not until the advent of *ROSAT* that there was access to a satellite which was sensitive enough to provide adequate timing information over the course of a relatively short (typically 50 kilosec) observation of a faint dwarf nova in quiescence. Moreover, high inclination systems are always feeble X-ray sources, especially in quiescence (Holcomb et al. 1994). Observations of eclipsing systems are at their most useful when temporal analysis is applied to the data: independent of whatever accretion regime may be in force at the time, phase-resolved timing observations of the eclipses in principle allow constraints to be placed on the source of the emission under investigation.

The use of phase-resolved timing observations to help locate the physical position of the X-ray emitting source in *quiescent* dwarf novae was first used successfully by Janet Wood and collaborators (Wood et al. 1995a). The *EXOSAT* observation of the 1985 May superoutburst of OY Car by Naylor et al. (1988) had failed to show an eclipse,

although it could be argued that this located the X-ray source away from the boundary layer. Chapter 3 contains a discussion of the implications of this, together with further observations.

In Wood et al. (1995a), a *ROSAT* observation of the eclipsing dwarf nova HT Cas in an unusual low state was used to show that the source of the X-rays from this system was eclipsed and came from the vicinity of the white dwarf. As Wood et al. state: “It must therefore be a boundary layer”. Van Teeseling (1997) then phase-folded archive *ROSAT* observations of a second eclipsing dwarf nova, Z Cha, and again found an eclipse of the X-rays that was concurrent with the optical eclipse of the white dwarf. Mukai et al. (1997) returned to observe HT Cas in quiescence (rather than a low state like previously) with both *ROSAT* and *ASCA*, and extracted such a high-quality light curve from the *ASCA* data that convincing physical constraints could be placed on the extent of the X-ray source. The X-ray emission was found to come from the immediate vicinity of the white dwarf, as was by now expected; the data implied that the size of the X-ray emission region $R_X \lesssim 1.15R_{\text{wd}}$. Mukai et al. thus could not rule out the intriguing possibility that the X-ray source region could be *smaller* in extent than the white dwarf. This result could obviously challenge the simple equatorial boundary layer picture.

Additionally in the case of OY Car, however, it is the question of the absorption to the X-ray source that is particularly curious. The *HST* FOS exposures of OY Car in quiescence obtained by Horne et al. (1994) suggest the existence of a significant local absorption due to a material with solar abundances veiling the ultraviolet spectrum of the white dwarf — the so-called ‘iron curtain’ (as described in Chapter 1). Model fits to these *HST* data implied a hydrogen column density of $n_{\text{H}} \approx 10^{22} \text{ cm}^{-2}$. Naylor & la Dous (1997) argue that this column density should be sufficient to extinguish the soft X-ray flux from the boundary layer. To overcome this discrepancy in the case of U Gem in outburst, Naylor & la Dous suggest that the X-ray flux detected from that high inclination system comes from a quiescent coronal region which emits $\sim 1/50$ of the boundary layer flux.

The aim of the X-ray observations presented here was thus twofold: to determine if the ‘iron curtain’ in OY Car in quiescence really has sufficient column density to extinguish the X-ray flux in the bandpass of the *ROSAT* detectors; and if not, to use the phase-resolved X-ray light curve to examine whether or not OY Car, like HT Cas and Z Cha, exhibits an eclipse. These observations have also been obtained with the same satellite as the superoutburst observations in Chapter 3, thus specifically removing the effects of differing bandpasses from their intercomparison.

From the optical observations, photometric light curves were obtained for the purpose

Table 4.1: A selection of optical observations that have required adjustments from the ephemeris of Wood et al. (1989) for the white dwarf eclipse to coincide with phase zero.

Date of observation	Correction needed (s)	Author (date published)
1979	0	Rutten et al. (1992)
1984	established	Wood et al. (1989)
1987	-84 ± 2	Hessman et al. (1992)
1992	-40 ± 5	Horne et al. (1994)
1994	-35 ± 5	Pratt et al. (1999b)

of updating the ephemeris of OY Car, so that a more accurate zero point could be used throughout the thesis to phase fold the X-ray data and the optical light curves for eclipse mapping. As the method of X-ray eclipse detection for the X-ray data involves binning and co-adding the data over many orbital cycles and subsequent folding on the orbital period of the system (see Sections 3.3 and 4.2), it is important that the ephemeris used does not have accumulated errors which would invalidate the search for an eclipse.

The last time the ephemeris of OY Car was updated was in Wood et al. (1989), in which both a single linear and a two-part linear ephemeris were presented. The data used for their calculation were acquired in 1984. Published papers utilising data obtained both previously and subsequently to that used in Wood et al. (1989) have required various adjustments in order for the white dwarf eclipse to coincide with orbital phase zero. A selection of these observations is shown in Table 4.1 — the deviations from the linear ephemeris, sometimes as much as 80 s (9.26×10^{-4} day), are highly significant compared with the formal error as given in Wood et al. (1989), which corresponds to just 0.8 seconds in the ephemeris over 3 years. Possible reasons for deviations from a linear ephemeris are discussed further in Section 4.3.2.

Optical and X-ray observations of OY Car in quiescence are presented in this Chapter. The X-ray observations were taken over two separate epochs, one with the *ROSAT* PSPC, giving both timing and spectral information, the other with the HRI, giving timing information only. They address different aspects of the thesis aims. Section 4.2 describes the data acquisition and reduction; in Section 4.3 an updated orbital ephemeris is derived; Section 4.4 deals with the analysis of the X-ray data (obtained at two different epochs); while in Section 4.5, the results are discussed and compared and contrasted to those found previously for VW Hyi. The conclusions of the Chapter are outlined in Section 4.6.

4.2 Observations and data reduction

4.2.1 PSPC X-ray and WFC EUV observations, 1994 July

OY Car was observed in quiescence with the *ROSAT* PSPC between 1994 July 5 and 1994 July 7 for a total of 1.6 kiloseconds. The PI was Prof. T. Naylor; the data is public and available at LEDAS. An observation duration of 1.6 kilosec is very short: further investigation has revealed that there were significant scheduling problems with this observation, and it was decided that 1.6 kilosec was better than nothing at all. As with the superoutburst observation obtained the same year and detailed in Chapter 3, no special effort was made to ensure that specific orbital phases were covered. OY Car was in the middle of a quiescent spell at the time — the previous normal outburst had taken place on 1994 May 30, and the subsequent superoutburst occurred on 1994 December 11. The start time of the observation was 1994 July 5 09:55:55 UT (HJED 244 9538.915 388). Information about the X-ray observation datasets can be found in Table 4.2.

The observation was taken off-axis and with a spacecraft wobble to avoid vignetting by PSPC support wires, so the source and background counts were extracted from larger regions than those used for the superoutburst HRI data discussed in Chapter 3 (Section 3.3). Data reduction was performed with the ASTERIX package. The radius of the source region used in this case was 250 arcsec, while the inner and outer radii for the background annulus, centred on the source, had radii of 300 and 900 arcsec, respectively. These dimensions were again chosen for compatibility with those used by van Teeseling et al. (1996). These data were extracted in 1s bins and background-subtracted, then the background-subtracted total flux light curve was corrected for vignetting, scattering and dead time. Lastly, all times were converted into HJED.

In addition, the PSPC spectrum from channels 11 to 235 was extracted in 1 second bins. It was then grouped, using FTOOLS (Breedon et al. 1997), into 11 spectral bins so that there were at least 5 counts in each bin.

OY Car was also observed by the *ROSAT* WFC for a total of 4.9 kiloseconds on 1994 July 5 with the S1a filter. These data were reduced using ASTERIX and WFCPACK software. There was, as with the superoutburst WFC observation, no detection, and using the method described for the superoutburst data, the 3σ upper limit found for the quiescent count rate is 1.5×10^{-3} counts s^{-1} .

Table 4.2: Journal of *ROSAT* PSPC X-ray observations, 1994 July.

<i>ROSAT</i> Observation ID	Date (244 9500+)	HJED start	Phase covered	Duration (seconds)	Source count rate ^a (counts s ⁻¹ × 10 ⁻²)
ror300275	1994 July 5	38.916	0.003 - 0.088	464	8.0 ± 1.3
		39.313	0.296 - 0.398	560	8.0 ± 1.2
.	1994 July 6	40.473	0.664 - 0.670	32	0.5 ± 1.3
.	1994 July 7	40.508	0.229 - 0.328	544	8.7 ± 1.3

^aThis is the time-averaged count rate from the source after background subtraction. The errors quoted are Poissonian — $\sqrt{\text{counts}/\text{duration}}$. Note that the errors may be a slight underestimate as the (small) contribution from the background is ignored.

4.2.2 Optical observations and HRI X-ray observations, 1998 Jan - Mar

According to monitoring observations made by the Variable Star Section of the Royal Astronomical Society of New Zealand, OY Car underwent two superoutbursts in 1998, reaching their respective maxima on 1998 Feb 10 and 1998 Nov 22. Figure 4.1 shows the overall VSS RAS NZ light curve of OY Car covering the period of the 1998 optical and X-ray observations.

X-ray observations, 1998 Jan

The main aim during the course of these observations was to obtain sufficient coverage of the eclipse phase (i.e., $-0.25 \lesssim \phi \lesssim 0.25$) for a significant detection, with additional coverage of the full orbital phase being of secondary importance. The PI was Dr. B.J.M. Hassall; Co-Is were the author, Prof T. Naylor and Dr. J.H. Wood.

Complications arise, however, due to the fact that the orbital period of OY Car, at ~ 91 min, is very similar to the orbital period of *ROSAT* (~ 96 min). As a consequence of this, the orbital phase of OY Car covered by *ROSAT* precesses by ~ 5 min per satellite orbit, leading to a very similar phase coverage for a set of contiguous observations. Additional difficulties in obtaining the desired orbital phase coverage include Earth occultations and the passage of the satellite through the South Atlantic Anomaly. Because of the cumulative effect of these difficulties, it was necessary to supply extrapolated eclipse times (based on the Wood et al. 1989 ephemeris) to the *ROSAT* scheduler, J. Engelhauser, approximately one week before the observations were obtained. These eclipse timings were then used to identify observation windows, generally ~ 20 mins in duration, during which a certain orbital phase could be observed. Luck played its part in the scheduling: Figure 4.1 shows that 18 days after the final *ROSAT* observation, OY Car went into superoutburst. The system had returned to quiescence by the time of the optical observations discussed below.

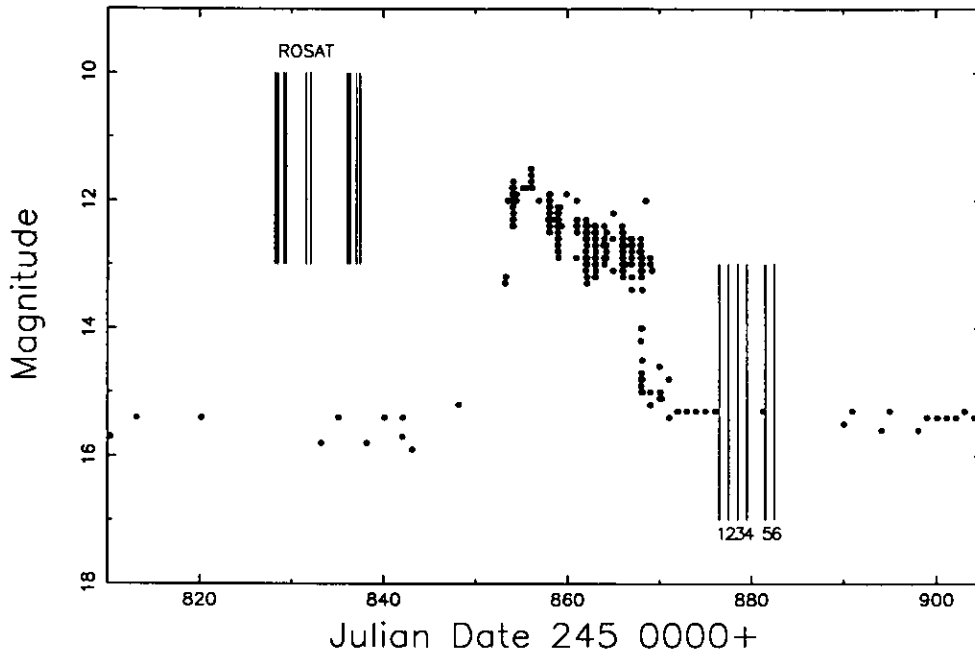


Figure 4.1: The light curve of OY Car, covering the period of both the *ROSAT* and optical observations. Circles show observations as supplied by the VSS RAS NZ. It can be seen that OY Car actually underwent a superoutburst that reached maximum on 1998 Feb 10, but had returned to quiescence by the time of the optical observations.

OY Car was observed 12 times in total by the *ROSAT* HRI for a total of 51.5 kiloseconds between 1998 January 14 and 1998 January 23. Information about the individual observations can be found in Table 4.3.

The data were again reduced using *ASTERIX* software. For each observation, source counts were extracted from a circular region of radius 50 arcsec. For the determination of the background, an annular region centred on the source was used, with inner and outer radii of 100 arcsec and 300 arcsec, respectively. Corrections and conversions were applied to the data as for the superoutburst HRI data.

In addition to extracting the source counts in this way, the extracted background data were scaled to the dimensions of the source extraction circle to create a background light curve.

Optical observations, 1998 Mar

High-speed photometry of OY Car was obtained between 1998 March 3 and 1998 March 9, with the 1.0m telescope at the South African Astronomical Observatory (SAAO). The PI was Dr. B.J.M. Hassall; the author was Co-I. The data were acquired by the author & BJMH. The data demonstrate that the system had returned to quiescence, despite the

Table 4.3: Journal of *ROSAT* HRI X-ray observations, 1998 Jan.

<i>ROSAT</i> Observation ID	Date (2450800+)	HJED start	Phase coverage	Duration (seconds)	Source count rate ^a (counts s ⁻¹ × 10 ⁻²)
ror300600	1998 Jan 14	28.216	0.875 - 0.146	1435	2.1 ± 0.4
ror300601	1998 Jan 14	28.476	0.990 - 0.004	83	2.4 ± 0.9
.	.	28.481	0.007 - 0.348	1456	1.8 ± 0.4
.	.	28.543	0.006 - 0.404	1856	1.9 ± 0.3
.	.	28.620	0.282 - 0.452	928	1.3 ± 0.4
.	.	28.666	0.009 - 0.165	848	1.1 ± 0.4
ror300602	1998 Jan 15	29.145	0.588 - 0.855	1440	1.3 ± 0.3
.	.	29.212	0.653 - 0.902	1280	0.7 ± 0.2
ror300603	1998 Jan 15	29.402	0.667 - 0.006	1920	1.0 ± 0.2
.	.	29.470	0.737 - 0.792	288	0.0 ± 0.2
.	.	29.475	0.819 - 0.103	1488	1.9 ± 0.4
.	.	29.538	0.813 - 0.160	1872	2.0 ± 0.3
ror300604	1998 Jan 18	31.598	0.453 - 0.477	96	3.4 ± 1.9
.	.	31.605	0.565 - 0.717	832	1.4 ± 0.4
.	.	31.652	0.316 - 0.477	864	2.9 ± 0.6
.	.	31.673	0.636 - 0.770	736	1.7 ± 0.5
.	.	31.714	0.296 - 0.550	1392	1.8 ± 0.4
.	.	31.741	0.715 - 0.818	560	1.0 ± 0.4
ror300605	1998 Jan 18	32.061	0.794 - 0.007	1520	1.3 ± 0.3
.	.	32.131	0.891 - 0.120	1248	0.6 ± 0.2
.	.	32.195	0.907 - 0.176	1408	0.3 ± 0.4
.	.	32.254	0.840 - 0.224	1824	1.2 ± 0.3
ror300606	1998 Jan 19	33.055	0.543 - 0.831	1574	1.1 ± 0.3
.	.	33.122	0.612 - 0.877	1408	1.4 ± 0.3
.	.	33.172	0.385 - 0.932	2895	2.3 ± 0.3
ror300607	1998 Jan 20	33.516	0.845 - 0.181	1834	2.1 ± 0.3
.	.	33.569	0.688 - 0.972	1378	0.9 ± 0.2
.	.	33.594	0.008 - 0.226	803	2.2 ± 0.5
.	.	34.121	0.420 - 0.632	1126	1.6 ± 0.4
.	.	34.182	0.399 - 0.688	1522	1.3 ± 0.3
ror300608	1998 Jan 22	36.036	0.771 - 0.009	1680	1.0 ± 0.2
.	.	36.102	0.815 - 0.144	1664	2.5 ± 0.4
ror300609	1998 Jan 22	36.316	0.207 - 0.301	512	0.8 ± 0.4
.	.	36.364	0.964 - 0.345	2000	2.0 ± 0.3
.	.	36.431	0.002 - 0.390	1968	1.8 ± 0.3
ror300610	1998 Jan 23	37.030	0.514 - 0.857	1840	1.3 ± 0.3
.	.	37.097	0.576 - 0.908	1696	1.2 ± 0.3
ror300611	1998 Jan 23	37.426	0.778 - 0.159	2064	1.5 ± 0.3

^aThis is the time-averaged count rate from the source after background subtraction. The errors quoted are Poissonian — $\sqrt{\text{counts}/\text{duration}}$. Note that the errors may be a slight underestimate as the (small) contribution from the background is ignored.

superoutburst between these observations and the *ROSAT* observations discussed above.

The single-channel SAAO St. Andrews Photometer was used with a 16 arcsec aperture at 1s time resolution. For much of the duration of the observing run, conditions were non-photometric, but as the primary aim of the run was the updating of the ephemeris, observations were continued through thin cloud. In most cases a *V* filter was used, with occasional observations in difficult conditions made in white light. Sky measurements were taken every 15-20 min, at a position ~ 1 arcmin to the south of the source. A typical eclipse light curve is shown in Figure 4.2; the journal of optical observations is shown in Table 4.4. In addition, E- and F-region photometric standard stars were observed several times each night, although these were not used in the subsequent reduction process because of the largely non-photometric conditions.

4.3 The orbital ephemeris

4.3.1 Optical eclipse timing measurements

In all, 12 useful optical eclipses were observed, details of which can be found in Table 4.4. As eclipse timings were the main aim of the observations, the data reduction process was simplified considerably. For each eclipse light curve, all times were converted to HJED. The times of mid-eclipse were then calculated automatically using a new program, written by the author, based on the method described in Wood et al. (1985). The light curves were first smoothed by passing them through a median filter of width 10s, roughly a quarter of the duration of the ingress of the white dwarf. Each light curve was then differentiated numerically, and the differential passed through a box car filter of width 42s. This filter width was chosen as it is the approximate duration of the ingress of the white dwarf (cf., Wood et al. 1985; Wood et al. 1989). This filtered derivative was then examined to detect the largest negative and positive points, which correspond to the mid-points of ingress and egress respectively. Mid-eclipse was then calculated as being the point halfway between the ingress and egress mid-points, i.e., $\phi_0 = (\phi_{wi} + \phi_{we})/2$. The HJED times of mid-eclipse are listed in Table 4.5.

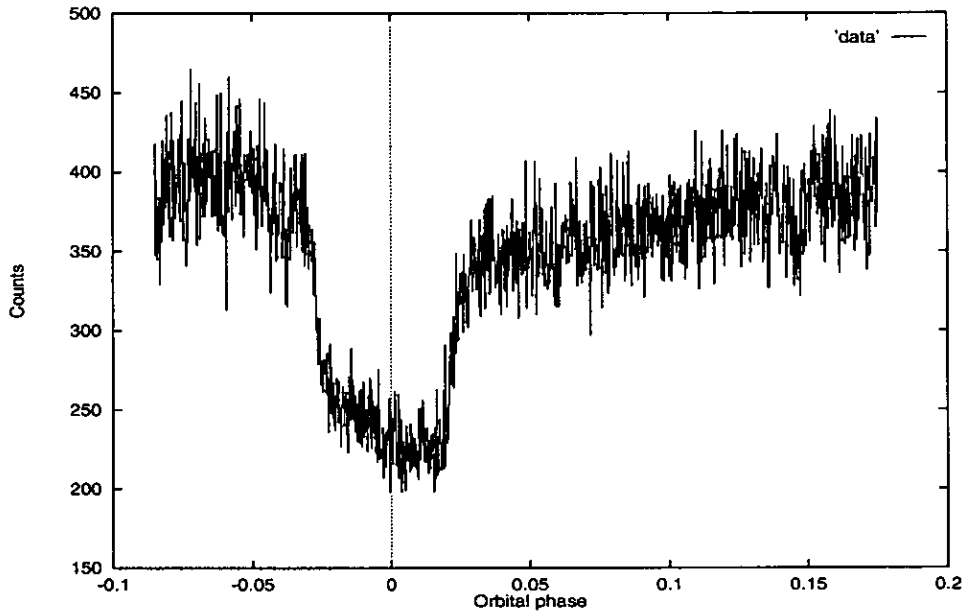


Figure 4.2: Typical optical light curve (1998 March 4), phased with the ephemeris derived in Section 4.3.

Table 4.4: Journal of optical observations, 1998 Mar.

Run	Date	UT start	Cycle	Filter
0007	1998 March 3	22:57:30	109036	V
0009	1998 March 4	01:22:43	109045	V
1008	1998 March 5	01:46:17	109061	V
2001	1998 March 6	00:33:42	109076	V
3009	.	18:41:45	109088	V
3017	.	23:10:31	109091	V
5015	1998 March 8	20:42:03	109121	V
5019	.	21:55:27	109122	V
5024	.	23:35:29	109123	V
5028	1998 March 9	01:09:48	109124	V
5030	.	02:07:23	109125	V
6013	.	18:53:30	109136	W

Table 4.5: Timings of mid-eclipse used for updating the ephemeris of OY Car, taken from a variety of sources and including the data obtained for this work. $O - C$ values are calculated with respect to the first linear ephemeris in Wood et al. (1989).

Timings of mid-eclipse			
Cycle	HJED (2400000+)	$O - C$ (10^{-4} day)	Reference
766	44042.53565	0.04	Vogt et al. (1981)
807	44044.49241	0.15	.
808	44044.55549	-0.25	.
823	44045.50236	0.31	.
3282	44200.71672	0.39	.
3283	44200.77984	0.38	.
3346	44204.75645	0.30	.
3585	44219.84232	-0.01	.
3600	44220.78911	-0.03	.
3616	44221.79907	0.0018	.
3711	44227.79558	0.22	.
5594	44346.65229	0.33	.
5608	44347.53596	0.10	.
6607	44410.59377	0.17	.
6621	44411.47749	0.44	.
6622	44411.54062	0.53	.
6623	44411.60369	0.02	.
9271	44578.74795	0.56	Schoembs & Hartmann (1983)
9272	44578.81111	0.95	.
12658	44792.53859	1.26	.
12673	44793.48538	1.02	.
12674	44793.54842	0.21	.
22231	45396.79503	-0.38	Cook (1985)
22246	45397.74183	-0.52	.
22261	45398.68875	0.54	.
22262	45398.75183	0.13	.
22278	45399.76170	-0.52	.
22294	45400.77170	0.14	.
22322	45402.53908	0.08	.
22339	45403.61215	0.22	.
22357	45404.74835	0.45	.
22390	45406.83125	-0.45	.
22405	45407.77813	0.21	.
22417	45408.53558	0.20	.
22437	45409.79795	-0.29	.
22451	45410.68168	0.09	.
22468	45411.75472	-0.07	.
22469	45411.81780	-0.48	.
22484	45412.76458	-0.82	.
22515	45414.72146	0.49	.
22561	45417.62506	0.87	.
22563	45417.75127	0.55	.
27410	45723.69839	0.57	Schoembs et al. (1987)
27427	45724.77144	0.52	.

Table 4.5: (continued)

Cycle	HJED (2400000+)	$O - C$ (10^{-4} day)	Reference
27428	45724.83456	0.50	.
27441	45725.65510	0.18	.
27442	45725.71823	0.27	.
27443	45725.78136	0.36	.
27444	45725.84448	0.35	.
27472	45727.61189	0.60	.
27473	45727.67500	0.49	.
27474	45727.73813	0.58	.
27475	45727.80121	0.17	.
27476	45727.86433	0.16	.
27504	45729.69487	0.40	.
27505	45729.69487	0.49	.
27506	45729.75797	0.28	.
27519	45730.57853	0.16	.
27520	45730.64167	0.35	.
27521	45730.70479	0.34	.
27522	45730.76791	0.33	.
27523	45730.83102	0.23	.
27535	45731.58846	0.11	.
27536	45731.65161	0.40	.
27537	45731.71474	0.50	.
27538	45731.77783	0.19	.
27551	45732.59841	0.27	.
27552	45732.66155	0.46	.
27553	45732.72462	-0.05	.
27554	45732.78778	0.34	.
27869	45752.67089	0.53	Wood et al. (1989)
27870	45752.73403	0.72	.
27871	45272.79714	0.61	.
27884	45753.61770	0.49	.
27902	45754.75388	0.52	.
27903	45754.81699	0.41	.
27904	45754.88012	0.50	.
27917	45755.70071	0.68	.
27918	45755.76382	0.58	.
27919	45755.82691	0.27	.
27949	45757.72055	0.39	.
27980	45759.67729	0.30	.
27981	45729.74040	0.19	.
27997	45760.75034	0.25	.
28010	45761.57089	0.03	.
28011	45761.63403	0.22	.
28012	45761.69714	0.11	.
28060	45764.72696	0.26	.
28076	45765.73690	0.32	.
28108	45767.75678	0.42	.
28122	45768.64047	0.39	.
28123	45768.70360	0.48	.

Table 4.5: (continued)

Cycle	HJED (2400000+)	$O - C$ (10^{-4} day)	Reference
28124	45768.76672	0.47	.
28125	45768.82983	0.36	.
28139	45769.71352	0.33	.
28140	45769.77665	0.42	.
28141	45769.83977	0.41	.
72897	48594.87939	-4.10	Horne et al. (1994)
85618	49397.84069	-3.80	This work
109036	50876.51124	-5.80	.
109045	50876.57449	-4.66	.
109061	50877.58431	-5.80	.
109076	50878.53116	-5.44	.
109088	50879.28858	-5.75	.
109091	50879.47795	-5.68	.
109121	50881.37157	-5.76	.
109122	50881.43479	-4.77	.
109123	50881.49785	-5.38	.
109124	50881.56107	-4.39	.
109125	50881.62408	-5.50	.
109136	50882.31834	-6.20	.

4.3.2 Method

In order to update the orbital ephemeris of OY Car, published eclipse timings ranging back to 1979 were used. Where needed, these eclipse timings were converted to HJED; all timings are listed and referenced in Table 4.5.

The ($O - C$) values were computed with respect to the first linear ephemeris of Wood et al. (1989) – these are plotted in Figure 4.3. The range of $O - C$ values derived from the 1998 Mar data is quite robust despite the poor observing conditions. Eclipse timings from Vogt et al. (1981), Schoembs & Hartmann (1983), Cook (1985), Schoembs et al. (1987), Wood et al. (1989), and Horne et al. (1994), are plotted in addition to the eclipse timings presented here. The Horne et al. (1994) timing was quoted in their paper as HJED but was actually HJD, and needed conversion. An additional eclipse timing, from the near-quiet light curve obtained at the end of the superoutburst on 1994 Feb 15 (seen in Chapter 2, Figure 2.4), was also used and is plotted.

Figure 4.3 shows the result of a linear least squares fit represented by the following updated ephemeris (uncertainties quoted in parentheses):

$$\text{HJED} = 2443993.553958(6) + 0.0631209180(2)E \quad (4.1)$$

This fit uses the single linear ephemeris calculated in Wood et al. (1989). This paper

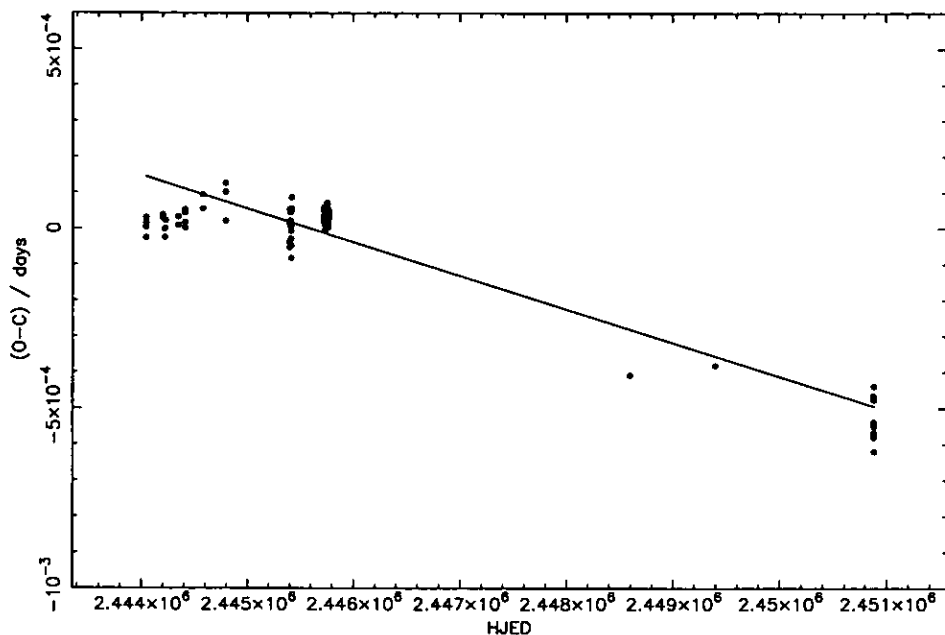


Figure 4.3: The $O-C$ diagram of OY Car. The residuals are calculated with respect to the single linear ephemeris of Wood et al. (1989). The solid line represents the updated ephemeris fit to the residuals corresponding to a constant period with a phase offset.

also contains a two-part linear ephemeris. $O - C$ values were calculated for the data defined at the most recent epoch, using the second of these ephemerides, which is valid for $E \geq 22230$. The resultant residuals were approximately twice as large (~ 0.001 d) as those obtained using the single linear ephemeris.

It can be seen from the $O - C$ diagram that the ephemeris determined by Wood et al. (1989) had drifted completely from the recent data. Unfortunately, the sampling of the data presented here precludes the establishment of a model for the evolution of the ephemeris of OY Car, a common problem with this type of observation. It is known that the ephemerides of both HT Cas and IP Peg have been observed to undergo apparently uncorrelated departures from their assumed linear paths (Naylor 1998, private comm.). It is not known what causes these departures, although changes in the radius of the secondary could conceivably provide a mechanism (e.g. Applegate 1992). In Applegate's model, suggested for non-degenerate binaries in which at least one star is magnetically active, the distribution of angular momentum in the magnetically active star changes as the star goes through its activity cycle. This produces variations in the oblateness of the star, and these changes are transferred to the orbit by gravity, changing the orbital period. Obviously the secondary star would be affected by these changes were the model applied

to dwarf novae. An observation to test if the secondary star in dwarf novae is magnetically active, using *XMM*, is suggested in Chapter 6.

The updated ephemeris is used throughout the remainder of this Chapter for the purposes of phasing the X-ray observations, and elsewhere in this thesis for X-ray and optical data.

4.4 The X-ray data

4.4.1 Spectral analysis of the 1994 July *ROSAT* PSPC observation

The PSPC data obtained in quiescence covered only ~ 30 per cent of the orbital phase with no coverage at phase zero, making it impossible to search for an X-ray eclipse of the boundary layer. It was, however, possible to use the spectral information of the PSPC observations to place constraints on the X-ray emitting source at quiescence.

First, the PSPC spectrum was binned into the photon channel bandpasses summarised in Table 4.6, and the count rates for each bandpass calculated. The average hardness ratio is defined as $(B-A)/(B+A)$; our analysis indicates a value of $(B-A)/(B+A) = 0.77 \pm 0.22$ for OY Car in quiescence.

The X-ray spectrum of OY Car was analysed using *XSPEC* software.

Table 4.6: Photon-channel bandpasses for the binned quiescent spectrum of OY Car.

Bandpass	Channels	Energy (keV)	Count Rate ($\times 10^{-3} \text{ s}^{-1}$)
A	11-41	0.1-0.5	4.5
B	52-201	0.6-2.4	33.8
C	52-90	0.6-1.1	11.6
D	91-201	1.1-2.4	22.3
D1	91-150	1.1-1.8	20.3
D2	151-201	1.8-2.4	1.9

Models with neutral absorbers

The original aim was to produce formal fits to the spectrum with three free parameters (the temperature, kT , the column density, N_H , and the normalisation) using the χ^2 -minimisation routines within *XSPEC*, but this was not possible due to the poor signal to noise of the observation.

In order to explore the parameter space and estimate limits on the temperature and column density, representative values of kT and N_H were chosen, based on previous *ROSAT*

PSPC observations of the similar systems of near identical inclination in quiescence. The usual practice in this case is that the X-ray spectrum of the source is fitted with a thermal bremsstrahlung (or Raymond-Smith optically thin plasma) model in conjunction with a neutral interstellar absorption. The X-ray spectra of both HT Cas and Z Cha have been fitted with single component thermal bremsstrahlung models, with temperatures of 2.4 keV in the case of HT Cas (Wood et al. 1995a) and 4.4 keV for Z Cha (van Teeseling 1997). The 6.0 keV temperature found for the optically thin plasma (e.g., Mewe et al. 1985) model fit to the *ROSAT/GINGA* EUV/X-ray spectrum of VW Hyi by Wheatley et al. (1996) was also used, which is perhaps the best-constrained quiescent dwarf nova spectrum. A temperature of 1.0 keV was also included for constraint purposes. Model fits to the X-ray spectra of various high-inclination non-magnetic CVs have yielded typical values of $N_H \sim 10^{20} - 10^{21} \text{ cm}^{-2}$ for the absorption, and the value of $N_H = 10^{22} \text{ cm}^{-2}$ from the quiescent *HST* ultraviolet study of OY Car by Horne et al. (1994) was also adopted. Within XSPEC, the normalisation was then allowed to be a free parameter, while freezing the chosen values of kT and N_H .

Table 4.7 gives values for the normalisation, emission measure and luminosities for the temperatures and absorbing columns under consideration. In general it was found that lower temperatures produced higher values of χ^2 . A representative thermal bremsstrahlung spectrum of $kT = 2.4 \text{ keV}$ and column densities of $N_H = 10^{20}, 10^{21}$ and 10^{22} cm^{-2} , folded through the instrumental response, is shown in Figure 4.4.

Figure 4.4 clearly shows that a neutral absorption with a column density of 10^{22} cm^{-2} does not agree with the data for this temperature of the X-ray emitting gas (2.4 keV). Similar results are found with this column density for the other temperatures under consideration; this is borne out by the χ^2 - values listed in Table 4.7.

The values obtained for the normalisation as a result of the single-component absorption fits were used to calculate the corresponding emission measure. The emission measure is a robust physical determination because, as can be seen from Table 4.7, a factor of 100 change in the column density of the absorption produces only a factor 7 change in the emission measure. The relatively low emission measures, of order 10^{53} cm^{-3} , in Table 4.7, agree with the observations of other high-inclination systems in van Teeseling et al. (1996).

Models with ionized absorbers

As the temperature of the veiling gas as derived by Horne et al. (1994) was found to be $\sim 10^4 \text{ K}$ (the primary diagnostic being the FeII features, which would not have appeared had the temperature been substantially hotter or cooler), it was considered that some

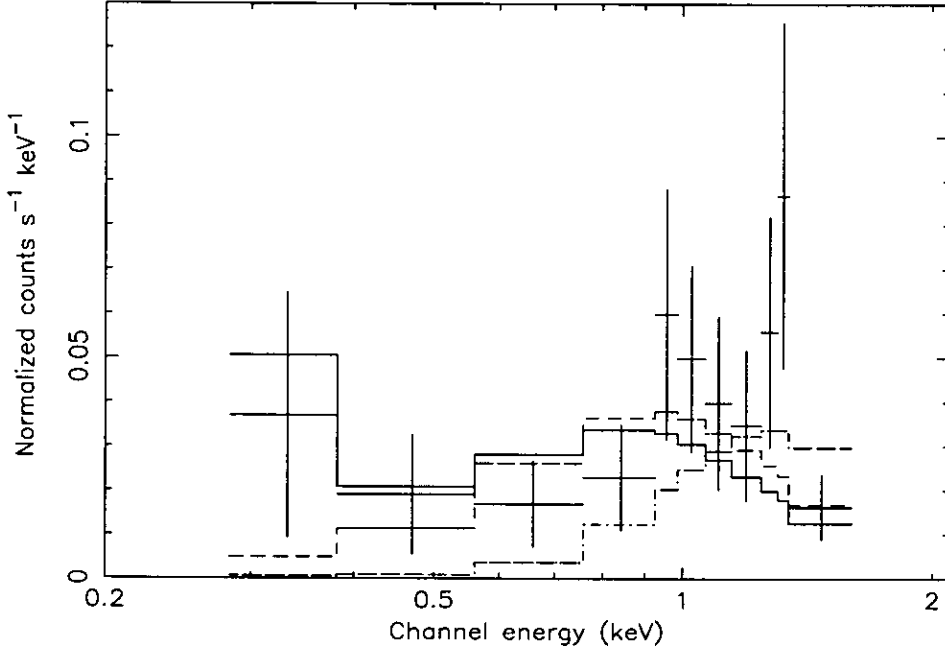


Figure 4.4: The *ROSAT* PSPC spectrum of OY Car in quiescence. Each line shows a thermal bremsstrahlung spectrum with $kT = 2.4$ keV folded through the instrumental response. The different absorbing columns are: solid: $N_H = 10^{20}$ cm $^{-2}$, dash: $N_H = 10^{21}$ cm $^{-2}$, and dash-dot: $N_H = 10^{22}$ cm $^{-2}$.

Table 4.7: Table of quiescent luminosities and emission measures, assuming a single-temperature thermal bremsstrahlung source and neutral interstellar absorption. The ‘normalisation’ is the normalisation of the thermal bremsstrahlung model in XSPEC, given by $K = (3.02 \times 10^{15})/4\pi D^2 EM$, where D is the distance (in cm) and EM is the emission measure. A 0.1 - 2.5 keV bandpass is used for the luminosity calculation. The χ^2 is evaluated for 11 data points.

kT (keV)	N_H ($\times 10^{22}$ cm $^{-2}$)	Normalisation ($\times 10^{-4}$)	$EM \times 10^{53}$ ($\int n_e n_I dV$)	Intrinsic luminosity ($\times 10^{30}$ erg s $^{-1}$)	χ^2
1.0	0.01	4.3 ± 1.5	1.1 ± 0.4	0.72	14.5
2.4	0.01	3.6 ± 1.2	1.0 ± 0.3	0.80	10.2
4.4	0.01	3.6 ± 1.1	1.0 ± 0.3	0.82	9.1
6.0	0.01	3.7 ± 1.2	1.0 ± 0.3	0.84	8.8
1.0	0.1	7.3 ± 2.4	1.9 ± 0.6	1.20	11.2
2.4	0.1	5.3 ± 1.7	1.4 ± 0.5	1.20	9.0
4.4	0.1	5.1 ± 1.6	1.4 ± 0.4	1.21	8.5
6.0	0.1	5.1 ± 1.7	1.4 ± 0.4	1.22	8.3
1.0	1.0	45.5 ± 11.4	12.1 ± 3.1	7.6	13.4
2.4	1.0	24.6 ± 7.5	6.6 ± 2.0	5.4	15.8
4.4	1.0	21.6 ± 6.9	5.7 ± 1.8	4.9	16.6
6.0	1.0	21.1 ± 6.8	5.6 ± 1.8	4.8	16.9

of the material would be ionized. *A priori* models with a two-component absorption, consisting of neutral (cold absorber) and ionized (warm absorber) components, were thus considered.

It was again found necessary to freeze various parameters because the χ^2 -minimisation routines persisted in returning both a value of zero for the neutral column density and a high degree of ionization for the warm absorber¹, both unlikely scenarios. The increased number of free parameters also served to make realistic minimisation difficult.

Underlying bremsstrahlung temperatures of 2.0 and 7.0 keV were chosen, to represent the extremes in the range of temperatures found thus far from X-ray observations of CVs. In order to investigate the variations in the intrinsic luminosity due to the ionized absorber, the interstellar absorption was frozen at $N_H = 10^{20} \text{ cm}^{-2}$ for these fits. The temperature of the ionized absorber was frozen at 10,000 K and the Fe abundance was not allowed to vary from solar (cf. Horne et al. 1994). The luminosities were calculated for two different values of ionized absorber N_H (10^{21} and 10^{22} cm^{-2}), and a free ionization parameter. The results are shown in Table 4.8.

For comparison, alternate fits were undertaken with a two-temperature model consisting of a bremsstrahlung+blackbody source absorbed by neutral gas. In these fits, the source temperatures were frozen and the normalisation and absorption were allowed to vary. The blackbody temperature was chosen to be 0.008 keV because this was the temperature found for the blackbody component found in VW Hyi by van Teeseling et al. (1993).

Figure 4.5 is an illustration of a statistically “good fit” to the quiescent spectrum of OY Car. The fit is better than the single component absorption models purely in terms of the χ^2 -value, but the value of the interstellar column is zero, which seems unlikely — the typical interstellar column in this region of the sky is $\sim 10^{21} \text{ cm}^{-2}$ (from GETNH; but see the caveats listed in Section 3.5).

Finally, comparison of Tables 4.7 and 4.8 allows calculation of values for the quiescent luminosity across the range of single- and two-component absorption models under consideration. While it is not possible to choose between them with real statistical confidence, it is clear that the best χ^2 -values return a typical quiescent X-ray luminosity of $L_x \lesssim 5 \times 10^{30} \text{ erg s}^{-1}$.

¹The degree of ionization of the warm absorber is parameterized in XSPEC as $\xi = L/n_e R^2$, where R is the distance.

Table 4.8: Table of quiescent luminosities, assuming an *a priori* model consisting of a thermal bremsstrahlung source absorbed by a partially ionized gas corresponding to a two-component (neutral and warm) absorber. The neutral absorption column density has been fixed at 10^{20} cm^{-2} . A bandpass of 0.1 - 2.5 keV is used for the luminosity calculation. Summary results for a two-temperature alternate fit, consisting of a bremsstrahlung+blackbody source absorbed by a single component neutral absorption, are shown for comparison. For this latter fit, the bremsstrahlung and blackbody temperatures were each frozen and the absorption was allowed to vary. See text for further details.

Single temperature bremsstrahlung, two-component absorber					
kT (keV)	N_H iabs ^a ($\times 10^{22} \text{ cm}^{-2}$)	ξ^b	Intrinsic flux ($\text{erg cm}^{-2} \text{ s}^{-1}$)	Intrinsic luminosity ($\times 10^{30} \text{ erg s}^{-1}$)	χ^2 ^c
2.0	0.1	< 0.01	1.46×10^{-12}	1.17	9.15
7.0	0.1	0.26	1.33×10^{-12}	1.07	7.76
2.0	1.0	3.26	4.33×10^{-12}	3.48	8.05
7.0	1.0	5.34	3.90×10^{-12}	3.14	9.55
Two-temperature (bremsstrahlung+bbody), neutral absorber					
kT (bremss) (keV)	kT (bbody) ($\times 10^{22} \text{ cm}^{-2}$)	N_H	Intrinsic flux ($\text{erg cm}^{-2} \text{ s}^{-1}$)	Intrinsic luminosity ($\times 10^{30} \text{ erg s}^{-1}$)	χ^2
2.0	0.008	0.17	3.59×10^{-12}	2.89	5.78
7.0	0.008	0.15	3.60×10^{-12}	2.90	5.85

^aThe column density of the warm absorber.

^bIonization parameter; defined as $\xi = L/n_e R^2$.

^cCalculated for 11 data points.

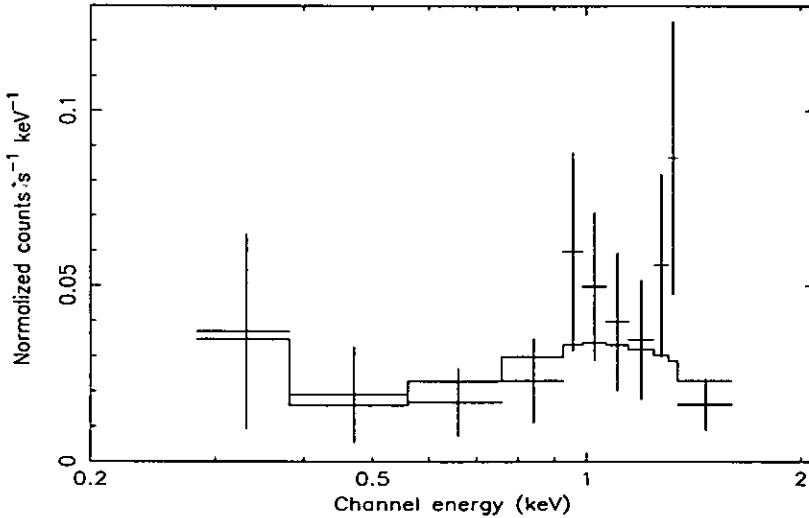


Figure 4.5: The *ROSAT* PSPC spectrum of OY Car in quiescence, this time fitted with a two-component absorption model (neutral interstellar and ionized local), *with cold and warm absorbers and normalisation allowed to vary*. The temperature of the X-ray source has been frozen at 6.0 keV. The fit is statistically better than the neutral absorption models, but disentangling the effect of the relative contributions is not possible with the signal to noise of this spectrum. The interstellar component in this fit is actually $n_H = 0.0 \text{ cm}^{-2}$.

4.4.2 The 1998 Jan *ROSAT* HRI observation - an X-ray eclipse

Figure 4.6 shows that the X-ray flux is variable over the duration of the observation. The data provide full coverage of 10 eclipses and partial coverage of 9. The mean HRI count rate over the course of the observation is $(1.60 \pm 0.06) \times 10^{-2}$ counts s^{-1} .

The mean quiescent X-ray light curve was obtained by folding all the available data into 96 phase bins on the orbital period of OY Car. The total exposure time of each of the 96 phase bins is shown in Figure 4.7. The duration of the optical white dwarf eclipse, defined as the difference between the second and third contact phases of the white dwarf, is 231 s (Wood et al. 1989). Thus with 96 phase bins, four bins cover the eclipse and have a total duration of 227 s. The bins were chosen such that the start of one bin coincided with orbital phase zero.

In Figure 4.8, the quiescent X-ray light curve of OY Car is shown, binned into 96 phase bins, phased on the ephemeris presented in Section 4.3 with a correction of -8s subtracted from the constant term. With the -8s correction, the σ -values of all four eclipse bins are at a simultaneous low, implying that this is the best ephemeris for the X-ray data. The spread of values in the optical $O - C$ determinations in Section 4.3 is $\sim 2.4 \times 10^{-4}$ days, or 20s, so the discrepancy in the ephemeris of the X-ray data is well within the spread of the $O - C$ values of the optical observations.

To investigate the significance of the eclipse, the data were binned into 24 bins such that the duration of one bin was marginally smaller than the duration of the optical white dwarf eclipse. Now the out of eclipse flux was $(1.70 \pm 0.06) \times 10^{-2}$ counts s^{-1} , and the flux in eclipse was $(0.14 \pm 0.06) \times 10^{-2}$ counts s^{-1} , where these are the mean values and the errors are 1σ Poissonian. The eclipse is thus significant at the $(1.70 - 0.14) / \sqrt{0.06^2 + 0.06^2} = 18\sigma$ level. The fact that the eclipse coincides with phase zero makes the detection more compelling.

Two methods were used to constrain the duration of the X-ray eclipse. First, the data were divided into 96 phase bins and the bins shifted backwards and forwards until in one of the four eclipse bins, the count rate deviated from zero by 2.5σ or greater (cf. van Teeseling 1997). This allows the estimate of the upper limit to the width of the X-ray eclipse of ~ 271 s, which is 40s longer than the optical eclipse. Secondly, assuming that the eclipse is symmetric, the symmetrized light curve folded at 20s time resolution was examined (cf. Wood et al. 1995a). The full width zero depth of the eclipse in this case is then $FWZD = 259$ s, or 28s longer than the optical eclipse of the white dwarf.

Finally, note the apparent similarities between the average X-ray light curve presented

here and that obtained for Z Cha by van Teeseling (1997): both light curves exhibit a dip near phase 0.7 — 0.8. The similarity in the structure of the light curves is striking. Similar dips at similar orbital phases have been observed extensively in low-energy X-ray observations of U Gem, both in quiescence by *ASCA* (Szkody et al. 1996) and in outburst by *EXOSAT* (Mason et al. 1988) and *EUVE* (Long et al. 1996b). The dips occurring in U Gem have been interpreted as analogous to the dips which occur in the light curves in low mass X-ray binaries (LMXBs), in that the dips occur at the correct orbital phase as predicted by the LMXB models. These models seek to explain the dipping seen in LMXB light curves by invoking disc-accretion stream effects. One set of models explains the modulation as due to structure on the disc rim particularly where the accretion stream hits, forming a bulge (White & Mason 1985, and references therein). The other main model is that of Frank et al. (1992), which also invokes stream effects, but explains the modulation as due to the interaction of the stream residual above and below the accretion disc with a ring that forms at $r \sim 10^{10}$ cm when the remnant stream circularizes.

The statistics of the individual orbits in this observation of OY Car are rather poor. It may be that the apparent dips seen in this and other light curves are due to the same effect that causes the dips in LMXBs, and while this is suggestive of flux variability with phase, the low signal to noise precludes a quantitative analysis of these features, even in the average light curve.

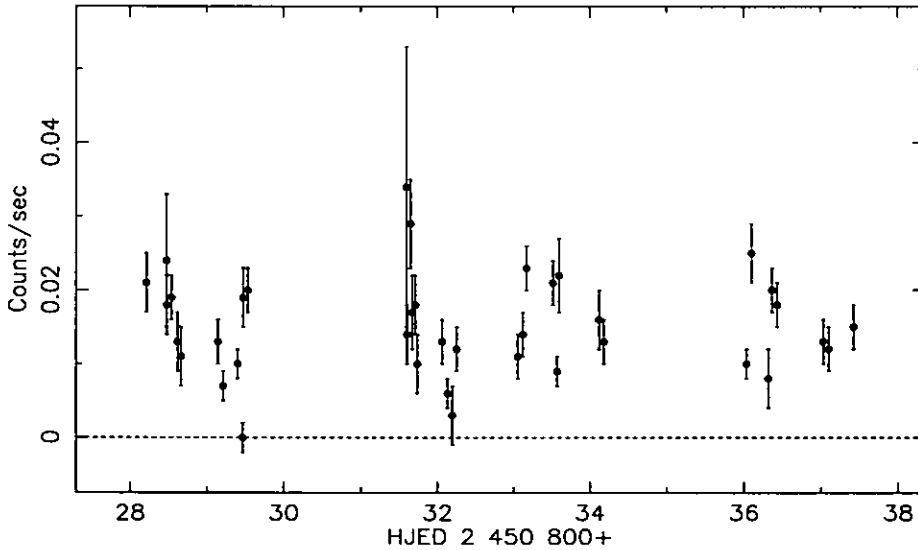


Figure 4.6: The behaviour of the X-ray flux over the duration of the *ROSAT* HRI observations. The panel shows each observation average with 1σ error bars. Eclipses have not been removed.

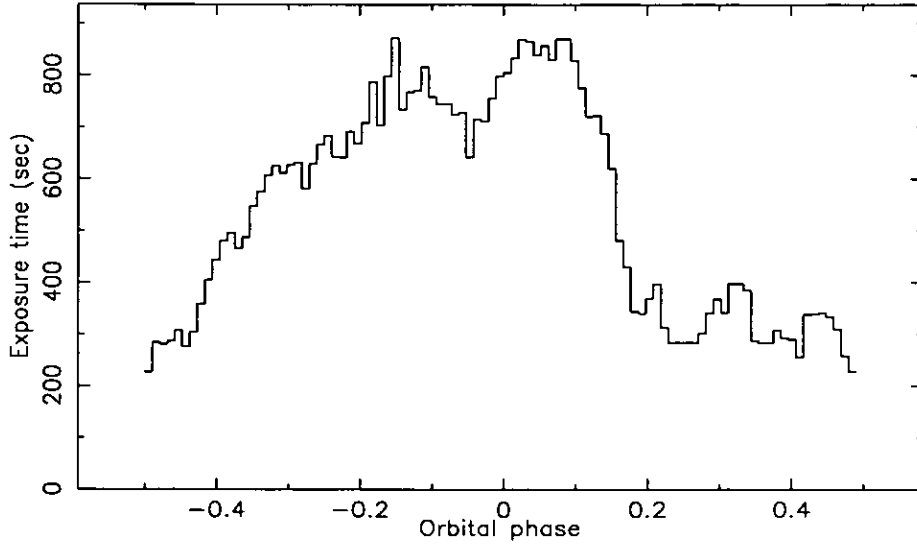


Figure 4.7: The effective exposure times of each of the 96 phase bins used for the quiescent light curve, in seconds.

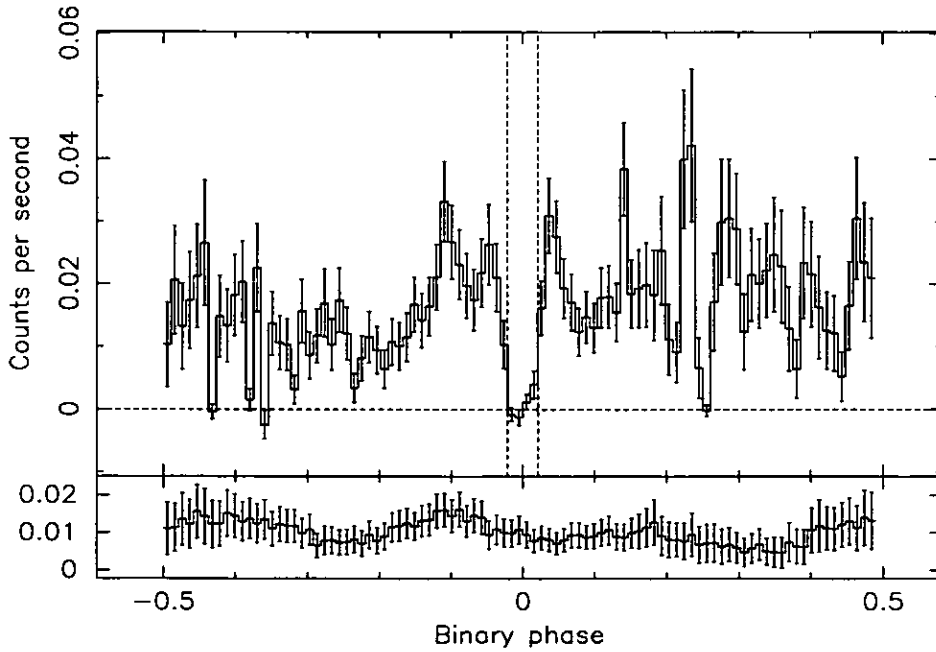


Figure 4.8: The *ROSAT* HRI quiescent X-ray light curve, folded on the orbital period of OY Car in 96 bins, is shown in the top panel. The bottom panel shows the corresponding folded background light curve, scaled to the dimensions of the source extraction circle. The dotted lines represent the times of the optical white dwarf eclipse (Wood et al. 1989), and the zero flux level. The error bars are 1σ Poissonian. The data have been phased using the ephemeris derived in Section 4.3, with an adjustment of -8s to optimise the X-ray eclipse.

4.5 Discussion

4.5.1 The quiescent X-ray spectrum

Comparison with VW Hyi

This Section is intended as a companion piece to Section 3.6.1, in which X-ray observations of OY Car and VW Hyi in outburst and superoutburst are discussed. To recap, comparison with VW Hyi is useful because VW Hyi is perhaps the canonical non-eclipsing dwarf nova, in much the same way as OY Car is the canonical high-inclination system. The inclination is one crucial aspect that must be taken into account in any comparison of these systems; the related quantity of the absorption to the X-ray source must also be considered, as should the differing bandpasses of the respective satellites involved.

VW Hyi is the only dwarf nova to have been detected in quiescence by the *ROSAT* WFC, likely due to the low interstellar column in this direction. VW Hyi was not observed above background in quiescence by either of the detectors on *EUVE* during the all-sky survey phase. It is shown in Section 4.2.1 that OY Car was not detected by the *ROSAT* WFC.

In contrast to the case in outburst and superoutburst, in quiescence the only components predicted to be present are those detectable by *ROSAT* and *GINGA* (and *ASCA*), i.e., hot, optically thin spectra. Fits to the quiescent X-ray spectrum of VW Hyi have produced various values for the temperature of the emitting gas, typically yielding $kT \lesssim 10$ keV, depending on the spectral response of the satellite involved. Belloni et al. (1991) derived a quiescent temperature of $kT = 2.17 \pm 0.15$ keV when their *ROSAT* PSPC observation was fitted with a single-component Raymond-Smith optically thin thermal plasma with line emission at ~ 1 keV. Wheatley et al. (1996) extended the analysis still further by combining the *ROSAT* PSPC observation of Belloni et al. with *ROSAT* WFC EUV data at the low end and *GINGA* hard X-ray data at the high end, giving unprecedented wavelength coverage of the high-energy spectrum of VW Hyi. The resulting fits are thus constrained to an unparalleled degree. Wheatley et al. fitted this combined spectrum with single and two-temperature Mewe optically thin plasma models, with and without line emission. They found that the dominant continuum temperature is ~ 6 keV for both model types, although the data did not distinguish between model types. For the two-temperature case, the components are at temperatures of ~ 6.0 keV and ~ 0.7 keV. Wheatley et al. (1996) suggest that the observed quiescent spectrum of VW Hyi is consistent with emission from material heated to ~ 12 keV and cooling to temperatures below the bandpasses of the instruments on *ROSAT* and *GINGA*.

Belloni et al. (1991) find a bolometric X-ray flux of $f_X \simeq 1.9 \times 10^{11} \text{ erg cm}^{-2}\text{s}^{-1}$ from their *ROSAT* observation of VW Hyi. This corresponds to a quiescent luminosity of $L_X \simeq 10^{31} \text{ erg s}^{-1}$ for a distance of 65 pc (Warner 1987a).

The *ROSAT* observation presented here of OY Car in quiescence does not contain enough information to do more than constrain the X-ray spectrum and the absorption to the X-ray source. The quiescent spectrum of OY Car is consistent with optically thin emission at a temperature of $kT \lesssim 10 \text{ keV}$, typical of the boundary layer emission for this type of object. The corresponding quiescent X-ray luminosity is $\sim 10^{30} \text{ erg s}^{-1}$.

4.5.2 The quiescent luminosity, the eclipse and the absorption

In terms of the emission measure and hardness ratio, OY Car is similar to the other high inclination dwarf novae investigated in van Teeseling & Verbunt (1994) and van Teeseling et al. (1996): the emission measure of the X-ray emitting source is small compared to that in lower inclination systems. This is almost certainly due to the effect of the disc edge, blocking the emission.

The quiescent X-ray luminosity of OY Car appears comparable to both Z Cha ('bolometric' X-ray luminosity $L_{X_q} \sim 2.5 \times 10^{30} \text{ erg s}^{-1}$; van Teeseling, 1997) and HT Cas in its unusually low state ('bolometric' $L_{X_q} \sim 5 \times 10^{30} \text{ erg s}^{-1}$; Wood et al. 1995a), but is lower than the X-ray luminosity of HT Cas in its normal quiescent state as derived from the *ASCA* observation of Mukai et al. (1997) ($L_{X_q} \sim 2.2 \times 10^{31} \text{ erg s}^{-1}$). Córdova & Mason (1984a) quote typical CV X-ray luminosities of $\sim 10^{31} \text{ erg s}^{-1}$ in quiescence, although it must be remembered that the proportion of high inclination CVs is small.

The X-ray luminosity of OY Car in quiescence is still lower than that of VW Hyi. There are several possible reasons why this could be so, including:

1. The white dwarf in these systems might be spinning rapidly. This is not inconceivable, given that Sion et al. (1995a), using high resolution *HST* spectra, found that the white dwarf of VW Hyi was spinning at $v \sin i \sim 600 \text{ km s}^{-1}$, although they subsequently show that even this rotation rate cannot account for the low L_X/L_{opt+UV} ratio for this system. Further, Cheng et al. (1997a) found that the white dwarf in WZ Sge is rotating at a $v \sin i \sim 1200 \text{ km s}^{-1}$. Observations of U Gem show that the white dwarf in that system is rotating at $v \sin i \sim 100 \text{ km s}^{-1}$ (Sion et al. 1994), while Mauche (1997a) calculates a $v \sin i \sim 300 \text{ km s}^{-1}$ for the white dwarf in SS Cyg. Of these systems, U Gem possesses the longest orbital period ($P_{orb} = 4.25 \text{ h}$) and slowest white dwarf rotation, while WZ Sge has the shortest orbital period ($P_{orb} = 1.36 \text{ h}$) and the fastest-spinning white dwarf. OY Car, Z Cha, and HT

Cas all have orbital periods closer to that of WZ Sge than that of U Gem. On this evidence, it could be that the white dwarf in OY Car is spinning relatively fast, and that this may have the effect of reducing the X-ray flux.

2. There may simply be a very low rate of mass transfer through the boundary layer onto the white dwarf. Assuming the steady state case (i.e., $L_{bl} = \frac{1}{2}GM_{wd}\dot{M}/R_{wd}$), then for the case of these observations of OY Car in quiescence, \dot{M} is $3 \times 10^{-13} - 2.7 \times 10^{-12}M_{\odot} \text{ yr}^{-1}$, the lower limit of which is an exceptionally low value. Wood et al. (1995a) find a mass transfer rate onto the white dwarf of $\dot{M} \sim 1 \times 10^{-12}M_{\odot} \text{ yr}^{-1}$ for the low state of HT Cas. By contrast, if the rate of mass transfer given by gravitational radiation is calculated using

$$\dot{M} = 2.4 \times 10^{15} \frac{M_{wd}^{\frac{2}{3}} P_{orb}^{-\frac{1}{6}} (\text{h})}{(1 - \frac{15}{19}q)(1 + q)^{\frac{1}{3}}} \text{ gs}^{-1} \quad (4.2)$$

(Warner 1995). Here M_{wd} is the white dwarf mass, P_{orb} is the orbital period, q is the mass ratio, and the accretion rate is measured in grammes per sec. With the value given in Wood et al. (1989) for the primary mass and the orbital period derived in Chapter 4, the average mass transfer rate is $\sim 1.4 \times 10^{-11}M_{\odot} \text{ yr}^{-1}$, a factor of 5 higher than that deduced from these observations.

An alternative formulation for the gravitational mass transfer rate is given in Patterson (1984), which can be rewritten as (Shafter et al. 1986):

$$\dot{M}_2 = 5.11 \times 10^{-11} \left(\frac{\beta}{\alpha} \right)^{3.67} \frac{M_{wd}^2 P^{-0.26}}{(M_{wd} + 0.07P^{1.22})^{1/3} (M_{wd} - 0.055P^{1.22})} M_{\odot} \text{ yr}^{-1} \quad (4.3)$$

where β and α are parameters of order unity, P is the orbital period in hours and it is assumed that $M_s/M_{\odot} \approx 0.07P(\text{hr})^{1.22}$ (empirically determined, Patterson 1984). Substituting the appropriate values as above, an average rate of mass transfer of $\sim 3.9 \times 10^{-11}M_{\odot} \text{ yr}^{-1}$ is obtained, more discrepant with the observationally derived value.

If the explanation for the low X-ray luminosity really is due to a low mass flux through the boundary layer, then OY Car would have to be in a low state at the time of these observations. An examination of the VSS RAS NZ light curve of OY Car during 1994 July was undertaken, but there are too few reliable observations (most observations are upper limits) from which to draw any conclusions.

Note that the calculations above do not include the increase in the average mass transfer rate due to the outbursts and superoutbursts,

3. There may be differing values of the absorption to the X-ray source, and this is discussed below.

Constraining the absorption

Constraining the absorption to the X-ray source should in principle be considerably easier to do when the system involved is in quiescence, rather than undergoing an outburst. As shown in Chapter 2, during outburst the accretion disc develops a considerable flare, which, in a high inclination system, causes the disc edge to contribute considerably to local absorption of the system. In quiescence, though, the only components that need to be considered are the interstellar absorption and the intrinsic local absorption of the system — the ‘iron curtain’.

The *HST* ultraviolet observation by Horne et al. (1994) showed an ‘iron curtain’ of veiling material superimposed on the spectrum of the white dwarf. Horne et al. (1994) could not pinpoint the exact position of this gas, although placing the material at the outer disc allows the plausible explanation that the disturbances that produce the material are driven by the gas stream (however, see Catálan et al. 1998). Independent of the location of the gas, Horne et al. (1994) find a column density of $N_H \simeq 10^{22} \text{ cm}^{-2}$.

Given that X-ray eclipses have been detected in HT Cas and Z Cha in quiescence, it is perhaps not surprising to have found the same for OY Car. The analysis in this Chapter shows that there is a clear and unambiguous (although not necessarily total) eclipse of the X-rays, and that the X-ray eclipse is coincident with the optical white dwarf eclipse. The very fact that X-rays are detected from OY Car, throughout the entire orbit bar the eclipse, demonstrates that the column density of the intervening material is not sufficient to extinguish the flux in the *ROSAT* passband. This effect would be noticeable if the column density were $N_H \sim 10^{22} \text{ cm}^{-2}$, as argued by Naylor & la Dous (1997).

So the real difficulty lies in constraining the value of the column density, N_H , and it is on this that the luminosity of the system is most dependent. It is perhaps premature to draw conclusions when this factor is such a relative unknown.

Irrespective of the quality of the X-ray spectrum, there are several possible resolutions to any discrepancy in the value of the absorption as calculated by different methods, as follows.

1. Variability could be the key: it may be that the ‘iron curtain’ is not a permanent feature and that the Horne et al. (1994) observation happened to view the source when the column density of the intervening material was higher than usual. One

obvious cause of a higher local absorption than usual is a recent outburst or super-outburst. However the Horne et al. (1994) observation was obtained in the middle of a quiescent period, strongly suggesting that the source of the veiling gas is not connected to the outbursts.

It seems possible that the absorption could be intimately connected to the accretion of material, and as this is variable, then so is the strength of the absorption. Three separate X-ray observations of HT Cas have yielded three widely differing values of N_H : $1.8 \times 10^{20} \text{ cm}^{-2}$ in the low state (Wood et al. 1995a), but between 6×10^{20} and $3 \times 10^{21} \text{ cm}^{-2}$ in quiescence (Patterson & Raymond 1985; Mukai et al. 1997). Naylor & la Dous (1997) show that the hydrogen column density of U Gem in outburst varies from $\lesssim 10^{19}$ to about $\sim 10^{22} \text{ cm}^{-2}$ (three orders of magnitude!); it is not inconceivable that smaller variations in the column density occur in quiescence.

2. Another manifestation of this inconstancy is variability on the orbital timescale. Because of the nature of the existing observations, it is not known how the absorption changes with orbital phase: it is quite possible that the local absorption varies azimuthally around the disc, even in quiescence. Catalán et al. (1998) test this hypothesis in the case of OY Car itself: it appears that the ‘iron curtain’ reaches a maximum absorption near $\phi = 0.5$ and is weakest just before the eclipse of the white dwarf.
3. Naylor & la Dous (1997) suggest that heavy element ionisation may also explain any discrepancy: they argue that if enough of the heavier elements responsible for the X-ray absorption were ionized, this would reduce the opacity and increase the X-ray column density. But they subsequently argue that a temperature of 10,000 K, as derived by Horne et al. (1994) for the ‘iron curtain’, is insufficient to produce significant heavy element ionization.

The results given in Table 4.8 show that both the 2 keV and the 7 keV spectra with a high column density ionized absorber require more ionization than the same respective spectrum with a lower column density. When the ionization parameter is frozen, the 2 keV spectrum with a low column density exhibits a considerable soft excess; this excess is lessened with the 7 keV spectrum. The spectral constraints attempted here do suggest that there may be some ionization.

Figure 4.4 shows that a single-component neutral absorption with a column density of 10^{22} cm^{-2} is not compatible with the data. Two-component absorption models featuring both neutral and ionized contributions do fare better in terms of the raw

χ^2 value, because an ionized (or, more likely, partially ionized in this case) absorber allows more of the soft X-ray/EUV flux through due to decreased opacity. Frustratingly, here a two-component absorption model fares no better at defining real constraints because realistic estimates for the relative contribution of each component are prevented by the data quality.

In the survey of PSPC observations of 37 CVs carried out by Richman (1996), systematic residuals were found in the soft (~ 0.2 keV) region of the spectrum. Instead of invoking warm local absorption, Richman suggests that the data may be better described by a distribution of temperatures, a suggestion which echoes the analysis of the EUV/X-ray spectrum of VW Hyi by Wheatley et al. (1996). Better quality quiescent spectra of many CVs should help to resolve this question.

This observation of OY Car in quiescence is similar to the previous detections of X-ray eclipses in dwarf novae in that the inferred size of the X-ray emitting region is comparable to the size of the white dwarf, and comes from a source close to the primary. This at least allows us to dismiss any suggestion of an alternative X-ray source in quiescence: the X-rays are definitely coming from the boundary layer region. Establishing a useful lower limit for the duration of the X-ray eclipse was unfortunately impossible; greater precision is precluded by data constraints.

4.6 Conclusions

Optical observations of OY Car in quiescence have allowed an updated ephemeris for the system to be calculated. The phase-resolved *ROSAT* HRI X-ray observations, phased with the updated ephemeris, have shown that there is an eclipse of the X-ray flux from OY Car in the quiescent state, and that the X-rays are emitted from a region very close to the white dwarf.

A further short (1.6 kilosec) observation of OY Car with the *ROSAT* PSPC has perhaps provoked more questions than answers. The quiescent X-ray luminosity seems very low compared to the luminosities of similar (but low inclination) systems. It is not possible, on the basis of this observation, to say with any real certainty what the extent of the absorption to the X-ray source is in quiescence. Be that as it may, reconciliation of measurements of the local absorption in the X-ray and ultraviolet is at the moment difficult. The X-ray data is not compatible with the column density of 10^{22} cm $^{-2}$ derived from model fits to *HST* data by Horne et al. (1994), when fitted with a single-component neutral absorber. When the data are fitted with a two-component absorption, it is impossible

to disentangle the effect of the interstellar column from that of the local column.

There are several plausible explanations for discrepancies between different measurements of the absorption. It may be that the 'iron curtain' is variable, but this is difficult to test observationally in that it requires data acquired simultaneously in the ultraviolet and X-ray. Alternatively, it may be that there is a degree of ionization in the 'iron curtain'.

From observations of suitable systems, we now know that eclipses of the X-ray flux occur when the accretion rate is low, and do not occur when the accretion rate is high. We know that there are discrepancies between X-ray and ultraviolet measurements of the local absorption in OY Car, and that the strength of the absorption appears to be variable and intimately connected to the accretion rate as illustrated by HT Cas.

There are a great number of possible explanations for why the quiescent X-ray luminosity of OY Car is lower than that of VW Hyi, some of which have been detailed above.

For OY Car itself, better quality phase-resolved X-ray light curves are needed, light curves that will enable the exact source of the X-ray emission to be pinpointed. Data with higher time and energy resolution would be desirable, such as is currently available from *ASCA* and which is discussed in Chapter 6. Simultaneous orbital phase dependent observations of these systems in the ultraviolet, such as with the *HST*, will enable the investigation of any variability of the local absorption with orbital phase in both ultraviolet and X-rays. Probing the extent of the ionization of the local absorption due to the 'iron curtain' is now a real and exciting possibility.

Looking further ahead, *XMM* will represent the next generation of X-ray satellites, and will be ideal for the study of these intriguing systems due to the higher energy resolution and especially the simultaneous optical monitoring. The potential for using *XMM* to study eclipsing CVs is discussed further in Chapter 6.

Chapter 5

Modelling of ultraviolet data in quiescence: critical review

5.1 Overview

This Chapter is concerned with the modelling of ultraviolet observations of nonmagnetic CVs, using data obtained from both the *IUE* and *HST* archives. Such ultraviolet observations have in the past been used to estimate various system parameters, and it was the *HST* observation of OY Car by Horne et al. (1994) which first led to the discovery of the ‘iron curtain’.

IUE is generally considered to be one of the most successful satellites ever launched. The *IUE* Final Archive is a testament to both this success and to the long lifetime of the spacecraft, containing as it does $\gtrsim 10^5$ spectra of thousands of objects, obtained over a time span of nearly two decades. Crucially with CVs, ultraviolet spectra may in some cases be used to constrain various primary star parameters, and the sheer number of available spectra made the Final Archive the ideal place to obtain many data sets.

Background details are given in Section 5.2, which contains an overview of the *IUE* observatory, its Final Archive, and explains the origin of this part of the thesis. Further background details are given in Section 5.3, in which the general appearance of dwarf nova spectra in the ultraviolet is discussed. These spectra differ radically depending on the outburst state of the system. In some cases, they offer an alternative way of estimating the temperature of the boundary layer region.

Ultraviolet spectra can also be used to constrain various primary star parameters. Section 5.4 is a review of the various methods used to estimate the white dwarf effective temperature and other physical properties, where possible, from spectroscopic (and

photometric) observations. In this connection, Section 5.5 describes the development of a basic but effective procedure to model *IUE* Final Archive spectra in order to estimate the temperature of the primary.

Where ultraviolet spectra can be used to constrain various primary star parameters, model atmospheres and synthetic spectra of white dwarfs are generally used. In Section 5.6 the development of modern computer codes to model atmospheres and calculate synthetic spectra is described, and brought up to date by describing the codes used for this analysis, TLUSTY and SYNSPEC, written by Dr. I. Hubeny and collaborators. Model atmospheres and synthetic spectra are calculated using TLUSTY, SYNSPEC and associated programs; the model construction process is entered into in some detail, including the calculation of veiled white dwarf spectra featuring an ‘iron curtain’ for high inclination systems.

Section 5.7 details the process of modelling the ultraviolet spectra of some dwarf novae using the basic method developed in Section 5.5. This allowed familiarisation with the modelling of white dwarf atmospheres in the ultraviolet spectral region, and permitted a quantitative assessment of the accuracy of primary temperatures derived using this method as compared to established published values. Additionally, veiled white dwarf synthetic spectral analyses are applied to *IUE* spectra of HT Cas, Z Cha and OY Car itself, to test the reproducibility of certain ‘iron curtain’ parameters with the method developed here. Example *HST* spectra are also included.

The penultimate Section 5.8 discusses the modelling of these spectra in terms of one or more components (physical, parameter or both). There is also a summary of the problems involved in the modelling, and a discussion of the prospects for improvements to the methods developed both here and elsewhere.

Finally Section 5.9 summarises this Chapter. The methods developed here, and improvements thereof, are expected to be applied to the upcoming *HST* data from the simultaneous *ASCA/HST* observations of OY Car scheduled for 2000 Mar; these aspects are discussed in more detail in Chapter 6.

5.2 *IUE*: the satellite and data archive

The very first ultraviolet observation of a CV was that of Nova Serpentis 1970, obtained with the Wisconsin Experiment Package on the OAO-2 satellite (Gallagher & Code 1974; reference from Warner 1995), but it was not until the launch of the hugely successful International Ultraviolet Explorer (*IUE*) satellite, a collaboration between ESA, NASA, and the former UK SRC, on 28 January 1978, that the study of CVs in the ultraviolet

really took off.

Overview of the *IUE* Satellite

Ultraviolet spectra were available from *IUE*¹ over the wavelength range $\sim 1150 - 3200 \text{ \AA}$. The *IUE* satellite was equipped with a 45cm Cassegrain telescope with 2 echelle spectrographs, each with 2 primary and 2 redundant Secondary Electron Conduction (SEC) integrating video cameras as detectors. The cameras were designated LWP, LWR for the long wavelength region (1900 - 3200 \AA), and SWP, SWR for the short (1150 - 1950 \AA); the wavelength resolutions were $\sim 0.2 \text{ \AA}$ and $\sim 6 \text{ \AA}$ in, respectively, the high resolution Echelle mode and low dispersion modes. The SWR camera was never used for scientific exposures because luckily the SWP camera did not fail.

IUE was operated from two ground control stations, situated in Goddard Space Flight Center in Greenbelt, Maryland, USA, and the ESA *IUE* Observatory at the Villafranca del Castillo Satellite Tracking Station (VILSPA) near Villanueva de la Cañada, Madrid, Spain. *IUE* was put into a geosynchronous orbit. Unlike the *HST*, *IUE* spacecraft control was through direct commanding, and the continuous visibility of the satellite from the two ground stations enabled *IUE* to be operated in an interactive mode that allowed modifications to the observation programme in real time. *IUE* was thus run in a similar fashion to general-user ground-based observatories.

Data processing was executed by pipeline software (IUESIPS) that performed complete data reduction to produce scientific results shortly after the observation, and supplied final data products within 48 hours after acquisition.

IUE continued scientific operations for over 18 years until it was switched off due to lack of funding on 27 September 1996.

Overview of the *IUE* Final Archive

Over 104,000 spectra were obtained with *IUE* over the course of the spacecraft lifetime; the *IUE* Final Archive (IUEFA) itself was under construction well before the end of operations. The archive is currently held at the former tracking station at Vilspa², with mirror sites at the Space Telescope Science Institute³ (STSCI) and in the UK at RAL⁴.

The data in the IUEFA used for this investigation were automatically extracted from the raw spectra using specially written software called NEWSIPS (New Spectral Image

¹For more information see the *IUE* Final Archive website at <http://www.vilspa.esa.es>

²<http://www.vilspa.esa.es/iue/iue.html>

³<http://archive.stsci.edu/iue/>

⁴<http://ast.star.rl.ac.uk/iues/iues.html>

Processing System), a direct replacement for the original standard data processing software, IUESIPS. NEWSIPS has, in the course of this investigation, been superseded by the final step in the archive and distribution phase of IUE data: INES (IUE Newly Extracted Spectra). Since the data used here were extracted using NEWSIPS, this extraction system is described below, followed by a brief summary of the improvements implemented in INES.

NEWSIPS was written in the later years of the spacecraft's operational life, and thus incorporates knowledge of the behaviour of the detectors, spectrographs and spacecraft gained over the years. NEWSIPS uses a non-interactive optimal extraction algorithm (Horne 1986) for low resolution spectra. The algorithm requires careful determination of the noise model, the background determination, the extraction profile and the treatment of bad pixels. The process is model-dependent and for automatic processing, parameters have to be fixed and chosen so as to maximise the number of spectra that can be extracted.

NEWSIPS was developed to address four basic requirements for the Final Archive (list from the NEWSIPS Information Manual V2.0 [*IUE* Newsletter #57]):

- To create a uniformly processed and calibrated archive as the final product of the *IUE* mission;
- To exploit new image processing techniques to improve the signal-to-noise ratio and photometric accuracy of the data;
- To verify and correct fundamental information for each image;
- To base the contents of the IUEFA on requirements from the research community.

To ensure a good correction for the intrinsic non-linearity of the SEC cameras when generating the IUEFA, a completely new calibration data set was obtained with which to determine a new non-linearity correction (synonymous with the intensity transfer function, or ITF). Existing *IUE* observations of field white dwarfs were used to establish the extent of the small scale irregularities in the detector sensitivity (or fixed pattern noise). The relative spectral energy distribution over the range 1150 - 3200 Å was eventually established to an accuracy of about 3%, and, according to the NEWSIPS Information Manual, the absolute spectroscopic flux calibration over the whole ultraviolet spectral range is now accurate to 8%.

INES is the final phase of *IUE* archive data extraction and all low dispersion spectra have now been corrected with this system. The improvements of INES over NEWSIPS are detailed in Rodríguez-Pascual et al. (1999). In brief, these are:

- re-derivation of the noise models for the cameras, which has corrected anomalies that were present in the NEWSIPS noise models at high and low exposure levels;
- new algorithms to compute the camera background and the extraction profile, building on knowledge gained over the lifetime of the spacecraft;
- treatment of weak or badly centred spectra, which are now reliably and more consistently dealt with;
- improved data quality flag propagation; and
- resampling of spectra to a linear wavelength scale.

“The purpose of the INES system is to reach the maximum number of scientists with a simple distribution scheme and to provide high-quality data in a form that does not require a detailed knowledge of the instrumental characteristics” (Vilspa Webpage).

Content of the IUEFA: relation to this thesis

The motivation for this Chapter came originally from a desire to expand the number of CV primary stars for which a temperature was known, and to investigate various correlations within the set of known temperatures. The intention here was to generalise the method of synthetic spectral analysis and initiate a systematic search of the IUEFA for CV spectra that might display the broad Ly α absorption profile characteristic of a white dwarf. This would imply a low rate of mass transfer through the accretion disc, and tie in well with the research programme initiated in the later years of *IUE* operation by Drs. B.J.M. Hassall and C. la Dous. Their stated aim was to increase the number of known low \dot{M} systems in the IUEFA, in order to apply a statistical analysis to the data set to find correlations between the white dwarf temperature and e.g., system inclination, or orbital period, and also to correlate cooling times with orbital period. In an independent investigation, Gänsicke & Koester (1999) have also recently searched the *IUE* archive for such low \dot{M} systems, and have modelled the three newly-discovered systems using the Kiel model atmosphere code. Their results are compared with those derived independently here in Section 5.7.2.

The IUEFA also contains quiescent spectra of OY Car and close relatives, Z Cha in particular (see Wade et al. 1994), where the ‘iron curtain’ is visible as a broad depression in the spectrum around 1600Å. When subjected to a synthetic spectral analysis, these spectra can give an estimate of the local column density. This can then be compared with results arrived at independently for X-ray spectral analyses such as that detailed in Chapter 4.

As detailed in Chapter 4, the *ROSAT* observation of OY Car in quiescence showed that a significant X-ray flux was detectable in quiescence, and that there was an X-ray eclipse. This was not expected if the argument of Naylor & la Dous (1997) was accepted, especially given the Horne et al. (1994) estimation of an ‘iron curtain’ with $N_H \simeq 10^{22} \text{ cm}^{-2}$; Naylor & la Dous (1997) argue for extinction of the soft X-ray flux at this column density. Furthermore, modelling of the X-ray spectrum was inconclusive on the extent of the absorption to the X-ray source. Hence, it was decided to propose a simultaneous *HST* and *ASCA* observation of OY Car in order to place simultaneous constraints on the local absorption in the system in ultraviolet and in X-ray. One advantage of observations of this kind is that time variability (see Chapter 4, Section 4.5.2) ceases to be a problem. These proposals were accepted after review by the respective satellite Time Allocation Committees, and the observations have been scheduled for 2000 Mar. There are more details of these proposals and the expected data in Chapter 6.

5.3 Non-magnetic CVs in the ultraviolet

Observations of dwarf novae in the ultraviolet are vitally important because temperatures of $\sim 10,000 - 40,000 \text{ K}$ and more occur in the accretion disc and white dwarf, so that they radiate predominantly in this spectral range. The disc is the dominant ultraviolet light source when the accretion rate is high, as in outburst or superoutburst (and novalikes: a spectroscopic signature of a primary star has not yet been *unambiguously* detected in the spectrum of a novalike variable, hence the focus of this discussion on dwarf novae). However, when the accretion rate is low, prominent Lyman α (and, outside the wavelength range of *IUE* and *HST*, Lyman β) absorption can be observed in the ultraviolet spectra of some dwarf novae, implying that the white dwarf primary is contributing substantially. Sometimes an observed rise in the flux levels towards longer wavelengths (very approximately, $\gtrsim 1600\text{\AA}$) is indicative of increasing disc contribution in the optical wavelengths.

5.3.1 Observational characteristics

Dwarf Novae

The majority of ultraviolet spectra of quiescent dwarf novae are characterised, as in the optical, by a blue continuum plus emission lines. Lines from ionized species such as HeII, CII - CIV, NIII - NV, OIII, OV, MgII, AlIII, SiII - SiIV, and neutral species such as Lyman α , CI and OI, arising from the disc, are often observed (Warner 1995, and references therein). Table 5.1 lists the most common emission lines seen in the ultraviolet spectra

of quiescent dwarf novae. The wide range of ionization states suggests multiple sites for the production of these lines. In some spectra, though, there is Ly α absorption and a decline in the continuum flux below ~ 1400 Å. While the most plausible explanation is that the source of the Ly α absorption is due to the photospheres of white dwarf primaries in the temperature range $15,000 < T_{\text{eff}} < 20,000$ K, there remains the possibility that a hot, optically thick inner portion of the accretion disc may be responsible for part of the absorption.

Table 5.1: An ultraviolet emission line list for dwarf nova quiescent spectra, adapted from Warner (1995).

Wavelength (Å)	Line
1026	Ly β
1216	Ly α
1175-76	CIII
1239,43	NV
1299	SiIII
1302-06	OI
1335	CII
1394,1402	SiIV
1548,51	CIV
1640	HeII
1855,63	AlIII+FeII
2979,2983	MgII

However, some ultraviolet spectra of dwarf novae in quiescence are almost totally dominated by absorption lines. One might expect this effect to be dependent on the rate of mass transfer through the disc. However, WX Hyi and YZ Cnc have very strong emission lines in the ultraviolet, whereas OY Car, VW Hyi, Z Cha and WZ Sge all have absorption line dominated spectra, despite all these systems having a low rate of mass transfer through the disc. The spectra dominated by absorption lines can be explained qualitatively in terms of an inclination effect: the strength of the emission line decreases with increasing inclination, changing to an absorption line for $i > 60^\circ$. It appears that in quiescence the hot inner regions of the disc are optically thin when viewed at low inclination, changing to optically thick at higher inclinations due to the increasing depth of material in the line of sight. The correlation is not perfect: the high inclination systems HT Cas and IP Peg have weak emission lines.

On the rise to outburst, the general spectrum, dominated by emission lines, is overwhelmed by the increasing continuum, and the emission lines are swamped by absorption. Figure 5.1 illustrates the development of the spectrum of VW Hyi from quiescence to normal outburst peak. There is often a delay between the optical rise to outburst and

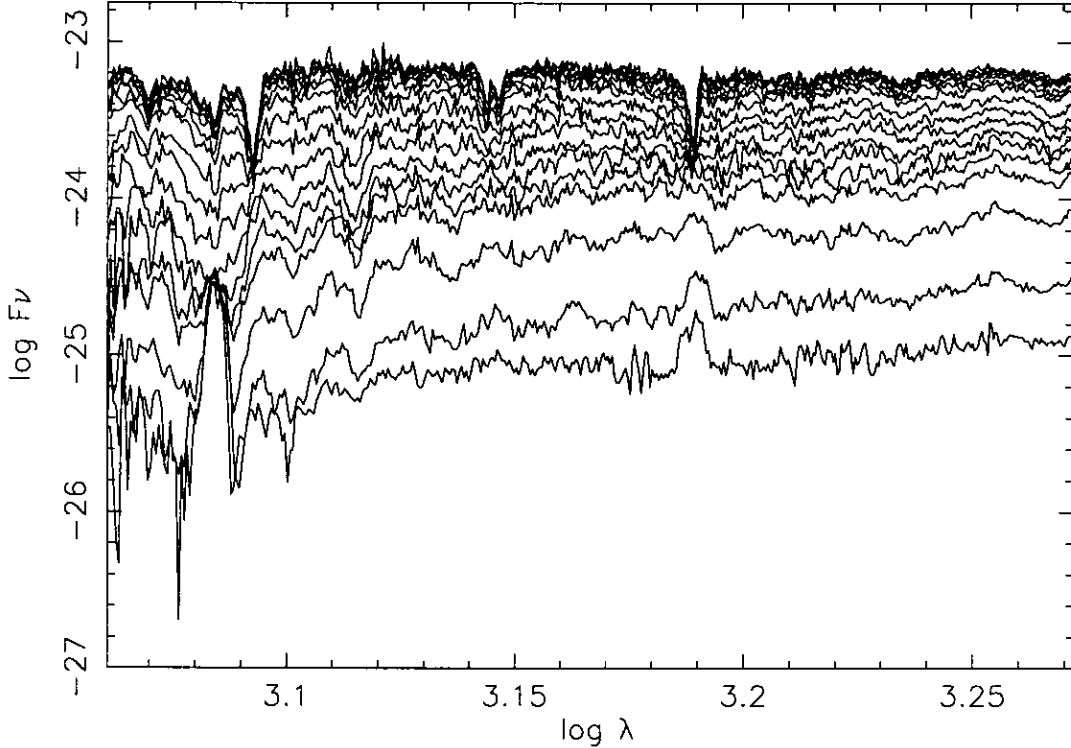


Figure 5.1: An illustration of the development of the ultraviolet spectrum of VW Hyi on the rise to normal outburst maximum, as observed by the *IUE* in April 1990. The spectra (SWP40028 - SWP40045; from the IUEFA) were taken in sequence and clearly show the development of the continuum due to the rise in flux from the disc, and the transition from a spectrum with emission lines to one dominated by absorption lines. The Figure is plotted in log-log form because of the large rise in flux over the course of the outburst.

the ultraviolet rise, although there are exceptions, e.g. CN Ori. While the propagation of the transition front itself across the disc produces a delay, this is insufficient to explain the observed delay durations. One of several explanations put forward for the ultraviolet delay is that it is due to a refilling of the innermost regions of the disc, which may be truncated due to irradiation by the primary (King 1997), or evacuated by a residual primary magnetic field (e.g., Livio & Pringle 1992).

The appearance of the ultraviolet spectrum at outburst maximum is strongly dependent on the inclination. For low inclination systems, the spectrum is dominated by absorption lines, with the exception of P Cyg profile emission, which is most often seen in CIV $\lambda 1550$. For inclinations $70^\circ \lesssim i \lesssim 80^\circ$ the spectrum is almost featureless, while for $i \gtrsim 80^\circ$, strong emission lines are seen.

The resonance lines in outburst are observed to have P Cyg profiles in many systems with $i \lesssim 65^\circ$, although the effect is by no means universal. Sometimes only the blue shifted

component of the P Cyg profile is seen. These profiles are thought to be evidence for a stellar wind during outburst; such winds are discussed further below.

Novalike variables

In general, the spectra of NLs display evidence for conditions of higher excitation than those of dwarf novae, in keeping with the interpretation (within the framework of the disc instability model) that these systems are similar to dwarf novae in a state of near-permanent outburst. Differences are apparent, however, between novalike spectra and those of dwarf novae at maximum. Additional lines of higher ionization are seen (e.g., SiIII λ 1206, OV λ 1371). The dwarf novae do not develop the deep NV, SiIV and CIV absorptions of the novalikes with optically thick discs, while emission lines appear strongly in such novalikes for $i \gtrsim 65^\circ$, but only become strong in dwarf novae at maximum for $i \gtrsim 75^\circ$.

5.3.2 Boundary layer temperatures from ultraviolet observations of CV winds

Emission lines from CVs in the ultraviolet, specifically P Cyg profiles, can be used to probe indirectly the temperature of the boundary layer region. This gives a very useful alternative determination of this important parameter, allowing comparison with the temperatures derived from X-ray observations.

It is the ultraviolet resonance lines in novalike variable spectra that show the most compelling evidence for partial reversal into P Cyg profiles, implying, as with spectra of dwarf novae in outburst, the presence of mass loss in a stellar wind. These winds are thought, by analogy with the winds of early-type stars, to be driven by radiation pressure; the P Cyg profiles of the ultraviolet resonance lines are formed by scattering in these winds (Drew & Verbunt 1985). The second source of winds from CVs, the solar-type wind from the secondary, has not yet been detected observationally. For a comprehensive review of CV wind observations and models, see Mauche & Raymond (1997).

The differences between early-type stellar winds and those observed from CVs originate in dissimilar wind geometries and discrete sources. In normal stars, the source for the scattered continuum is the photosphere of the star itself; in CVs it is the accretion disc. Furthermore, the presence of the accretion disc introduces a different wind geometry, and an inclination dependence, as described below.

The lines most affected by P Cyg profiles in the *IUE* (and *HST*) wavelength ranges are the resonance lines CIV λ 1549, SiIV λ 1397 and NV λ 1240. The derived terminal

velocities of these winds (V_∞) are comparable to the escape velocity from the primary ($\sim 5000 \text{ km s}^{-1}$), and it is only material from the inner disc, boundary layer region or surface of the white dwarf itself that is likely to have been accelerated to these velocities (Córdova & Mason 1982b). Mauche & Raymond (1997) list four reasons why accretion disc winds are the more likely cause:

1. the gravitational potential at the surface of an accretion disc is much lower than that at the surface of a white dwarf. This implies lower energies are needed to accelerate the wind to escape velocity; -
2. the spatially extended nature of a disc wind has implications for the duration and depth of eclipses of the line-forming region: the eclipses are often observed to be shallow, indicating an extended zone;
3. spherically symmetric winds are observed to undergo an $r^{-2}V(r)^{-1}$ density decrease (where V is the velocity and r is distance). In a disc wind this decrease is likely to be far less and the high-density component of the wind near the boundary layer could be removed, allowing soft X-rays to emerge. This constraint also requires the terminal velocity to be reached at a distance from the primary comparable to the disc radius; and
4. lastly, since a disc wind will be produced in the same region as the region responsible for the resonant scattering that produces the P Cyg profiles, lower mass loss rates are required for a given column density, and hence a given line strength, than those required for a wind emanating from near the white dwarf.

As is the case in dwarf nova spectra, the P Cyg profiles are only seen in those systems where $i \lesssim 65^\circ$. This inclination dependence can be understood by considering a spherically symmetric wind emanating from the centre of an accretion disc (e.g., Mauche & Raymond 1997). When the disc is viewed edge on, no part of the wind lies in front of the disc, so all that is seen is the emission component whose full width is proportional to the terminal velocity of the wind: $\Delta\nu = 2\nu_0 V_\infty/c$. As the system inclination decreases, the fraction of the wind seen in projection against the disc increases, giving rise to the absorption component. At the same time, the strength of the emission component decreases. This inclination effect is illustrated in Figure 5.2.

The ionization state of the wind is thought to be largely determined by the flux from the boundary layer. Early investigations (e.g., Drew & Verbunt 1985; Kallman & Jensen 1985) encountered problems in explaining the ionization state of the wind within the

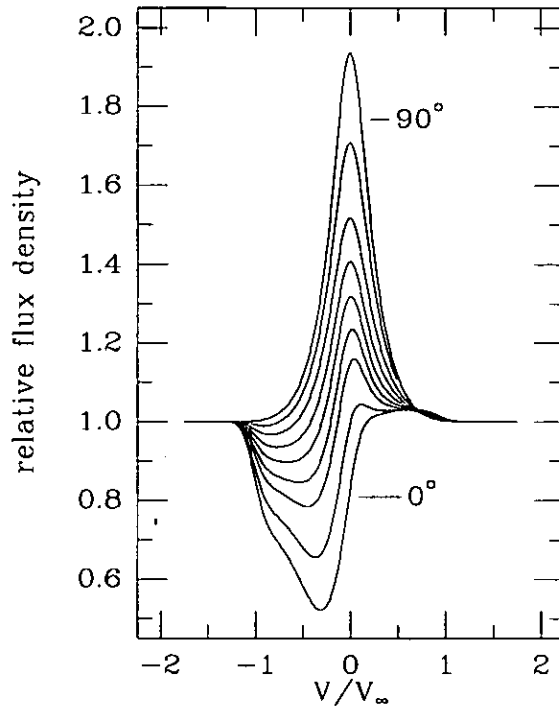


Figure 5.2: Theoretical dependence of the strength and profile of the P Cyg feature on the inclination of the system. When the disc is seen edge-on, only the emission component is seen; the situation is reversed when the disc is viewed face-on, and only the absorption component is seen. From Mauche & Raymond (1997).

framework of a classical (i.e. steady state) boundary layer and a smooth wind, where the latter represented a mass loss rate that was a small fraction of the accretion rate. If these assumptions are included in the models, the wind is ionized further than the observed ionization states of NV, SiIV and CIV. Models by Mauche & Raymond (1987) predicted some 100 times the observed HeII $\lambda 1640$ flux on the basis of these assumptions.

Hoare & Drew (1991) use the theoretical Zanstra (1931) method⁵ to derive limits on the boundary layer temperature of several novalikes and dwarf novae during outburst, using the observed HeII $\lambda 1640$ and $\lambda 4686$ recombination lines. These lines occur if the central ionising source is hotter than 50,000 K, and the observed strength of these recombination lines can be used to estimate the number of He⁺ ionizing photons produced by the boundary layer flux. Because all the emission is assumed to come from the wind, the derived boundary layer temperatures are upper limits. Their results suggest $50,000 \lesssim T_{BL} \lesssim 100,000$ K.

Hoare & Drew (1993) followed up this work by constructing photoionization wind models from discs with cool boundary layers (5 -9 eV) with the canonical mass flow rate

⁵See Appendix A.

of $\dot{M} = 5 \times 10^{-9} M_{\odot} \text{ yr}^{-1}$, and for discs with no boundary layer at all (i.e. primary rotating near break-up speed). They then compared the ionization state of the winds predicted by the models with those observed from spectra of low inclination novalikes (Hoare & Drew 1993). Their results implied that the observed strengths of the CIV and NV lines could be matched by models with a cool, luminous boundary layer at 60,000 - 100,000 K, or disc-only models (no boundary layer) where the accretion rate is $2 - 4 \times 10^{-8} M_{\odot} \text{ yr}^{-1}$. In the latter case the accretion rate was constrained by the need to have inner disc temperatures of $\sim 7 \times 10^4$ K. The deduced mass loss rates from the wind were $\dot{M}_{\text{wind}} \approx 6 \times 10^{-10} M_{\odot} \text{ yr}^{-1}$, which appear to be reasonable values given the mass accretion rate and the agreement with observed line strengths.

The temperatures derived from the Hoare & Drew studies are lower than the $T_{BL} \sim 300,000$ K boundary layer temperature expected from standard consideration of X-ray production in the high accretion rate regime (see Chapter 1, Section 1.2), and suggest that even if $T_{BL} = 300,000$ K, then the boundary layer luminosity can only be a small fraction of the disc luminosity, another manifestation of the missing boundary layer problem. It is not clear why this should be so. This discrepancy between the theory and the observation of CV boundary layers has been a bone of contention since the very first X-ray luminosities were calculated. The analysis of multiwavelength, multi-object observations by Howell et al. (1999) suggests that, in all cases, high energy observations return high temperatures and small emitting areas for the boundary layer, while ultraviolet and redward data return lower temperatures and larger emitting areas. Howell et al. (1999) conclude that high energy observations yield the best measurements of boundary layer temperatures because the ultraviolet data is compromised by emission from the inner accretion disc.

5.4 The white dwarf primary

The accretion of matter onto the central object in a CV is a heating process, and as such will delay the primary from suffering the eventual cold fate of an isolated white dwarf. In addition to heating the white dwarf, accretion of matter from the secondary through a disc also adds mass. This extra mass will have either solar abundances, or the abundances of material processed from previous nova explosions, and will contribute angular momentum to the white dwarf envelope. Thus studying the primaries in accreting CVs and the subsequent comparison of these with isolated white dwarfs can provide illuminating insights into the physics of the accretion process itself.

This Section is a summary of the use of ultraviolet spectroscopic observations to study

the white dwarfs in CVs. For an extensive, very recent, review of white dwarfs in CVs, see Sion (1999); for an introduction to satellite observations of CV primaries, see e.g., Long (1999).

5.4.1 Detection

Ultraviolet light from a CV is typically dominated by that from the accretion disc. Circumstances fortuitously conspire, however, to allow the detection of the primary from ultraviolet (and sometimes optical) spectra in three cases:

- in some dwarf novae with low mass transfer rates in quiescence;
- in some VY Scl novalike variables, where the mass transfer rate can drop temporarily to reveal the spectrum of the primary;
- in some magnetic CVs during the low state, when the accretion appears to have shut off.

For some years now the possibility of using ultraviolet spectra to parameterise the primary (typically the temperature, the abundances of the accreted atmosphere and, more recently, the rotational velocity) has been recognised. The first detections of primaries came from observations of magnetic CVs during low optical brightness states when the accretion appears to stop. Pioneering detections of photospheric light from the primary of nonmagnetic CVs were carried out by Panek & Holm (1984; U Gem), Mateo & Szkody (1984; VW Hya), Shafter et al. (1985; TT Ari) and others. Modelling of the newly-detected primary spectra became an urgent priority.

However, in the case of CVs the modelling is not entirely straightforward because the primaries are not isolated white dwarfs. They will be heated by the accretion process itself and may preferentially be heated in the equatorial plane due to the boundary layer. In fact, several high resolution *HST* Faint Object Spectrograph (FOS) observations of U Gem by Long, Sion and collaborators have revealed evidence for an additional hot, possibly equatorial, component at a considerably higher temperature than the white dwarf (e.g. Long et al. 1993). Additional components are discussed further in Section 5.8.

The primary in a CV differs from a field white dwarf in another crucial respect: the atmosphere is constantly accreting material from the accretion disc. In field white dwarfs, the strong gravity drives a sedimentary process which causes the heavier elements to sink towards the centre; at sufficiently low temperatures the structure of the white dwarf is (theoretically) stratified, with a layer of nearly pure hydrogen on top of a layer of nearly

pure helium, and so on, through progressively heavier elements. The spectra of field white dwarfs, therefore, have very little contribution from any elements other than hydrogen or helium. To a very good approximation then, the ultraviolet spectra of field white dwarfs can be modelled as pure hydrogen (DA type) or pure helium (DB type), with only trace contributions from heavier elements. Note that there is considerable evidence for metal absorbers in the atmospheres of high temperature white dwarfs ($T_{\text{eff}} \gtrsim 50,000$ K), as shown from optical follow-ups to the *ROSAT* WFC all-sky survey (Barstow et al. 1993; Marsh et al. 1997). Marsh et al. found that all white dwarfs detected in the WFC all-sky survey above $T_{\text{eff}} \approx 55,000$ K contain metals in their atmospheres, and a steep rise in opacity is seen at 54,000 K, which they interpreted as arising from the appearance of radiatively supported Fe and Fe-group elements.

The CV primary, though, is likely to acquire a mixed-composition atmosphere through the accretion process. Heavier elements may also be dredged up from deeper in the atmosphere due to turbulent mixing driven by the shear of the boundary layer at the equator. Solar abundance white dwarf spectra can thus be expected to provide better fits to CV white dwarfs than pure hydrogen models alone.

5.4.2 Temperature determination of the primary

Background

Various heating mechanisms affect the white dwarf in a nonmagnetic CV. These include (Sion 1999): instantaneously reradiated accretional heating, slow time-averaged release of gravitational potential energy due to structure changes, angular momentum transport via shear mixing and compressional heating. In shear mixing the rotational kinetic energy is converted into heat and stored in the white dwarf for eventual release as a component of surface luminosity. Sion (1999) states that the time-averaged surface luminosity L_s and temperature T_{eff} for a white dwarf of mass M_{wd} and radius R_{wd} , accreting at a time-averaged accretion rate of \dot{M} is:

$$L_s = L_{\text{accg}} + L_{\text{shear}} + L_{\text{rad}} + L_{\text{cool}} - L_{\nu} \quad (5.1)$$

where, as usual,

$$T_{\text{eff}} = \left(\frac{L_s}{4\pi R_{\text{wd}}^2 \sigma} \right)^{1/4} \quad (5.2)$$

where L_{cool} is the thermal cooling luminosity, L_{rad} is the luminosity due to the instantaneous reradiation of the accretion luminosity, L_{shear} is the shear mixing luminosity and L_{ν} is the neutrino luminosity (from reactions in nova events). L_{accg} is the long term average

rate at which gravitational potential energy is liberated as a response to accretion and is given by:

$$L_{\text{accg}} = \beta \left(\frac{GM_{\text{wd}}\dot{M}}{R_{\text{cold}}} - \frac{GM_{\text{wd}}\dot{M}}{R_{\text{wd}}} \right) \quad (5.3)$$

Here R_{cold} is the Hamada-Salpeter (Hamada & Salpeter 1961) radius of a zero-temperature white dwarf and β is the fraction of the total energy stored in the white dwarf. Iben (1982) modelled spherical accretion and showed that $\beta \sim 0.15 - 0.25$ of the total gravitational potential energy difference.

As dwarf novae have typical outburst recurrence times of a few months, the primary does not have a characteristic temperature as such: one would expect that the outer layers of the white dwarf are heated to a certain temperature during an outburst and from that point continue cooling down until the next outburst. At the same time, accreted metals should diffuse towards the centre of the white dwarf, causing a change in the metal abundance. Because of the cyclical nature of the accretion, derived surface temperatures are thus an upper limit to the baseline (lowest temperature reached in quiescence before another outburst) T_{eff} value.

Observations suggest that white dwarf cooling is definitely detectable. In an example relevant to this thesis, Gänsicke & Beuermann (1996) detail an investigation of the cooling timescale for the white dwarf in VW Hyi after both normal outburst and superoutburst, using modelling of *IUE* archive spectra with $\log g = 8$ synthetic spectra. The cooling timescale is the Kelvin time of the heated envelope layer:

$$\tau_{\text{K}} = \int \frac{c_v T}{L_s} dM_r \quad (5.4)$$

where c_v is the specific heat at constant volume, T is the temperature at the base of the heated layer, L_s is the luminosity and the integral is evaluated over the mass of the layer. Gänsicke & Beuermann (1996) found that following an outburst, the accretion-heated white dwarf cooled exponentially to a mean temperature of $T_{\text{eff}} \simeq 19,000$ K. In addition, they found that the cooling timescale was considerably longer after superoutburst ($\tau_{\text{S}} = 9.8$ days) than after normal outburst ($\tau_{\text{N}} = 2.8$ days).

Strong evidence for the cooling of the white dwarf has also been found in observations of U Gem. Long et al. (1994a) took two *HST* FOS observations of U Gem ~ 13 and 70 days after the return, from the same outburst, to mean quiescent magnitude. During this period of 57 days, the ultraviolet flux dropped by $\sim 28\%$ at 1400 Å. This change is much greater than the photometric variability and must therefore be considered as real evidence for cooling. Long et al. then fitted synthetic white dwarf spectra to the data;

results suggested temperatures of 39,400 K for the first observation and 32,100 K for the second. Further compelling evidence for a cooling of the white dwarf was given by consideration of carbon and silicon spectral lines. The lines centred on SiIII λ 1260 Å, SiIII λ 1300 Å and CII λ 1333 Å were found to be weaker in the earlier spectrum. This is important because, in a white dwarf photosphere, these lines are strongest at \sim 30,000 K, and weaken significantly as the effective temperature rises towards 40,000 K.

Another system in which the cooling of the white dwarf can easily be seen is WZ Sge, a system that has very rare (each 33 years) outbursts which last approximately a month. The most recent of these was in 1978, and the system was observed by *IUE* many times over the years (1978 - 1992). The system is a unique laboratory for studying the cooling of a white dwarf after outburst because of its long quiescence. Model fits to the quiescent ultraviolet spectrum, which appears to have no disc contribution, show that the white dwarf has been cooling ever since (Szkody & Sion 1989; Sion & Szkody 1991; Sparks et al. 1993). The last *IUE* spectrum of WZ Sge was acquired in 1992; subsequent *HST* FOS observations have allowed more accurate temperature determinations to be made for the white dwarf (e.g., Sion et al. 1995c, who find $T_{wd} = 14,800$ K), and have allowed the estimation of abundances in the primary photosphere.

These observations present compelling evidence that, in these low \dot{M} systems, the white dwarf is cooling down during the quiescent periods.

Temperature determination methods

There are several methods that can be employed to estimate an average temperature for the white dwarf in a CV. Among the first to be used were eclipse depth measurements. For this method, photometric light curves of high-inclination systems are decomposed into their component parts (e.g. Wood et al. 1985) and the flux of the white dwarf component measured across a range of different passbands (e.g. *U*, *B*, *V*, *R*). Blackbody approximations or white dwarf model atmospheres are then fitted to these points. The application of this method is obviously limited to eclipsing systems; in addition, it suffers from the restriction that one can only have as many points as one has passbands, leading to poor temperature discrimination. However, it does have the advantage of removing any disc contributions. Generally, primary star temperatures deduced from this method are cooler than the temperatures derived from ultraviolet data, perhaps reflecting the fact that the white dwarf radiates primarily in the ultraviolet spectral range. Examples of temperature determinations of the white dwarf in OY Car using infrared and optical photometry can be found in Berriman (1987) and Wood et al. (1989). Berriman found

$T_{wd} \simeq 10,000 - 15,000$ K, while Wood et al. found $T_{wd} \lesssim 15,000$ K.

In the case of ultraviolet spectra, fits to the Lyman α line and ultraviolet continuum can give a reasonable temperature estimate in those systems where the spectroscopic signature of the primary can be identified and there is minimal disc contribution. Broad Ly α absorption is indicative of a cool primary; the hotter the white dwarf is, the narrower the Ly α absorption (see Figure 5.3).

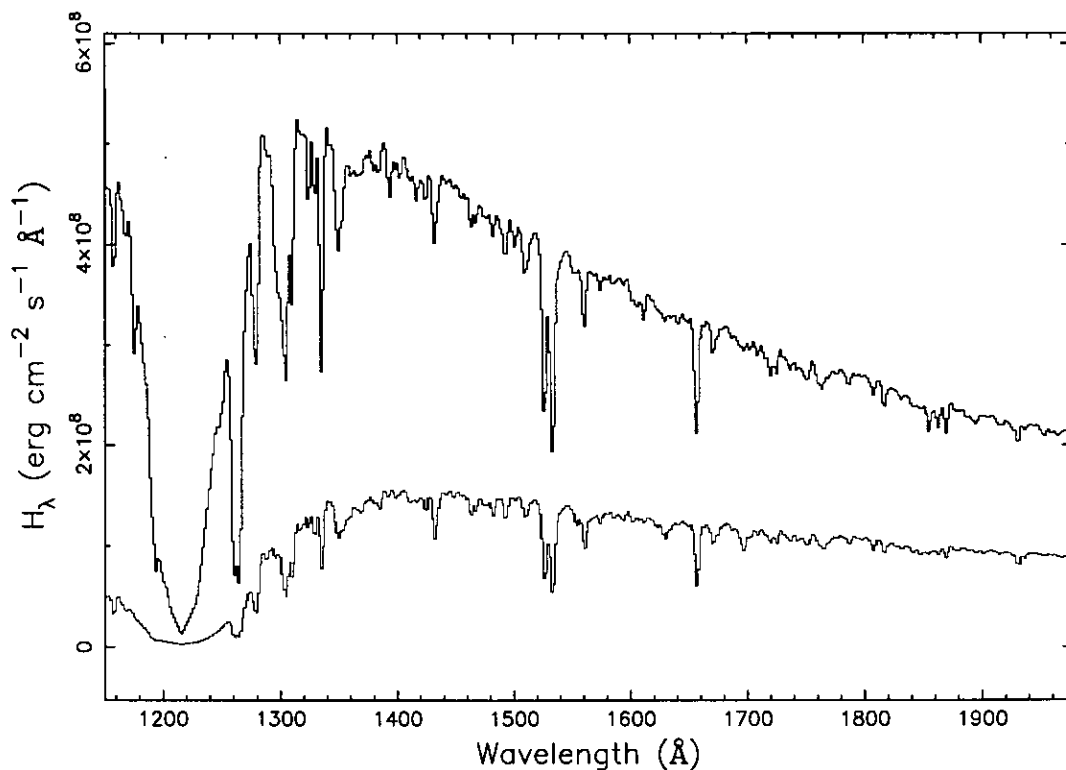


Figure 5.3: Synthetic solar abundance ultraviolet spectra for $T_{\text{eff}} = 16,000$ K (light grey) and $T_{\text{eff}} = 20,000$ K (black), illustrating how the Lyman α absorption profile narrows with a hotter white dwarf. Both spectra cover the *IUE* wavelength range, have been convolved with a Gaussian of FWHM 6 \AA to match the *IUE* wavelength resolution, and resampled to the *IUE* binsize.

The results are potentially far more accurate than those from optical eclipse depth measurements. The fitted spectra may be the spectra of field white dwarfs (e.g., Hassall & la Dous 1996), or more sophisticated model fits such as those by Sion, Long, Hubeny and collaborators (e.g. Long et al. 1993; Sion et al. 1995), or the Kiel group (e.g. Gänsicke & Koester 1999). Warner (1995) lists 27 nonmagnetic CVs where temperatures have been derived for the white dwarf. The mean temperatures from the best determined measurements (i.e., synthetic spectral modelling), are $50,000$ K for novalikes and $19,200$ K for dwarf novae, which is (unsurprisingly) higher than the median temperature of $10,000$ K

for field white dwarfs (Sion 1984).

5.4.3 Other measurable primary parameters

Rotational velocities

Quantitative estimates of the global rotational velocities of CV white dwarfs have only been possible since the advent of the high resolution spectra available from the *HST* and the *Hopkins Ultraviolet Telescope (HUT)*. Field white dwarfs are as a rule slow rotators: Heber et al. (1997) establish an upper limit for the rotation rate of DA white dwarfs of $v \sin i < 40 \text{ km s}^{-1}$. But white dwarfs in CVs are accreting material. High resolution *HST* FOS and *HUT* spectra have allowed questions concerning the amount of angular momentum transferred to the white dwarf due to the accretion process to be addressed. Other questions, such as whether the white dwarfs in CVs are rotating near breakup velocity and hence would explain weak or missing boundary layer flux, can also be addressed. The resolution of the *IUE* spectra is insufficient for this type of analysis.

Values for the rotational velocity of 8 CV white dwarfs are listed in Sion (1999). The values found range from 1200 km s^{-1} for WZ Sge (Cheng et al. 1997b) to $\leq 100 \text{ km s}^{-1}$ in the case of the white dwarf in U Gem (Sion et al. 1994). Since the time-averaged accretion rate of a CV white dwarf is $\sim 10^{-10} M_{\odot} \text{ yr}^{-1}$, and a typical CV lifetime is $\sim 10^9 \text{ yr}$, this implies that most CV white dwarfs should be rotating near breakup (e.g., Sion 1999, and references therein).

However, on the basis of the 8 rotational velocities so far derived, only WZ Sge is rotating at anything like this velocity: the white dwarf in this system is rotating at $\sim 30\%$ of breakup (Sion 1999). WZ Sge is generally acknowledged to be an exceptionally old system, aged $\sim 10^9$ years (Sion et al. 1995b), and it has the fastest white dwarf rotational velocity yet found.

To explain slow rotational velocities, earlier models invoked ejecta from nova explosions taking angular momentum away from the white dwarf. While this is still viable, the effect is too small to explain the quantitative results now available. Instead, Livio & Pringle (1998) suggest that the common envelope phase of the nova is capable of braking the primary rotation rate in relatively old CVs. In this scenario, shear between the surface of the primary and the bottom of the convective envelope generates a magnetic field of sufficient strength to exert the torque needed to slow the white dwarf.

Chemical abundances

Estimates of the metal abundances in CV white dwarfs have also only been possible since the advent of the high signal to noise spectra available from *HST* and *HUT*. The white dwarfs in CVs can and do display spectroscopic features with abundance ratios and chemical species that cannot have an origin in accreted matter from a normal secondary star: these can provide important clues to the evolutionary past of the system and of the white dwarf itself.

Chemical abundances of 8 CV white dwarfs have been reported up to the time of writing, primarily from analysis of *HST* FOS spectra (see Sion 1999, Table 7). These systems display a wide range of overabundances and underabundances. The Sion et al. (1997) analysis of VW Hyi determined a N abundance far in excess of the abundances of C and O, and even more interestingly, discovered elevated levels of P and Al (P at 900 times solar!). Sion et al. interpret these abundances as evidence for a prehistoric nova outburst in VW Hyi: P and Al are products of proton capture nucleosynthesis which takes place during a thermonuclear runaway. Interestingly, theoretical calculations for the diffusion timescale in the atmosphere of a white dwarf similar to that seen in VW Hyi yield timescales of 3-4 days. Sion et al. (1997) interpret the fact that P is seen at all as being evidence for dredge-up due to shear mixing with the accretion belt observed on the white dwarf in quiescence. This may also explain why changes in the chemical abundances have not been detected in observations obtained at different times after the same outburst.

Sion et al. (1998a) find a subsolar C abundance for the white dwarf in U Gem, which they also attribute to an ancient thermonuclear runaway event. The justification runs thus (Sion 1999): During a thermonuclear runaway, C captures a proton to form N. The more supersolar the C, the stronger the thermonuclear runaway (Starrfield 1993); the supersolar C abundance comes from mixing of the accreted material with white dwarf core material (Starrfield et al. 1972). If there is no core mixing, then the thermonuclear runaway will be weak. In a slowly accreting white dwarf (such as a dwarf nova), the thermonuclear runaway is relatively weak, little material will be ejected from the system, and a large common envelope will form. Some of this envelope will be ejected, but a large fraction will be deposited on the secondary and a similar fraction will be consumed in the H-burning shell around the white dwarf which has been rekindled by the thermonuclear runaway. This shell will leave a He-rich layer enriched in N and depleted in C. Subsequent thermonuclear runaways exacerbate the C depletion. Later dwarf novae deposit C-depleted material due to the thermonuclear runaway and common envelope, to be mixed with even stronger

C-depleted white dwarf material due to the thermonuclear runaway and the remnant H-burning shell source. This complex explanation leads to a C-depleted and N-enhanced white dwarf photosphere, which has been observed (Sion et al. 1998a, Long & Gilliland 1998). There is a necessarily speculative element, but assuming that present theories of CV evolution are correct, the model plausibly explains the observed abundances by placing them within the current evolutionary framework.

Abundance determinations, then, can yield important information concerning the history of a given system, provided the white dwarf is visible. There is further discussion of this subject in Section 5.8.

5.4.4 Summary

The preceding Sections have detailed the use of ultraviolet spectroscopic investigations to estimate various CV primary star parameters.

What follows is an investigation of the modelling of ultraviolet spectra, examining how the method may be honed to obtain the best possible results from the upcoming *HST* data. Because of the great number of spectra available in the IUEFA, much of the investigation concentrates on *IUE*; however, some *HST* FOS spectra, notably those of OY Car itself and VW Hyi, are also modelled.

5.5 Spectrum dearchival and initial development of the fitting process

In dearchiving CV spectra from the IUEFA with a view to modelling the Lyman α region and ultraviolet continuum, certain selection criteria had to be imposed. These included:

- Only SWP (1150 - 1950 Å) spectra were dearchived as the disc contribution usually rises to unacceptable levels in the LWP/LWR (1900 - 3200 Å) spectra⁶.
- Those spectra with the lowest flux levels were then needed, as these will have the least disc contribution. Some of these spectra were the result of poor acquisition, so these were excluded on grounds of quality.
- Only dwarf nova spectra were dearchived as these objects are the main subject of this work.

As a starting point, the catalogue of *IUE* spectra of dwarf novae and novalikes assembled by la Dous (1990) was used, which lists all dwarf nova spectra obtained by *IUE* up

⁶Although see Gänsicke & Koester (1999), in which the entire SWP/LWP spectrum of CU Vel is convincingly modelled with a $T_{\text{eff}} = 18500$ K, $\log g = 8$ synthetic spectrum. This is unusual.

to 1987. In some cases the selection of the lowest flux spectrum was complicated by poor quality low flux spectra caused by bad centering of the star in the aperture, inadequate exposure times or poor trailing by the satellite during the exposure. Table 5.2 lists the lowest flux DN spectra dearchived from the la Dous (1990) catalogue; thumbnail plots of these spectra can be seen in Figures 5.4, 5.5 and 5.6. For those low \dot{M} systems where the primary contribution was clearly seen, the whole data set was subsequently dearchived.

The initial aim was to develop a simple program that would optimise the fitting of field DA white dwarf spectra to those of quiescent dwarf novae, thus yielding a first approximation of the temperature of the primary. To this end, some 57 *IUE* field DA white dwarf spectra with well determined temperatures were dearchived. The white dwarfs themselves were chosen from a preliminary version of an atlas being developed by Sion and la Dous (la Dous, private comm.). This procedure contributed to familiarisation with the IUEFA interface and dearchival procedures, in addition to white dwarf spectra in the ultraviolet.

Each spectrum was converted from the initial FITS format to an ASCII file using a publicly available conversion program (mxconv2.osf) written by Dr. M. Currie at UCL (available from <http://www.star.ucl.ac.uk/mjc/iuedr/iuefa.html>). Some of the files were also converted using the STARLINK CONVERT package as a check of the reliability of the conversion program. Results were exactly the same in each case. The output is in the form of a six-column table: the wavelength (\AA), the absolute flux (f_λ), net flux (f_λ), background flux (f_λ), flux error, and a quality flag.

The low flux dwarf nova spectra were then individually compared to the atlas of white dwarfs, and the best fitting white dwarf spectrum was selected by the use of the reduced χ^2 statistic⁷, and which for these exploratory purposes was evaluated across the whole *IUE* SWP wavelength range: 1150 - 1950 \AA , except for a 20 \AA region centred on Ly α . The errors on each *IUE* spectrum are of the order of 10%; see Figure 5.7 for an illustration. Any data points flagged as bad quality were excluded from the fit. *In those cases where a white dwarf was visible in the CV spectrum*, the results agreed relatively well with published values of the primary temperature where available, giving temperature determinations that were generally consistent to within ± 3000 K in all cases.

The WZ Sge post-outburst dataset can be used to illustrate that temperature discrimination is even possible with this rudimentary white dwarf spectrum-fitting method. The first “quiescent” post-outburst spectrum of WZ Sge was best modelled with a spectrum

⁷Notation χ_ν^2 . The χ^2 statistic is defined in eqn. 2.8. $\chi_\nu^2 = \chi^2/\nu$, where ν is the number of degrees of freedom (the number of data points minus the number of parameters to be determined from the data points).

corresponding to a white dwarf at $T_{\text{eff}} \sim 25,000$ K. The subsequent spectrum, acquired almost exactly six months later and by now more clearly exhibiting the Ly α absorption expected for a white dwarf, was best modelled with a spectrum corresponding to a white dwarf at $T_{\text{eff}} \sim 17,000$ K. Figures 5.8 and 5.9 illustrate these fits. Obvious areas of poor fit are in the absorption lines due to the solar composition of the white dwarf photosphere, especially in SiIII $\lambda 1300$, CII $\lambda 1335$, SiIV $\lambda\lambda 1394, 1403$ and CIV $\lambda\lambda 1548, 1551$. In addition, and for later comparison, Figure 5.10 is a plot of χ^2_{ν} vs. white dwarf temperature for the latter fit, and shows quantitatively the temperature discrimination available when fitting field white dwarf spectra to those of CVs.

The validity of the procedure and program now having been established, more detailed and realistic modelling was undertaken, which is described in the following Sections.

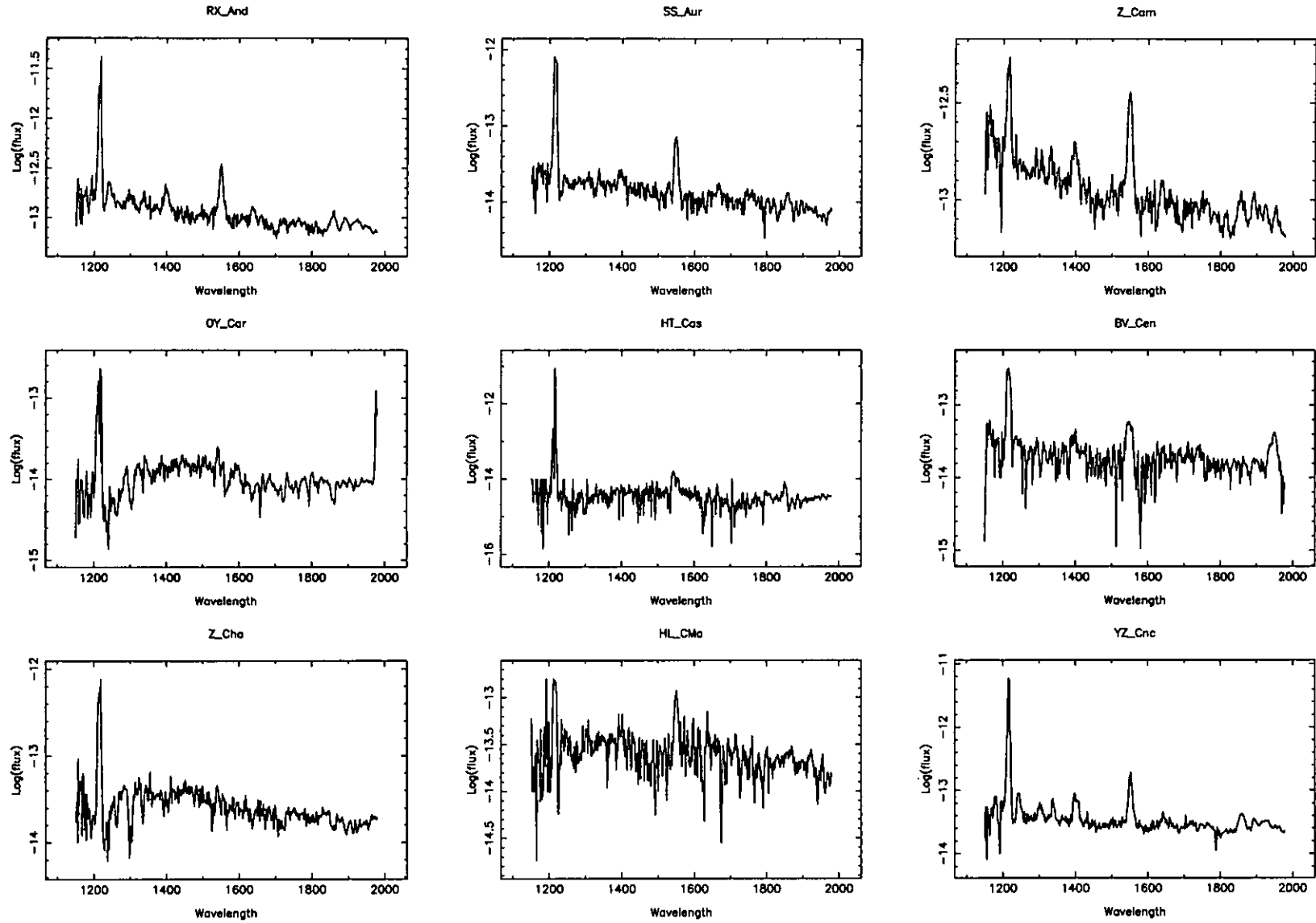


Figure 5.4: Plots of quiescent dwarf nova spectra used in the initial modelling with field white dwarf spectra. The spectra were selected from la Dous (1990) and are listed in Table 5.2. All y -axes are on a log scale because the geocoronal airglow emission in the Ly α line can be bright enough to overwhelm the continuum flux when plotted on a normal scale. The signature Lyman α absorption from the white dwarf primary can be seen in the spectra of OY Car, Z Cha and possibly HT Cas.

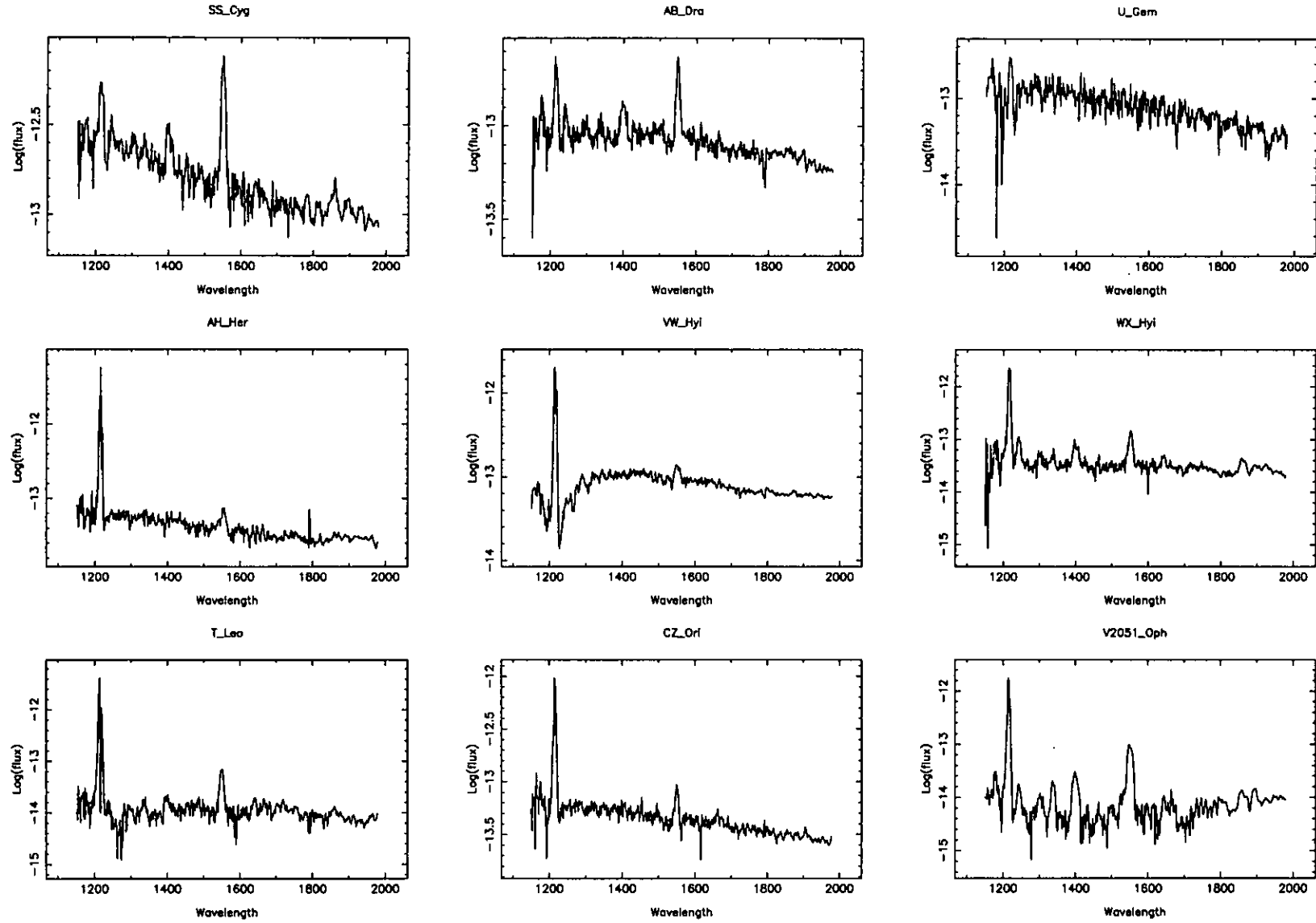


Figure 5.5: Plots of quiescent dwarf nova spectra used in the initial modelling with field white dwarf spectra. The spectra were selected from la Dous (1990) and are listed in Table 5.2. All y -axes are again on a log scale. Lyman α absorption from the primary star can be seen in the spectra of U Gem and (very strongly) VW Hyi.

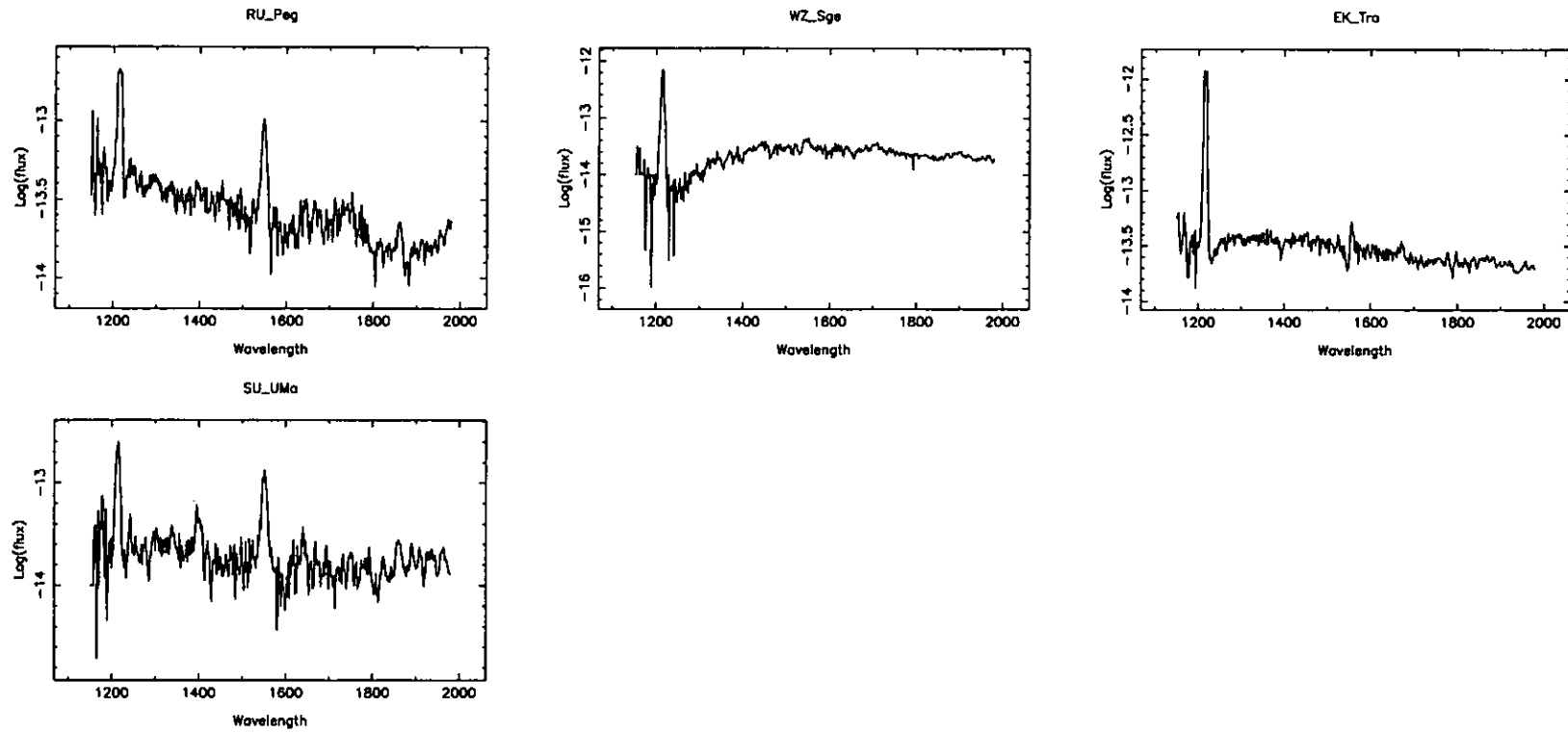


Figure 5.6: Plots of quiescent dwarf nova spectra used in the initial modelling with field white dwarf spectra. The spectra were selected from la Dous (1990) and are listed in Table 5.2. All y -axes once again on a log scale. Lyman α absorption from the primary star can be seen in the spectrum of WZ Sge, and may also be present in EK Tra. It is difficult to tell in the latter case because the Lyman α absorption is swamped by the geocoronal Lyman α emission.

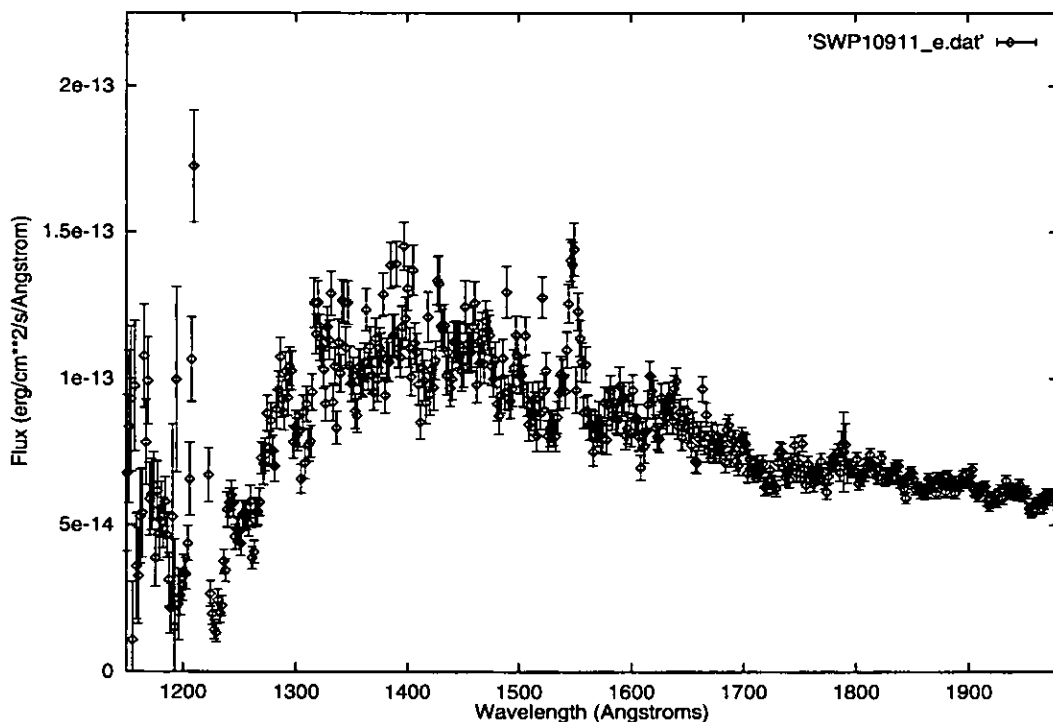


Figure 5.7: A spectrum of VW Hyi in quiescence (SWP10911), illustrating the typical extent of the errors in an *IUE* spectrum, as calculated by the NEWSIPS extraction process.

Table 5.2: A list of the most quiescent dwarf nova spectra (good quality spectra having the lowest flux) obtained from the IUEFA. Asterisks indicate a system for which the whole data set was dearchived; the stars are listed in the alphabetical order of their respective constellations.

Object	Spectrum	Object	Spectrum
RX And	SWP17642	U Gem*	SWP24716
SS Aur	SWP16036	AH Her	SWP08089
Z Cam	SWP18844	VW Hyi*	SWP23865
OY Car	SWP28263	WX Hyi	SWP09704
HT Cas	SWP21080	T Leo	SWP27683
BV Cen	SWP03857	CZ Ori	SWP16042
Z Cha*	SWP30780	V2051 Oph	SWP21091
HL CMa	SWP22211	RU Peg	SWP28449
YZ Cnc	SWP07312	WZ Sge*	SWP31294
SS Cyg	SWP24533	EK Tra	SWP09768
AB Dra	SWP07413	SU UMa	SWP18845

SWP03768_scr.dat

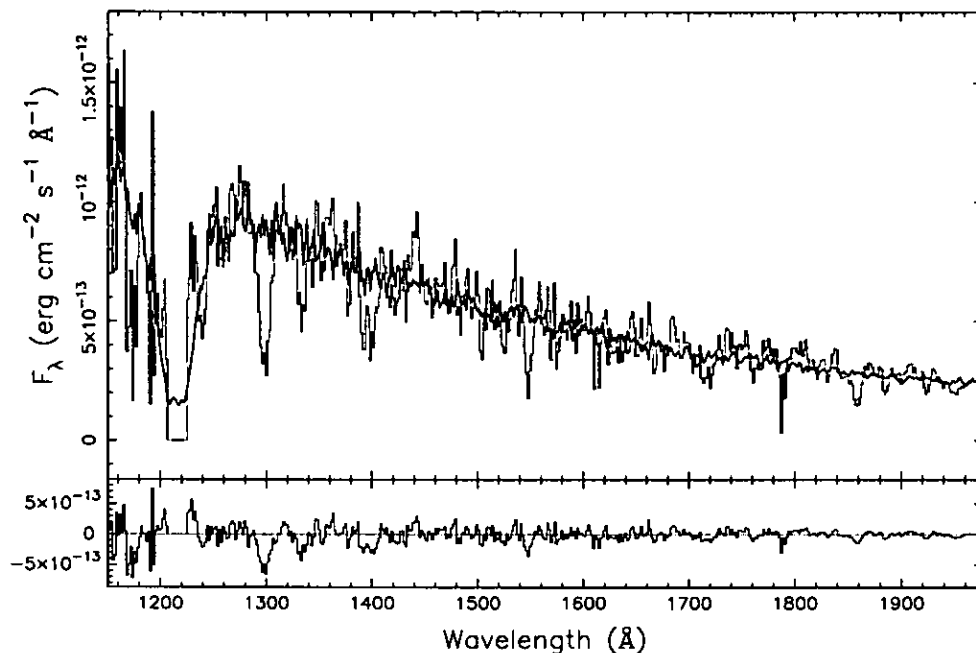


Figure 5.8: The first “quiescent” post-outburst spectrum of WZ Sge (SWP03768; grey), modelled with the spectrum of a field white dwarf at a temperature of $T_{\text{eff}} \sim 25,700$ K (SWP17014; black). The $\chi^2_\nu = 3.4$. Residuals are plotted (not to the same scale) in the bottom panel.

SWP05744_scr.dat

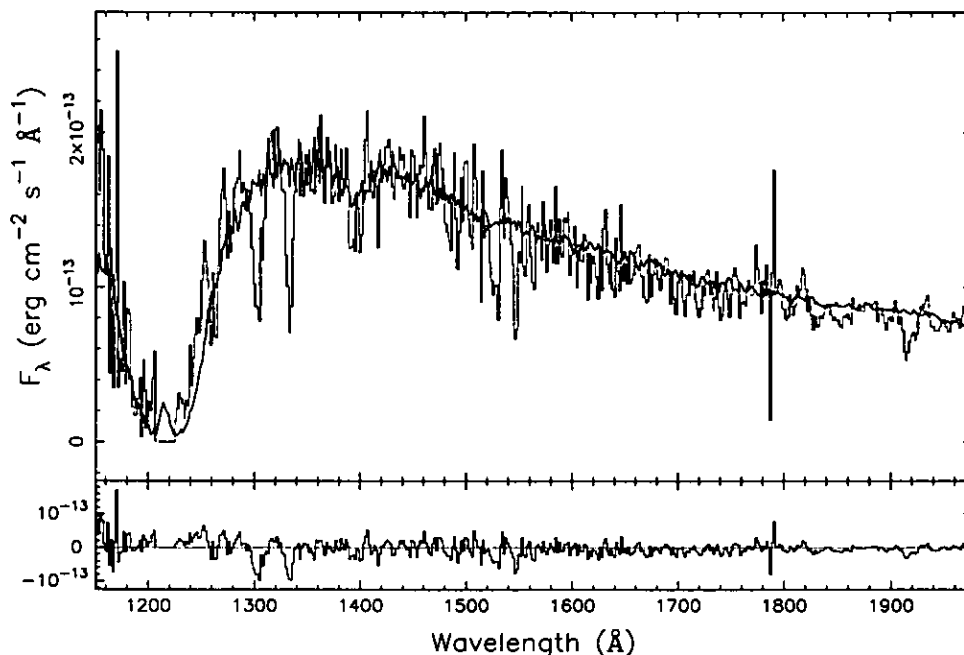


Figure 5.9: The spectrum subsequent to that in Figure 5.8 (SWP05744), obtained six months after, modelled with the spectrum of a field white dwarf at a temperature of $T_{\text{eff}} \sim 17,000$ K. The $\chi^2_\nu = 2.4$. The field white dwarf spectrum (SWP07973) is again black. Residuals are again plotted, not to the same scale, in the bottom panel.

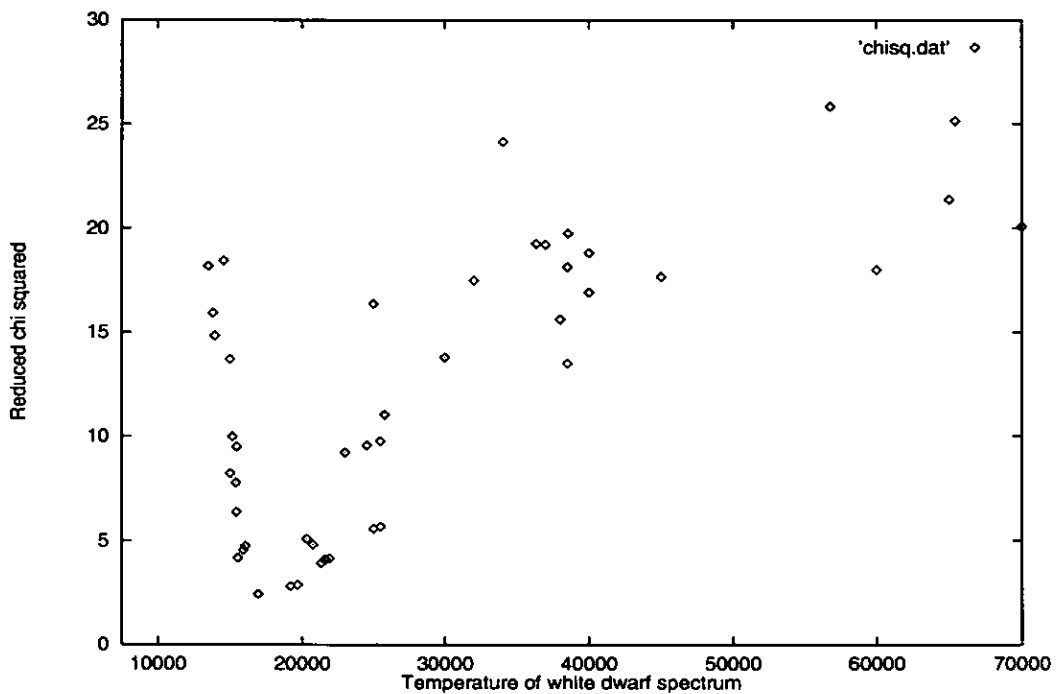


Figure 5.10: The *IUE* spectrum of WZ Sge (SWP07973) has been fitted with field DA white dwarf spectra in the temperature range 10,000 – 70,000 K. The χ^2 vs. white dwarf temperature plot for the sequence of fits is shown above. It can be seen that there is a clear, but broad, minimum in the χ^2 -distribution centred around $T_{\text{eff}} \sim 17,000$ K. This fit is shown in the previous Figure (5.9). For comparison with the similar plot obtained from a synthetic spectral fit to the same WZ Sge spectrum (Figure 5.15).

5.6 Model construction using TLUSTY and SYNSPEC

Section 5.5 showed that approximate effective temperature determinations for the primary star could be achieved by simply fitting the observed spectrum of a field white dwarf star to that of a quiescent dwarf nova. The main problem with the method is the inappropriate abundances of field white dwarf spectra when applied to the analysis of CV primary star spectra. It is also useful to have a regular grid of different temperature spectra with which to analyse the CV data, rather than the unevenly spaced grid of variable quality spectra available from field white dwarf observations.

In order to improve the effective temperature estimates for the primaries in the sample, and to provide a reliable measure of the quality of the fitting, several grids of white dwarf model atmospheres and synthetic spectra were calculated.

For a review of the development of stellar atmosphere computations, see e.g. Kudritzki & Hummer (1990), or Werner & Dreizler (1999). Kudritzki & Hummer define the photosphere of a star in the context of stellar atmosphere models: it is “... that part of a star in which radiative equilibrium and hydrostatic equilibrium hold but the Saha-Boltzmann and Planck distributions cannot be assumed”. The structure of the photosphere of a star is determined not only by radiative and hydrostatic equilibrium, but also by the radiative transfer equation and by the condition of statistical equilibrium, which requires the number of transitions into and out of each atomic level to be equal. To calculate the model atmosphere, an equation of state (usually the ideal gas law), the elemental abundances, and the geometry of the atmosphere must be specified, in addition to the collisional and radiative cross sections and rate constants. For a review of the basic equations used in the calculation of model atmospheres and synthetic spectra, see Appendix B.

All model atmosphere codes work in approximately the same way. This involves simultaneously solving the basic equations of radiative transfer, hydrostatic equilibrium, radiative equilibrium, particle conservation and statistical equilibrium. The model atmosphere itself is then a set of tables of e.g., the source function and/or temperature vs. pressure and/or optical depth.

In order to solve the basic equations, several simplifying assumptions are necessary. These include:

- the assumption of plane parallel geometry, which streamlines matters considerably as all variables are then a function of only one spatial coordinate. This assumption is valid when the mean distance between the emission and the next absorption or scattering of the photons is very small compared with the stellar radius at that point;

- that the atmosphere is in radiative and hydrostatic equilibrium. If this is the case, no large scale accelerations occur;
- that there are no starspots, granulations or prominences, or gas flows in any direction other than radial (a manifestation of the plane parallel assumption); and
- that there are no magnetic fields.

Early model atmospheres (pre-1970) also assumed, for simplicity, the condition of local thermodynamic equilibrium (LTE) holds; that is:

- that the spectral density of the radiation is described by the Planck function;
- that the total energy density of the radiation is described by the Stefan-Boltzmann Law;
- that the velocity distributions of the atoms, ions and electrons is described by the Maxwell-Boltzmann distribution; and
- that the atomic-level populations are specified by the Saha-Boltzmann equations at the local electron temperature.

The computational technique that made it possible to abandon the assumption of LTE was “complete linearization”, introduced in 1969 by Auer & Mihalas. They demonstrated that models based on statistical equilibrium produced spectra that agreed substantially with observations, where LTE models had always failed to do so. These statistical equilibrium models, often termed non-LTE (NLTE), differ from LTE models in that the populations of some selected energy levels of some selected atoms and/or ions are allowed to depart from their LTE values.

There are many different model stellar atmospheres available, perhaps the most famous of which in the astrophysical community are the LTE models from ATLAS, by Kurucz, first published in 1970. Up to date versions of the Kurucz model atmospheres and synthetic spectra are currently available on CD ROM or from <http://cfaku5.harvard.edu/>. There is also the Kiel code, written over 20 years primarily by Dr. D. Koester (see, e.g. Dreizler & Werner 1993; Finley et al. 1997).

This Chapter will use the programs TLUSTY and SYNSPEC, written by Dr. I. Hubeny and collaborators, which are extensively used by Sion, Long et al. in the modelling of ultraviolet/EUV spectra of CVs.

5.6.1 The basics of TLUSTY

For the original detailed description of TLUSTY, see Hubeny (1988). The code has undergone a considerable number of revisions and upgrades since original publication; the major new developments are described in Hubeny & Lanz (1992), Hubeny et al. (1994) and Hubeny & Lanz (1995).

The latest version of TLUSTY (TLUSTY195) uses a computational method known as the hybrid complete linearization/accelerated lambda iteration (hybrid CL/ALI; described in Hubeny & Lanz 1995 and Werner & Dreizler 1999), an evolution of the original complete linearization method first introduced by Auer & Mihalas (1969).

In essence, the CL method allows the discretisation (by depth and frequency) of the nonlinear and strongly coupled equations describing the atmosphere. These equations can then be solved iteratively using a set of linear equations for corrections to the values of all quantities (temperature, atomic-level populations, densities and the intensity of the radiation at each frequency) from the previous iteration (Kudritzki & Hummer 1990). This method gives a fast convergence rate.

The ALI method is conceptually based on work by Cannon (1973b) and Rybicki (1972), was reformulated by Scharmer (1982), and was first applied to the construction of model atmospheres by Werner (1986). The basis of the ALI method is to express the radiation intensity through an approximate (“lambda”) operator operating on the source function, plus a correction term known from the previous iteration. This reduces the time per iteration and thus increases the speed of computation.

Fully line-blanketed NLTE models are available using TLUSTY195; this is achieved by introducing the concept of “superlevels”. The term line blanketing involves the study of the influence of the thousands to millions of spectral lines on the atmospheric structure and emergent spectrum. Despite the combination of fast convergence rate and reduced time per iteration introduced by the hybrid CL/ALI method, its use is limited, because each energy level is treated separately. This effectively means that atoms with a very complex energy level structure, such as the iron-peak elements, cannot be treated. To overcome this limitation, TLUSTY195 uses the approach of Anderson (1989), in which the problem of radiative transfer in the millions of atomic transitions is addressed with a statistical solution based on grouping many energy levels into a small number of “superlevels”.

TLUSTY195 is an extremely flexible piece of code. It solves the basic equations (radiative transfer, hydrostatic equilibrium, radiative equilibrium, particle conservation and statistical equilibrium); the program has options for calculating semi-empirical models

where the temperature distribution is fixed and all other equations are solved exactly. It is fully data oriented with no built-in opacity values, and it is highly portable, having been written in Fortran 77.

Output files are in the form of H_ν vs. wavelength, where H_ν is the first moment of the specific intensity and is defined in e.g., Gray (1992; see also Appendix B).

TLUSTY (Hubeny 1988) is the basic plane-parallel, horizontally homogeneous model stellar atmosphere calculation program. Departures from LTE are allowed for selected atomic and ionic energy levels, and the program also incorporates convection (based on the mixing-length formulation). Version 195 allows fully consistent NLTE metal line blanketing. The most up to date versions of these programs are available from Dr. I. Hubeny himself. The older version TLUSTY185 is available for download from the TLUSTY home page at <http://tlusty.gsfc.nasa.gov>. The still older versions TLUSTY178 and SYNSPEC36 are also distributed by the CCP7 Project (<http://ccp7.dur.ac.uk>).

Associated programs

The companion program is SYNSPEC (Hubeny et al. 1994; now at version 42), which calculates the spectrum emergent from the model atmosphere (SYNSPEC can also take Kurucz model atmospheres as input). If the input model atmosphere was calculated in LTE, then SYNSPEC assumes the source functions for the continuum and lines is given by the LTE value, i.e., the Planck function. If, however, some of the atomic energy levels depart from LTE, then the lines from these levels can be calculated using an NLTE source function. SYNSPEC includes two kinds of NLTE treatment of the line source function: exact NLTE; and approximate NLTE. The latter assumes that the source function is given by an analytical expression derived from second-order escape probability theory (e.g. Hummer & Rybicki 1982).

A further program, CIRCUS (unpublished, version 1) calculates stellar spectra under the influence of external emitting or absorbing bodies, i.e. veiled spectra. Each circumstellar body is assumed to be an homogeneous, isothermal slab, characterised by its geometrical parameters (including column density, radial velocity, relative projected area and position), and physical parameters (including temperature, electron density, mass density and velocity dispersion). Additionally, each body may absorb or emit radiation.

Convolutions of the resulting spectrum with the rotational profile and/or the instrumental profile are achieved by the use of the program ROTIN (unpublished; now at version 4).

For a summary of the various input and output files and optional parameters available,

with examples, see Appendix C.

5.6.2 Calculating the model atmospheres and synthetic spectra

Once TLUSTY195 and SYNSPEC42 were downloaded and compiled at Preston, some tests were undertaken to ensure that the programs were in working order, using sample input and output files supplied with the codes for this purpose. It was first found to be necessary that the instantaneous data storage capacity at the disposal of the program be expanded in order to run these programs on the Preston STARLINK node, not surprising considering the line list contains more than 185,000 lines in the SWP spectral region. Several program arrays also had to be extended.

Because of the complex format and arrangement of input and output (I/O) files (see Appendix C), and the necessity of renaming the output files to prevent overwriting by a subsequent run, it was found easiest to run TLUSTY and SYNSPEC using a new front-end written by the present author as a UNIX C-shell script. C-shell scripts introduce a large amount of flexibility into the running of TLUSTY and SYNSPEC, giving complete control of the I/O files (including renaming on completion of a run), and permitting the batch processing of jobs to be undertaken in a relatively painless fashion.

All of the following model atmospheres were calculated in LTE only, with an approximate NLTE treatment applied to the calculation of the resulting synthetic spectrum. At the temperatures and gravities in question here, departures from LTE have been shown by other studies to have negligible effects on both the structure of the atmosphere or the resulting synthetic spectrum as produced by these programs (Long et al. 1993; Horne et al. 1994). Lanz & Hubeny (1995) provide a detailed discussion of NLTE effects in hot, metal-rich white dwarfs: NLTE effects become important at temperatures of $\gtrsim 60,000$ K. Figure 5.11 illustrates the difference between synthetic spectra resulting from calculations using LTE and approximate NLTE treatments. The continuum level and slope, and the Lyman α line are almost unaffected; some lines are deeper in the NLTE spectrum, but line depths are unimportant in this analysis. Differences between LTE and NLTE are undetectable at *IUE* resolution.

Pure H/He model atmospheres and synthetic spectra

Pure H/He models were the first to be produced for the present work. These model atmospheres composed of pure hydrogen and helium in their solar abundances, were the first to be produced. These so-called “pure hydrogen” models (with $\log g = 8$) have been very successful in the past when applied to the determination of the temperatures of field

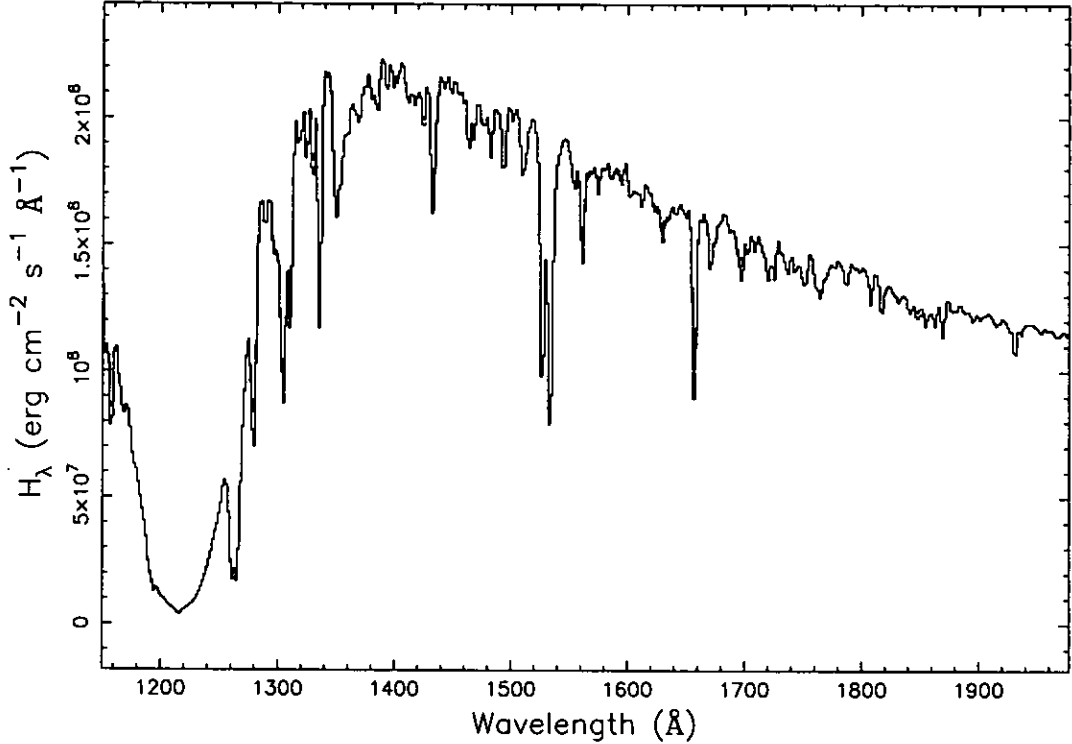


Figure 5.11: An illustration of the difference between an LTE spectrum produced from an LTE model atmosphere with that produced from the same model atmosphere but using an NLTE approximation (red). The spectrum covers the *IUE* wavelength range and has been convolved to *IUE* instrumental resolution and resampled to the *IUE* binsize.

white dwarfs. $\log g = 8$ models are generally used as a simplification: the gravity is then a fixed parameter corresponding to a canonical $M_{\text{wd}} \approx 0.6M_{\odot}$ white dwarf. The effect of the white dwarf mass on the final calculated spectrum is discussed further in Section 5.8.

When utilized in the context of *IUE* spectra of CVs, pure H/He models allow an alternative approach, in that the estimate of the effective temperature of the primary is not limited by the signal to noise of field white dwarfs, as described in Section 5.5. The generation of these relatively simple models was a useful step in the process of familiarisation with calculating model atmospheres and synthetic spectra using TLUSTY and SYNSPEC.

A grid of H/He-only, $\log g = 8$, LTE model atmospheres was generated in the temperature range 14,000 - 50,000 K, with appropriate increments in T_{eff} . The models were initially produced on a very fine wavelength scale ($\delta\lambda = 0.1 \text{ \AA}$). It was found that models with $T_{\text{eff}} \lesssim 15,500 \text{ K}$ would not converge with a “standard” TLUSTY input file. This is because convection becomes progressively more important as a means of energy transport at lower temperatures. A special set of “cool” input files, incorporating convection, was

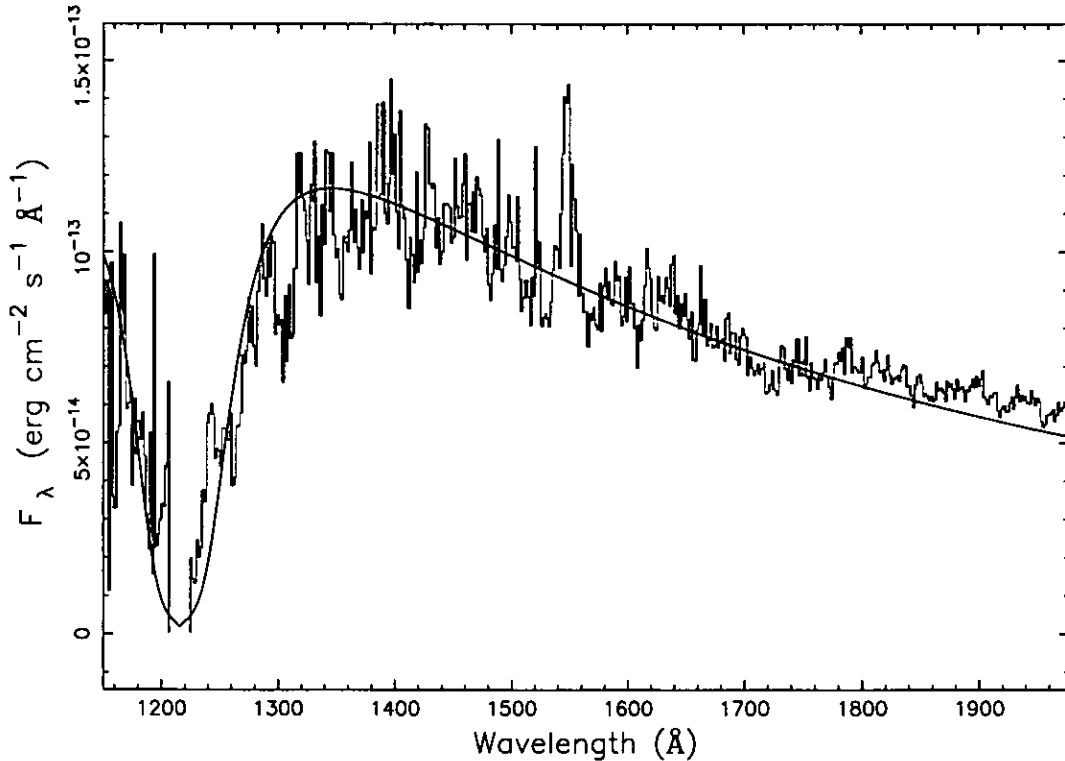


Figure 5.12: An example of an H/He synthetic spectral fit to the quiescent *IUE* spectrum of VW Hya, at $T_{\text{eff}} = 18,000$ K. The Ly α absorption and the shape of the overall continuum is very well described, but individual features from heavier elements are (obviously) not.

thus obtained in order to generate model atmospheres with $T_{\text{eff}} \lesssim 15,500$ K (Hubeny, private comm.). The final synthetic spectra were produced from the model atmospheres using SYNSPEC, then convolved with a Gaussian of suitable FWHM to match the resolution of *IUE* using the rotational and instrumental convolution program ROTIN4; values for the *IUE* resolution (~ 6 Å FWHM mean) were obtained from the ESA *IUE* Newsletter # 57.

Figure 5.12 shows an example H/He synthetic spectral fit to a quiescent spectrum of VW Hya. In common with the white dwarf spectral fits described in Section 5.5, the Lyman α region and the overall shape of the continuum are very well described, but fits to individual lines (non H/He) are obviously not possible.

Solar abundance model atmospheres and synthetic spectra

A grid of solar abundance, $\log g = 8$ model atmospheres was next generated. Long, Sion and collaborators use H and He as the continuum opacity sources when calculating the structure of the model atmosphere, the rationale being that at the temperatures and

gravities of interest in the study of white dwarfs, metals do not affect the opacity of the atmosphere significantly. However, for the calculation of the solar abundance synthetic spectra used here, hydrogen, helium *and carbon* were used in the calculation of the model atmospheric structure. This was the approach taken in the model atmosphere calculations in Horne et al. (1994). The neglect of full metal line blanketing on the final calculated spectrum is discussed further in Section 5.8; Figure 5.25 in that Section illustrates the temperature difference that results from the inclusion of C.

Synthetic spectra for the *IUE* spectral range were then produced using SYNSPEC, covering an effective temperature range of $T_{\text{eff}} = 14,000 - 50,000$ K, with appropriate increments in T_{eff} . The source functions of the resonance lines for the first 20 elements (H - Ca) were calculated using the approximate NLTE option, while an LTE source function was assumed for all other transitions (cf. Horne et al. 1994). The intrinsic line profiles have the form of a Voigt function and account for the contributions of natural, van der Waals, Stark and thermal Doppler broadening. As with the H/He synthetic spectra, a very fine wavelength grid was used initially ($\delta\lambda \leq 0.1 \text{ \AA}$); the spectra were then convolved with a Gaussian of FWHM equal to *IUE* instrumental resolution (6 \AA) and resampled to match the *IUE* bin size.

Veiled spectra

Finally, veiled spectra were calculated using TLUSTY, SYNSPEC and CIRCUS. The procedure for calculating these spectra was quite complicated. Firstly, normal solar abundance white dwarf spectra were produced in the usual way in the temperature range of interest. In this case, spectra were generated in the temperature range $T_{\text{eff}} = 14,000 - 25,000$ K, with appropriate temperature increments. Next, a grid of opacity tables was produced for absorbing bodies at temperatures of $T_{\text{eff}} = 7500, 10,000$ and $12,000$ K, and column densities of $N_H = 10^{20}, 10^{21}$ and 10^{22} cm^{-2} . The models assume a uniform density slab for which an electron density of $n_e = 10^{13} \text{ cm}^{-3}$ has been chosen, in keeping with the values found in the Horne et al. (1994) study. Obviously this is a gross simplification: a realistic model would utilize a density gradient and a more realistic geometry, but the inclusion of these factors is beyond the scope of the present work. It will be seen that order of magnitude results are possible with these simplifications. These calculations required the use of the ‘iron curtain’ mode of SYNSPEC, which calculates monochromatic opacities for a homogeneous slab of a given temperature and density. The spectral files and the opacity tables were then used as input to CIRCUS, which calculates the resulting spectrum after absorption by the circumstellar body. Figure 5.13 illustrates the effect of the veiling gas

on a $T_{\text{eff}} = 16,000$ K $\log g = 8$ synthetic spectrum.

As a result of the various assumptions used here, the temperature and column density uncertainties on any fits to ‘iron curtain’ spectra are 2,500 K and a factor of ten, respectively. The proposed improvements to the method to lessen the uncertainties are discussed in Section 5.7 and Chapter 6.

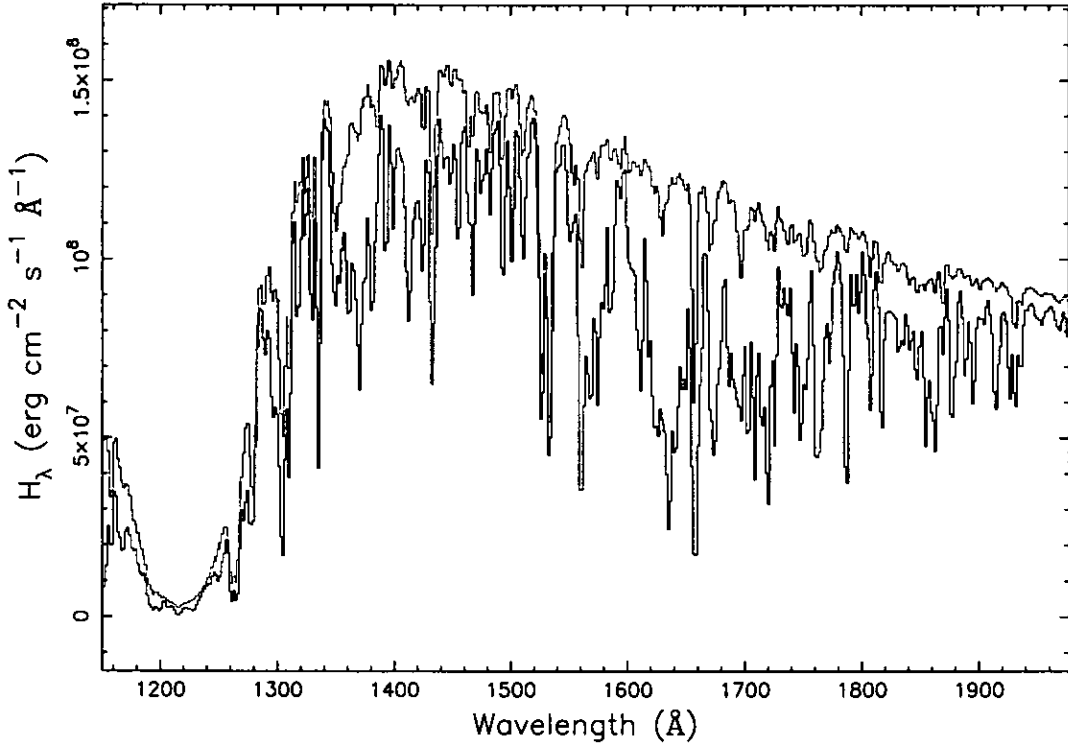


Figure 5.13: A comparison of an unobscured $T_{\text{eff}} = 16,000$ K, $\log g = 8$ synthetic spectrum (light grey), and the same spectrum veiled by absorbing gas at $T_{\text{eff}} = 10,000$ K, with a column density of $N_H = 10^{22}$ cm^{-2} (black). Both spectra cover the *IUE* wavelength range and have been convolved to *IUE* resolution and rebinned to *IUE* binsize. It can be seen that the effects of the ‘iron curtain’ are strongest around 1600\AA in this spectral range.

5.7 Spectral Modelling

5.7.1 Overview — and some caveats

The need to apply the same criteria to the maximum number of spectra dictated which regions of each observed spectrum would be used for modelling purposes. A distinction should also be made here between **normal spectrum fits**, in which the spectrum of the white dwarf is modelled with one or more components, and **veiled spectrum fits**, in which an obscured white dwarf spectrum is modelled. It should be noted that the normal spectrum fits presented and discussed below are *one component only*. There is further review and discussion of the need, or otherwise, for consideration of extra components when modelling these spectra in Section 5.8. In the latter case, fitting the white dwarf spectrum with more than one temperature component, or with spectra of different abundances, is potentially difficult because of the difficulties in disentangling the contribution of the ‘iron curtain’.

A 20Å wide region centred on Lyman α was excluded in all the fits as this region is usually contaminated by emission due to geocoronal airglow. In comparing the synthetic spectra with the spectra of actual dwarf novae, the most prominent deviation from solar abundances was found in the two SiII doublets (1260,65Å, 1527,33Å), which are consistently stronger in the models than in the observed spectra. For this reason, 15Å wide regions centred on these doublets were also excluded from the fit; the possible reasons for this marked deviation of the models from observed data are discussed later in the Chapter. Finally, many of the observed spectra exhibit CIV (1550Å) in emission, due to the disc; this region has also been excluded from the fits. The exclusion of these regions was achieved by invoking a window function that gave zero weight to the unwanted parts of the spectrum. The goodness of fit was assessed by the use of the reduced χ^2 statistic, as discussed previously, calculated across the entire range bar the regions listed above.

Closer examination of the dearchived IUEFA data files revealed that the bin size is variable at the ~ 0.001 Å level (presumably due to rounding errors). A scrunching program was thus written to resample the dearchived *IUE* spectra into bins with exactly the same width as the model spectra. The program was written for use within the STARLINK package FIGARO, and propagates the errors in the standard fashion. Since the actual wavelength shifts as a result of the rebinning were only of order 0.001 Å, the quality arrays were mapped directly back into the output file.

The low flux spectra listed in Table 5.2 are plotted in Figures 5.4, 5.5 and 5.6 (see Section 5.5 above). An attempt was made to fit each of these spectra with a synthetic solar

abundance white dwarf spectrum, but even a cursory examination of the Figure shows that the characteristic Ly α profile of a white dwarf is absent in the majority of the spectra. *In these cases, convincing white dwarf fits were impossible to achieve.* Of the spectra listed in Table 5.2, only 6 could be modelled with a synthetic white dwarf spectrum. These were SWP spectra of U Gem, VW Hyi, WZ Sge, HT Cas, Z Cha and OY Car.

At this point it was decided to concentrate efforts on establishing that the method developed here would give primary star temperatures that were in good agreement with published values. This would then serve as a foundation for an updated and improved method to be used on the upcoming *HST* data from OY Car. It should be stressed that the aim here was not to reproduce the temperature of every white dwarf in every system where synthetic photospheric spectral analysis is possible, but rather to assess the various aspects of the modelling of CV spectra in the ultraviolet in a critical fashion.

In the following Sections, *IUE* spectra of four CVs listed above (WZ Sge, U Gem, HT Cas and Z Cha), with the addition of CU Vel and SW UMa (for reasons explained below), are modelled to evaluate the reproducibility of the primary star temperature. The *IUE* spectra of HT Cas and Z Cha are modelled with veiled white dwarf synthetic spectra. An *HST* FOS spectrum of VW Hyi is modelled, and finally, illustrative modelling of *IUE* and *HST* FOS spectra of OY Car is undertaken. Contributions to the error in each temperature determination include the step size in the temperature grid and arbitrary decisions (taken for maximum applicability of the method) concerning which regions of the spectrum to use in the modelling and which regions to use for purposes of normalisation. It is estimated that the overall uncertainty in the final temperature value, due to such systematic effects, is ± 1500 K. This applies equally to the normal spectrum and the veiled spectrum fits, although, as discussed above, the temperature discrimination of the ‘iron curtain’ is ± 2500 K due to the coarseness of the grid employed.

5.7.2 Some synthetic spectral analyses

WZ Sge

WZ Sge is a member of the TOAD (Tremendous Outburst Amplitude Dwarf nova) subclass of dwarf novae; outbursts are observed to occur every ~ 33 years and last approximately a month for WZ Sge itself⁸. There appears to be no detectable disc contribution to the

⁸However, see Lasota et al. (1999), who argue, based on oscillations recently found in optical observations, that WZ Sge is a rapidly spinning magnetic rotator which evolves through a cycle of spin-up and spin-down phases. During the spin-down phase it is a DQ Her star which eventually spins down to a certain equilibrium period; an increase in the mass transfer rate causes spin-up of the white dwarf and the

ultraviolet spectrum.

Sparks et al. (1993) compared the white dwarf cooling curve from *IUE* observations of WZ Sge with theoretical cooling curves. Sparks et al. (1993) found that a spherical accretion model did not agree with the observed cooling curve. It was only after including the angular momentum and shear mixing of the accreted material in the calculations, and confining the accreted material to a wide ($\pm 27.5^\circ$) belt at the white dwarf surface, that a curve was produced that agreed with the observations to a factor of two. WZ Sge has now been extensively studied with the *HST* FOS revealing a white dwarf with a current baseline $T_{\text{eff}} = 14,800$ K (Sion et al. 1995c), rotating at ~ 1200 km s $^{-1}$ (Cheng et al. 1997b).

It is worthwhile using the *IUE* spectrum of WZ Sge, modelled in Section 5.5 with a field white dwarf model at $\sim 17,000$ K (SWP05744), to illustrate the improvement in the temperature discrimination afforded by the synthetic spectra. When the same spectrum was modelled with a synthetic solar abundance white dwarf spectrum, the best-fitting temperature was $T_{\text{eff}} = 20,500 \pm 1500$ K. This example spectrum was obtained ~ 6 months after the 1978 outburst of WZ Sge, when the white dwarf was still considerably hotter than when the object was observed most recently by Sion et al. (1995c). Figure 5.14 shows the fit, while Figure 5.15 shows the difference in the χ^2_{ν} distribution available when using synthetic spectra (cf., Figure 5.10).

U Gem

Two *IUE* data sets of U Gem can be modelled and used to compare with cooling times obtained from *HST* FOS observations, *at a different resolution*, by Long et al. (1994a) and Sion et al. (1998a).

The first *IUE* data set was that used by Panek & Holm (1984) to argue that the vast majority of the flux from the system was due to the white dwarf. The second *IUE* data set, obtained by Kiplinger et al. (1991), provided inconclusive evidence for a cooling of the white dwarf based on their analysis of the evolution of flux levels. These *IUE* observations are modelled here using synthetic spectra for the first time. Table 5.3 summarises the best synthetic spectral fits to these data sets.

A plot of temperature vs. days-post-outburst is, unfortunately, not particularly revealing, mainly because of the lack of data obtained in the immediate aftermath of the outburst and early in the decline. Table 5.3 does show, however, that the temperature of the white dwarf has cooled to a baseline effective temperature of $T_{\text{eff}} = 27 - 28,000$ K by

system becomes an ER UMa star.

SWP05744_scr.dat

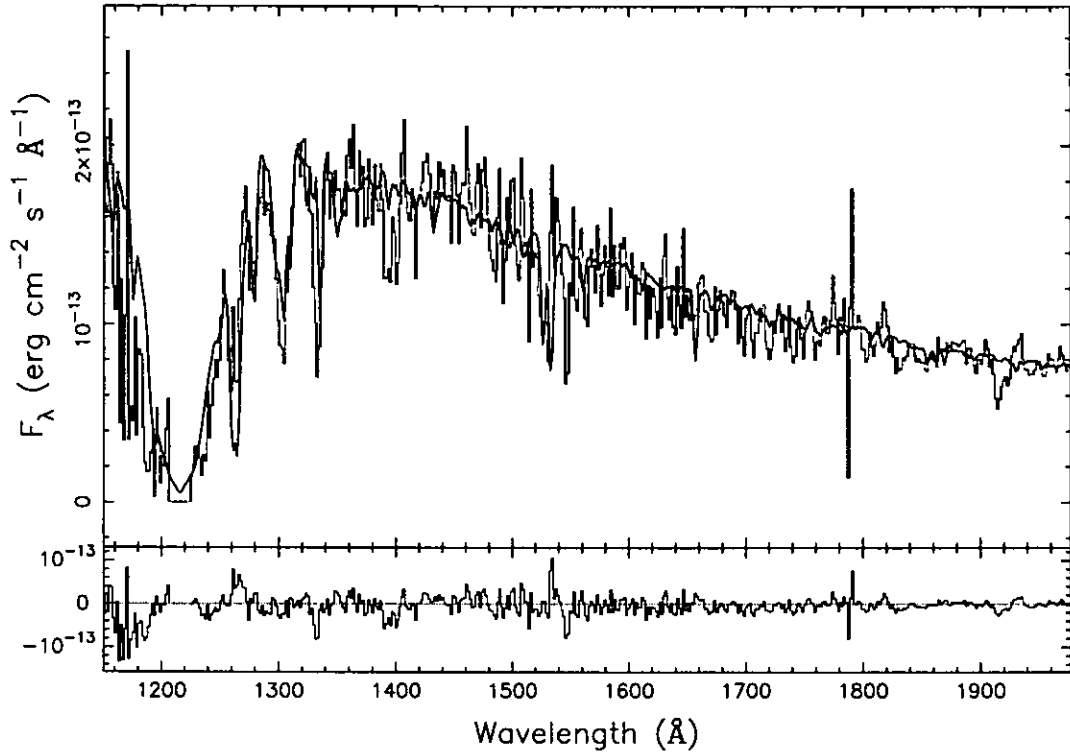


Figure 5.14: A synthetic spectral fit to a spectrum of WZ Sge obtained six months after the 1978 outburst. The temperature of the white dwarf is 20,500 K, and $\chi^2_{\nu} = 1.78$. This plot is for comparison with Figure 5.9, in which the same spectrum is modelled with that of a field white dwarf.

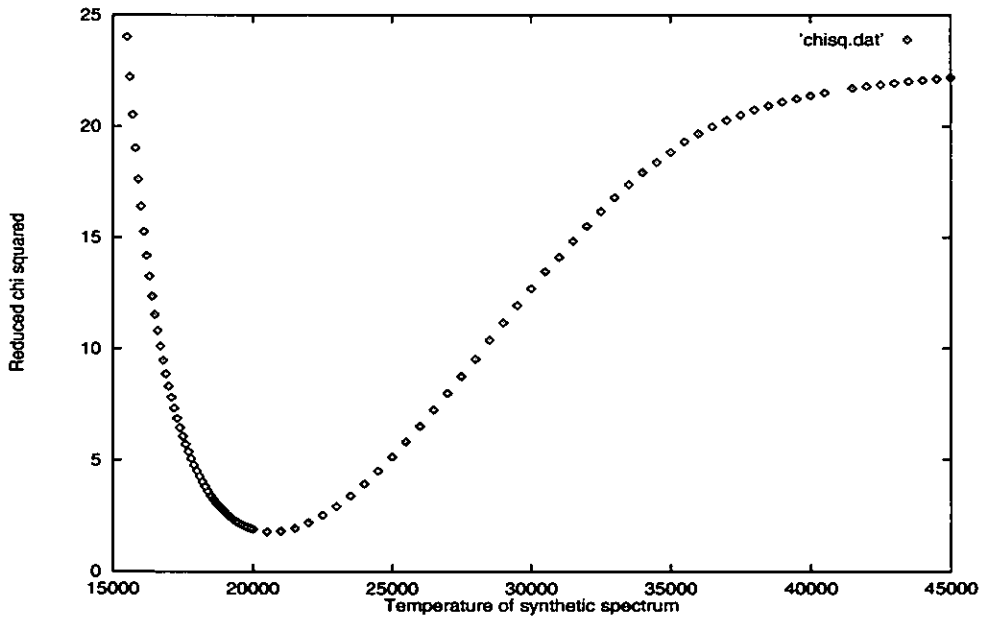


Figure 5.15: The χ^2_{ν} vs. temperature plot for the fit of the WZ Sge spectrum SWP05744 with the solar abundance synthetic spectra (cf. Figure 5.9, where the same spectrum is modelled with a field white dwarf spectrum). For comparison with the similar plot obtained from the field white dwarf fit (Figure 5.10).

Table 5.3: A table of synthetic spectral fits to two quiescent data sets for U Gem, obtained with *IUE*.

Spectrum	Date	Days after max	$T_{wd} \pm 1500$ (K)	χ^2_ν
Panek & Holm (1984)				
PI: Panek				
SWP10536	04/11/80	26	33000	2.54
SWP10836	19/12/80	71	29000	1.34
SWP11144	25/01/81	108	28000	1.74
Kiplinger et al. (1991)				
PI: Kiplinger				
Swp24074	29/09/84	22	31000	1.39
SWP24154	09/10/84	32	27000	0.48
SWP24385	04/11/84	58	28000	1.86
SWP24520	21/11/84	75	27000	1.39
SWP24634	08/12/84	92	28500	0.68
SWP24716	19/12/84	103	27500	1.25
SWP25371	06/03/85	75	28000	0.43

about 30 days into quiescence after the 1984 outburst. In the absence of any evidence to the contrary, it seems likely that the same timescale is involved after the 1980 outburst.

The conclusions of the *HST* FOS studies of the cooling of the white dwarf in U Gem differ slightly both one from the other, and from the above *IUE* - based temperature determinations.

Long et al. (1994a) find a flux decline of 28% between spectra obtained 13 days and 70 days post-outburst, from an outburst in 1992, and estimate that the white dwarf had cooled from 39,400 K to 32,100 K between the observations. The e -folding time of the white dwarf temperature decay can be calculated by

$$T_{wd} = T_b + \Delta T \exp[-(t - t_0)/\tau] \quad (5.5)$$

where T_b is the equilibrium temperature, ΔT is the increase in temperature over the equilibrium value, t_0 is the start time of an outburst and τ is the e -folding time. The e -folding time for the Long et al. (1994a) observation is 30 days. A later observation by Sion et al. (1998a), using a higher resolution grating, found white dwarf temperatures of 32,000 K and 29,000 K at 13 days and 61 days after a 1995 outburst, respectively. It is believed that the differences in these estimated temperatures are due to an unusually long quiescent interval experienced by U Gem in 1994/1995. Sion (1999) suggests that “In this scenario, the long quiescence could have disrupted a normal time-averaged *equilibrium* between accretional heating of the upper envelope and cooling by radiation. The normal (average) equilibrium would be reestablished only after a sufficient number of dwarf nova cycles” (Sion’s italics). The Long et al. (1994a) and *IUE* observations were not affected by

this lowering of the T_{eff} , having been obtained during normal duration quiescent intervals.

Considering the limitations of the *IUE* spectra, and that the white dwarf in U Gem obviously has a variable baseline temperature as shown by both this and the *HST* studies, the temperatures found here are not considerably different from those found in the *HST* studies.

CU Vel and SW UMa

In a recent paper Gänsicke and Koester (1999) searched the entire IUEFA for CV spectra which carried the broad Ly α feature characteristic of an underlying white dwarf. As a result of this search, Gänsicke and Koester found this signature in the spectra of three further CVs: the dwarf novae CU Vel and SW UMa, and the novalike variable AH Men. All of the exposures were obtained in late 1995; the spectra of CU Vel and SW UMa had been obtained for the Hassall & la Dous project to find more low \dot{M} systems. These spectra were then modelled by Gänsicke and Koester using the Kiel model atmosphere code. The spectra of the dwarf novae were unequivocally the result of photospheric emission from a white dwarf; the best fitting primary temperatures were $18,500 \pm 1500$ K for CU Vel and $16,000 \pm 1500$ K for SW UMa. However, in their discussion, Gänsicke and Koester point out the inconclusive nature of the results obtained from the modelling of the spectrum of AH Men. The spectrum could be modelled as a white dwarf at $\sim 19,000$ K, but it could be equally well modelled as an accretion disc with a mass transfer rate of $\dot{M} = 10^{-9.5} M_{\odot} \text{ yr}^{-1}$.

The spectra of CU Vel and SW UMa that were analysed by Gänsicke & Koester (SWP54235 and SWP56269, respectively) were dearchived and modelled by the author using synthetic spectra generated using TLUSTY and SYNSPEC. This is thus a good opportunity to assess the reproducibility of the primary temperature as a result of using different spectral codes. One difference between the synthetic spectra used here and those of Gänsicke and Koester (1999) is that C has been included as a continuum opacity source in these model atmosphere calculations.

The spectra were initially modelled in exactly the same way as Gänsicke & Koester (1999), in that the fits were obtained over the wavelength range 1225 - 1900 Å (rather than the 1150 - 1950 Å full wavelength range). The resulting white dwarf temperature determinations agree with Gänsicke and Koester's within their errors.

The spectra were also modelled across the whole range 1150 - 1950 Å, except for the masked regions listed in the introduction. This allows, in principle, the estimation of slightly more accurate white dwarf temperatures because of the extra constraints imposed

SWP54235_scr.dat

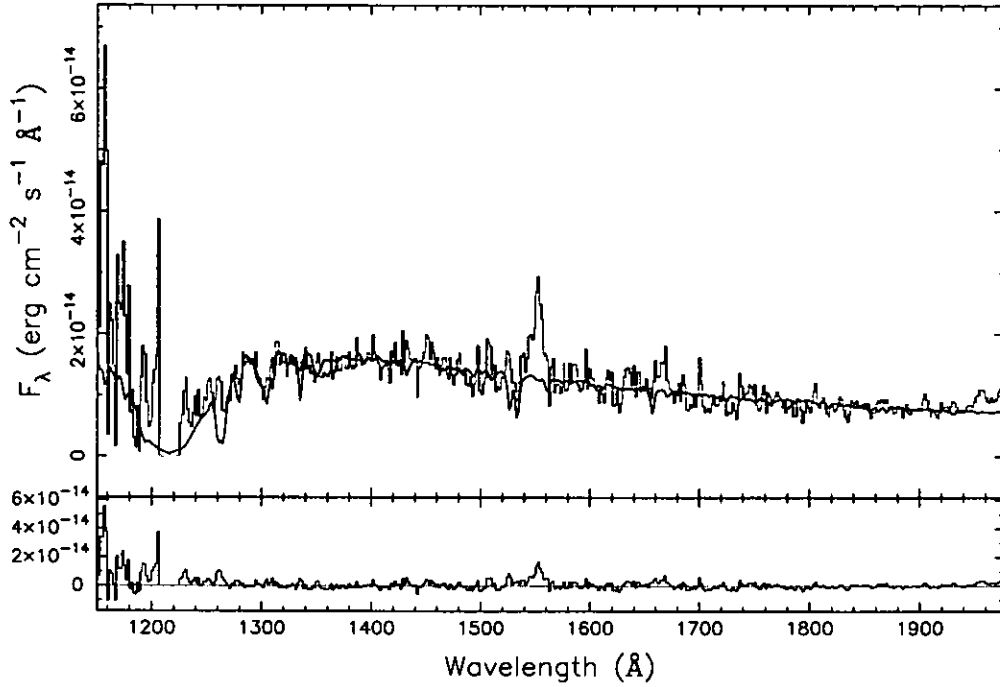


Figure 5.16: The best-fitting solar abundance white dwarf model fit to the spectrum of CU Vel (SWP54235), which has a $\chi^2_\nu = 0.66$. The temperature of the model is 19,500 K.

SWP56269_scr.dat

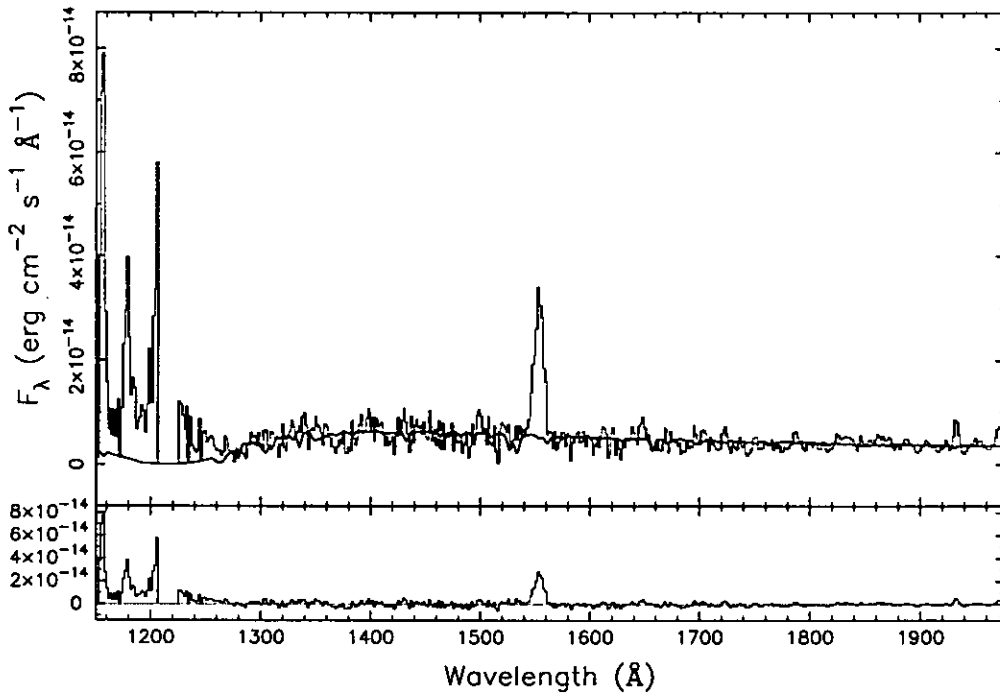


Figure 5.17: The best-fitting solar abundance white dwarf model fit to the quiescent spectrum of SW UMa (SWP56269), which has a $\chi^2_\nu = 1.81$. The temperature of the model is 16,200 K.

by the data shortward of Ly α . These full continuum fits resulted in a primary temperature of $19,500 \pm 1500$ K for CU Vel, and $16,200 \pm 1500$ K for SW UMa, although both spectra are rather poorly constrained shortward of Lyman α (the main reason for this is the poor absolute flux calibration of the IUEFA at wavelengths shortward of $\lambda < 1200$ Å). The result for CU Vel may possibly argue for a slightly hotter white dwarf, but the temperature of SW UMa is practically the same as the Gänsicke & Koester (1999) determination and both cases agree within the errors. These fits are shown in Figures 5.16 and 5.17.

HT Cas and Z Cha

Both of these are high inclination systems, sufficiently so that the bright spot, accretion disc and white dwarf are all eclipsed in each. Wade et al. (1994a) examined the evidence for an ‘iron curtain’ in *IUE* spectra of Z Cha and OY Car, but neglected HT Cas, perhaps because there exists only one, rather noisy spectrum of this system obtained in quiescence.

There are several quiescent spectra of Z Cha, some of which were obtained after the decline from outburst and superoutburst, so that different temperatures would be expected in different spectra. Synthetic spectral fits for each of these, using unabsorbed spectra, were made in the present study, revealing that the effect of the ‘iron curtain’ is present in each. Figures 5.18 and 5.19 illustrate the improvement that occurs with a veiled spectrum fit for one particular spectrum of Z Cha. These spectra were thus modelled with veiled spectra in an attempt to quantify any variations in the column density of the ‘iron curtain’ at different epochs.

Table 5.4 summarises the veiled white dwarf fits to these Z Cha spectra, together with the single quiescent spectrum of HT Cas. The HT Cas spectrum is noisy and the temperature discrimination is poor shortward of the Ly α absorption. The temperature found for the white dwarf, $15,900 \pm 1500$ K, is slightly hotter, than the temperature found in the *optical* study by Wood et al. (1992), 14,000 K, who used eclipse decomposition and flux measurements across a range of optical passbands. The limitations of using that method are discussed in Section 5.4.2.

The veiled spectrum model (Figure 5.19) shows marked deviations from the observed spectrum particularly in the Si abundances (SiIII $\lambda\lambda 1260, 65$ and SiIV $\lambda\lambda 1394, 1403$) One possible explanation may be that there is an inhomogeneous chemical abundance distribution on the white dwarf surface (cf. Gänsicke & Beuermann 1996), another may be a deviation from solar abundances in the ‘iron curtain’; yet another may be that the overabundance is due solely to an overestimation in the models. Abundance adjustments are beyond the scope of the present work; suffice it to say that it is potentially difficult to

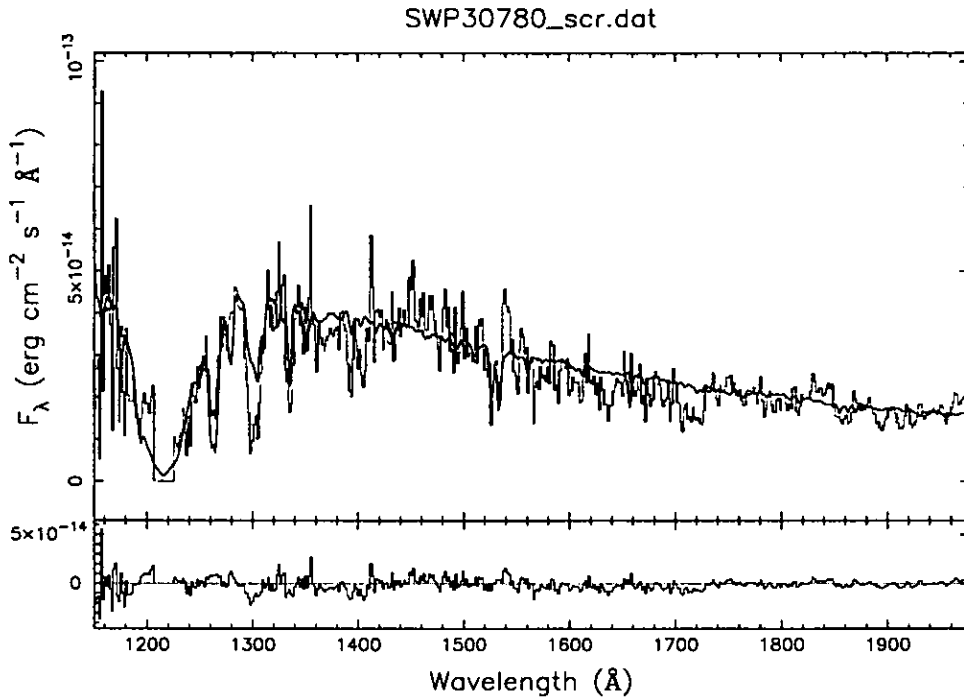


Figure 5.18: The best fitting normal (unveiled) synthetic spectrum fit to a quiescent spectrum of Z Cha. The $\chi^2_{\nu} = 2.5$, and the temperature of the primary star is 21,500 K; cf. Figure 5.19.

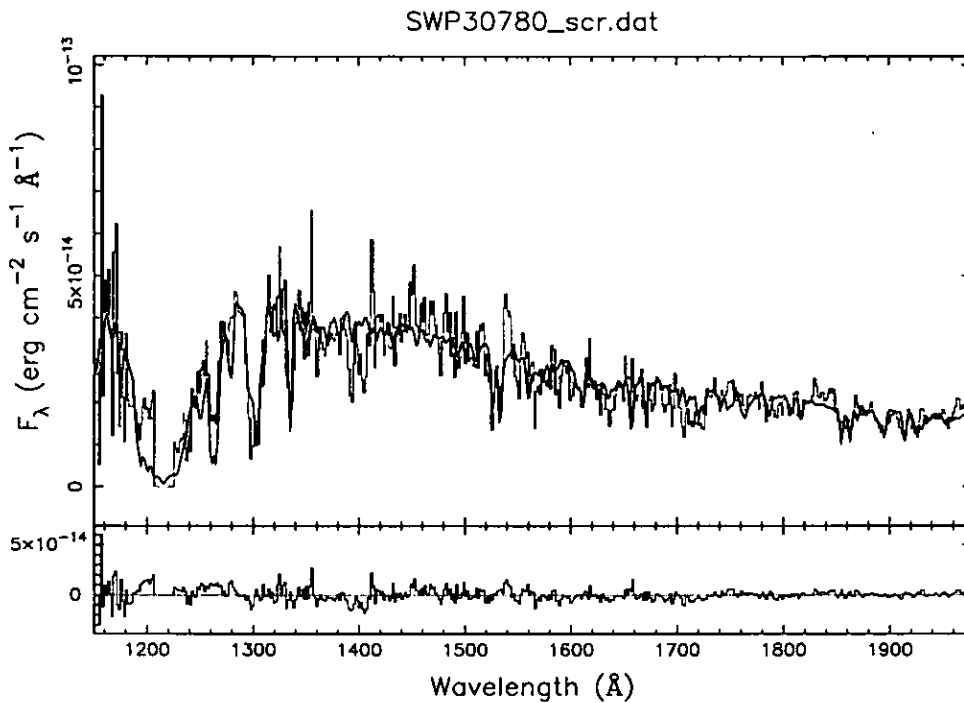


Figure 5.19: The best fitting veiled synthetic spectrum fit to the same quiescent spectrum of Z Cha (cf. Figure 5.18). The $\chi^2_{\nu} = 1.7$, the temperature of the white dwarf is 21,000 K, the veiling gas is 12,000 K, and the $n_{\text{H}} = 10^{22}$.

Table 5.4: Veiled solar abundance white dwarf synthetic spectral fits to the *IUE* spectra of HT Cas and Z Cha.

Object	Spectrum	Date	T_{wd} (K)	T_{gas} (K)	n_H (cm^{-2})	χ^2_ν
HT Cas	SWP21080	17/09/83	15900	10000	10^{22}	1.45
Z Cha	SWP06385	04/07/79	18100	10000	10^{21}	1.52
	SWP28262	05/05/86	17300	10000	10^{21}	3.12
	SWP30780	14/04/87	21000	12000	10^{22}	1.74
	SWP30796	16/04/87	20500	10000	10^{21}	1.54
	SWP32827	31/01/88	19900	10000	10^{20}	2.12

disentangle the three effects mentioned above. This is discussed further in Section 5.8.

The Z Cha spectral fits show discrimination both in the column density of the veiling gas and the white dwarf temperature. Of all these ‘quiescent’ spectra, the one with the lowest flux level is also the one that delivers the coolest white dwarf, SWP28262. The subsequent spectra, SWP30780 and SWP30796, were obtained at the very end of an outburst and appear to show not only a cooling of the white dwarf itself, but also a change in the temperature and column density of the ‘iron curtain’. Both of these effects are (naively) expected as the system settles down to quiescence. These results must be treated with caution, however, because of the coarse grid (temperature and column density) employed here for ‘iron curtain’ spectra. Wade et al. (1994a) found similar values for the white dwarf temperature, but found a cooler absorbing curtain than the hotter of the two indicated here. Ways of improving the method are discussed later in this Chapter and also in Chapter 6.

VW Hyi and OY Car

VW Hyi The *HST* FOS spectrum of VW Hyi in quiescence was next modelled. A new set of synthetic spectra was generated by convolving the original raw (0.1 Å resolution) synthetic to the *HST* FOS spectral resolution and rebinning the resulting spectrum to the FOS binsize. Figure 5.20 illustrates the resulting fit of a 22,000 K solar abundance synthetic spectrum, an identical figure to that found for the same spectrum by Sion et al. (1995b). For a better fit still (an improved χ^2), Sion et al. (1995b) adjusted the abundances and found that best fitting chemical abundances were O at 0.3 times solar, N at 5 times solar and all other heavy elements at 0.15 times solar. Sion's interpretation of the overabundance of N and the underabundance of C has been discussed previously (Section 5.4.3). Adjusting chemical abundances is beyond the scope of this work and in any case is complicated by the 'iron curtain' in the spectrum of OY Car.

Multi-component fits to this and other quiescent spectra of VW Hyi by Sion and collaborators, and other groups, are discussed in Section 5.7. Multi-component fits are again beyond the present scope of this work, and will have to be considered very carefully if they are to be applied to the forthcoming *HST* data.

OY Car The *IUE* spectra of OY Car, HT Cas and Z Cha are from long exposures obtained over several orbits of the binary, and thus were acquired in a different way from the time tagged eclipse spectrophotometric observation that yielded the Horne et al. (1994) *HST* spectrum. As a result, any parametric determinations from synthetic spectral fitting of *IUE* spectra are orbit-averaged. Wade et al. (1994a) have applied an 'iron curtain' analysis to the available *IUE* spectra of OY Car and Z Cha, and in the case of OY Car obtained primary and 'iron curtain' parameters to within a factor of 2 of the Horne et al. (1994) determinations.

Figure 5.21 illustrates the improvement in the fit to the quiescent *IUE* spectrum of OY Car when a veiled spectrum model is introduced. The fit becomes progressively better with an increase in the column density. It is clear from the Figure that $N_H = 10^{22}$ is a slight overestimate, as some of the 'iron curtain' features are over-fitted.

Finally, an illustrative fit was performed on the Horne et al. (1994) *HST* FOS spectrum of OY Car. The pipeline-processed data was downloaded from the *HST* archive⁹ and manipulated in IRAF.

Some 237 spectra were obtained by Horne et al. (1994) in the course of the observation,

⁹STSCI archive at <http://archive.stsci.edu>, ESO ST-ECF archive at <http://archive.eso.org/archive/hst>

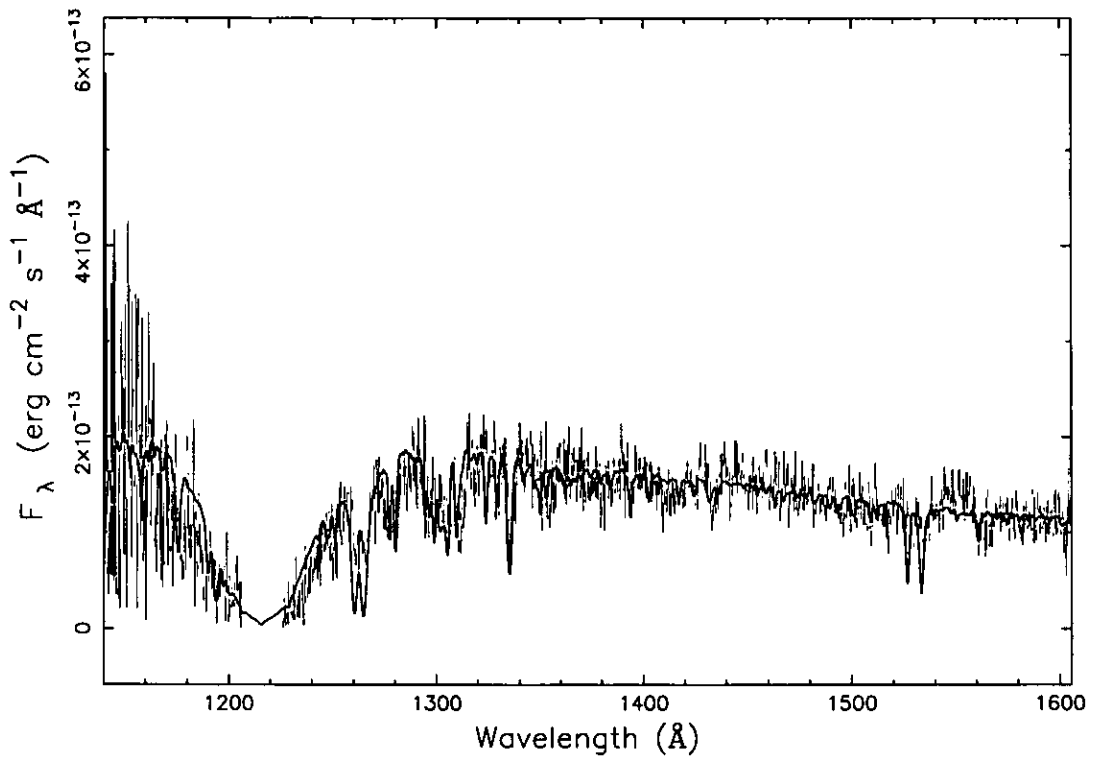


Figure 5.20: An unveiled, solar abundance synthetic spectral fit to the quiescent *HST* FOS spectrum of VW Hya. The temperature is 22,000 K.

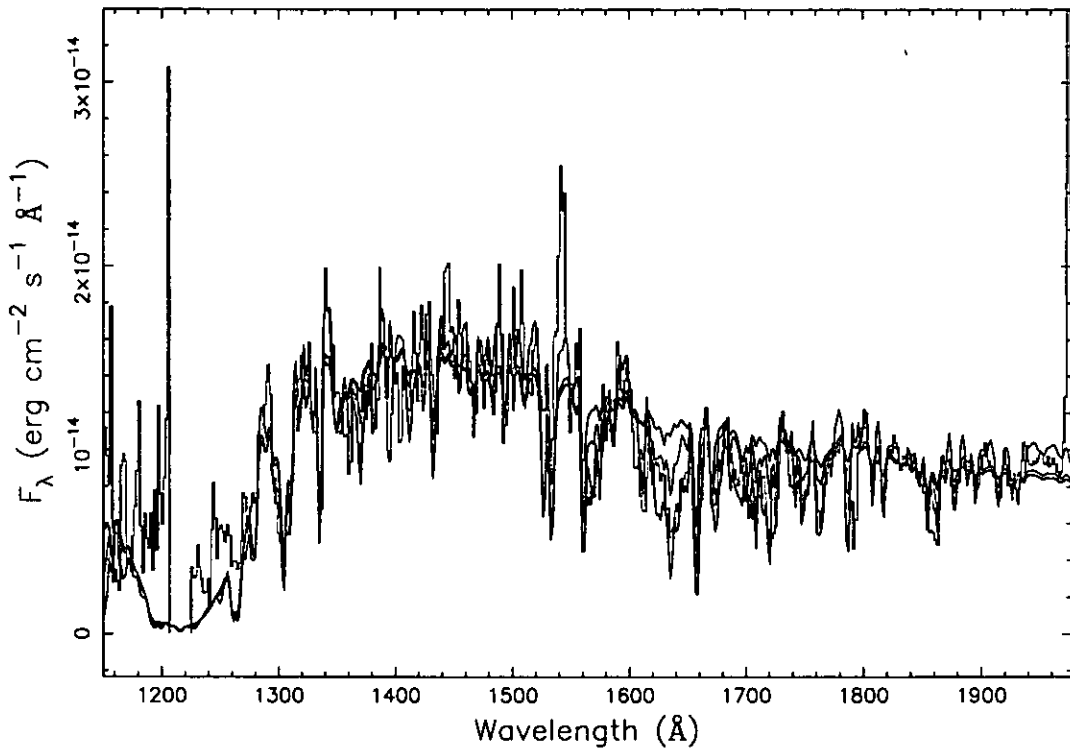


Figure 5.21: A quiescent spectrum of OY Car (SWP28263), modelled with the spectrum of a solar abundance white dwarf at $T_{\text{eff}} = 16,500$ K, veiled by gas at $T_{\text{gas}} = 10,000$ K, with a column density of $n_{\text{H}} = 10^{20}$ cm^{-2} (green), 10^{21} cm^{-2} (blue) and 10^{22} cm^{-2} (red). The fit to the ‘iron curtain’ features at $\lambda \sim 1600 - 1800$ \AA becomes progressively better with an increase in the column density.

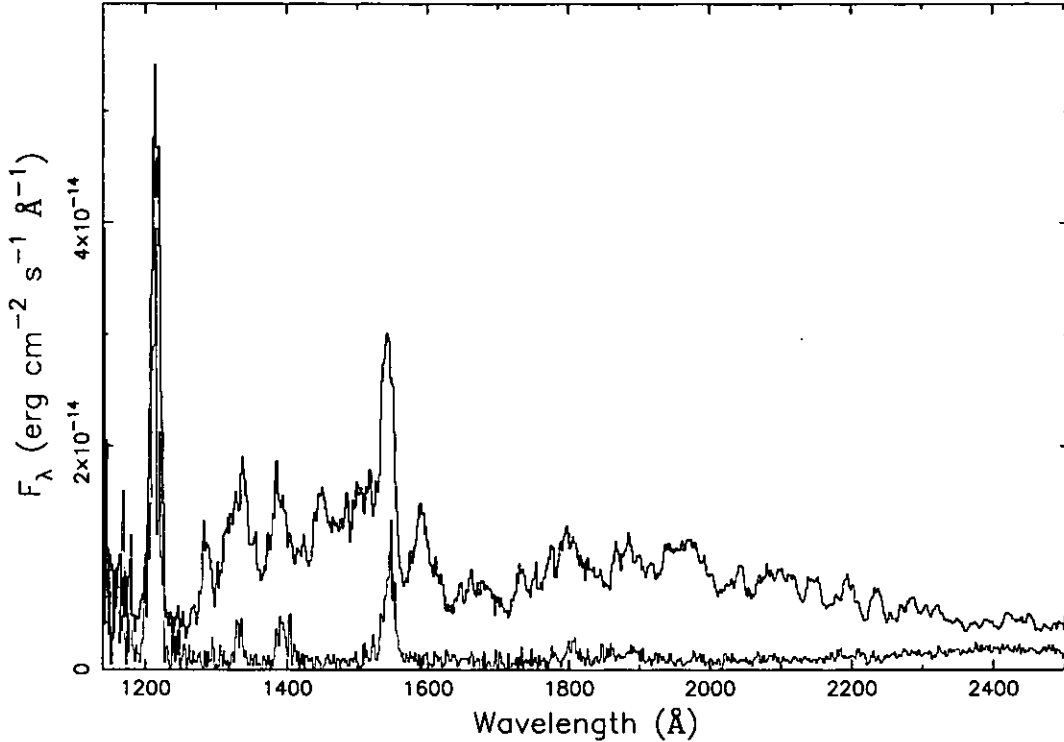


Figure 5.22: The *HST* FOS spectrum of OY Car, obtained by averaging the spectra acquired during out-of-eclipse phases (black) and by averaging in-eclipse phase spectra (grey).

which covered one eclipse. Full eclipse decomposition is beyond the scope of this work, but the next-best approach involves subtracting the in-eclipse spectrum of the white dwarf from the out-of-eclipse spectrum. In order to separate out the spectra acquired while the white dwarf was in eclipse from those acquired when it was visible, an average flux value was calculated for each of the 237 spectra. When the resulting average flux values are plotted, there is a clear ‘eclipse’ in the average flux as the primary star is occulted by the secondary, leaving residual emission primarily from the disc but also from the hot spot. The spectra obtained while the primary was in eclipse were separated out in this way and the resulting in- and out-of-eclipse spectra averaged; these average spectra can be seen in Figure 5.22.

The average in-eclipse spectrum was subtracted from the average out-of-eclipse spectrum in order to obtain a mean white-dwarf-only spectrum. This was then compared with a veiled spectrum at 16,500 K, with $T_{cur} = 10,000$ K, $N_H = 10^{22}$ cm $^{-2}$, the Horne et al. parameters. The resulting comparison can be seen in Figure 5.23: while the bulk of the disc and bright spot emission has been removed, it is obvious that there is still a residual contribution.

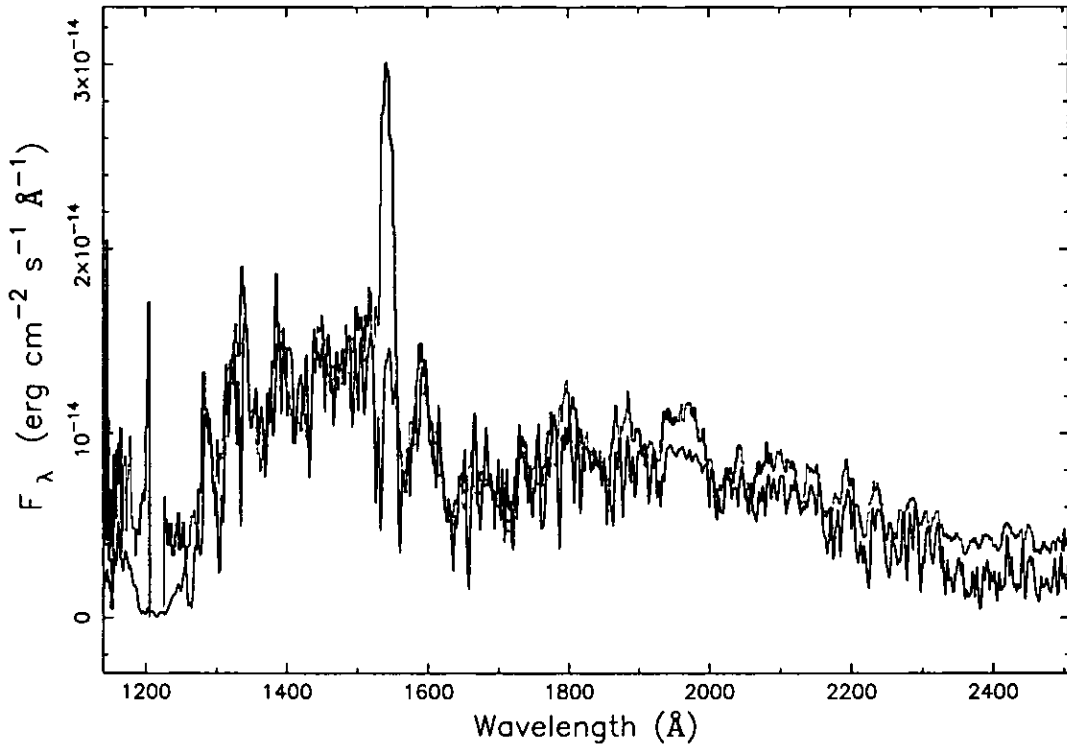


Figure 5.23: A representative veiled white dwarf synthetic spectrum fit (black) to the average *HST* FOS spectrum of OY Car (grey), obtained from the subtraction of the mean in-eclipse spectrum from the mean out-of-eclipse spectrum. The parameters are the same as those found in the Horne et al. (1994) study.

The most recent *HST* observations of OY Car and its veiling gas have been undertaken by Catalán et al. (1998), again with the FOS. Their preliminary analysis of full orbital coverage of the ultraviolet spectrum of OY Car shows that the ‘iron curtain’ is present throughout the orbit, supporting the suggestion that the veiling gas originates in the upper atmosphere of the disc and is not necessarily connected to the bright spot/gas stream region.

In the next Chapter, the possibilities for modelling of the *HST* Space Telescope Imaging Spectrograph (STIS) spectrum of OY Car, which covers a slightly different wavelength range but more of the ‘iron curtain’, are discussed.

5.8 Discussion

The modelling of white dwarfs in CV spectra is a difficult business. One must first identify whether or not the spectral signature of the white dwarf is present. In most cases any emission from the white dwarf is drowned by that from the disc, and in the absence of any satisfactory quiescent accretion disc models, establishing the properties of the white dwarf from its underlying spectrum is not possible.

Even in the few cases where the white dwarf can be seen in the spectrum, the results can be ambiguous. In high inclination systems there is the effect of the ‘iron curtain’. The global approach applied to *IUE* spectra, which was reasonable given its resolution and signal to noise, would ignore the higher resolution and sensitivity offered by the newer *HST* and *HUT* experiments. Each system is different and must be dealt with uniquely. To set up appropriate modelling, one must first answer the following questions:

- Can the white dwarf be seen?
- What is the extent of the disc contribution?
- Is there an ‘iron curtain’?
- In the absence of an ‘iron curtain’, is there any evidence for more than one temperature component in the white dwarf spectrum?
- In the absence of an ‘iron curtain’, is there any evidence for unusual chemical abundances?

Two component models for unobscured white dwarfs

In the case of the (unobscured by an ‘iron curtain’, quiescent) *HUT* spectrum of U Gem, Long et al. (1993) tried to explain the difference between their single temperature model with the *IUE* temperature derivation by Panek & Holm (1984) — a difference of 8,000 K — by modelling with a composite two-component dual-temperature synthetic spectrum. The rationale here is that during an outburst (and during accretion in quiescence), the equatorial regions of the white dwarf photosphere are preferentially heated, and provide the hot component in the resulting spectrum. When the *HUT* spectrum of U Gem was modelled this way, temperatures of $\sim 38,000$ K with an underlying $\sim 57,000$ K component were inferred, with a consequent improvement in the χ^2 -value (Long et al. 1993). Long et al. (1993) estimated that the hot component occupied $\sim 15\%$ of the white dwarf surface. The improvement in the χ^2 was primarily due to a better fit below 970\AA , in this context a wavelength range unique to *HUT*.

Gänsicke & Beuermann (1996) took this idea further in their analysis of *IUE* observations of a post-outburst VW Hyi. They address the prominent deviations of the SiII doublets (1260,65Å, 1527,33Å) from model solar abundances in these spectra (mentioned here in Section 5.7.2, and visible in plots of the models in the *IUE* example fits) by suggesting that, in addition to there being two temperature components, there may be a variation in the chemical composition across the surface. Their intuitive model uses a cool pure-hydrogen component for the polar regions, and a hotter, solar-abundance component for the equatorial regions. There was a considerable improvement in the fit to the SiII doublets because of the reduced contribution of the solar abundance component.

Routine approximations

Various approximations that are routinely used when modelling the white dwarfs in CVs can have quite a bearing on the final temperature determination. Most modelling assumes, for instance, that the white dwarf will have $\log g = 8$ at its surface, which corresponds to a white dwarf mass of $M_{\text{wd}} \sim 0.6M_{\odot}$, the canonical mass for single white dwarfs. This is usually a simplifying assumption and is fine when comparative temperature estimations are wanted. As an illustration of the effect that the white dwarf mass can have on the resulting spectrum, three example spectra in the *IUE* wavelength range and spectral resolution, at a temperature of 17,000 K, were calculated. $\log g$ values of 7.5, 8.0 and 8.5 were used, which correspond to $M_{\text{wd}} \approx 0.25M_{\odot}$, $M_{\text{wd}} \approx 0.6M_{\odot}$ and $M_{\text{wd}} \approx 1.0M_{\odot}$, respectively (assuming the radius of a C-core Hamada-Salpeter [Hamada & Salpeter 1961] white dwarf). The resulting spectra can be seen in Figure 5.24: the mass of the white dwarf has a marked effect on the Lyman α region, which is a crucial diagnostic of the white dwarf temperature in this wavelength range.

Webbink (1990) redetermined the mass ratios of a large sample of CVs, utilising empirical calibrations derived from several well known relations between observed features and the underlying physical parameters of the system (e.g., velocity separation of double emission peaks, parameters of emission line profiles). Webbink (1990) calibrated observable quantities against CVs and Algol binaries with well-determined mass ratios, and from this an empirical mass-radius relation for the secondary stars was derived. Webbink then estimated white dwarf masses from this relation, and found that white dwarf masses for dwarf novae were $0.50 \pm 0.10M_{\odot}$ below the period gap, and $0.91 \pm 0.08M_{\odot}$ above.

The Webbink (1990) result can be contrasted with the white dwarf masses derived from observations of eclipse durations. All the well-known eclipsing dwarf novae reside below the period gap, but the derived masses in the literature are almost exclusively greater than

$0.5M_{\odot}$ and more usually $\sim 0.7 - 0.8M_{\odot}$. The mass of the white dwarf in OY Car, derived from eclipse timing measurements in Wood et al. (1989) and Wood & Horne (1990), is in the range $0.68 - 0.84M_{\odot}$. Sion et al. (1998a) find $M_{\text{wd}} = 0.86M_{\odot}$ ($\log g = 8.44$) for VW Hyi from the gravitational redshift of the white dwarf in a recent *HST* observation. VW Hyi is a system which, in common with OY Car, lies below the period gap. This result obviously does not agree with the Webbink (1990) analysis.

It should be noted here that there has been a long discussion in the literature concerning the discrepancies between white dwarf masses as measured by spectroscopic means and those determined from eclipse timings. Constraining the parameters of the components from the measured radial velocity of emission lines is still quite controversial, and ultimately depends on what assumptions are used in the modelling process. In particular, the assumption that the radial velocity variations in emission lines in the accretion disc reflect the orbital motion of the primary star has been queried. Detailed explanations and critiques of parameter estimation from spectroscopic measurements can be found in Wade & Ward (1985) and Warner (1995).

If the masses are uncertain, then so too will be the derived temperature. To try and quantify the uncertainty, a 17,000 K, $\log g = 8.5$ solar abundance synthetic spectrum was calculated by the author over the *IUE* wavelength range, and fitted with $\log g = 8$ spectra in exactly the same way as detailed earlier. The best fitting temperature was $\sim 15,100$ K. Thus on the basis of the continuum distribution and particularly the crucial Ly α absorption region, a difference of $\log g = 0.5$ can produce a corresponding systematic uncertainty in the temperature of ~ 2000 K. This uncertainty is not important for secular changes in an individual system, but is important for temperature comparisons between different systems. This uncertainty affects low temperature white dwarfs preferentially because of the broader Lyman α absorption in these objects, and so will affect low \dot{M} systems to a considerable extent.

The other routine approximation which has the potential to add to the uncertainty of the derived white dwarf temperature is the neglect of metal line blanketing in the calculation of the opacity/temperature structure of the atmosphere. Although at these temperatures and densities the dominant continuum opacity sources are H, He and C, the cumulative effect of neglecting the other opacity sources will lead to a systematic temperature shift. To illustrate this, solar abundance synthetic spectra were calculated here, first using only H and He as the continuum opacity sources in TLUSTY, then using H, He and C as the opacity sources. Synthetic spectra were produced from the model atmospheres as described in Section 5.6.2. The result is shown in Figure 5.25: even the

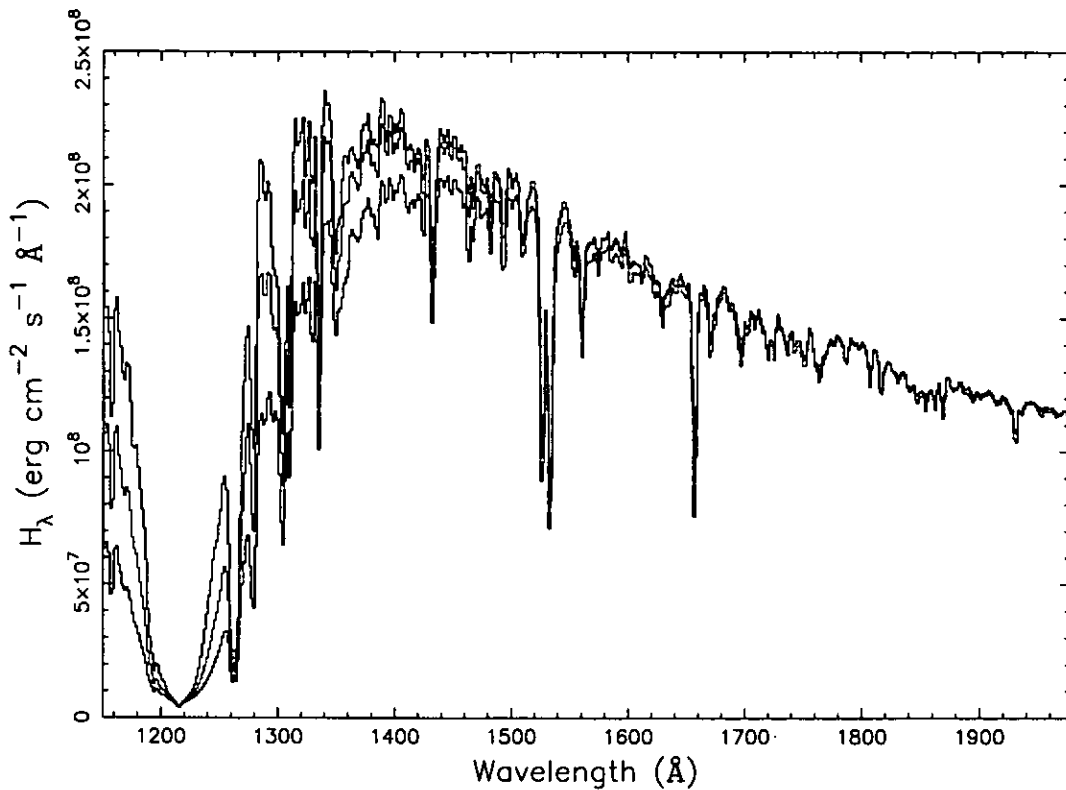


Figure 5.24: This diagram shows the spectrum of a 17,000 K solar abundance white dwarf calculated with $\log g$ values of 7.5 (blue), 8.0 (black) and 8.5 (red). The differences are most dramatic around the region of the Ly α absorption, which is a crucial temperature diagnostic.

neglect of C in the atmosphere has an appreciable effect on the resulting spectrum (a reduction of ~ 100 K in this illustrative case involving only C). The inclusion of metals in the model atmosphere calculations has the effect of *reducing* the effective temperature at a given spectral type. This effect is mentioned briefly in Horne et al. (1994), and Horne and collaborators have reported calculations of some fully line-blanketed model atmospheres and synthetic spectra for a 15,000 K white dwarf (Lanz et al. 1992). Lanz & Hubeny (1995) describe the effect of metal line blanketing on hot, metal-rich white dwarfs ($\sim 60,000$ K): at this temperature, they find that if the Fe/H abundance is greater than 10^{-5} , the line opacity is such that Fe must be considered in the model atmosphere construction.

Another cause for concern is the extent of the contribution of the disc remnant, even in quiescence. The spectra modelled here were chosen specifically because there was little or no disc contribution.

Gänsicke & Beuermann (1996) circumvent the disc contribution problem in their study of the cooling of the white dwarf in VW Hyi after outburst, by using an average observed

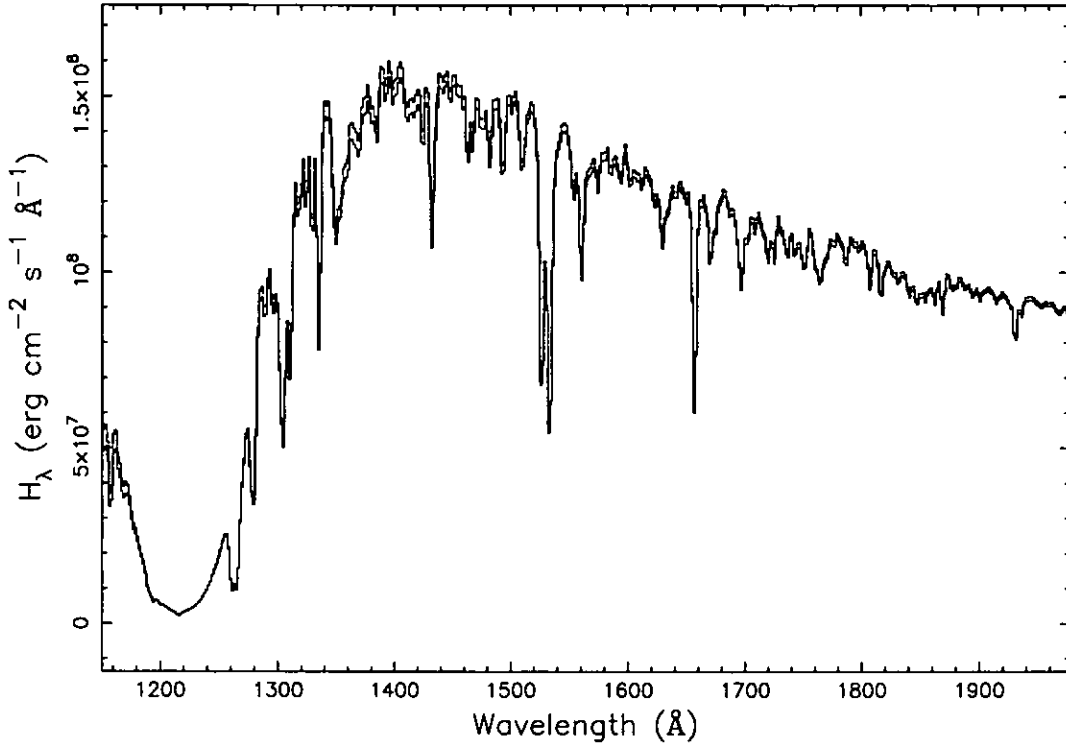


Figure 5.25: A comparison of the spectrum obtained from a $\log g = 8$, 16,000 K model atmosphere when only H and He are used as continuum opacity sources in TLUSTY (red), with the spectrum resulting from the use of H, He and C as the dominant continuum opacity sources (black). The effect of including C is to reduce the effective temperature at a given spectral type. The spectrum covers the *IUE* wavelength range and has been convolved with the *IUE* spectral resolution and rebinned to *IUE* binsize.

ultraviolet spectrum of VW Hyi at maximum (when the contribution of the white dwarf is negligible). This approach should be treated with some skepticism because the disc is optically thick in outburst and the method involves application of an optically thick model to quiescent disc material which should be optically thin. There are, at the time of writing, no satisfactory quiescent disc spectrum models since the disc structure is not yet known in sufficient detail.

An alternative manifestation of a disc remnant in quiescence is the accretion belt detected in VW Hyi. Huang et al. (1996) modelled the *HST* spectrum of VW Hyi with a two component synthetic spectral fit, combining a white dwarf and a disc contribution. The disc contribution can be seen most prominently in a broad continuum hump centered around 1450Å, and in a velocity broadened emission feature centred on CIV 1550Å. Huang et al. (1996) generated synthetic disc spectra using Dr. I. Hubeny's unpublished DISKSYN code. They divided the axially symmetric, Keplerian disc into annuli, each annulus behaving as an independent radiating slab. Since the disc is optically thick in

the vertical direction, they integrated spectra derived from model *stellar* atmospheres, using DISKSYN, over the individual annuli on the disc surface. This procedure is proven to be a good approximation for optically thick discs (see also Long et al. 1994b). The two component fit indicated that the ultraviolet emitting area of the disc was a ring of width $0.06R_{wd}$ (presumably indistinguishable from the boundary layer, or a belt on the white dwarf itself), inclination 60° and rotating at a Keplerian velocity on the white dwarf surface of 3350 km s^{-1} . The ring had $\log g = 6.0$ and $T_{\text{eff}} = 28,000 \text{ K}$, with C and Si at 20 and 15 times solar abundance respectively. The contribution of the disc to the total ultraviolet flux was estimated to be $\sim 12\%$.

It is now almost routine that a *HST* or *HUT* observation of an unobscured white dwarf will be modelled with dual component/temperature synthetic spectra. The outcome of these spectral fits suggests that a hot component is in evidence in VW Hyi — Huang et al.’s 1996 analysis is unusual in that the second component is modelled as a disc, rather than just a contribution from a hotter white dwarf photosphere — and U Gem (Long et al. 1993), where the components are at 38,000 K and 57,000 K 10 days after the return to optical quiescence. The usual interpretation is that the hotter component is due to the preferentially heated equatorial region of the white dwarf photosphere, as mentioned above. If it is due to the disc, then as yet there is no totally satisfactory treatment of this component.

The realistic modelling of ultraviolet spectra is a process of assessing the contributions of all of the components mentioned above, in the light of what is known about the system at the time. It must be stressed yet again, however, that in the case of ‘iron curtain’ systems, the obscuration of the white dwarf makes it very difficult to apply two-temperature component models to its spectrum.

For the forthcoming data, analysis similar to the method used in Horne et al. (1994) is envisaged, with improvements designed to extract the best possible results out of the data. A grid of fully line blanketed NLTE veiled solar abundance white dwarf spectra, close to the average quiescent temperature of the white dwarf, will be calculated. Various values of $\log g$ will be used, corresponding to a white dwarf of $M_{wd} \approx 0.6 - 0.85M_\odot$, as derived from eclipse durations. Models with various values for the velocity dispersion, ΔV (which was essential to the Horne et al. fit), column density, N_H , and electron density, n_e , of the ‘iron curtain’, will be calculated. The optimal synthetic spectrum will then be found using a multidimensional χ^2 minimisation algorithm such as AMOEBA (Press et al. 1992), or a possibly by the use of an evolutionary strategy (genetic) algorithm. Other possible improvements to the method are outlined in the next Chapter.

5.9 Summary and conclusions

In this Chapter, a wide ranging review of the use of ultraviolet spectroscopy to estimate various system parameters has been undertaken. In the majority of most dwarf novae and CVs in general, the emission from the disc is such that light from the photosphere of the white dwarf is drowned out. In a certain select few objects, however, it is possible to see the broad Lyman α absorption and blue continuum distribution of the white dwarf, and to model these spectra to a remarkable degree of precision. In these systems, the white dwarf is successfully modelled using synthetic spectra with *solar abundances*, reflecting the effect of continued accretion from the disc. White dwarf temperatures derived independently in the present work agree substantially with previously published values

However, care needs to be taken when these spectra are modelled. A residual disc contribution has not yet been modelled to a satisfactory level, due to uncertainties in the knowledge of the structure of a quiescent accretion disc. Wade et al. (1994b) model the *IUE* spectrum of VW Hyi as the sum of a solar abundance white dwarf spectrum and a steady state accretion disc. Occultation of part of the star by the disc is taken into account, and vice versa. Wade et al. find that the fluxes from the disc and the white dwarf can be comparable at intermediate inclinations. They find that the spectrum of VW Hyi (SWP10911) can be described equally well with a white dwarf at $T_{\text{eff}} \sim 18,000\text{K}$ and no disc, implying a distance of 52pc, or by a white dwarf with $T_{\text{eff}} \sim 18,000\text{K}$ and an accretion disc with $\dot{M} = 10^{-10}M_{\odot} \text{ yr}^{-1}$, viewed at an inclination angle of 60° . The implied distance is now 80 pc, and the disc contributes 40% of the flux at 1400\AA .

There is evidence for more than one temperature component in some *HST* and *HUT* spectra (e.g., Long et al. 1993), and there may be evidence for an inhomogeneous chemical abundance distribution in VW Hyi (Gänsicke & Beuermann 1996). Systematic temperature inaccuracies are introduced primarily if it is assumed that the white dwarf has $\log g = 8.0$, but also from the neglect of metal line blanketing in the model atmosphere calculations. The estimated temperatures derived in this Chapter agree well with those already published, considering the simplicity of the method used and the signal to noise of the data. However, there is much scope for improvement, and the modelling of the upcoming *HST* spectrum of OY Car will have to be more sophisticated.

It is possible to see the effect of the ‘iron curtain’ in the ultraviolet spectra of several eclipsing dwarf novae. An examination of the spectra available in the IUEFA certainly suggests that the curtain is variable. It is not possible to apply more than one temperature white dwarf component to the modelling of these spectra because it is then difficult to

separate out the effect of the extra component from the effect of the 'iron curtain'. The advantage of OY Car and similar eclipsing systems is that the disc contribution can be successfully excluded by decomposing the light curve.

With the forthcoming ultraviolet/X-ray observations, it will be possible, for the first time, to make measurements of the extent of the 'iron curtain' across these wavelengths simultaneously.

Chapter 6

Conclusions and Further work

6.1 Summary of results and conclusions

In this Section, the main findings of the thesis work are summarised. Some of the work has been published (Pratt et al. 1999a, b). Other aspects of the work (reported in Chapter 5) will be used in the analysis of *ASCA* and *HST* observations which are scheduled but not yet obtained; these analyses and results are not included in the thesis because of time constraints.

X-ray and optical observations of OY Carinae in both quiescence and superoutburst have been used to deduce information about the disc and boundary layer region of this eclipsing SU UMa-type dwarf nova. Archive ultraviolet observations have provided the data for a critical evaluation of the methods used to deduce parameters of the white dwarf primary star in a number of low mass transfer rate CVs.

Future work following from this thesis will concentrate on interweaving the techniques involved in each spectral region, X-ray, ultraviolet and optical, in order to develop a self-consistent picture of OY Carinae itself, and by extension, other nonmagnetic CVs, in each accretion regime.

OY Car: superoutburst

Eclipse mapping of optical observations of OY Car on the decline from superoutburst has shown that the disc displays a substantial disc full-opening angle of $\sim 10^\circ$ even three days into the superoutburst decline. Two days earlier, the opening angle was $\sim 11^\circ$, implying that there is evidence for a decrease in the extent of the opening angle between 1 and 3 days after the end of the supermaximum. There was also evidence for a change in the mass flux rate through the disc over the same timescale, from, very approximately,

$\dot{M} \sim 10^{-9} M_{\odot} \text{ yr}^{-1}$ to $\dot{M} \sim 4 \times 10^{-10} M_{\odot} \text{ yr}^{-1}$.

Contemporaneous *ROSAT* HRI X-ray observations supported the conclusion that the disc was flared. There was no eclipse of the X-ray flux, which implied the existence of an extended X-ray source region, and the superoutburst X-ray luminosity, at $L_X \sim 10^{32} \text{ erg s}^{-1}$ was a factor of 100 times lower than the corresponding luminosity, derived from *EXOSAT* observations, of the non eclipsing system, VW Hyi. This evidence pointed towards an obscuration of the boundary layer regions in superoutburst, as both HT Cas and Z Cha had been previously observed to undergo quiescent X-ray eclipses (Wood et al. 1995a; Mukai et al. 1997; van Teeseling 1997). It also indicated a contributory effect from the different spectral responses of the instruments on the satellites involved.

OY Car: quiescence

What is the column density of the absorption to the X-ray source in OY Car in quiescence? There is not, at present, a straightforward answer. It is complicated by the detection of the ‘iron curtain’ of material veiling the *HST* ultraviolet white dwarf spectrum, which was found by Horne et al. (1994) to have a column density of $n_{\text{H}} = 10^{22} \text{ cm}^{-2}$. A similar figure was found by Wade et al. (1994a), and in the current work, from modelling of a single *IUE* spectrum. At this column density, as argued by Naylor & la Dous (1997), much of the soft X-ray flux should be extinguished.

Follow-up *ROSAT* HRI observations of OY Car were obtained to prove that the X-ray source region in quiescence was not obscured. Because of a lag of $\sim 40\text{s}$ discovered in phasing the superoutburst optical light curves, optical observations were also obtained in quiescence in order to update the ephemeris of the system. The ephemeris update was also useful because accurate optical ephemerides are required for phasing of X-ray light curves.

There was a deep eclipse of the X-ray flux in quiescence ($\sim 93\%$ with four bins across eclipse phases) which was coincident with the optical white dwarf eclipse, illustrating that the X-ray flux was neither obscured by the disc (in which case there would be no eclipse), nor by the ‘iron curtain’ (in which case the X-ray flux would be exceptionally low, or nonexistent).

A *ROSAT* PSPC observation of OY Car in quiescence, obtained previously, was used to constrain the temperature of the X-ray emitting gas, to constrain the absorption to the X-ray source, and to estimate the quiescent luminosity. It was found that the temperature of the emitting gas is typical for this type of object, at $kT \lesssim 10 \text{ keV}$, but the quiescent luminosity, at $L_x \sim 10^{30-31} \text{ erg s}^{-1}$, is an order of magnitude lower than the corresponding

luminosity of VW Hyi as measured by the same satellite. Two alternative explanations are possible without invoking the absorption to the X-ray source — the white dwarf may be spinning rapidly, or there may be a low rate of mass transfer through the boundary layer.

The 1.6 kilosec observation, frustratingly, did not allow a quantitative estimate to be made of the absorption due to interstellar hydrogen and locally to the ‘iron curtain’. Single component absorption models were not compatible with the column density of 10^{22} cm^{-2} derived by Horne et al. (1994). Model fits using a dual-component absorption could not realistically disentangle the relative contributions of a local, ionized absorber and an interstellar neutral absorber.

Tentatively, evidence presented here does seem to point to some contribution from ionized material, reducing the X-ray opacity and allowing the detection of soft X-rays. This is the first time a warm absorber has been invoked in the context of X-ray observations of CVs.

Archive ultraviolet observations

In most cases the ultraviolet light from the system is dominated by the accretion disc, but in some cases the characteristic spectroscopic signature of a white dwarf can be detected and modelled. This modelling allows the parameterisation of several attributes of the white dwarf primary star.

As the largest archive store of ultraviolet observations, the IUEFA contains thousands of CV spectra. In actual fact, the white dwarf can be observed in only a very small number of these spectra. White dwarf model atmospheres and synthetic spectra were generated, and those *IUE* CV spectra where the white dwarf could be seen were fitted using a fitting routine based on the χ^2 value of the fit; this resulted in white dwarf temperatures in good agreement with published values. In the case of CU Vel and SW UMa, the derived temperatures agreed very well with (the same within the errors: ± 1500 K) those of Gänsicke & Koester (1999), who used the Kiel model atmosphere code.

In most of the above cases, the *IUE* spectrum can be modelled as a single white dwarf, but the higher quality of *HST* and *HUT* spectra allow dual temperature models to be fitted (Long et al. 1993), or allow the modelling of, for instance, accretion belts (Huang et al. 1996). Outburst-quiescent datasets show that a substantial proportion of the decline in the ultraviolet flux after outburst can be attributed to a cooling white dwarf (e.g., Gänsicke & Beuermann 1996).

An investigation of the accepted methods used to generate the model atmospheres and

synthetic spectra has suggested that derived white dwarf temperatures in CVs are subject to some systematic uncertainties in the derived temperatures. This does not affect relative temperature determinations, where the simple change in temperature is measured. The two main causes of error are the neglect of metal line blanketing, which is acknowledged in Horne et al. (1994) to be an important effect, and the general assumption that the model atmospheres will have a gravity $\log g = 8$ ($M_{wd} \approx 0.6M_{\odot}$). This is rather low compared to estimates of the white dwarf mass in OY Car itself, based on eclipse durations (between 0.68 and $0.89M_{\odot}$). NLTE effects are negligible at the temperatures and gravities typical of white dwarfs in dwarf novae.

6.2 Further work

6.2.1 Forthcoming observations with *ASCA* and the *HST*

Introduction

Early on in the course of this work, it was realised that the quality of the quiescent X-ray spectrum of OY Car was sufficient only to weakly constrain the extent of the column density of the absorption to the X-ray source. It was also recognised that potentially serious discrepancies could develop between measurements of the column density in the ultraviolet and those obtained in the X-ray (Naylor & la Dous 1997), and that these potential discrepancies might be exacerbated by comparing observations obtained at different epochs. Simultaneous ultraviolet/X-ray observations in quiescence were needed to specify the extent of the absorption in each spectral region.

A programme to observe OY Car **simultaneously** with *ASCA* and the *HST* was thus drawn up for, respectively, *ASCA* AO-7 and *HST* Cycle 8. The proposals were drawn up by the author and Dr. B.J.M. Hassall, in collaboration with Drs. J.H. Wood and K. Mukai, and Prof. T. Naylor; the present author was a major contributor to the scientific cases for both of these proposals. Each proposal was accepted after review by the respective Time Allocation Committees, (60 kilosec and 2 orbits, respectively) and the observations are scheduled to be acquired in 2000 Mar, unfortunately not in time for inclusion in this thesis.

The reduction and analysis methods undertaken during the course of this thesis are an excellent preparation for the forthcoming observations.

ASCA

With its increased throughput and spectral energy resolution, *ASCA* (Tanaka et al. 1994) observations will be a significant improvement over those already acquired with *ROSAT*. The mean count rate of the *ROSAT* PSPC observation detailed in Chapter 4 was 0.08 counts s^{-1} (note however that the count rate in the PSPC all-sky survey was 0.024 counts s^{-1}). PIMMS (Mukai 1993) predicts an *ASCA* count rate of 0.15 - 0.2 counts s^{-1} per instrument, assuming the PSPC count rate above and a 2 - 10 keV bremsstrahlung model absorbed with $N_H = 10^{22}$ cm^{-2} . This should be compared with ~ 0.12 counts s^{-1} for the HT Cas observation by Mukai et al. (1997).

Were it not for noise contributions from the background, the 60 kilosec observation would yield a folded light curve of the quality of that obtained by Mukai et al. (1997). That said, with the *ASCA* count rate estimated above, and assuming enough eclipses are covered, it may be possible to measure the eclipse width and depth accurately. The summed *ASCA* eclipse can be used to compare X-ray and optical eclipse timings, and in principle the phase duration of the X-ray ingress and egress can be compared with those in the optical. The feasibility of this is illustrated by Mukai et al. (1997), who model the *ASCA* X-ray eclipse of HT Cas to put real limits on the size of the X-ray emitting region, and the location of the emission relative to the white dwarf.

The observational aspect that is expected to bear the most scientific fruit, however, is the X-ray spectrum. The *ASCA* X-ray instruments have a wider passband (0.4 - 10 keV) and finer energy resolution than those on *ROSAT*, which will result in a substantial refinement of the X-ray spectrum of OY Car. A summed spectrum obtained over 60 kilosec will enable concrete constraints to be placed on the absorption to the X-ray source. Dual-component absorption models will be used to estimate the relative contributions of the local absorption due to the 'iron curtain' and the neutral interstellar absorption. This will then be compared to the absorption deduced from the *HST* ultraviolet observations. A boundary layer X-ray luminosity and accretion rate will also be estimated. In the absence of an X-ray eclipse (highly unlikely), modelling of the highly absorbed boundary layer component will be undertaken.

Finally, the occurrence of absorption dips in the X-ray light curve, at other orbital phases away from eclipse, will be investigated. This will probe the phase dependence of any absorption variation, and if detected will imply azimuthal variation of extended structure in the outer disc. If such dips are present at $\phi \sim 0.7 - 0.8$, it is likely that they will be due to the bright spot. If there are dips at other orbital phases, these should be

detectable by comparing hard ($E > 2$ keV) and soft ($E < 2$ keV) light curves.

HST

The simultaneous observations from the *HST* will enable well-defined constraints to be placed on the absorption in OY Car in the ultraviolet spectral range. Initially, this observation will help assess the effect of time variability as a cause of the discrepancy between the measured column densities in each spectral range.

OY Car will be observed with the STIS, using the CCD detectors rather than the MAMA (Multi-Anode Microchannel Array), which would be vulnerable if the system undergoes an outburst in mid-observation. The G230LB grating will be used to cover a wavelength range of 1685 - 3065 Å, with a central wavelength of 2375 Å. Signal to noise is expected to be ~ 10 per resolution element for a five minute exposure. The white dwarf spectrum should be relatively flat and featureless over this spectral region, whilst the 'iron curtain' has many individual lines and a large depression between 2000 and 3000 Å, which should amount to over 50% percent of the flux at the column densities expected. Figure 6.1 illustrates the predicted effect of the 'iron curtain' on the flux in the wavelength range of the forthcoming observations. The Ly α region will be absent as the forthcoming observations do not cover that wavelength; however, the slope of the continuum will be a sufficient diagnostic of the temperature. Meanwhile, the 'iron curtain' effects are more pronounced at ~ 2500 Å than at ~ 1600 Å, which will enable better constraints to be placed on the column density and other parameters than has been possible thus far.

The author is under no illusions that the *HST* spectrum of OY Car will require careful reduction and analysis. Contributions to the spectrum from the residual disc and bright spot emission will have to be removed so that the spectrum that is eventually modelled is that of the veiled white dwarf only. Judging from the 1150 - 2500 Å spectrum obtained by Horne et al. (1994), the combined disc/bright spot contribution will begin to be noticeable longward of ~ 2200 Å. The method envisaged for spectrum decomposition will be similar to that developed in Horne et al. (1994) and in the *HST* observations of UX UMa and V2051 Oph by Baptista et al. (1998a, b). In order to do this, the spectra will have to be binned and flux-calibrated, to give spectrophotometric light curves. This will involve dividing the spectra into short (15-30 Å) passbands and computing the average flux in each. From these light curves, the system can be modelled and the spectra decomposed into each contributory element.

The light curves reconstructed from the spectra will then be decomposed into white dwarf, bright spot and accretion disc components in a similar fashion to that described

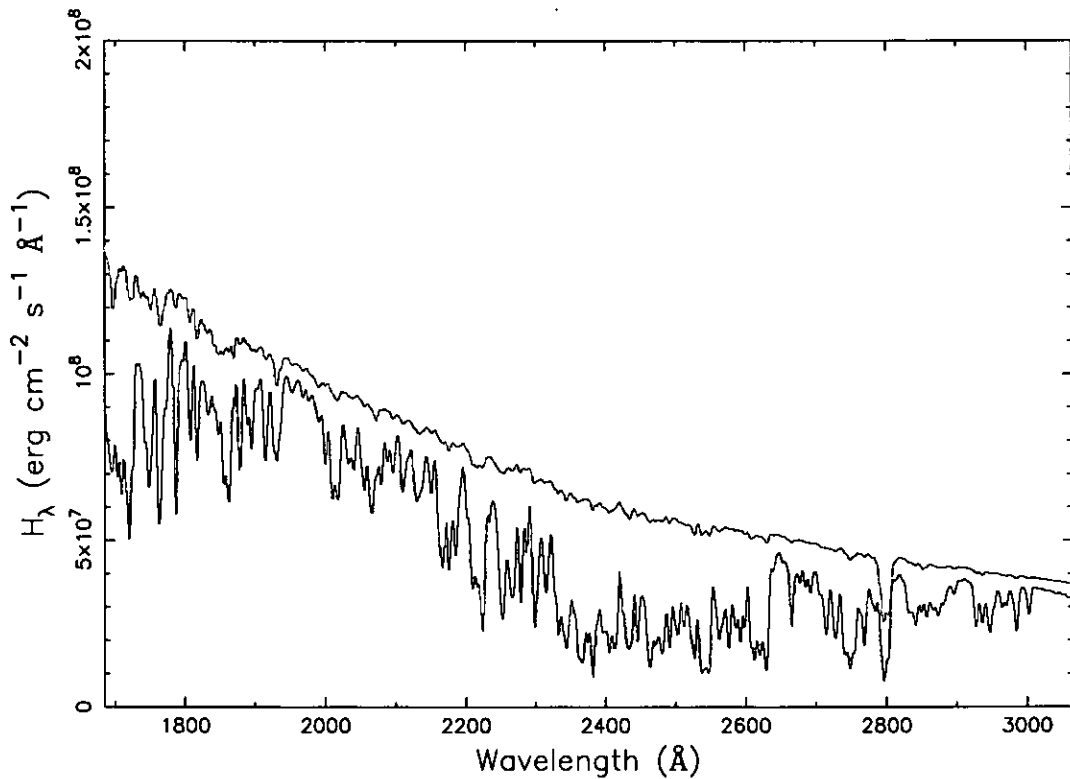


Figure 6.1: Synthetic spectra of a solar composition white dwarf with $T_{\text{eff}} = 16,500$ K (grey), and the same spectrum obscured with a solar abundance LTE veiling gas with $T_{\text{eff}} = 10,000$ K, $n_{\text{H}} = 10^{22}$ cm^{-2} (black). The wavelength range and resolution is identical to that of the forthcoming *HST* observations. While the Ly α absorption is not covered, the continuum slope should provide a sufficient diagnostic for the white dwarf temperature.

as follows, using a variation of the method of Wood et al. (1985): in this way the data $D(\phi, \lambda)$ are acquired. In Horne et al. (1994), the data $D(\phi, \lambda)$ are modelled as $M(\phi, \lambda)$ given by the sum of several components:

$$M(\phi, \lambda) = \sum_{i=1}^N L_i(\phi) S_i(\lambda) \quad (6.1)$$

where $L_i(\phi)$ is the light curve and $S_i(\lambda)$ is the spectrum of component i . Each data component light curve (white dwarf, bright spot, and accretion disc) can be modelled by imposing model light curve constraints such as assuming that the white dwarf and accretion disc light curves be symmetric about phase 0. Also, since the white dwarf and bright spot are totally eclipsed in OY Car, these model component light curves must have a flux of zero between second and third contact points. The component light curves and spectra can then be adjusted as parameters in the model $M(\phi, \lambda)$ in order to achieve the best fit to the data $D(\phi, \lambda)$, using the χ^2 statistic. The corresponding spectra will be reconstructed from a linear combination fit of the three model component light curves to the data.

Once the veiled white dwarf spectrum is extracted, it will be modelled with synthetic spectra generated using TLUSTY and SYNSPEC. Fully line blanketed models can be used, as the temperature of the white dwarf should at this stage be known to within a few thousand degrees. Optimised model parameters will be calculated using the improved methods outlined in Section 5.8, i.e., using the multidimensional downhill simplex AMOEBA algorithm from Press et al. (1992). However, optimisation using this method requires vigilance as the algorithm sometimes lodges in a local minimum.

An alternative approach to optimising model parameters would be to use an evolutionary strategy (genetic) algorithm (GA). Although GAs cannot be guaranteed to find the global local minimum, they do have the advantage of being able to climb “uphill” to some extent, which is a feature downhill simplex and similar methods lack. GAs work along the following lines:

1. Generate a set of random solutions to the problem.
2. Evaluate the solutions, minimise according to an appropriate statistic (e.g., χ^2) and rank accordingly.
3. Generate the next generation of solutions. “Natural selection” is used here in GAs, meaning that the fittest solutions (i.e. the ones ranked best in terms of the minimising function) are more likely to produce offspring than those ranked lower. In practice, this is achieved by assigning a success probability to each of the solutions

in the previous population. Then pairs of solutions to mate are picked, according to their probability of success, to produce offspring. To produce the offspring, so-called “uniform crossover” (Beasley et al. 1993b) is used, which means that each parameter of the offspring solution is taken from either one or the other parent solution.

GAs have been introduced into astrophysics only recently. For reviews of the method, see Beasley et al. (1993a, b). Example applications of GAs to the mapping of the accretion stream and in finding the geometry of the accretion region in polar CVs can be found in Hakala (1995) and Potter et al. (1998).

It is envisaged that a method similar to that used for field white dwarfs by Finley et al. (1997) will be used to calculate very accurate values for several parameters, including the temperature and gravity, in OY Car. Once the χ^2 is calculated for each model, Finley et al. (1997) find the best fitting values for the T_{eff} and $\log g$ by fitting bicubic polynomials to each χ^2 surface in the region of the minimum χ^2 . Finley et al. (1997) then find 1σ and 2σ limits on the derived T_{eff} and $\log g$ by polynomial interpolation of the χ^2 array onto a denser $T_{\text{eff}} - \log g$ grid. This method can potentially be applied to other parameters such as the column density etc.

In this way, accurate values for not only the ultraviolet column density, but also the white dwarf temperature and gravity, electron density of the veiling curtain, veiling curtain temperature and veiling curtain velocity dispersion will be derived, simultaneously with X-ray spectral temperature, column density and eclipse parameters. The use of improved and more accurate model atmospheres and synthetic spectra will enable further constraints to be placed on system parameters in the ultraviolet, while the greater spectral and temporal resolution of *ASCA* will improve our knowledge of the system in the X-ray.

6.2.2 Future observations

A new generation of X-ray satellites with ever-higher sensitivity and capabilities will soon be available. The main two are *Chandra*, a NASA satellite launched successfully on 1999 July 23, and an ESA Cornerstone project, the X-ray Multi-mirror Mission (*XMM*), which at the time of writing is scheduled for launch 1999 mid-December. As *XMM* is an ESA mission, the lion’s share of the observing time is set aside for European astronomers. This Section will concentrate on how the increased capability of *XMM* can be used to investigate some of the still outstanding questions regarding CVs in outburst or high mass accretion rate systems.

XMM carries three grazing incidence Wolter type-1 X-ray telescopes which have a total effective area of 4650 cm^2 at 1keV, approximately 6 times that of *Chandra* and 12

times that of *ROSAT*. *XMM* science instruments are:

- The European Photon Imaging Camera (EPIC), consisting of 3 CCD cameras for X-ray imaging, moderate resolution spectroscopy ($E/\Delta E \sim 20 - 50$) and X-ray photometry. *XMM* carries two different types of EPIC cameras. Two of the X-ray telescopes are equipped with an EPIC MOS (Metal Oxide Semiconductor) and the third focuses onto an EPIC pn. The main differences between the cameras are that the MOS CCD is front-illuminated while the pn camera is back-illuminated, and a considerably faster readout time for the pn chips.
- The Reflection Grating Spectrometer (RGS), fitted to two of the X-ray telescopes, consisting of two essentially identical spectrometers for high-resolution spectroscopy and spectrophotometry ($E/\Delta E \sim 200 - 800$), operable in either spectroscopy or high-time resolution modes.
- The Optical Monitor (OM): *XMM* is unique in being equipped with an additional co-aligned 30cm optical/UV telescope, the OM, providing for the first time the opportunity to observe simultaneously across optical/UV and X-ray wavelengths. The total bandwidth of the OM is 1600-6000 Å, and its detector is operated as a photon-counting instrument. The OM is more sensitive than a ground-based telescope of equivalent aperture because of the lack of atmospheric extinction. The OM is equipped with a filter wheel containing several filters (*U, B, V, white*), and two gratings covering different wavelength ranges and capable of moderate resolution optical/UV spectroscopy (~ 5 Å in the UV).

All six science instruments are operated simultaneously, and each instrument can be operated independently in different data acquisition modes.

Enduring questions concerning CVs in the *high mass accretion rate regime*, may be answered by further X-ray and ultraviolet observations. The author, in collaboration with Drs. B.J.M. Hassall, J.H. Wood, K. Mukai, and Prof. T. Naylor, has submitted two proposals for observing time on *XMM* (AO-1). The intention was to observe the X-ray brightest eclipsing novalike variable, UX UMa, and our old friend OY Car in superoutburst, in complementary proposals.

The UX UMa proposal, for which the present author is PI, has recently (1999 Dec) been allocated the requested 51 kilosec of observing time (the OY Car proposal, which was TOO, was unfortunately not allocated time). 51 kilosec is approximately 3 orbital periods of UX UMa. The orbit of *XMM* is highly elliptical, and in principle allows continuous target visibility of up to 70 kilosec. Thus UX UMa will be observed continuously for an

unprecedented length of time for an X-ray observation, allowing any variability of the X-ray flux to be investigated. Other questions which may be answered by these observations include:

- **What is the source of the X-ray emission in the high mass accretion rate regime?:** In Chapter 3, Section 3.6.1, there is a discussion of the different X-ray spectral components observed in the spectrum of VW Hyi in outburst and superoutburst. To recap briefly, the X-ray emitting region of VW Hyi and some other non-eclipsing systems in outburst (and superoutburst) display a two-component X-ray spectrum. The optically thick blackbody-like component at $kT \sim 10 - 50$ eV originates from the boundary layer and dominates up to ~ 0.5 keV. The hard, optically thin component is modelled with a 5 - 10 keV thermal bremsstrahlung spectrum and can be detected down to ~ 0.1 keV if the absorption is low. However the source of the latter component is still unknown. If the component is residual optically thin emission from the boundary layer, as suggested by the *EXOSAT* observations of VW Hyi (van Teeseling et al. 1993), then this component will undergo an eclipse in a high inclination system. This has not been the case with OY Car in superoutburst (Naylor et al. 1988; and this work), and may be due to a considerable contribution of the blackbody component to the flux detected in each satellite filter. The vastly increased sensitivity of *XMM* should enable the separate detection of the hard component, and in principle enable constraints to be placed on it.
- **Is the extended X-ray source in outburst a wind or a static corona?:** The timing observations of UX UMa and OY Car in superoutburst make it clear by the lack of eclipse that extended regions produce the UV emission lines (the wind) and the X-rays. However, it is still unclear whether the sources of each emission are coincident. For example, it is perfectly possible that the hard X-rays have their origin in a static, hot, optically thin corona rather than in an outflow such as a wind (Naylor & la Dous 1997). The high time resolution RGS spectrum will provide an answer to this question, because a static coronal X-ray source will produce narrow emission lines (FWHM ~ 300 km s⁻¹) while an X-ray source originating in a wind will produce broad emission lines (FWHM ~ 1500 km s⁻¹). Figure 6.2 simulates the expected appearance of the O VIII emission line at 0.65 keV when the source is (a) a static corona and (b) a wind.
- **What is the extent of the ‘iron curtain’/absorption in outburst?:** The ‘iron curtain’ appears in quiescence and contributes to the opacity (and hence absorption)

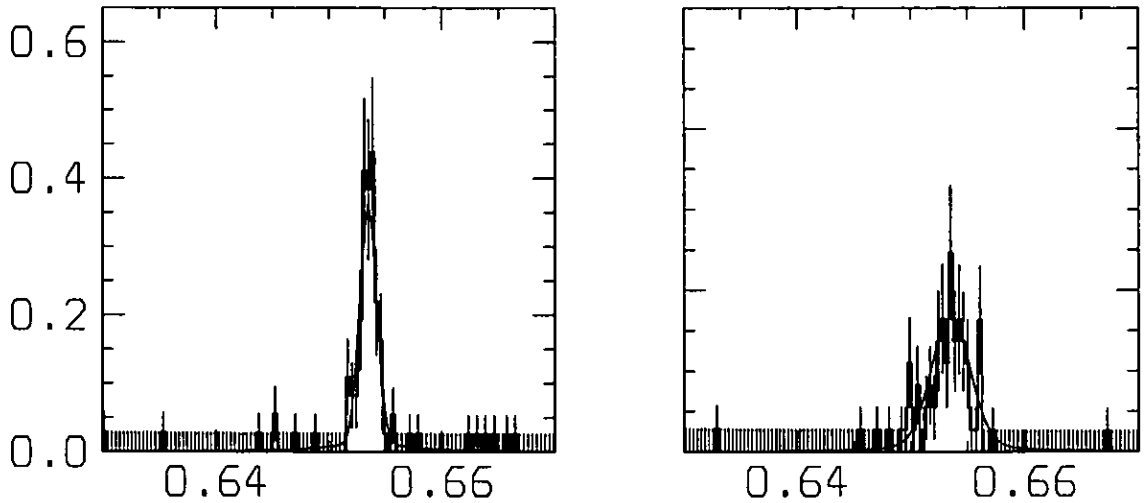


Figure 6.2: *Left*: A simulated RGS spectrum representing an X-ray source that is a static corona, producing a narrow emission line. *Right*: If the source of the X-ray emission in superoutburst is the wind, then the emission line will be broad. The difference between the two can clearly be seen. The FWHM of the narrow simulation is $\sim 325 \text{ km s}^{-1}$, while the width of the broad simulation (FWHM 1500 km s^{-1}) can be determined to about 30% accuracy. Simulation by Dr. K. Mukai (private comm.).

in the ultraviolet and the X-ray. But there are no measurements of the extent of the X-ray column in outburst. Any investigation of this particular aspect should also have simultaneous ultraviolet coverage to measure and search for variations, orbital or otherwise, in the ultraviolet column.

With *XMM*, absolutely simultaneous coverage in the optical/UV and X-ray is possible, removing the need to use two different satellites such as those observations detailed in Section 6.2.1. The *XMM* OM spectral resolution is sufficient to resolve the broad depression at $\lambda \sim 2500\text{\AA}$, and again, the increased spectral and temporal resolution will allow further constraints, over and above those available from *ROSAT* and *ASCA*, to be placed on the absorption to the X-ray source.

- **What fraction of the X-ray flux, if any, comes from the secondary star?:** As pointed out in the Introduction, the corona of the secondary star is potentially a source of X-rays. Like in the quiescent case, timing observations of eclipsing systems are the most useful method for detecting physical components. The disc will eclipse the secondary star, producing a drop in the X-rays at orbital phase 0.5 which is in principle detectable. An observation of this kind would show for the first time whether or not the secondary star is a significant contributor to the X-ray flux from CVs.

Figure 6.3 shows a simulated eclipse of the secondary star by the accretion disc in

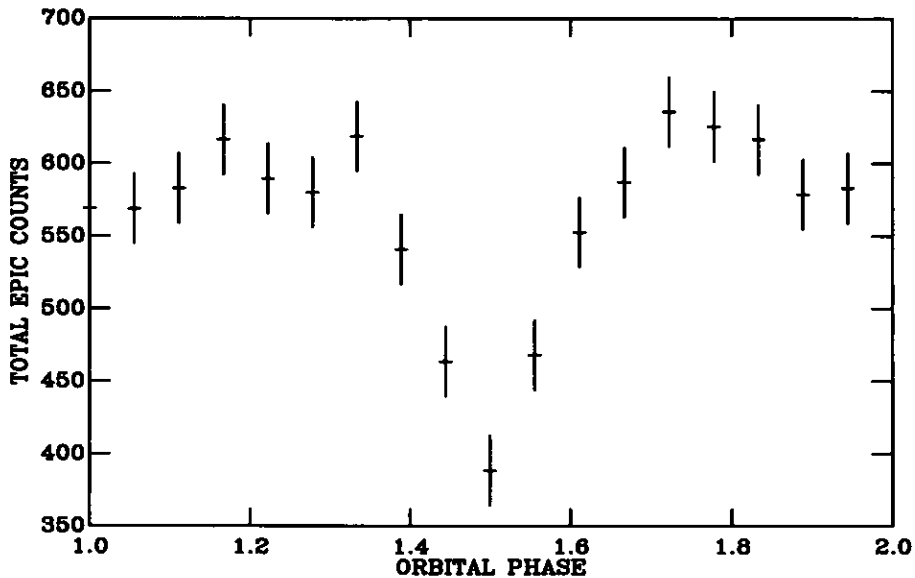


Figure 6.3: A simulation of an eclipse of the X-ray emitting secondary star by the accretion disc in UX UMa (feature at phase 0.5) as observed by *XMM* (predicted). This is a best case scenario, assuming that all X-rays come from the secondary star. Simulation by Prof. T. Naylor (private comm.).

UX UMa, obtained from the total count expected from all three *XMM* detectors, folded on orbital phase. The total exposure time corresponds to 3 orbital cycles (51ks). The parameters assumed are the best available for UX UMa, and include a disc with a semi-opening angle of 10° . For this simulation it is assumed that the secondary star is the only source of the X-rays. This eclipse is significant at the 9σ -level. If, say, only a third of the X-rays had an origin on the secondary star, the eclipse would be significant at the 3σ -level.

Endpiece

The observations presented here have provided further insights into the characterisation of the components, both physical and spectral, in CVs. Further, multiwavelength, preferably simultaneous, observations are necessary. These will test whether the conclusions of this thesis can hold up in the face of the greater and greater spectral/temporal resolution available from the next generation of satellites and telescopes. Only by observing CVs in the entire range of their emissions can a self-consistent picture of their behaviour be built up. As the quality of our observations improve, so too does our understanding of these intriguing systems.

Appendix A

The Zanstra method applied to CV winds

The Zanstra method has been used for many years as a way of determining the temperature of the exciting stars in nebular astrophysics. It is fully described in Osterbrook (1989); this is the version used by Hoare and Drew (1991) to estimate CV boundary layer temperatures.

If the CV wind is optically thick in the He II Lyman continuum, it will absorb all the ionizing photons. Thus the total number of ionizations is equal to the total number of ionizing photons emitted. Ionization equilibrium requires that:

$$\int_{\nu_0}^{\infty} \frac{L_{\nu}}{h\nu} d\nu = \int n_{\text{He}^{++}} n_e \alpha_B(\text{He}^+, T) dV \quad (\text{A.1})$$

number of photoionizations = number of recombinations,

where L_{ν} is the energy distribution of the ionizing source, $\nu_0 = 54.4$ eV is the frequency corresponding to the ionization potential of He II, and α_B is the recombination coefficient. The ionizing source is the accretion disc plus boundary layer.

The number of recombinations can be measured by observing an He II recombination line such as $\lambda 1640$ or $\lambda 4686$. Hoare & Drew (1991) follow Bohlin et al. (1982) and express the ratios in fluxes, obtaining

$$\int_{\nu_0}^{\infty} \frac{f_{\nu}}{h\nu} d\nu = 1.56 \times 10^{11} f(\lambda 1640) \quad (\text{A.2})$$

and

$$\int_{\nu_0}^{\infty} \frac{f_{\nu}}{h\nu} d\nu = 9.8 \times 10^{11} f(\lambda 4686) \quad (\text{A.3})$$

assuming that T_e in the wind is 10^4 K. Hoare & Drew (1991) state that if the wind temperature was as high as 50,000 K the values would increase by only 20 percent and 60 percent, respectively.

The Zanstra ratio is defined as

$$G(\lambda_{228}, \lambda_*) = \frac{\int_{\nu_0}^{\infty} f_{\nu}/h\nu d\nu}{f_*/h} \quad (\text{A.4})$$

where f_* is the continuum flux of the ionizing source at wavelength λ_* , which has been chosen to be next to the recombination line question to avoid the effects of reddening. The Zanstra ratio gives the ratio of the number of photons with $E > 54.4$ eV to the ultraviolet/optical flux.

Foreshortening effects due to the inclination of the disc relative to the observer's line of sight are corrected by dividing the continuum flux by $\cos i$. Hoare & Drew (1991) comment that another effect of the disc geometry is that approximately half the recombination line photons will be intercepted by the disc and destroyed, and therefore they multiply the observed recombination line flux by a factor of two.

Hoare & Drew (1991) then combined equations A.2, A.3 and A.4 to express the Zanstra ratio in terms of observable quantities:

$$G(\lambda_{228}, 1800\text{\AA}) = 2.4 \times 10^{-3} \frac{f(\lambda_{1640})}{f_*(1800\text{\AA})} \quad (\text{A.5})$$

and

$$G(\lambda_{228}, 4700\text{\AA}) = 1.3 \times 10^{-3} \frac{f(\lambda_{4686})}{f_*(4700\text{\AA})}. \quad (\text{A.6})$$

The quantity $f(\text{line})$ is the observed recombination line flux ($\text{ergs cm}^{-2} \text{s}^{-1}$) and f_* is the observed continuum flux/ $\cos i$ in $\text{ergs cm}^{-2} \text{s}^{-1} \text{\AA}^{-1}$). Backscattering losses are included in the numerical constant.

Hoare & Drew calculated a theoretical spectrum for the ionizing continuum from a two component model consisting of a steady state accretion disc (calculated by either integrating blackbodies or Kurucz model atmospheres at appropriate temperatures over the disc), and a boundary layer component represented by a blackbody, an NLTE model atmosphere, or a Raymond-Smith plasma model.

Appendix B

Overview of the basic equations used in model stellar atmosphere generation

The reader is referred to Mihalas (1978), Gray (1992) or Werner & Dreizler (1999) for a discussion of this subject from first principles, and a review of the CL/ALI method of solution. As discussed in Section 5.6, a typical model atmosphere generation program simultaneously solves the 5 basic equations, namely: radiative transfer, hydrostatic equilibrium, radiative equilibrium, particle conservation and statistical equilibrium.

Definitions

Consider radiation coming from a small portion, area ΔA , of a surface. The **specific intensity** of the radiation is defined as:

$$I_\nu = \lim \frac{\Delta E_\nu}{\cos \theta \Delta A \Delta \omega \Delta t \Delta \nu} \quad (\text{B.1})$$

$$= \frac{dE_\nu}{\cos \theta dA d\omega dt d\nu} \quad (\text{B.2})$$

where the limit is taken as all quantities, ΔA , $\Delta \omega$ the increment of solid angle, Δt the increment of time, and $\Delta \nu$ the spectral band, diminish towards zero. The units of specific intensity can be I_ν or I_λ , where the relation between these quantities is:

$$I_\nu d\nu = I_\lambda d\lambda. \quad (\text{B.3})$$

The **mean intensity**, J_ν , is defined as the directional average of the specific intensity, and is related to the energy density of the radiation field, where:

$$J_\nu = \frac{1}{4\pi} \oint I_\nu d\omega. \quad (\text{B.4})$$

J_ν is sometimes referred to as the zeroth moment of the specific intensity. The first moment, H_ν , is related to the flux, where:

$$H_\nu = \frac{1}{4\pi} \oint I_\nu \cos \theta \, d\omega, \quad (\text{B.5})$$

while the second moment, K_ν , is related to the radiation pressure and is used in the hydrostatic equation:

$$K_\nu = \frac{1}{4\pi} \oint I_\nu \cos^2 \theta \, d\omega. \quad (\text{B.6})$$

The **flux** is the measure of the net energy flow across the area ΔA in time Δt , in spectral range $\Delta\nu$, as these quantities approach the limit:

$$F_\nu = \frac{\oint dE_\nu}{dA dt d\nu}. \quad (\text{B.7})$$

The flux and specific intensity can then be related using eq. B.2 to get:

$$F_\nu = \oint I_\nu \cos \theta d\omega. \quad (\text{B.8})$$

and, following similar arguments,

$$F_\nu = 4\pi H_\nu \quad (\text{B.9})$$

Two physical processes contribute to the **absorption coefficient**, κ_ν . The first is true absorption where the photon is absorbed and the energy thermalized (bound-free), the second is scattering, where the photon is scattered out of the solid angle being considered (free-free). The amount by which the specific intensity is diminished in a length dx is:

$$dI_\nu = -\kappa_\nu \rho I_\nu dx, \quad (\text{B.10})$$

where ρ is the density in mass per unit volume. κ_ν has units of area per unit mass. Most of the absorption comes from hydrogen in one form or other.

The **optical depth** τ_ν can now be defined over the path length L as:

$$\tau_\nu = \int_0^L \kappa_\nu \rho dx. \quad (\text{B.11})$$

Eq. B.10 can now be rewritten as:

$$dI_\nu = -I_\nu d\tau_\nu. \quad (\text{B.12})$$

This simple form of the radiative transfer equation can be solved to reveal the extinction law:

$$I_\nu = I_\nu^0 \exp(-\tau_\nu). \quad (\text{B.13})$$

The **emission coefficient** j_ν is a measure of the amount of radiation emitted. In an analogous fashion to the case for absorption, the two contributing factors to the emission coefficient are emission itself and scattering of photons into the line of sight. The increase in the specific intensity in a length dx due to emission is:

$$dI_\nu = j_\nu \rho dx. \quad (\text{B.14})$$

We finally come to the definition of the **source function**, defined as the ratio of emission to absorption:

$$S_\nu = j_\nu / \kappa_\nu. \quad (\text{B.15})$$

The source function has the same units as the specific intensity. In LTE, $S_\nu = B_\nu(T)$, where B_ν is the blackbody function and T is the temperature.

Radiative transfer equation

If we consider radiation travelling in a direction u , the change in the specific intensity, dI_ν , over a small element of path length du , is the sum of the losses and gains from emission and absorption:

$$dI_\nu = -\kappa_\nu \rho I_\nu du + j_\nu \rho du. \quad (\text{B.16})$$

Dividing across by $\kappa_\nu \rho du$ (eq. B.11), and using eq. B.15, this reduces to:

$$dI_\nu / d\tau_\nu = -I_\nu + S_\nu \quad (\text{B.17})$$

This is a basic form of the radiative transfer equation.

TLUSTY uses a radiative transfer equation written as

$$\mu \partial I(z, \mu, \nu) = -\kappa(z, \nu) I(z, \mu, \nu) + j(z, \nu), \quad (\text{B.18})$$

where z is the geometrical depth, μ is the cosine of the angle between the direction of propagation and the normal to the surface, ν is the frequency, and I , κ and j have their usual meanings. The transfer equation is considered by TLUSTY in two different forms — the full angle-dependent form, and the Eddington-factor form, used for linearization. Further details of these treatments, including the variables introduced and boundary conditions used, can be found in Hubeny (1988).

The hydrostatic equilibrium equation

TLUSTY uses a generalisation of the hydrostatic equation:

$$dP/dm = g, \quad (\text{B.19})$$

where P is the pressure, m is the mass and g is the gravity. Now,

$$P = p_{\text{gas}} + p_{\text{rad}} + p_{\text{turb}}. \quad (\text{B.20})$$

In TLUSTY, these contributions to the pressure are defined by:

$$p_{\text{gas}} = nkT \quad (\text{B.21})$$

$$p_{\text{rad}} = \frac{4\pi}{c} \int K_{\nu} d\nu \quad (\text{B.22})$$

$$p_{\text{turb}} = (1/2)\rho v_{\text{turb}}^2 \quad (\text{B.23})$$

where these are the gas, radiative and turbulent pressures respectively, and the K -integral, K_{ν} , is defined in eq. B.6. Here, n is the particle number density and k is the Boltzmann constant.

The radiative equilibrium equation

The radiative equilibrium equation arises from the application of conservation of energy to the flow of energy upward through the stellar photosphere. TLUSTY uses two different forms of the radiative equilibrium equation, one an integral equation, the other a differential equation. The standard integral form is:

$$\int_0^{\infty} (\kappa_{\nu} J_{\nu} - S_{\nu}) d\nu = 0, \quad (\text{B.24})$$

while the differential form is:

$$\int_0^{\infty} \frac{dK_{\nu}}{d\tau_{\nu}} d\nu = \frac{\sigma}{4\pi} T_{\text{eff}}^4 \quad (\text{B.25})$$

Hubeny (1988) finds that the differential form is more accurate at large depths, while the integral form is preferable for small depths.

The statistical equilibrium equations

The equations of statistical equilibrium (or rate equations) are used to calculate the actual occupation numbers of the bound and free states of atoms in stellar atmospheres. The general form is derived in Mihalas (1978), p 127, and the application of these equations to model stellar atmosphere generation can be found in Mihalas (1978) p 137-145, and Hubeny (1988).

Application in TLUSTY

The reader is referred to Hubeny (1988) for a complete description of TLUSTY, from which this *précis* is derived, and also to Section 5.6.1. TLUSTY computes model stellar atmospheres assuming a plane-parallel, horizontally homogeneous atmosphere in radiative and hydrostatic equilibrium. It allows for departures from LTE for a set of occupation numbers of selected atomic and ionic energy levels.

The set of equations comprising radiative transfer, hydrostatic equilibrium, radiative equilibrium and statistical equilibrium is highly coupled and non-linear. TLUSTY solves this set of equations using the complete linearization technique pioneered by Auer & Mihalas (1969), which in essence involves the discretization of the equation set by depth and frequency. This allows iterative solutions to be found by the use of a different set of linear equations for corrections to the values of all quantities from the previous iteration.

With TLUSTY, computer time is saved by the introduction of so-called fixed-option atomic transitions, which are treated exactly but are not linearized. The program offers several options to avert divergences. Additionally, the program can allow options which accelerate convergence of the complete linearization iterations, based on a set of the equivalent two-level-atom procedures for selected atomic transitions performed between two consecutive iterations.

The synthetic spectrum

The calculation of the synthetic spectrum from the model atmosphere is achieved by expanding the flux integral (eq. B.7) in spherical polar coordinates and assuming no azimuthal dependence in I_ν . The emergent flux in a line at frequency ν be calculated using:

$$F_\nu = 2\pi \int_{-\infty}^{\infty} S_\nu E_2(\tau_\nu) \frac{\kappa_\nu \tau_0 d \log \tau_\nu}{\kappa_0 \log e}. \quad (\text{B.26})$$

Here, the surface flux is the sum of the source function (S_ν) at each depth multiplied by an extinction factor, E_2 , appropriate to that depth; the integral is evaluated over all appropriate depths. The optical depth scales are related by

$$dx = d\tau_\nu / \kappa_\nu \rho = d\tau_0 / \kappa_0 \rho$$

where κ_ν is the mass absorption coefficient, τ_ν is the optical depth, and κ_0 and τ_0 are the same quantities at some reference wavelength used in the iteration of the spectrum. In LTE, $S_\nu(\tau_0) = B_\nu[T(\tau_0)]$.

Appendix C

Details of TLUSTY and SYNSPEC input and output files

All input and output files are in ASCII format.

TLUSTY195

- Input files:
 - **Unit 5:** Main control data. This file contains the values of T_{eff} and $\log g$, the LTE/LTGRAY switch, the name of the file that details the non-standard parameters (of which there are about 90, ranging from auxiliary physical parameters to flags for selecting the treatment of the statistical equilibrium equation), the number of frequency points to read (these describe the continua), the filenames of the explicit ions used in the calculation of the opacities, the filenames containing the data for the explicit ions (including all energy levels, bound-free transitions and bound-bound transitions);
 - **Unit 8:** Starting model atmosphere. This is not needed if the model being calculated is the initial LTE model atmosphere - in this case the input model atmosphere is assumed grey (i.e. κ_{ν} is independent of ν).

A sample Unit 5 input file for a simple LTE model atmosphere with $T_{\text{eff}} = 35,000$ K, $\log g = 4$, composed of H and He only, is shown below:

```
35000. 4.0      ! TEFF, GRAV
T T           ! LTE, LTGRAY
''           ! no change of general non-standard parameters
```

```

*-----
* frequencies
50                ! NFREAD
*-----
* data for atoms
*
2                ! NATOMS
* mode abn modpf
  2  0  0
  2  0  0
*-----
* data for ions
*
*iat   iz   nlevs  ilast  ilvlin  nonstd  typion  filei
*
  1    0    9      0    100     0    ' H 1'  'h1.dat'
  1    1    1      1     0      0    ' H 2'  ' '
  2    0   14      0    100     0    'He 1'  'he1.dat'
  2    1   14      0    100     0    'He 2'  'he2.dat'
  2    2    1      1     0      0    'He 3'  ' '
  0    0    0     -1     0      0    '   '  ' '
*
* end

```

• Output files:

- **Unit 6:** Standard output. This is a general log of the model construction procedure in which tables display input data and performance messages;
- **Unit 7:** Condensed, machine-readable model atmosphere, for use as the input to another run of TLUSTY or for use as the input Unit 8 with SYNSPEC;
- **Unit 9:** Convergence log. This file is very important because it contains the information on whether the model converged or not;
- **Unit 10:** Performance and error log.

SYNSPEC42

SYNSPEC42 has five basic modes of operation, controlled by the switch **IMODE**. These modes are (Hubeny & Lanz 1997):

- **IMODE = 0**: Normal synthetic spectrum (identification table and emergent flux);
- **IMODE = 1**: Detailed profiles of a few individual lines;
- **IMODE = 2**: Emergent flux in the continuum + hydrogen and helium lines;
- **IMODE = -1**: Line identification table only - a list of lines which contribute to the opacity at a given wavelength;
- **IMODE = -2**: The “iron curtain” option, detailed in Section 5.6.2.

The **IMODE** switch is located in Unit 55.

- Input files:
 - **Unit 5**: Same main control data used for TLUSTY;
 - **Unit 55**: Basic parameters for the synthetic spectrum including the LTE/NLTE switch, the standard depth parameter (the depth at which the continuum optical depth is of order unity), the start and end wavelengths of the spectrum, the wavelength scale, a switch giving the name of the file containing new chemical abundances if necessary, etc;
 - **Unit 8**: Input mode atmosphere (TLUSTY Unit 7);
 - **Unit 19**: The line list, which in the *IUE* spectral range contains about 185 000 lines.
 - Optional input files, of which there are 9, containing data for detailed line profiles, changes in chemical composition etc.

A sample Unit 55 input file containing the basic parameters for a simple H/He only synthetic spectrum in the wavelength range 1000 - 2200 Å, is shown below:

```
2 46 0          !IMODE, IDSTD, IPRIN
1 0 0 1        !INPUT MODEL (1=TLUSTY), INTRPL, ICHANGE, ICHEMC
0              !IOPHLI
1 0 0 0 1     !IFREQ, INLTE, ICONTL, INLIST, IFHE2
0 0 0         !IHYRPR, IHEIPR, IHE2PR
```

```
1000 2200 5 10 1.d-4 0.1 !ALAMO,ALAST,CUTOFO,CUTOFFS,RELOP,SPACING (A)
1. !VTB
10 0.1 1 ! NMUO, ANGO, IFLUX
```

- Output files

- **Unit 6:** Standard output, a general log of the procedure;
- **Units 7 and 17:** Emergent flux of the spectrum and theoretical continuum;
- **Units 12 and 14:** Line identification tables;
- **Unit 16:** Approximate equivalent widths of the lines;
- **Optional Units 10 and 18:** emergent specific intensities for the spectrum and continuum.

On output from SYNSPEC42, the synthetic spectrum is ready for rotational and instrumental convolution using ROTIN4.

Appendix D

Acronyms used

ALI — accelerated lambda iteration

ASCA — Advanced Satellite for Cosmology and Astrophysics (formerly ASTRO-D)

BL — boundary layer

CL — complete linearization

CTIO — Cerro Tololo Inter-American Observatory (Chile)

CV — cataclysmic variable

DN — dwarf nova

EPIC — European Photon Imaging Camera (*XMM* instrument, of which there are two types with different sensitivity and readout characteristics: the EPIC MOS [Metal Oxide Semiconductor] and the EPIC pn)

EUVE — Extreme Ultraviolet Explorer

EXOSAT — European X-ray Observatory Satellite

FOS — Faint Object Spectrograph (*HST* instrument)

GSOC — German Science Operations Centre

HRI — High Resolution Imager (*ROSAT* instrument)

HST — Hubble Space Telescope

IUE — International Ultraviolet Explorer

IUEFA — *IUE* Final Archive

LEDAS — Leicester Database and Archive Service

LMXB — Low Mass X-ray Binary

MAMA — Multi-Anode Microchannel Array (*HST* instrument)

MCP — Microchannel Plate

MEM — Maximum Entropy Method

(N)LTE — (non-) Local Thermodynamic Equilibrium

NL — novalike variable
NMCV — non-magnetic cataclysmic variable
OM — Optical Monitor (*XMM* instrument)
PPEM — Physical Parameter Eclipse Mapping
RGS — Reflection Grating Spectrograph (*XMM* instrument)
ROSAT — Röntgen Satellite
SAAO — South African Astronomical Observatory
STIS — Space Telescope Imaging Spectrograph (*HST* instrument)
SUI — Spectrum Under the Influence (of an emitting or absorbing body)
TOAD — Tremendous Amplitude Outburst Dwarf nova, the WZ Sge subclass.
VSS RAS NZ — Variable Star Section of the Royal Astronomical Society of New Zealand
WD — white dwarf
WFC — Wide Field Camera (*ROSAT* instrument)
XMM — X-ray Multi-mirror Mission
XRT — the X-ray Telescope on *ROSAT*

References

- Aeur L.H., Mihalas D., 1969, *ApJ*, 158, 641.
- Allan D.J., Vallance R.J., 1995, *ASTERIX — X-ray data processing system*, STARLINK User Note 98.
- Anderson L.S., 1989, *ApJ*, 339, 558.
- Applegate, J.H., 1992, *ApJ*, 385, 621.
- Arnaud K.A., 1996, in *Astronomical Data Analysis Software and Systems V*, eds. Jacoby G. and Barnes J., ASP Conf. Series volume 101.
- Baptista R., Steiner J.E., 1991, *A&A*, 249, 284.
- Baptista R., Steiner J.E., 1993, *A&A*, 277, 331.
- Baptista R., Horne K., Wade R.A., Long K.S., Rutten R.G.M., 1998, *MNRAS*, 298, 1079.
- Baptista R., Catalan S., Horne K., Zilli D., 1998, *MNRAS*, 300, 233
- Barstow M.A., Fleming T.A., Diamond C.J., Finley D.S., Sansom A.E., Rosen S.R., Koester D., Holberg J.B., Marsh M.C., Kidder K., 1993, *MNRAS*, 264, 16
- Bath G.T., 1969, *ApJ*, 158, 571.
- Bath G.T., 1975, *MNRAS*, 171, 311.
- Bath G.T., Evans W.D., Pringle J.E., 1974, *MNRAS*, 166, 113.
- Beasley D., Bull D.R., Martin R.R., 1993a, *University Computing*, 15(2), 58.
- Beasley D., Bull D.R., Martin R.R., 1993b, *University Computing*, 15(4), 170.
- Belloni T., Verbunt F., Beuermann K., Bunk W., Izzo C., Kley W., Pietsch W., Ritter H., Thomas H.C., Voges W., 1991, *A&A*, 246, L44.
- Berriman G., 1987, *MNRAS*, 228, 729.
- Billington I., Marsh T.R., Horne K., Cheng F.-H., Thomas G., Bruch A., O'Donoghue D., Eracleous M., 1996, *MNRAS*, 279, 1274.
- Breedon L., et al. (The FTOOLS Group) 1997, *The User's Guide to FTOOLS*, High-Energy Astrophysics and Space Research Centre, NASA-GSFC.
- Briel U.G., Pfeffermann E., 1995, *SPIE (Soft X-ray Optics and Technology)*, 2518, 120.
- Briel U.G., et al. 1996, *ROSAT User's Handbook*, Max-Planck-Institut für extraterrestrische Physik, 85740 Garching, Germany.
- Bryan R.K., Skilling J., 1980, *MNRAS*, 191, 69.
- Burch S.F., Gull S.F., Skilling J., 1983, *Comp. Vis. Graph. Im. Proces.*, 23, 113.
- Cannon C.J., 1973b, *ApJ*, 185, 621.
- Catalán M.S., Horne K., Cheng F.-H., Marsh T.R., Hubeny I., 1998, in *ASP Conf. Ser. 137, Wild Stars in the Old West*, eds. S. Howell, E. Kuulkers, C. Woodward, ASP San Francisco.
- Cheng F.-H., Sion E.M., Horne K., Hubeny I., Huang m., Vritelek S.D., 1997a, *AJ*, 114, 1165.
- Cheng F.-H., Sion E.M., Szkody P., Huang M., 1997b, *ApJ*, 484, L149.
- Cook M.C., 1985, *MNRAS*, 215, 211.
- Córdova F.A., Mason K.O., *ApJ*, 260, 716.
- Córdova F.A., Mason K.O., 1984a, *MNRAS*, 206, 879.

- David L.P., Harnden F.R., Kearns K.E., Zombeck M.V., 1991, *ROSAT* Mission Description, Appendix F.
- David L.P., Harnden F.R., Harris D.E., Kearns K.E., Prestwich A., Primini F.A., Silverman J.D., Snowden S.L., Zombeck M.E., 1997, *ROSAT* HRI Calibration Report, Harvard-Smithsonian Centre for Astrophysics.
- Denby M., McGale P., 1995, WFCPACK — *ROSAT* Wide Field Camera data reduction, STAR-LINK User Note 62.5.
- Dreizler S., Werner K., 1993, in *Lecture Notes in Physics*, 401, *The Atmospheres of Early Type Stars*, eds. U. Herber, C.S. Jeffery, Springer-Verlag, Berlin.
- Drew J.E., Verbunt F., 1985, *MNRAS*, 213, 191.
- Eracleous M., Halpern J., & Patterson J., 1991a, *ApJ*, 370, 330.
- Eracleous M., Halpern J., & Patterson J., 1991b, *ApJ*, 382, 290.
- Finley D.S., Koester D., Basri G., 1997 *ApJ*, 488, 375.
- Fleming T.A., Snowden S.L., Pfeffermann E., Briel U., Greiner J., 1996, *A&A*, 316, 147.
- Frank J., King A.R., Raine D.J., 1992, *Accretion Power in Astrophysics*, 2nd ed., Cambridge University Press, Cambridge.
- Gallagher J.S., Code A.D., 1974, *ApJ*, 189, 303.
- Gänsicke B.T., Beuermann K., 1996, *A&A*, 309, L47.
- Gänsicke B.T., Koester D., 1999, *A&A*, 346, 151.
- Gizis J.E., 1998, *AJ*, 115, 2053.
- Gray D.F., 1992, *The Observation and Analysis of Stellar Photospheres*, Cambridge Univ. Press, Cambridge.
- Gull S.F., Daniel G.J., 1978, *Nature*, 272, 686.
- Hakala P.J., 1995, *A&A*, 296, 164.
- Hamada T., Salpeter E.E., 1961, *ApJ*, 134, 683.
- Harlaftis E.T., Hassall, B.J.M., Naylor T., Charles P.A., Sonneborn G., 1992a, *MNRAS*, 257, 607.
- Harlaftis E.T., Naylor T., Hassall B.J.M., Charles P.A., Sonneborn G., Bailey J., 1992b, *MNRAS*, 259, 593.
- Harlaftis E.T., Steeghs D., Horne K., Martín E., Magazzú A., 1999, *MNRAS*, 306, 348.
- Hartmann H.W., Wheatley P.J., Heise J., Mattei J.A., Verbunt F., 1999, *A&A*, 349, 558.
- Hassall B.J.M., la Dous C., 1996, in *IAU Colloquium No. 158: Cataclysmic Variables and Related Objects*, eds. A. Evans, Janet H. Wood, Kluwer Acad. Pub., Dodrecht.
- Heber U., Napiwotzki R., Reid I.N., 1997, *A&A*, 323, 819.
- Hessman F.V., Mantel K.-H., Barwig H., Schoembs R., 1992, *A&A*, 263, 147.
- Hoare M.G., Drew J.E., 1991, *MNRAS*, 249, 452.
- Hoare M.G., Drew J.E., 1993, *MNRAS*, 260, 647.
- Holcomb S., Caillault J.-P., Patterson J., 1994, *BAAS*, 185, #21.17.
- Horne K., 1985a, *MNRAS*, 213, 129.
- Horne K., 1986, *PASP*, 98, 609.

- Horne K., Cook M.C., 1985, MNRAS, 214, 307.
- Horne K., Marsh T.R., Cheng F.-H., Hubeny I., Lanz T., 1994, ApJ, 426, 294.
- Hoshi R., 1979, Prog. Theor. Phys., 61, 1307.
- Howell S.B., Ciardi D.R., Szkody P., van Paradijs J., Kuulkers E., Cash J., Sirk M., Long K.S., 1999, PASP, 111, 342.
- Huang M., Sion E.M., Hubeny I., Cheng F.-H., Szkody P., 1996, AJ, 111, 2386.
- Hubeny I., 1988, Computer Physics Comm., 52, 103.
- Hubeny I., Hummer D.G., Lanz T., 1994, A&A, 282, 151.
- Hubeny I., Lanz T., 1992, A&A, 262, 501.
- Hubeny I., Lanz T., Jeffery C.S., 1994, in Newsletter on Analysis of astronomical Spectra No. 20, ed. C.S. Jeffery, St. Andrews Univ.
- Hubeny I., Lanz T., 1995, ApJ, 439, 875.
- Hubeny I., Lanz T., 1997, SYNSPEC — A User's Guide, unpublished.
- Hubeny I., 1998, private communication.
- Hummer D.G., Rybicki G.B., 1982, ApJ, 263, 925.
- Iben I., 1982, ApJ, 259, 244.
- Kallman T.R., Jensen K.A., 1985, ApJ, 299, 277.
- King A.R., 1997, MNRAS, 288, L16.
- King A.R., 1998, MNRAS, 296, L45.
- Kiplinger A.L., Sion E.M., Szkody P., 1991, ApJ, 366, 569.
- Kley W., 1991, A&A, 247, 95.
- Krezeminski W., Vogt, N., 1985, A&A, 144, 124.
- Kruszewski A., 1966, Adv. Astr. Astrophys., 4, 233.
- Kudritzki R.P., Hummer D.G., 1990, ARA&A, 28, 303.
- Kurucz R.L., 1970, Smithsonian Astrophys. Obs. Report No. 309.
- la Dous C., 1990, Sp. Sci. Rev., 52, 203.
- Lanz T., Hubeny I., 1995, ApJ, 439, 905.
- Lanz T., Hubeny I., Cheng F.-H., Horne K., 1992, BAAS, 181, #50.04.
- Lasota J.-P., Kuulkers E., Charles P., 1999, MNRAS, 305, 473.
- Livio M., Pringle J.E., 1992, MNRAS, 259, 23p.
- Livio M., Pringle J.E., 1998, ApJ, 505, 339.
- Long K.S., Blair W.P., Bowers C.W., Davidsen A.F., Kriss G.A., Sion E.M., Hubeny I., 1993, ApJ, 405, 327.
- Long K.S., Sion E.M., Huang M., Szkody P., 1994a, ApJ, 424, L49.
- Long K.S., Wade R.A., Blair W.P., Davidsen A.F., Hubeny I., 1994b, ApJ, 426, 704.
- Long K.S., Mauche C.W., Raymond J.C., Szkody P., Mattei J.A., 1996b, ApJ, 469, 841.
- Long K.S., Gilliland R., 1998, ApJ, 511, 916.
- Long K.S., 1999, to be published in Proceedings of Cataclysmic Variables: A 60th Birthday Symposium in Honour of Brian Warner (astro-ph/9907010).

- Lynden-Bell D., Pringle J.E., 1974, MNRAS, 168, 603.
- Marsh M.C., Barstow M.A., Buckley D.A., Burleigh M.R., Holberg J.B., Koester D., O'Donoghue D., Penney A.J., Sansom A.E., 1997, MNRAS, 287, 705
- Mateo M., Szkody P., 1984, AJ, 89, 863.
- Mason K.O., Córdova F.A., Watson F.G., King A.R., 1988, MNRAS, 232, 779.
- Mason K.O., Drew J.E., Knigge C., 1997, MNRAS, 290, L23.
- Mauche C.W., Raymond J.C., 1987, ApJ, 323, 690.
- Mauche C.W., Raymond J.C., Mattei J., 1995, ApJ, 446, 842.
- Mauche C.W., 1996, in *Cataclysmic Variables and Related Objects*, eds. A. Evans, J.H. Wood, Kluwer Academic Press, Dodrecht.
- Mauche C.W., 1997a, ApJ, 476, L85.
- Mauche C.W., 1997b, in *Proceedings of the 13th North American Workshop on Cataclysmic Variables*, eds. S. Howell, E. Kuulkers, C. Woodward, ASP, San Francisco.
- Mauche C.W., Raymond J.C., 1997, in *Cosmic Winds and the Heliosphere*, eds. J.R. Jokipii, C.P. Sonett, M.S. Giampapa, Univ. of Arizona Press, Tucson.
- Mewe R., Gonschild E.H.B.M., van den Oord G.H.J., 1985, A&AS, 62, 197.
- Meyer F., 1984, A&A, 131, 303.
- Meyer F., Meyer-Hofmeister E., 1981, A&A, 104, L10.
- Meyer F., Meyer-Hofmeister E., 1983, A&A, 128, 420.
- Mihalas D., 1978, *Stellar Atmospheres*, Freeman & Co., San Francisco.
- Mineshige S., Shields G.A., 1990, ApJ, 351, 47.
- Morales-Reuda L., Marsh, T., Billington I., 1999, astro-ph/9911088 (accepted for publication in MNRAS).
- Mukai K., 1993, *Legacy*, 3, 21.
- Mukai K., Shiokawa K., 1993, ApJ., 418, 863.
- Mukai K., Wood J.H., Naylor T., Schlegel E.M., Swank J.H., 1997, ApJ, 475, 812.
- Murray J.R., 1996, MNRAS, 279, 402.
- Murray J.R., 1998, MNRAS, 297, 323.
- Narayan R., Popham R., 1993, *Nature*, 362, 820.
- Naylor T., 1989, MNRAS, 238, 587.
- Naylor T., Charles P.A., Hassall B.J.M., Bath G.T., Berriman G., Warner B., Bailey J., Reinsch K., 1987, MNRAS, 229, 183.
- Naylor T., Bath G.T., Charles P.A., Hassall B.J.M., Sonneborn G., van der Woerd H., van Paradijs J., 1988, MNRAS, 231, 237.
- Naylor, T., la Dous, C., 1997, MNRAS, 290, 160.
- Naylor T., 1998, private communication.
- Neustroev V.V., Borisov N.V., 1998, A&A, 336, L73.
- Oke J.B., 1974, ApJSS, 27, 21.
- Osaki Y., 1974, PASJ, 26, 429.

- Osaki Y., 1985, *A&A*, 144, 369.
- Osaki Y., 1996, *PASP*, 108, 39.
- Osaki Y., 1989b, in *Theory of Accretion Disks*, eds. F. Meyer, W.J. Duschl, J. Frank, E. Meyer-Hofmeister, Kluwer Academic Press, Dodrecht, p183.
- Osterbrock D.E., 1989, *Astrophysics of Gaseous Nebulae and Active Galactic Nuclei*, Oxford Univ. Press, Oxford.
- Paczýnsky B., 1977, *ApJ*, 216, 822.
- Paczýnski B., Ziolkowski J., Zytkow A., 1969, in *Mass loss from Stars*, ed. M.Rack, Reidel, Dordrecht.
- Panek R., Holm A.V., 1984, *ApJ*, 277, 700.
- Patterson J., 1984, *ApJSS*, 54, 443.
- Patterson J., Raymond J.C., 1985a, *ApJ*, 292, 535.
- Patterson J., Raymond J.C., 1985b, *ApJ*, 292, 550.
- Patterson J., Kepp J., Shambrook A., Thomas E., Halpern J.P., Skillmand D.R., Harvey D.A., Vanmunster T., Retter A., Fried R., Bucklet D., Nogami D., Kato T., Baba H., 1997b, *PASJ*, 109, 1100.
- Pfeffermann E., Briel U.G., 1986, *SPIE (Soft X-ray Optics and Technology)*, 97, 208.
- Popham R., Narayan R., 1995, *ApJ*, 442, 337.
- Potter S.B., Hakala P.J., Cropper M., 1998, *MNRAS*, 297, 1261P.
- Pounds K.A., et al., 1993, *MNRAS*, 260, 77.
- Pratt G.W., Hassall B.J.M., Naylor T., Wood J.H., *MNRAS*, 307, 413.
- Pratt G.W., Hassall B.J.M., Naylor T., Wood J.H., Patterson J., 1999, *MNRAS*, 309, 847.
- Press W.H., Teukolsky S.A., Vetterling W.T., Flannery B.P., *Numerical Recipes (2nd edition)*, CUP, Cambridge.
- Pringle J.E., 1977, *MNRAS*, 178, 195.
- Pringle J.E., 1985, in *Interacting Binaries*, eds. J.E. Pringle, R.A. Wade, CUP, Cambridge.
- Pringle J.E., Savonije G.J., 1979, *MNRAS*, 187, 777.
- Reiter J., Pfeleiderer J., 1986, *A&A*, 166, 381.
- Richman H.R., 1996, *ApJ*, 462, 404.
- Ritter H., Kolb U., 1998, *A&ASS*, 129, 83.
- Robinson E.L., Wood J.H. Bless R.C., Clemens J.C., Dolan J.F., Elliot J.I., Nelson, M.J., Percival J.W., Taylor J., van Citters G.W., Zhang E., 1995, *ApJ*, 443, 295.
- Robinson E.L., Wood J.H., Wade R.A., 1999, *ApJ*, 514, 952.
- Rodríguez-Pascual P.M., Gonzalez-Riestra R., Schartel N., Wamsteker W., 1999, *A&ASS*, 139, 183.
- Rutten R.G.M., 1998, *A&ASS*, 127, 581.
- Rutten R.G.M., van Paradijs J., Tinbergen J., 1992a, *A&A*, 260, 213.
- Rutten R.G.M., Kuulkers E., Vog, N., van Paradijs J., 1992b, *A&A*, 265, 159.
- Rybicki G.B., 1972, in *Line Formation in the Presence of Magnetic Fields*, eds. R.G. Athy, L.L.

- House, G. Newkirk, High Altitude Obs., Boulder.
- Scharmer G., 1982, ApJ, 249, 720.
- Schoembs R., 1986, A&A, 158, 233.
- Schoembs R., Hartmann, K., 1983, A&A, 128, 37.
- Schoembs R., Dreier, H., Barwig, H., 1987, A&A, 181, 50.
- Sfeir D.M., Lallement R., Crifo F., Welsh B.Y., 1999, A&A, 346, 785.
- Shafter A.W., Szkody P., Liebert J., Penning W., Bond H., Grauer A., 1985, ApJ, 290, 707.
- Shafter A.W., Wheeler J.C., Cannizzio J.K., 1986, ApJ, 305, 261.
- Shakura N.I., Sunyaev R.A., 1973, ApJ, 24, 337.
- Shore S.N., 1992, in ASP Conf. Ser. 22, Nonisotropic and Variable Outflows from Stars, eds. L. Drissen, C. Leitherer, A Nota, ASP, San Francisco.
- Sims M.R., Barstow M.A., Pye J.P., Wells A., Willingale R., 1990, Opt. Engineering, 29, 649.
- Singh K.P., Drake S.A., Gotthelf E.V., White N.E., 1999, ApJ, 512, 874.
- Sion E.M., 1999, PASP, 111, 532.
- Sion E.M., Szkody P., 1991, in IAU Colloquium No. 122: Physics of Classical Novae, eds. A. Cassatella, R. Viotti, Springer-Verlag, Berlin.
- Sion E.M., Long K.S., Szkody P., Huang M., 1994, ApJ, 430, L53.
- Sion E.M., Cheng F.-H., Long K.S., Szkody P., Huang M., Gilliland R., Hubeny I., 1995a, ApJ, 439, 957.
- Sion E.M., Huang M., Szkody P., Cheng F.-H., 1995b, ApJ, 445, L31.
- Sion E.M., Cheng F.-H., Long K.S., Szkody P., Gilliland R., Huang M., Hubeny I., 1995c, ApJ, 439, 957.
- Sion E.M., Cheng F.-H., Sparks W., Szkody P., Hubeny I., 1997, ApJ, 480, L17.
- Sion E.M., Cheng F.-H., Szkody P., Sparks W., Gänsicke B., Mattei J., 1998a, ApJ, 496, 449.
- Skilling J., Bryan R.K., 1984, MNRAS, 211, 111.
- Smak J., 1992, Acta Astr., 42, 323.
- Sparks W.M., Sion E.M., Starrfield S.G., Austin S., 1993, Ann. Isr. Phys. Soc. 10, 96.
- Starrfield S.G., 1993, in The Realm of Interacting Binary Stars, eds., J. Sahade, G. Mcluskay, Y. Kondo, Kluwer Acad. Press., Dordrecht.
- Starrfield S.G., Truran J., Sparks W.M., Kutter S., 1972, ApJ, 176, L69.
- Steehgs D., Horne K., Marsh T., Donati J.F., 1996, MNRAS, 281, 626.
- Steehgs D., Harlaftis E.T., Horne K., 1997, MNRAS, 270, L28.
- Szkody P., Sion E.M., 1989, in White Dwarfs, ed. G Wenger, Springer-Verlag, Berlin.
- Szkody P., Long K.S., Sion E.M., Raymond J.C., 1996, ApJ, 469, 834.
- Szkody P., Hoard D.W., Sion E.M., Howell S.B., Cheng F.-H., Sparks W.M., 1998, ApJ, 497, 928.
- Tanaka Y., Inoue H., Holt S.S., 1994, PASJ, 46, L37.
- Tylenda R., 1981a, Acta Astron., 31, 127.
- van der Woerd H., Heise J., Bateson F.M., 1986, A&A, 156, 252.
- van Teeseling A., Verbunt F., Heise J., 1993, A&A, 270, 159.

- van Teeseling A., Verbunt F., 1994, *A&A*, 219, 519.
- van Teeseling A., Beuermann K., Verbunt F., 1996, *A&A*, 315, 467.
- van Teeseling A., 1997, *A&A*, 319, L25.
- Verbunt F., 1987, *A&ASS*, 71, 339.
- Verbunt, F., Bunk W.H., Ritter H., Pfeffermann E., 1997, *A&A*, 327, 602.
- Voges W., et al., 1999, *A&A*, 349, 389.
- Vogt N., 1982, *ApJ*, 252, 563.
- Vogt N., Schoembs R., Krzeminski W., Pedersen H., 1981, *A&A*, 94, L29.
- Vrielmann S., Horne K., Hessman F.V., 1999, *MNRAS*, 306, 766.
- Wade R.A., Ward M.J., 1985, in 'Interacting binary stars', eds. J.E. Pringle, R.A. Wade, CUP, Cambridge.
- Wade R.A., Cheng F.-H., Hubeny I., 1994a, *BAAS*, 184, #46.05.
- Wade R.A., Hubeny I., Polidan R.S., 1994b, in *Interacting Binary Stars*, ASP Conf. Ser., 56.
- Warner B., 1987a, *MNRAS*, 227, 23.
- Warner B., O'Donoghue D., 1988, *MNRAS*, 233, 705.
- Warner B., 1995, *Cataclysmic Variable Stars*, Cambridge Univ. Press, Cambridge, UK.
- Webbink R.F., 1990a, in 'Accretion Powered Compact Binaries', ed. C.W. Mauche, CUP, Cambridge.
- Werner K., 1986, *A&A*, 161, 177.
- Werner K., Dreizler S., 1999, in press in *J. Comp. App. Math., Comp. Astrophysics*, eds. H. Riffert, K. Werner (astro-ph/9906130)
- Wheatley P.J., Verbunt F., Belloni T., Watson M.G., Naylor T., Ishida M., Duck S.R., Pfeffermann E., 1996, *A&A*, 307, 137.
- White N.E., Mason K.O., 1985, *Sp. Sci. Rev.*, 40, 167.
- Whitehurst R., 1988a, *MNRAS*, 232, 35.
- Whitehurst R., 1988b, *MNRAS*, 233, 529.
- Whitehurst R., King A.R., 1991, *MNRAS*, 249, 25.
- Wood J.H., 1994, in 'Interacting Binary Stars', ed. A.W. Shafter, ASP Conf. Ser., 56, p48.
- Wood J.H., Irwin M.J., Pringle J.E., 1985, *MNRAS*, 214, 475.
- Wood J.H., Horne K., Berriman G., Wade R.A., 1989, *ApJ*, 341, 974.
- Wood J.H., Horne K., 1990, *MNRAS*, 242, 606.
- Wood J.H., et al. 1993, in 'Cataclysmic Variables and Related Physics', ed. O. Regev, G. Shaviv, IPP, Bristol.
- Wood J.H., Naylor T., Hassall B.J.M., Ramseyer T., 1995a, *MNRAS*, 273, 772.
- Wood J.H., Naylor T., Marsh T., 1995b, *MNRAS*, 274, 31.
- Zanstra H., 1931, *Publ. Dom. Astrophys. Obs.*, 4, 209.

An eclipse of the X-ray flux from the dwarf nova OY Carinae in quiescence

Gabriel W. Pratt,¹ B. J. M. Hassall,¹ T. Naylor² and Janet H. Wood²

¹Centre for Astrophysics, University of Central Lancashire, Preston PR1 2HE

²Department of Physics, Keele University, Keele ST5 5BG

Accepted 1999 March 1. Received 1999 February 26; in original form 1999 January 26

ABSTRACT

We present a phase-resolved *ROSAT* HRI X-ray light curve of the dwarf nova OY Car in quiescence. The X-ray flux is eclipsed at the same time as the optical eclipse of the primary, and the region of X-ray emission is comparable in size to the white dwarf. We use subsequent optical observations to update the orbital ephemeris of the system.

Key words: accretion, accretion discs – binaries: eclipsing – stars: individual: OY Car – novae, cataclysmic variables – X-rays: stars.

1 INTRODUCTION

Many non-magnetic cataclysmic variables (CVs), binary stars in which mass transfer is occurring between a Roche lobe filling secondary star and a white-dwarf primary, have been detected in X-rays. Steady-state theory suggests that half the accretion luminosity is released in the accretion disc of such a system, whilst the other half is released in the region of the boundary layer, where the material of the accretion disc is decelerated to match the surface velocity of the primary. In quiescence, the boundary layer is believed to be an optically thin gas emitting relatively hard ($\sim 2\text{--}20\text{ keV}$) X-rays. In outburst, the accretion rate rises significantly, and the X-ray region becomes optically thick, now emitting softer ($\sim 0.1\text{--}1.0\text{ keV}$) X-rays (Pringle & Savonije 1979). Provided the white dwarf is not spinning rapidly, theory predicts that the boundary layer is the dominant source of the X-ray emission in non-magnetic CVs (Pringle 1977).

The dwarf novae are a subset of the non-magnetic CVs which are observed to undergo outbursts of $\sim 2\text{--}5$ mag on time-scales of weeks to years. SU UMa dwarf novae also undergo additional infrequent superoutbursts, brighter by ~ 1 mag and lasting ~ 5 times longer than normal outbursts. See Warner (1995) for a comprehensive review.

OY Carinae is among the best-studied of the SU UMa dwarf novae, mainly because the favourable inclination of the system allows eclipses of the white dwarf, bright spot and accretion disc. In principle, the simplest observational test to determine the source of the X-rays is to observe systems in which the inclination is such that these full eclipses occur. Then if the X-ray flux is eclipsed, as it should be with a simple equatorial boundary layer around the white dwarf, the location of the X-ray source can be pinpointed to a relatively high degree of accuracy by comparing the timings of the X-ray eclipse with optical light curves.

There are several high-inclination dwarf novae that can be tested in this way. The *ROSAT* observation of HT Cas in a low

state by Wood et al. (1995a) showed that the X-ray source was indeed eclipsed, and that as expected, the X-ray eclipse is coincident with the optical eclipse of the white dwarf. Follow-up observations of the system in quiescence using both *ASCA* and *ROSAT* (Mukai et al. 1997) again showed an eclipse. The high time resolution of the *ASCA* data even allowed Mukai et al. (1997) to establish an approximate upper-boundary-layer dimension of $\sim 1.15R_{\text{wd}}$. An X-ray eclipse has also been found in *ROSAT* observations of the quiescent Z Cha (van Teeseling 1997).

In contrast, observations of the high-accretion-rate cases show that X-ray eclipses do not occur. This was the case with the *ROSAT* observations of the nova-like variable UX UMa (Wood, Naylor & Marsh 1995b). Observations of dwarf novae in outburst or superoutburst are difficult owing to their inherent unpredictability; of the high inclination systems, only OY Car has been observed in X-ray in superoutburst, and on both occasions there was no evidence for an eclipse of the X-ray flux (Naylor et al. 1988; Pratt et al., in preparation). It appears that in these cases the X-ray emitting boundary layer is obscured, and the X-rays we see have an origin in a more extended, coronal source. The present challenge is to disentangle the effects of the disc, which becomes considerably thicker in the outburst state (e.g. Robinson et al. 1995, Pratt et al., in preparation), and the increased local absorption resulting from the enhanced accretion, likely to be material in the upper atmosphere of the disc.

Indeed, in the case of OY Car, it is the question of the absorption to the X-ray source that is particularly intriguing. *Hubble Space Telescope* (*HST*) observations in quiescence (Horne et al. 1994) have suggested the existence of significant local absorption owing to disc material veiling the spectrum of the white dwarf, which Horne et al. (1994) dubbed the ‘iron curtain’ after Shore (1992). Horne et al. (1994) modelled this material taking all relevant opacity sources into account, not just the Fe, but found it convenient to refer to the veiling material as the ‘iron

curtain' owing to the prevalence of blended Fe II features in the spectrum.

The aim of these observations is thus two-fold: to determine if the 'iron curtain' in OY Car in quiescence has sufficient column density to extinguish the X-ray flux in the bandpass of the *ROSAT* detectors (0.1–2.5 keV), and if not, to examine whether or not OY Car, like HT Cas and Z Cha, exhibits an X-ray eclipse.

In this paper, we present phase-resolved *ROSAT* X-ray observations of OY Car in quiescence. In Section 2 we describe the optical and X-ray observations and data reduction, in Section 3 we derive an updated orbital ephemeris for the system, in Section 4 we discuss the X-ray data, in Section 5 we discuss our results, and in Section 6 we present our summary and conclusions.

2 OBSERVATIONS AND DATA REDUCTION

2.1 Optical observations

Previous optical and *HST* UV observations of OY Car obtained in 1992 and 1994 (Horne et al. 1994; Pratt et al., in preparation) show that the ephemeris of OY Car as calculated in Wood et al. (1989) had drifted by ~ 40 s at this time. Further observations of OY Car in quiescence were needed to update the ephemeris.

High-speed photometry of OY Car was obtained with the 1.0-m telescope at the South African Astronomical Observatory (SAAO), between 1998 March 3 and 1998 March 9. Our data demonstrated that the system was in quiescence at the time. According to monitoring observations made by the Variable Star Section of the Royal Astronomical Society of New Zealand (VSS RAS NZ), the last superoutburst had reached maximum on 1998 February 10 and the following outburst/superoutburst had not occurred at the time of writing (1998 September). Fig. 1 shows the overall VSS RAS NZ light curve of OY Car covering the period of our optical and X-ray observations. The single-channel SAAO St Andrews Photometer was used with a 16-arcsec aperture at 1-s time resolution. For much of the duration of the observing run, conditions were non-photometric, but as the primary aim of the

run was the updating of the ephemeris, we continued observing through thin cloud. In most cases a *V* filter was used, with occasional observations in difficult conditions made in white light. Sky measurements were taken every 15–20 min, at a position ~ 1 arcmin to the south of the source. A typical eclipse light curve is shown in Fig. 2.

2.2 X-ray observations

OY Car was observed 12 times by the *ROSAT* High Resolution Imager (HRI) for a total of 51.5-ks between 1998 January 14 and 1998 January 23. Information about the individual observations is presented in Table 1, the journal of X-ray observations.

The orbital period of OY Car, at ~ 91 min, is very similar to the orbital period of *ROSAT*. As a consequence of this, the orbital phase of OY Car covered by *ROSAT* precesses by ~ 5 min per satellite orbit, leading to a very similar phase coverage for a set of contiguous observations. Additional difficulties in obtaining the desired orbital phase coverage include Earth occultations and the passage of the satellite through the South Atlantic Anomaly. Our main aim during the course of these observations was sufficient coverage of the eclipse phase (i.e. $-0.25 \leq \phi \leq 0.25$), with additional coverage of the full orbital phase being of secondary importance.

The data were reduced using *ASTERIX* software. For each observation, source counts were extracted from a circular region of radius 50 arcsec. For the determination of the background, we used an annular region centred on the source, with inner and outer radii of 100 and 300 arcsec, respectively. Source and background data were extracted in 1-s bins and the data were then background-subtracted. The resulting background-subtracted total-flux light curves were then corrected for vignetting, dead time and scattering. We then converted all times to Heliocentric Julian Ephemeris Date (HJED).

In addition to extracting the source counts in this way, the

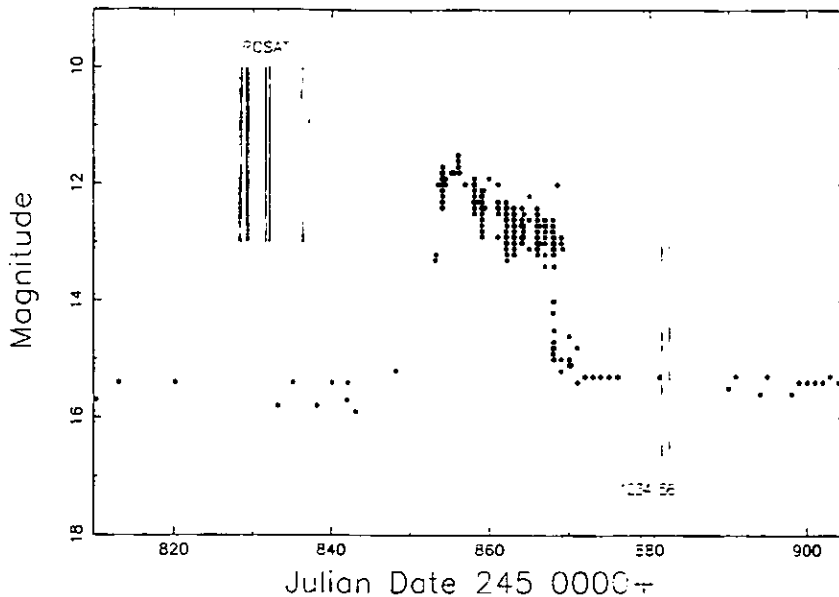


Figure 1. The light curve of OY Car, covering the period of both the *ROSAT* and optical observations. Circles show observations as supplied by the VSS RAS NZ. It can be seen that OY Car actually underwent a superoutburst that reached maximum on 1998 February 10, but had returned to quiescence by the time of our optical observations.

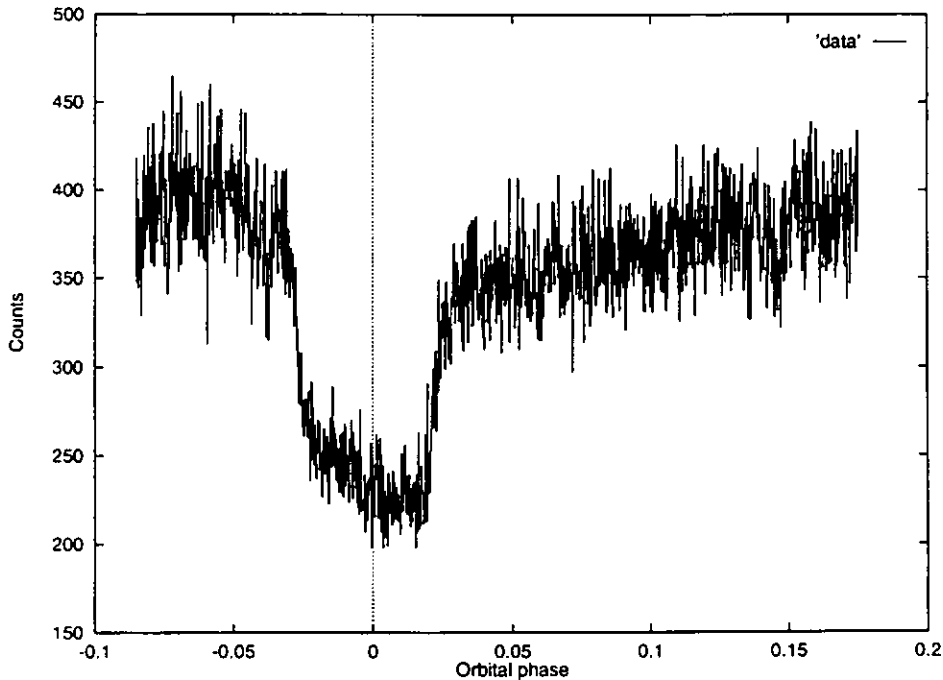


Figure 2. Typical optical light curve (1998 March 4), phased with the ephemeris derived in Section 3.

extracted background data were scaled to the dimensions of the source extraction circle to create a background light curve.

3 THE ORBITAL EPHEMERIS

3.1 Optical-eclipse timing measurements

In all, we observed 12 useful optical eclipses, details of which can be found in Table 2. As we were only interested in eclipse timings, the data-reduction process was simplified considerably. For each eclipse light curve, all times were converted to HJED. The times of mid-eclipse were then calculated automatically using the method described in Wood, Irwin & Pringle (1985). The light curves were first smoothed by passing them through a median filter of width 10 s, roughly a quarter of the duration of the ingress of the white dwarf. Each light curve was then differentiated numerically, and the differential passed through a box car filter of width 42 s. This filter width was chosen as it is the approximate duration of the ingress of the white dwarf (cf. Wood et al. 1989). This filtered derivative was then examined to detect the largest negative and positive points, which correspond to the mid-points of ingress and egress, respectively. Mid-eclipse was then calculated as being the point halfway between the ingress and egress mid-points, i.e. $\phi_0 = (\phi_{wi} + \phi_{we})/2$. The HJED times of mid-eclipse are listed in Table 3.

3.2 Method

In order to update the orbital ephemeris of OY Car, we used published eclipse timings ranging back to 1979 in addition to those timings presented in Table 3.

The $(O-C)$ values were computed with respect to the first linear ephemeris of Wood et al. (1989; this paper also contains a two-part linear ephemeris), and these are plotted in Fig. 3. Eclipse timings from Vogt et al. (1981), Schoembs & Hartmann (1983),

Cook (1985), Schoembs, Dreier & Barwig (1987), Wood et al. (1989), Horne et al. (1994), and Pratt et al. (in preparation) are plotted in addition to the eclipse timings presented here. Where needed, the published eclipse timings were converted to HJED.

Fig. 3 shows the result of a linear least-squares fit represented by the following updated ephemeris (uncertainties quoted in parentheses):

$$\text{HJED} = 2443993.553958(6) + 0.0631209180(2)\text{E}.$$

This linear ephemeris fit to observations over a baseline of 19 yr suggests that the two-part ephemeris calculated in Wood et al. (1989) is unnecessary. A quadratic ephemeris offered no significant improvement to the fit.

We note that the data used by Wood et al. (1989) describes a totally different ephemeris. Unfortunately, the sampling of the data presented here precludes the establishment of a model for the evolution of the ephemeris of OY Car, a common problem with this type of observation. It is known that the ephemerides of both HT Cas and IP Peg have been observed to undergo apparently uncorrelated departures from their assumed linear paths. It is not known what causes these departures, although changes in the radius of the secondary could conceivably provide a mechanism (e.g. Applegate 1992).

This updated ephemeris is used throughout the remainder of this paper for the purposes of phasing the X-ray observations.

4 THE X-RAY ECLIPSE

Fig. 4 shows that the X-ray flux is variable over the duration of the observations. The data cover 10 full eclipses and nine partial eclipses. The mean HRI count rate over the duration of the observations is $(1.60 \pm 0.06) \times 10^{-2} \text{ count s}^{-1}$.

We obtained the mean quiescent X-ray light curve by folding all the available data into 96 phase bins on the orbital period of OY

Table 1. Journal of X-ray observations.

<i>ROSAT</i> Observation ID	Date	HJED start (245 0800+)	Phase coverage	Duration (s)	Source count rate ^a (count s ⁻¹ × 10 ⁻²)
rh300600	1998 Jan 14	28.216	0.875–0.146	1435	2.1±0.4
rh300601	1998 Jan 14	28.476	0.990–0.004	83	2.4±0.9
.	.	28.481	0.007–0.348	1456	1.8±0.4
.	.	28.543	0.006–0.404	1856	1.9±0.3
.	.	28.620	0.282–0.452	928	1.3±0.4
.	.	28.666	0.009–0.165	848	1.1±0.4
rh300602	1998 Jan 15	29.145	0.588–0.855	1440	1.3±0.3
.	.	29.212	0.653–0.902	1280	0.7±0.2
rh300603	1998 Jan 15	29.402	0.667–0.006	1920	1.0±0.2
.	.	29.470	0.737–0.792	288	0.0±0.2
.	.	29.475	0.819–0.103	1488	1.9±0.4
.	.	29.538	0.813–0.160	1872	2.0±0.3
rh300604	1998 Jan 18	31.598	0.453–0.477	96	3.4±1.9
.	.	31.605	0.565–0.717	832	1.4±0.4
.	.	31.652	0.316–0.477	864	2.9±0.6
.	.	31.673	0.636–0.770	736	1.7±0.5
.	.	31.714	0.296–0.550	1392	1.8±0.4
.	.	31.741	0.715–0.818	560	1.0±0.4
rh300605	1998 Jan 18	32.061	0.794–0.007	1520	1.3±0.3
.	.	32.131	0.891–0.120	1248	0.6±0.2
.	.	32.195	0.907–0.176	1408	0.3±0.4
.	.	32.254	0.840–0.224	1824	1.2±0.3
rh300606	1998 Jan 19	33.055	0.543–0.831	1574	1.1±0.3
.	.	33.122	0.612–0.877	1408	1.4±0.3
.	.	33.172	0.385–0.932	2895	2.3±0.3
rh300607	1998 Jan 20	33.516	0.845–0.181	1834	2.1±0.3
.	.	33.569	0.688–0.972	1378	0.9±0.2
.	.	33.594	0.008–0.226	803	2.2±0.5
.	.	34.121	0.420–0.632	1126	1.6±0.4
.	.	34.182	0.399–0.688	1522	1.3±0.3
rh300608	1998 Jan 22	36.036	0.771–0.009	1680	1.0±0.2
.	.	36.102	0.815–0.144	1664	2.5±0.4
rh300609	1998 Jan 22	36.316	0.207–0.301	512	0.8±0.4
.	.	36.364	0.964–0.345	2000	2.0±0.3
.	.	36.431	0.002–0.390	1968	1.8±0.3
rh300610	1998 Jan 23	37.030	0.514–0.857	1840	1.3±0.3
.	.	37.097	0.576–0.908	1696	1.2±0.3
rh300611	1998 Jan 23	37.426	0.778–0.159	2064	1.5±0.3

^aThis is the time-averaged count rate from the source after background subtraction. The errors quoted are Poissonian.

Car. The total exposure time of each of the 96 phase bins is shown in Fig. 5. The duration of the optical-white-dwarf eclipse, defined as the difference between the second and third contact phases of the white dwarf, is 231 s (Wood et al. 1989). Thus with 96 phase bins, four bins cover the eclipse and have a total duration of 227 s.

Table 2. Journal of optical observations.

Run	Date	UT start	Cycle	Filter
0007	1998 March 3	22:57:30	109036	V
0009	1998 March 4	01:22:43	109045	V
1008	1998 March 5	01:46:17	109061	V
2001	1998 March 6	00:33:42	109076	V
3009	.	18:41:45	109088	V
3017	.	23:10:31	109091	V
5015	1998 March 8	20:42:03	109121	V
5019	.	21:55:27	109122	V
5024	.	23:35:29	109123	V
5028	1998 March 9	01:09:48	109124	V
5030	.	02:07:23	109125	V
6013	.	18:53:30	109136	W

Table 3. Timings of optical mid-eclipse.

Cycle	HJED (240 0000+)	<i>O</i> – <i>C</i> (10 ⁻⁴ d)
85618 ^a	49397.84069	–3.8
109036	50876.51124	–5.8
109045	50876.57449	–4.7
109061	50877.58431	–5.8
109076	50878.53116	–5.4
109088	50879.28858	–5.8
109091	50879.47795	–5.7
109121	50881.37157	–5.8
109122	50881.43479	–4.8
109123	50881.49785	–5.4
109124	50881.56107	–4.4
109125	50881.62408	–5.5
109136	50882.31834	–6.2

^aEclipse timing from a near quiescent light curve in Pratt et al. (in preparation).

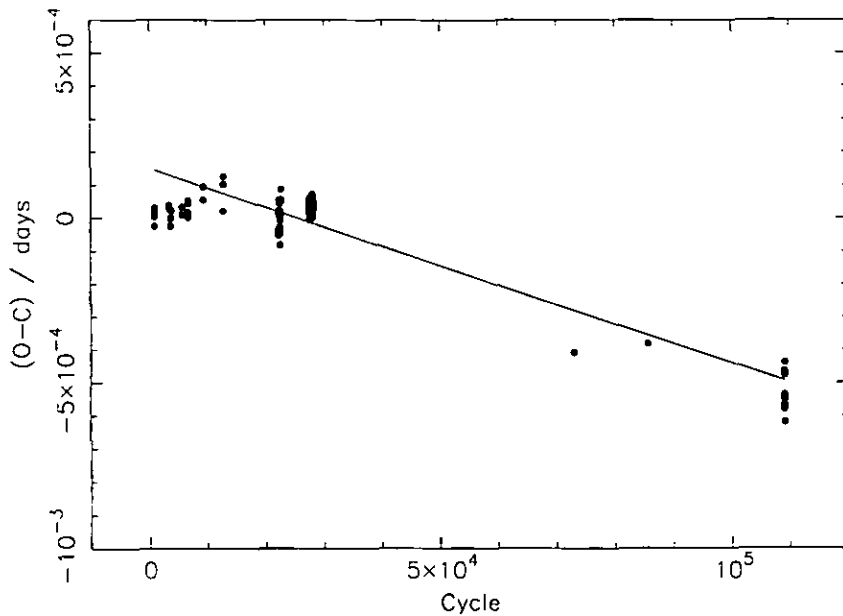


Figure 3. The $O-C$ diagram of OY Car. The residuals are calculated with respect to the linear ephemeris of Wood et al. (1989). The solid line represents the fit to the residuals corresponding to a constant period with a phase offset.

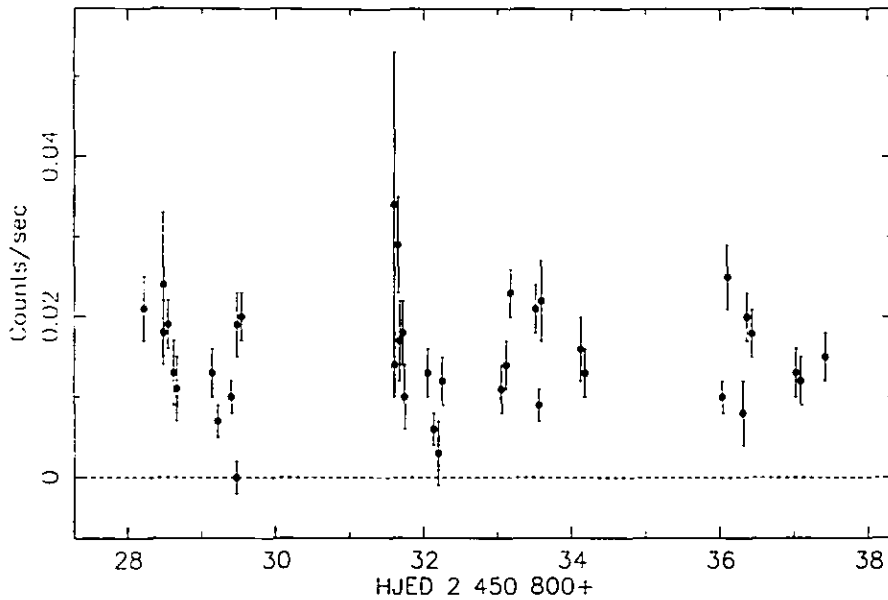


Figure 4. The behaviour of the X-ray flux over the duration of the *ROSAT* observations. The panel shows the data averages with 1σ error bars. Eclipses have not been removed.

The bins were chosen such that the start of one bin coincided with orbital phase zero.

In Fig. 6, we show the quiescent X-ray light curve of OY Car, binned into 96 phase bins, phased on the ephemeris presented in this paper with a correction of -8 s subtracted from the constant term. With the -8 s correction, the σ -values of all four eclipse bins are at a simultaneous low, implying that this is the best ephemeris for the X-ray data. The spread of values in the optical $O-C$ determinations in Section 3 is $\sim 2.4 \times 10^{-4}$ of a day, or 16 s, so the discrepancy in the ephemeris of the X-ray data is well within the error of the optical observations.

To investigate the significance of the eclipse, the data were binned into 24 bins such that the duration of one bin was marginally smaller than the duration of the optical-white-dwarf eclipse. Now the out of eclipse flux was $(1.70 \pm 0.06) \times 10^{-2}$ counts $^{-1}$, and the flux in eclipse was $(0.14 \pm 0.06) \times 10^{-2}$ counts $^{-1}$. The eclipse is thus significant at the 2.3σ level. The fact that the flux drops at exactly phase zero adds significance to the detection.

We used two methods to estimate the duration of the X-ray eclipse. First, we divided the data into 96 phase bins and shifted the bins backwards and forwards until in one of the four eclipse

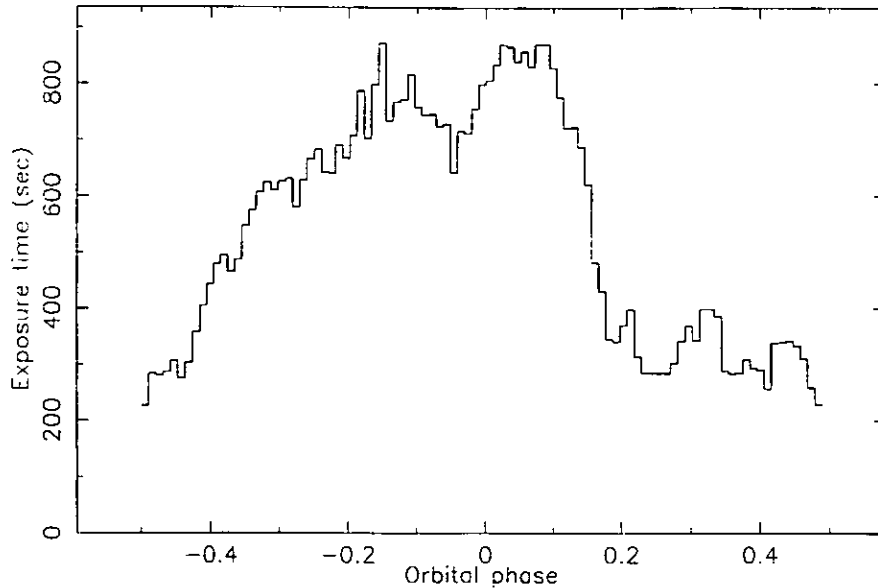


Figure 5. The effective exposure times of each of the 96 phase bins used for the superoutburst light curve, in seconds.

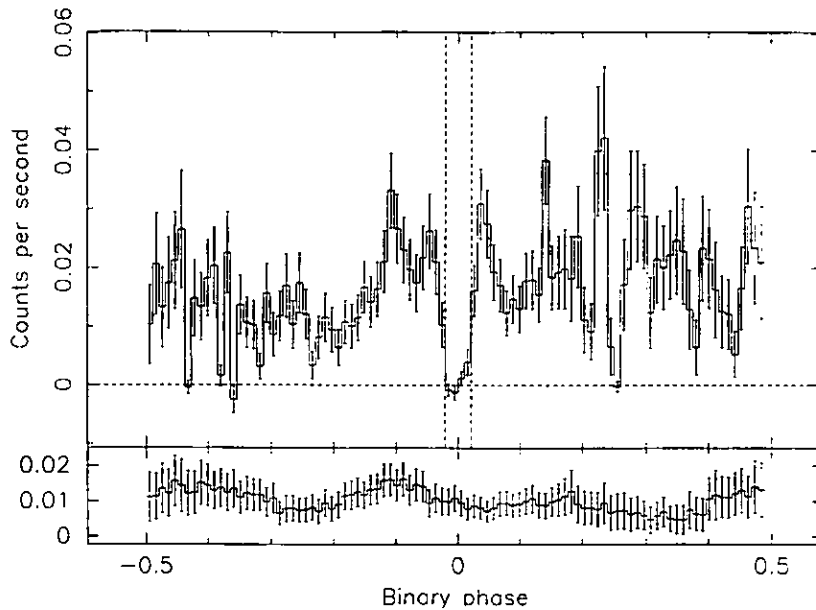


Figure 6. The *ROSAT* HRI quiescent X-ray light curve, folded on the orbital period of OY Car in 96 bins, is shown in the top panel. The bottom panel shows the corresponding folded background light curve, scaled to the dimensions of the source extraction circle. The dotted lines represent the times of the optical-white-dwarf eclipse (Wood et al. 1989). The error bars are 1σ Poissonian. The data have been phased using the ephemeris derived in this paper with an adjustment of -8 s. See text for explanation.

bins, the count rate deviated from zero by 2.5σ or greater (cf. van Teeseling 1997). This allows us to estimate an upper limit to the width of the X-ray eclipse of ~ 271 s, which is only 40 s longer than the optical eclipse. Secondly, assuming that the eclipse is symmetric, we examined the symmetrized light curve folded at 20-s time resolution (cf. Wood et al. 1995a). The full width zero depth of the eclipse in this case is then $\text{FWZD} = 259$ s, or only 28 s longer than the optical eclipse of the white dwarf.

Finally, we note the apparent similarities between the average X-ray light curve presented here and that obtained for Z Cha by van Teeseling (1997), in that both light curves exhibit a dip near

phase 0.7–0.8. While this is suggestive of flux variability with phase, the low signal-to-noise ratio precludes a quantitative analysis of these features, even in the average light curve.

5 DISCUSSION

Given that X-ray eclipses have been detected in HT Cas and Z Cha in quiescence, it is perhaps not surprising to have found the same for OY Car. But it is OY Car that has recently been the focus of X-ray and UV investigations which have raised some interesting questions concerning the local absorption of the system. The *HST*

UV observation by Horne et al. (1994) showed an 'iron curtain' of veiling material superimposed on the spectrum of the white dwarf. Horne et al. (1994) cannot pinpoint the exact position of this gas, although placing the material at the outer disc allows the more plausible explanation that the disturbances that produce the material are driven by the gas stream. Independent of the location of the gas, Horne et al. (1994) fit a column density of $n_{\text{H}} \approx 10^{22} \text{ cm}^{-2}$. However, at this column density, the material in front of the white dwarf should absorb all the X-rays (see e.g. Naylor & la Dous 1997).

In this paper we show that there is a clear and unambiguous (although not necessarily total) eclipse of the X-rays, demonstrating the column density of the intervening material is not sufficient to extinguish the flux in the *ROSAT* passband.

Variability could be the key: it may be that the 'iron curtain' is not a permanent feature and that the Horne et al. (1994) observation happened to catch the system when the column density of the intervening material was higher than usual. One obvious cause of a higher local absorption than usual is a recent outburst or superoutburst; however, the Horne et al. (1994) observation was obtained in the middle of a quiescent period, strongly suggesting that the source of the veiling gas is not connected to the outbursts.

An alternative explanation is variability on the orbital time-scale. Because of the nature of the existing observations, we do not know how the absorption changes with orbital phase: it is quite possible that the local absorption varies azimuthally around the disc. This can be seen in the *International Ultraviolet Explorer* (*IUE*) spectra of Z Cha, in which it can be seen that the 'iron curtain' is present in some spectra but not in others (Wade, Cheng & Hubeny 1994).

It does seem clear that the absorption is intimately connected to the accretion of material, and as this is variable, then so is the strength of the absorption. Three separate X-ray observations of HT Cas have yielded three widely differing values of n_{H} : $1.8 \times 10^{20} \text{ cm}^{-2}$ in the low state (Wood et al. 1995a), but between 6×10^{20} and $3 \times 10^{21} \text{ cm}^{-2}$ in quiescence (Patterson & Raymond 1985; Mukai et al. 1997).

Finally, our observation is similar to the previous detections of X-ray eclipses in dwarf novae in that the inferred size of the X-ray emitting region is comparable to the size of the white dwarf, and comes from a source close to the primary. However, we were unable to establish a reliable lower limit for the duration of the X-ray eclipse. We now know that the X-rays in quiescence are definitely emitted from a region in the neighbourhood of the white dwarf, but we cannot be any more precise than that owing to data constraints.

6 SUMMARY AND CONCLUSIONS

We have shown that there is an eclipse of the X-ray flux from OY Car in the quiescent state, and that the X-rays are emitted from a region very close to the white dwarf.

From observations of suitable systems, we now know that, in general, eclipses of the X-ray flux occur where the accretion rate

is low, and do not occur where the accretion rate is high. We know that there are discrepancies between the X-ray and UV measurements of the local absorption in OY Car, and that the strength of the absorption appears to be variable and intimately connected to the accretion rate in the case of HT Cas.

For OY Car we now need higher quality X-ray light curves that will enable us to pinpoint the exact source of the X-ray emission. Data with higher time and energy resolution would be desirable, such as is currently available from *ASCA*. Simultaneous orbital-phase-dependent observations of these systems in the UV, such as with the *HST*, will enable the investigation of the variability of the local absorption with orbital phase in both UV and X-rays. Looking further ahead, *XMM* will represent the next generation of X-ray satellites, and will be ideal for the study of these intriguing systems owing to the higher throughput and especially the simultaneous optical monitoring.

ACKNOWLEDGMENTS

We thank Jakob Engelhauser for his help with the difficult scheduling of the *ROSAT* observations. We acknowledge the data analysis facilities provided by the Starlink Project, which is run by CCLRC on behalf of PPARC. GWP is in receipt of a University of Central Lancashire research studentship.

REFERENCES

- Applegate J. H., 1992, *ApJ*, 385, 621
 Cook M. C., 1985, *MNRAS*, 215, 211
 Horne K., Marsh T. R., Cheng F. H., Hubeny I., Lanz T., 1994, *ApJ*, 426, 294
 Mukai K., Wood J. H., Naylor T., Schlegel E. M., Swank J. H., 1997, *ApJ*, 475, 812
 Naylor T., la Dous C., 1997, *MNRAS*, 290, 160
 Naylor T., Bath G. T., Charles P. A., Hassall B. J. M., Sonneborn G., van der Woerd H., Heise J., 1988, *MNRAS*, 231, 237
 Patterson J., Raymond J. C., 1985, *ApJ*, 292, 535
 Pringle J. E., Savonije G. J., 1979, *MNRAS*, 187, 777
 Pringle J. E., 1977, *MNRAS*, 178, 195
 Robinson E. L. et al., 1995, *ApJ*, 443, 295
 Schoembs R., Hartmann K., 1983, *A&A*, 128, 37
 Schoembs R., Dreier H., Barwig H., 1987, *A&A*, 181, 50
 Shore S. N., 1992, in Drissen L., Leitherer C., Nota A., eds. *ASP Conf. Ser.* R1 Vol. 22, Non-isotropic and Variable Outflows from Stars, Astron. Soc. Pac., San Francisco, p. 342
 van Teeseling A., 1997, *A&A*, 319, L25
 Vogt N., Schoembs R., Krzeminski W., Pedersen H., 1981, *A&A*, 94, L29
 Wade R. A., Cheng F. H., Hubeny I., 1994, *BAAS*, 184, #4605
 Warner B., 1995, *Cataclysmic Variable Stars*, Cambridge University Press, Cambridge
 Wood J. H., Horne K., Berriman G., Wade R. A., 1989, *ApJ*, 341, 974
 Wood J. H., Naylor T., Hassall B. J. M., Ramseyer T. F., 1995a, *MNRAS*, 273, 772
 Wood J. H., Irwin M. J., Pringle J. E., 1985, *MNRAS*, 214, 475
 Wood J. H., Naylor T., Marsh T. R., 1995b, *MNRAS*, 274, 31

This paper has been typeset from a \TeX/L\AA\TeX file prepared by the author.

Optical and *ROSAT* X-ray observations of the dwarf nova OY Carinae in superoutburst and quiescence

Gabriel W. Pratt,¹ B. J. M. Hassall,¹ T. Naylor,² Janet H. Wood² and J. Patterson³

¹Centre for Astrophysics, University of Central Lancashire, Preston PR1 2HE

²Department of Physics, Keele University, Keele ST5 5BG

³Department of Astronomy, Columbia University, 538 West 120th Street, New York, NY 10027, USA

Accepted 1999 June 15. Received 1999 June 14; in original form 1999 February 23

ABSTRACT

We present *ROSAT* X-ray and optical light curves of the 1994 February superoutburst of the eclipsing SU UMa dwarf nova OY Carinae. There is no eclipse of the flux in the *ROSAT* HRI light curve. Contemporaneous 'wide *B*'-band optical light curves show extensive superhump activity and dips at superhump maximum. Eclipse mapping of these optical light curves reveals a disc with a considerable physical flare, even three days into the superoutburst decline.

We include a later (1994 July) *ROSAT* PSPC observation of OY Car that allows us to put constraints on the quiescent X-ray spectrum. We find that while there is little to choose between OY Car and its fellow high-inclination systems with regard to the temperature of the emitting gas and the emission measure, we have difficulties reconciling the column density found from our X-ray observation with the column found in *Hubble Space Telescope* UV observations by Horne et al. The obvious option is to invoke time variability.

Key words: accretion, accretion discs – binaries: eclipsing – stars: individual: OY Car – novae, cataclysmic variables – X-rays: stars.

1 INTRODUCTION

Dwarf novae are a subclass of non-magnetic cataclysmic variable (CV), binary systems consisting of a Roche lobe filling late-type secondary star in the process of mass transfer, via an accretion disc, on to a white dwarf primary. Sudden increases in the accretion rate through the disc and on to the white dwarf, most likely a result of thermal instability, cause outbursts of ~ 2 – 5 mag on time-scales of weeks to years. The SU UMa subclass undergo additional infrequent superoutbursts, brighter by ~ 1 mag and lasting ~ 5 times longer than ordinary outbursts, thought to be triggered by a tidal resonance of the material in the outer disc. See Warner (1995) for a comprehensive review.

Steady state theory predicts that half the accretion luminosity from these systems is released in the disc, the other half in the boundary layer between the disc and the white dwarf. This is the region where the material of the disc is decelerated to match the surface velocity of the primary, and in quiescence it is believed to consist of an optically thin gas emitting relatively hard (~ 2 – 20 keV) X-rays. In outburst, the accretion rate rises and the X-ray emitting region is predicted to become optically thick, with a characteristic emission of softer (~ 0.1 – 1.0 keV) X-rays (Pringle & Savonije 1979). Provided the primary is not spinning fast, the boundary layer is thought to be the dominant source of the X-ray emission from non-magnetic CVs (Pringle 1977).

Observations have, to a great extent, borne out the theoretical

predictions. Those systems in which the white dwarf, bright spot and accretion disc are all eclipsed allow in principle the simplest observational test to determine the source of the X-ray emission: if it is in the vicinity of the white dwarf, as expected for a boundary layer, then there will be an eclipse of the X-ray flux. In general these X-ray observations are a few tens of ks in length and require the binning of the data. The location of the X-ray source can be further pinpointed by comparing the X-ray light curves with optical light curves.

Of the high inclination dwarf novae, three have so far been examined in this way. A *ROSAT* observation of HT Cas in the low state showed an eclipse (Wood, Naylor & Marsh 1995b); this system was subsequently observed in quiescence by both *ROSAT* and *ASCA* (Mukai et al. 1997), the latter observation being of sufficient quality to allow approximate source dimensions to be extracted from the X-ray data. In addition, van Teeseling (1997) has observed an eclipse of the X-ray flux from Z Cha in quiescence, while Pratt et al. (1999) have confirmed that the X-ray source in OY Car is also eclipsed in quiescence.

Observations of dwarf novae in outburst or superoutburst are difficult because of their inherent unpredictability and the short time-scales (at least in terms of satellite response times) involved. Generally, the hard X-ray emission is seen to drop in many systems during outburst, often accompanied by a surge in the soft X-ray flux. The deepest insights into the outburst state can again be derived from observations of the high inclination systems.

Perhaps most interestingly, the *EXOSAT* observation of OY Car by Naylor et al. (1988) showed that there was no X-ray eclipse during superoutburst. Contemporaneous observations at other wavelengths (Naylor et al. 1987, 1988) inferred considerable vertical structure in the outer disc, causing material to block the view of the central regions at all orbital phases. This interpretation is supported by the lack of eclipse in the *ROSAT* PSPC observation of the high inclination nova-like variable UX UMa (Wood et al. 1995b), which is believed to be similar to a dwarf nova in a state of permanent outburst. Additionally, advances in eclipse mapping have recently allowed modelling of outburst discs: *Hubble Space Telescope (HST)* UV observations of Z Cha at normal outburst peak by Robinson et al. (1995) reveal a flared disc with an opening full-angle of $\alpha = 16^\circ$. Thus it appears that in the case of OY Car in superoutburst, we are seeing the X-ray flux from an extended (or 'coronal') source, and not from the boundary layer directly, a result of the obscuration arising from a physically thick, vertically extended disc.

Discrepancies exist between boundary layer theory and observation, however. The most famous (and still unsolved) problem remains the fact that the X-ray luminosity rarely approaches the predicted value, being typically down by an order of magnitude on the optical + UV luminosity from the disc. The ratio is most discrepant for the optically thick cases, where the accretion rate is high, such as in the case of dwarf novae in outburst, or nova-like variables (van Teeseling & Verbunt 1994). One possible explanation is that the difference is a result of a loss of a kinetic energy in the wind that is often observed to come from the inner regions of the accretion disc during high mass transfer episodes. Another possible explanation is a combination of this wind energy loss in conjunction with enhanced absorption as a result of the outburst. *EUVE* observations of U Gem in outburst have shown that the spectrum is composed of emission lines, probably produced in the corona or wind, and a highly absorbed blackbody-like continuum (Long et al. 1996). Another explanation, applicable to both high and low accretion rate systems, may simply be that the white dwarf is spinning fast. The low $L_X/L_{\text{opt+UV}}$ ratio is also observed in quiescence (e.g. Belloni et al. 1991); here it may be a result of the non-steady state conditions caused by the mass accretion rate on to the primary being lower than the mass flux rate through the outer disc.

OY Car is one of the best studied of the dwarf novae, mainly because it is a fully eclipsing system with an inclination angle of 83° . However, with the benefits of a full eclipse come other difficulties, chief among them the effect of the disc, which is seen nearly edge-on in OY Car. We know that the disc becomes physically thick during outburst and superoutburst (see, e.g., Naylor et al. 1988; Robinson et al. 1995), but we do not know the extent of the contribution this makes to the overall rise in the local absorption during these episodes. The extent of the absorption to OY Car, both interstellar and local, is still very much a mystery. Horne et al. (1994) use *HST* observations of OY Car in quiescence to deduce the existence of a significant local absorption arising from a veiling material, subsequently modelled by a solar abundance local thermodynamic equilibrium (LTE) gas. Horne et al. dubbed this veiling gas the 'iron curtain' after Shore (1992); mainly because of the existence of many blended Fe II lines in its spectrum. They derive a column density of $n_H \approx 10^{22} \text{ cm}^{-2}$, which, as pointed out by Naylor & la Dous (1997), is sufficient to absorb much of the soft X-ray emission from the boundary layer. If the absorption is this high in quiescence, how much more local absorption is added during outburst and superoutburst?

The aim of the observations herein is to address not only the extent of the thickening of the disc during superoutburst and the question of the absorption to the X-ray source, but also the missing boundary layer problem. To this end, we present contemporaneous optical and *ROSAT* X-ray observations of the eclipsing SU UMa system OY Car in superoutburst, together with a later *ROSAT* X-ray observation of the system in quiescence. We compare past and present X-ray observations of OY Car with previous observations of the canonical low inclination SU UMa system, VW Hydr, in order to illustrate the effects of the disc in the high inclination case. The high time-resolution optical photometry, obtained at the end of the superoutburst peak and on the decline, enables us to use a new version of the eclipse mapping method (originally developed by Horne 1985, since updated to include disc flaring, e.g. Robinson et al. 1995; Wood 1994) to investigate the extent of the physical flaring of the disc as the system returns to quiescence. We use the quiescent *ROSAT* X-ray observation to delimit the extent of the absorption in quiescence, and compare this to the results from the *HST* data from Horne et al. (1994).

Section 2 describes the X-ray and EUV observations and reduction. In Section 3 we describe the analysis of the X-ray data, Section 4 describes the superoutburst optical data, and in Section 5 we discuss our results and compare and contrast them with those found previously for VW Hyi.

2 OBSERVATIONS AND DATA REDUCTION

Monitoring observations made by the Variable Star Section of the Royal Astronomical Society of New Zealand (VSS RAS NZ) reveal that OY Car underwent a superoutburst on 1994 February 1, stayed at maximum for seven days, and returned to quiescence over a subsequent 13-day period. The first X-ray observation, obtained with the *ROSAT* High Resolution Imager (HRI; David et al. 1991) was taken at the height of the superoutburst. The optical observations were taken at the end of the superoutburst plateau and on the decline, and so the full data set includes one contemporaneous optical/X-ray observation (1994 February 8). The second X-ray observation took place in 1994 July, when the quiescent OY Car was observed with the *ROSAT* Position Sensitive Proportional Counter (PSPC; Pfeffermann & Briel 1986). Both the superoutburst and the quiescent *ROSAT* observations had simultaneous Wide Field Camera (WFC; Sims et al. 1990) coverage.

Fig. 1 shows the magnitude of OY Car before, during, and after the 1994 January superoutburst, using both data from the VSS RAS NZ and our own optical observations. The figure also shows the timing of the X-ray observations relative to the optical observations. Exact times are given in Table 1.

The orbital period of OY Car is ~ 91 min, very similar to the ~ 96 -min orbit of *ROSAT*. The orbital phase of OY Car as seen by the satellite thus precesses through the satellite orbit (with a step size of ~ 5 min per orbit), necessitating careful scheduling of observations to obtain the required phase coverage. For the remainder of this paper, to avoid confusion when referring to the X-ray data, we will use 'observation' to describe the actual n -day baseline over which the individual 'data sets' were obtained.

2.1 X-ray and EUV observations

2.1.1 Superoutburst

OY Car was observed by the *ROSAT* HRI for a total of 7.4 ks

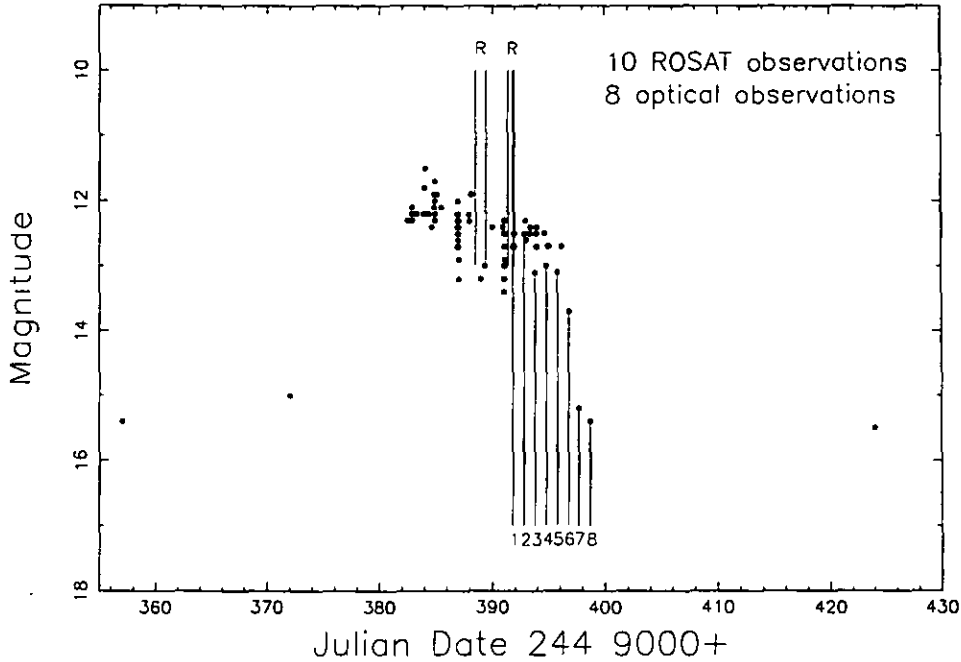


Figure 1. The light curve of OY Car during the 1994 January superoutburst, from observations supplied by the VSS RAS NZ. Our optical data, obtained on the decline, and the times of the *ROSAT* observations (R) are also shown. The optical data have been converted to Oke AB magnitudes using $AB = -2.5 \log f_{\nu} - 48.60$ (Oke 1974).

Table 1. Journal of X-ray observations.

State	Date	HJED start	Phase covered	Duration (seconds)	Source count rate ^a (count s ⁻¹ × 10 ⁻²)
Superoutburst		(244 9300+)			
	1994 Feb 4	88.492	0.885–0.916	160	4.8 ± 1.7
	.	88.499	0.997–0.224	1240	3.7 ± 0.5
	1994 Feb 5	89.419	0.579–0.600	112	-0.4 ± 0.6
	.	89.427	0.709–0.945	1288	3.0 ± 0.5
	1994 Feb 7	91.352	0.197–0.433	1288	2.5 ± 0.4
	1994 Feb 8	91.799	0.277–0.599	1624	2.5 ± 0.4
	.	91.870	0.405–0.428	80	3.0 ± 2.0
	.	91.879	0.549–0.716	904	2.2 ± 0.5
	.	91.891	0.745–0.839	512	1.7 ± 0.6
	.	91.930	0.353–0.404	280	3.9 ± 1.2
				Average	2.8 ± 0.2
Quiescence		(244 9500+)			
	1994 July 5	38.916	0.003–0.088	464	8.0 ± 1.3
	.	39.313	0.296–0.398	560	8.0 ± 1.2
	1994 July 6	40.473	0.664–0.670	32	0.5 ± 1.3
	1994 July 7	40.508	0.229–0.328	544	8.7 ± 1.3
				Average	8.1 ± 0.7

^aThis is the time-averaged count rate from the source after background subtraction. The errors quoted are Poissonian.

between 1994 February 4 and 1994 February 8, with an observation start time of 1994 February 4 23:43:33 UT (HJED 244 9388.489 639). The dates, times and durations of the individual X-ray observation data sets are given in Table 1, the journal of X-ray observations.

The data were reduced using *ASTERIX* software. We extracted source counts from a circular region of radius 150 arcsec. The background annulus, centred on the source, had inner and outer radii of 200 and 600 arcsec respectively. These dimensions were

chosen for compatibility with those used in the comprehensive compilation of *ROSAT* CV observations by van Teeseling, Beuermann & Verbunt (1996). Source and background data were then binned into 1s bins and background subtracted. The resulting background-subtracted total flux light curve was corrected for vignetting, dead time, and scattering. Finally, all times were converted to HJED.

The *ROSAT* WFC observed OY Car for 26.6 ks on 1994 February 5 and 5.9 ks on 1994 February 7, with the S1a filter,

which is sensitive to the spectral range 90–206 eV. The data were extracted using *ASTERIX* and *WFCPACK* software. Using a source radius of 5 arcmin and a background annulus, centred on the source, of inner and outer radii 10 and 20 arcmin, respectively, we estimate a 3σ upper limit to the superoutburst count rate of 1.2×10^{-3} counts s^{-1} .

2.1.2 Quiescence

OY Car was observed in quiescence with the *ROSAT* PSPC between 1994 July 5 and 1994 July 7 for a total of 1.6 ks. OY Car was in the middle of a quiescent spell – the previous normal outburst took place on 1994 May 30, and the subsequent superoutburst occurred on 1994 December 11. The start time of the observations was 1994 July 5 09:55:55 UT (HJED 244 9538.915 388). Information about these X-ray observations can also be found in Table 1.

The observations were taken off-axis and with a spacecraft wobble to avoid vignetting by PSPC support wires, so the source and background counts were extracted from larger regions than those used for the superoutburst data. The data were again reduced using the *ASTERIX* package. The radius of the source region used was 250 arcsec, while the inner and outer radii for the background annulus, centred on the source, were 300 and 900 arcsec, respectively. These dimensions were again chosen for compatibility with van Teeseling et al. (1996). These data were then corrected as described for the superoutburst data.

In addition, the spectrum from channels 11 to 235 was extracted in 1-s bins. It was then binned, using *FTOOLS*, into 11 spectral bins so that there were at least 5 counts in each bin.

The WFC also observed OY Car for a total of 4.9 ks on 1994 July 5 with the S1a filter. The data were reduced using *ASTERIX* and *WFCPACK* software. There was again no detection, and using the method described for the superoutburst data, the 3σ upper limit found for the quiescent count rate is 1.5×10^{-3} counts s^{-1} .

2.2 Optical observations

High time-resolution optical photometry was obtained on the 1-m telescope at CTIO, Chile. The dates and times of each observation are presented in Table 2, the journal of optical observations. The Automated Single-Channel Aperture Photometer (ASCAP) was used in conjunction with a Hamamatsu R943-02 photomultiplier tube. All observations were taken using an integration time of 5 s through a CuSO_4 filter. This filter has a wide bandpass (3300 – 5700 Å) which gives a broad B response, but includes a substantial amount of U . The counts per 5 s were corrected for atmospheric extinction and phased with the orbital period using the updated ephemeris of Pratt et al. (1999).

3 THE X-RAY DATA

3.1 The superoutburst X-ray light curve

The average count rates decline during the course of the observation, but recover by the last data set. We divided the observation into two groups along the lines of the natural break in the data sets (February 5/February 7), and found that there is a negligible drop in the average count rate between the first three data sets, Set 1, and the last five, Set 2.

The total superoutburst light curve was obtained by folding all the data sets into 24 bins on the orbital period of OY Car using the

Table 2. Journal of optical observations.

UT date	UT start	Duration (seconds)
1994 Feb 8	06:21:22	9452
1994 Feb 9	07:26:04	5647
1994 Feb 10	08:12:09	3606
1994 Feb 11	07:24:47	6358
1994 Feb 12	07:26:03	6324
1994 Feb 13	07:22:58	6521
1994 Feb 14	06:32:42	8641
1994 Feb 15	06:48:22	8427

ephemeris of Pratt et al. (1999). The duration of each bin was marginally smaller, at 227.2 s, than the totality of the white dwarf eclipse as given in Wood et al. (1989), of 231.2 s. The starting point of the binning was chosen so that one phase bin was exactly centred on phase zero. The effective exposure time of each of the 24 bins is illustrated in Fig. 2. The phase coverage in the data was such that ~ 97 per cent of the orbit was covered, including one eclipse. The resulting phase-folded superoutburst light curve can be seen in Fig. 3. The large error bars on the bin centred on phase $\phi = 0.95$ are a result of the poor coverage in this bin. This lack of coverage extends ~ 25 per cent into the white dwarf eclipse phase bin at phase $\phi = 0.0$.

The mean out-of-eclipse flux is $(2.8 \pm 0.2) \times 10^{-2}$ counts s^{-1} , while the flux in WD eclipse is $(3.8 \pm 1.7) \times 10^{-2}$ counts s^{-1} . We can thus ascertain that there is no total eclipse of the X-rays in the vicinity of the white dwarf at the 2.2σ level.

If we instead take only the first four data sets, which cover the eclipse phase, and apply the above analysis, we find that there is no eclipse of the X-ray flux at the 2.3σ level.

3.2 The superoutburst luminosity

As the *ROSAT* HRI data contains no spectral information, we have used the total time-averaged count rate in order to make a rough estimate of the intrinsic luminosity of the system in superoutburst.

The derivation of an approximate luminosity in superoutburst involved generating simulated spectra within *XSPEC*. As a basis for a temperature estimate, we used $kT = 6.0$ keV, the dominant temperature found for the high-energy spectrum of VW Hyi by Wheatley et al. (1996). The simulated spectra were normalized to the count rate of our observation, with intervening absorptions of 10^{20} , 10^{21} and 10^{22} cm^{-2} included in the models. The n_{H} parameter is completely unknown for the superoutburst case. As discussed in the introduction, it is likely that the *local* absorption becomes the dominant contributor to the global column in superoutburst as a result of the inclination of the system. Removal of the estimated total intervening absorption allowed the calculation of the corresponding intrinsic luminosities. Using a distance of 82 pc (Wood et al. 1989) and a bandpass of 0.001 to 20 keV for a ‘bolometric’ value, the resulting superoutburst luminosity as deduced by this method is $L_{\text{X}} \sim 2 \times 10^{32}$ erg s^{-1} .

3.3 Spectral analysis of the quiescent data

The PSPC data obtained in quiescence covered only ~ 30 per cent of the orbital phase with no coverage at phase zero, making it impossible to search for an X-ray eclipse of the boundary layer. We were, however, able to use the spectral information of the

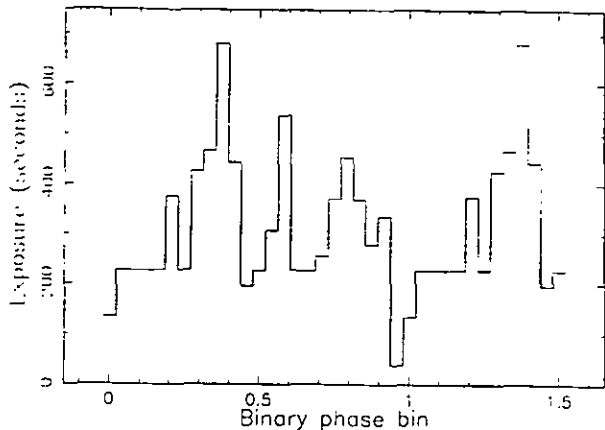


Figure 2. The effective exposure times of each of the 24 phase bins used in the generation of the superoutburst X-ray light curve.

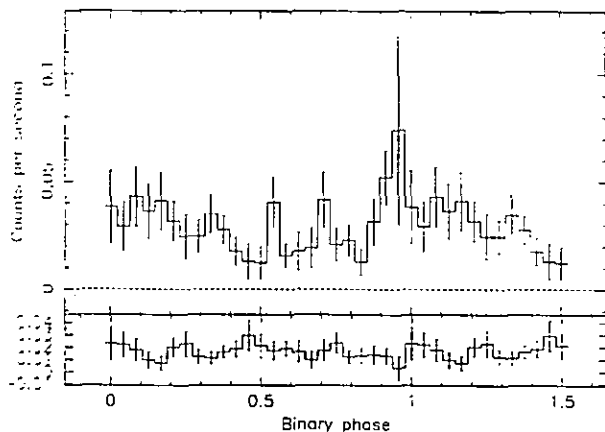


Figure 3. The upper panel shows the ROSAT HRI superoutburst X-ray light curve folded, in 24 bins, on the orbital period of OY Car. The lower panel shows the background light curve scaled to the dimensions of the source extraction circle. All error bars are Poissonian.

PSPC observations to place constraints on the X-ray emitting source at quiescence.

First, the PSPC spectrum was binned into the photon channel bandpasses summarized in Table 3, and the count rates for each bandpass calculated. The average hardness ratio is defined as $(B - A)/(B + A)$; our analysis indicates a value of $(B - A)/(B + A) = 0.77 \pm 0.22$ for OY Car in quiescence.

3.3.1 Spectral fitting

The spectral data were analysed using XSPEC software. We were unable to produce formal fits to the spectrum with three free parameters (the temperature, kT , the column density, n_H , and the normalization) using the χ^2 -minimization routines within XSPEC because of the poor signal-to-noise ratio of the observation.

In order to explore the parameter space and estimate limits on the temperature and column density, we chose representative values of kT and n_H , based on previous ROSAT PSPC observations of similar systems of near-identical inclination in quiescence. The X-ray spectra of both HT Cas and Z Cha have been fitted with single component thermal Bremsstrahlung models, with temperatures of 2.4 keV in the case of HT Cas (Wood et al. 1995) and

Table 3. Photon-channel bandpasses for the binned quiescent spectrum of OY Car.

Bandpass	Channels	Energy (keV)	Count rate ($\times 10^{-3}$)
A	11–41	0.1–0.5	4.5
B	52–201	0.6–2.4	33.8
C	52–90	0.6–1.1	11.6
D	91–201	1.1–2.4	22.3
D1	91–150	1.1–1.8	20.3
D2	151–201	1.8–2.4	1.9

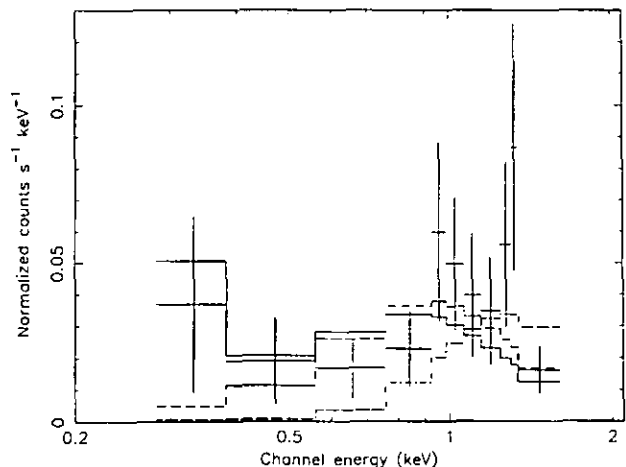


Figure 4. The ROSAT PSPC spectrum of OY Car in quiescence. Each line shows a thermal Bremsstrahlung spectrum with $kT = 2.4$ keV folded through the instrumental response. The different absorbing columns are: solid, $n_H = 10^{20} \text{ cm}^{-2}$; long dash, $n_H = 10^{21} \text{ cm}^{-2}$; and dot-dash, $n_H = 10^{22} \text{ cm}^{-2}$.

4.4 keV for Z Cha (van Teeseling 1997). We also used the 6.0-keV temperature found for the optically thin plasma (e.g., Mewe, Gronenschild & Van den Oord 1985) model fit to the EUV/X-ray spectrum of VW Hyi by Wheatley et al. (1996). Model fits to the X-ray spectra of various high-inclination non-magnetic CVs have yielded typical values of $n_H \sim 10^{20} - 10^{21} \text{ cm}^{-2}$ for the absorption, and we also adopted the value of $n_H = 10^{22} \text{ cm}^{-2}$ from the quiescent HST UV study of OY Car by Horne et al. (1994). Within XSPEC, we then allowed the normalization to be a free parameter, freezing the chosen values of kT and n_H .

Table 4 gives values for the normalization, emission measure and luminosities for the temperatures and absorbing columns under consideration. In general we found that lower temperatures produced higher values of χ^2 .

We also attempted to fit the quiescent spectrum with a dual-absorption model, including both neutral and ionized absorbers. While the fits were formally as good as those discussed previously, the quality of the data does not allow us to constrain the contributions of each component.

A representative thermal Bremsstrahlung spectrum of $kT = 2.4$ keV and column densities of $n_H = 10^{20}$, 10^{21} and 10^{22} cm^{-2} , folded through the instrumental response, is shown in Fig. 4. The figure shows that a single-component column density of 10^{22} cm^{-2} does not agree with the data for this temperature. Similar results are found for the other temperatures under consideration.

We used the values obtained for the normalization as a result of the spectral investigation to calculate the corresponding emission measure. The emission measure is a robust physical determination because, as can be seen from Table 4, a factor of 100 change in the column density produces only a factor of 7 change in the emission measure. The relatively low emission measures, of order 10^{53} cm^{-3} , in Table 4, agree with the observations of other high-inclination systems in van Teeseling et al. (1996).

Finally, within XSPEC, we estimated the luminosity of OY Car in quiescence (Table 4), using the temperatures and column densities mentioned earlier. We used the same values for the distance and bandpass as for the superoutburst luminosity, Section 3.2. The quiescent X-ray luminosity cannot be constrained by this method to any better than $L_{\text{Xq}} \sim 10^{30-31} \text{ erg s}^{-1}$.

4 THE SUPEROUTBURST OPTICAL DATA

4.1 Optical light curves

The overall behaviour of the system over the eight days of observations is shown in Fig. 5. The decline in flux is marked over the period of the observations, with an especially sharp drop (~ 28 per cent) between the light curves of February 13 and 14. Figs 6 and 7 show the individual optical light curves obtained over the period 1994 February 8 to 1994 February 15, phased on to the orbital period of OY Car.

The apparent rise in flux between the observations of 1994 February 8 and 9 is real. Much of the excess flux in the light curve of February 9 appears to come from the large superhump feature.

Table 4. Table of quiescent luminosities and emission measures. The 'normalization' is the normalization of the thermal Bremsstrahlung model in XSPEC, given by $K = (3.02 \times 10^{15})/4\pi D^2 EM$, where D is the distance (in cm) and EM is the emission measure. A bandpass of 0.001–20 keV is assumed to be bolometric.

kT (keV)	n_{H} ($\times 10^{22} \text{ cm}^{-2}$)	Normalization ($\times 10^{-4}$)	$EM \times 10^{53}$ ($\int n_e n_i dV$)	Intrinsic luminosity (erg s^{-1})	χ^2 ($\nu = 10$)
1.0	0.01	4.24 ± 1.52	1.13 ± 0.41	9.15×10^{29}	14.70
2.4	0.01	3.59 ± 1.21	0.96 ± 0.32	1.16×10^{30}	10.33
4.4	0.01	3.59 ± 1.19	0.96 ± 0.32	1.53×10^{30}	9.14
6.0	0.01	3.69 ± 1.21	0.98 ± 0.32	1.80×10^{30}	8.77
1.0	0.1	7.31 ± 2.41	1.95 ± 0.64	1.58×10^{30}	11.22
2.4	0.1	5.32 ± 1.73	1.42 ± 0.46	1.72×10^{30}	9.03
4.4	0.1	5.09 ± 1.64	1.36 ± 0.44	2.17×10^{30}	8.51
6.0	0.1	5.16 ± 1.66	1.38 ± 0.44	2.52×10^{30}	8.30
1.0	1.0	45.46 ± 11.44	12.11 ± 3.05	9.80×10^{30}	13.36
2.4	1.0	24.59 ± 7.53	6.55 ± 2.01	7.95×10^{30}	15.77
4.4	1.0	21.49 ± 6.85	5.73 ± 1.83	9.17×10^{30}	16.57
6.0	1.0	21.10 ± 6.79	5.62 ± 1.81	1.03×10^{31}	16.88

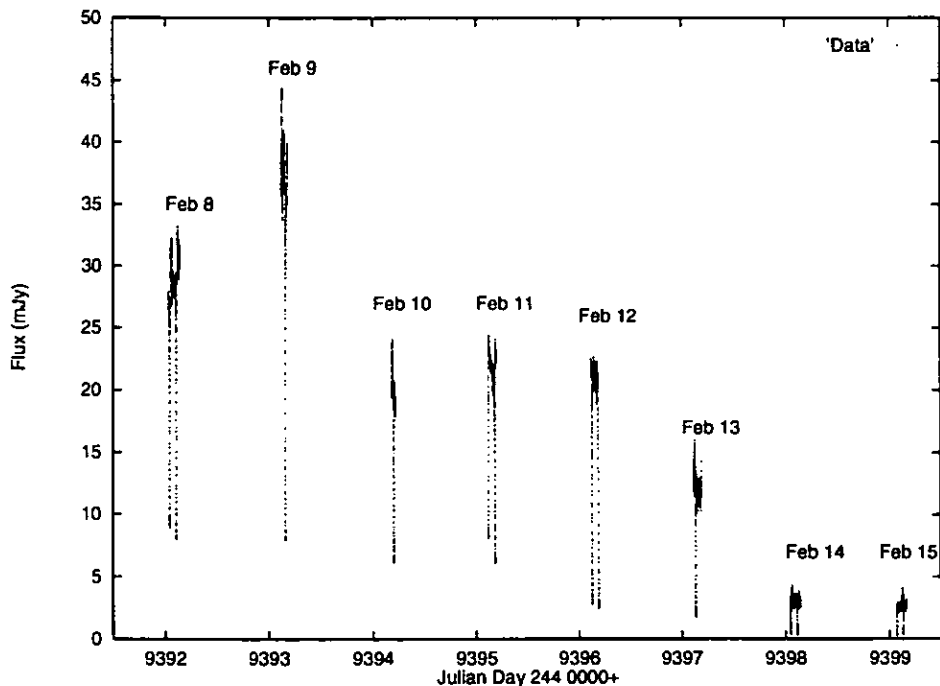


Figure 5. All the optical light curves of OY Car obtained at the end of the superoutburst of February 1994. The decline in flux over the period in question is clearly seen. The observations taken on 1994 February 14 and 15 are virtually at the quiescent level.

Orbital coverage is such that it is difficult to find a 'continuum' level from which to make a quantitative estimate of the flux rise, but if we take the flux immediately after eclipse as a 'continuum' level, then the rise in flux above the average flux level of the previous day is ~ 20 per cent.

The early eclipses appear to be roughly symmetric, but become increasingly asymmetric as the decline progresses. On February 14, the superhump is at $\phi \sim 0.2$, and the eclipse shape is strikingly

similar to that for quiescence; however, by February 15, the superhump is at $\phi \sim 0.8$, and the feature previously identified as the bright spot egress gives way again to a more round-bottomed eclipse. For the 'most quiescent' light curve, that of February 14, we used the method of Wood, Irwin & Pringle (1985) to measure the half-flux points of the eclipse, which in quiescence correspond to mid-ingress and egress of the white dwarf. We found a value of 255 s for the eclipse width, slightly longer than that of the white

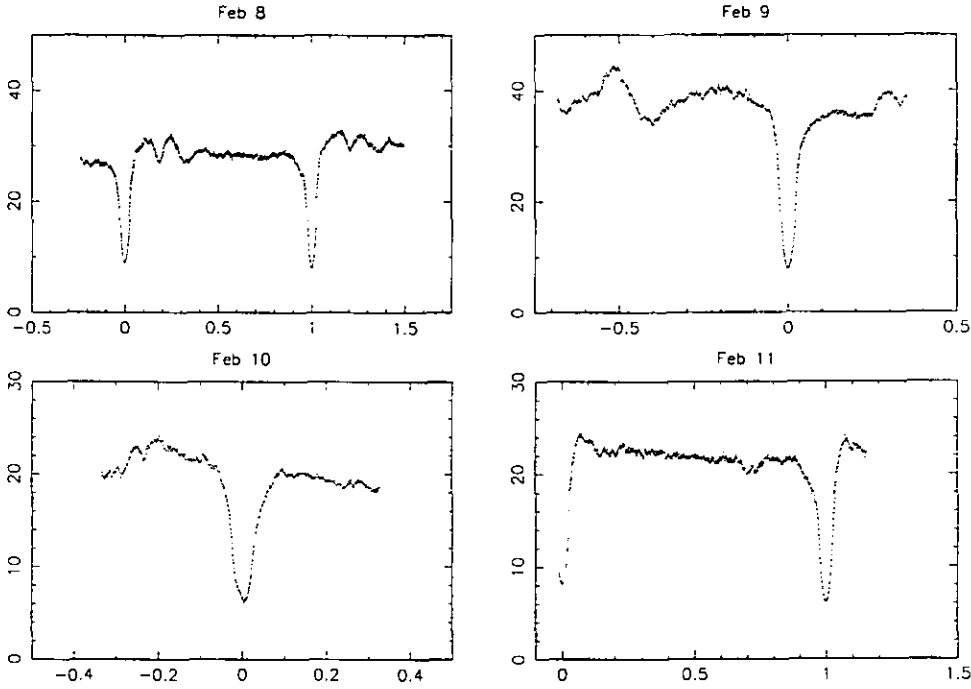


Figure 6. Four optical light curves of OY Car in superoutburst. The x -axis is orbital phase, the y -axis mJy. Note that the scale of the y -axis changes from February 9 to February 10.

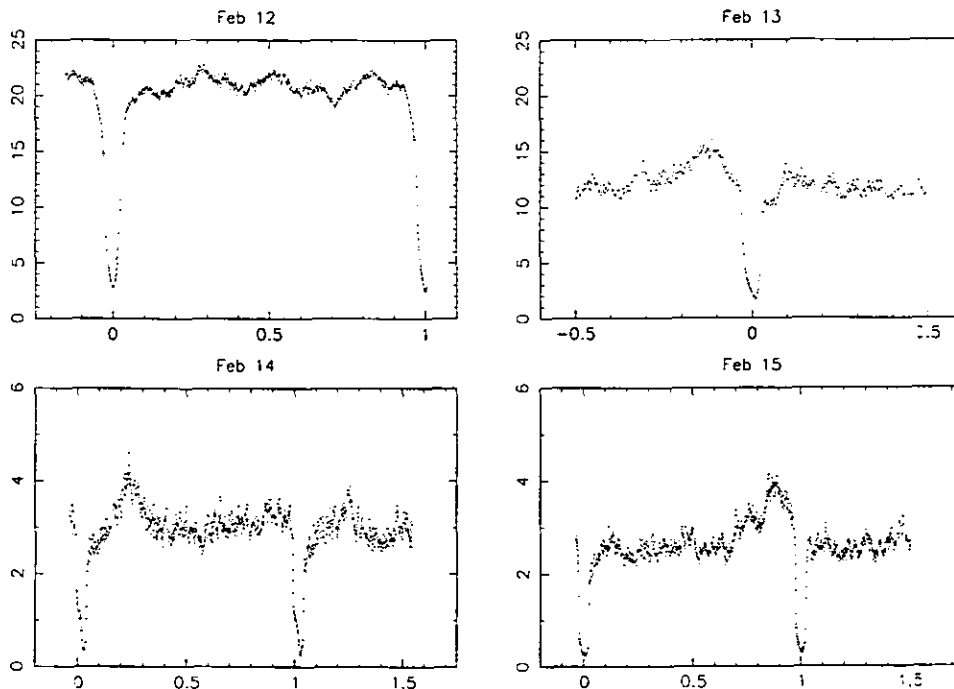


Figure 7. Four more optical light curves of OY Car on the decline from superoutburst. The x - and y -axes are as for Fig. 6. Note that the scale of the y -axis has changed.

dwarf eclipse in quiescence (231 s; Wood et al. 1989), and a value that probably results from an over-estimation due to the superhump feature that is near the eclipse.

The superhumps themselves show marked variations. On February 8 and 9, the superhump is ~ 0.25 mag; it becomes less distinct on February 11 and 12, and again becomes visible from February 13. Also visible are dips arising from self-absorption, similar to those seen in *HST* observations of OY Car in superoutburst by Billington et al. (1996). They can be attributed to obscuration of the central parts of the disc, by the superhump material itself, explained by Billington et al. (1996) as time dependent changes in the thickness of the disc at the outer edge. This azimuthal asymmetry is distinct from the wholesale physical flaring of the disc. The best example of the dip phenomenon is in the light curve of February 8, where it can be seen to occur in the superhump over two consecutive orbital periods. The dips also come and go over the course of our observations, being visible in the light curves of February 8, 9, 13, and 15, but not visible in the light curves of February 10, 11, 12 and 14. The superhump peaks are difficult to define when the dips are significant. Calculations using an approximate superhump ephemeris reveal that the superhumps visible in the light curves of February 14 and 15 are late superhumps, shifted in phase from the normal superhumps by 180° . Both the late superhump ($\phi \sim 0.25$) and a faint quiescent orbital hump ($\phi \sim 0.85$) can be seen in the light curve of February 14. The late superhump visible in the February 15 light curve is enhanced in intensity as a result of a coincidence with the quiescent orbital hump.

4.2 The superoutburst disc

4.2.1 Introduction

To investigate the surface brightness distribution of the disc during the superoutburst, we used the eclipse mapping method developed by Horne (1985). The original method rests on the following three basic assumptions.

- (1) The surface of the secondary star is given by its Roche potential.
- (2) The accretion disc lies flat in the orbital plane.
- (3) The emitted radiation is independent of the orbital phase, i.e., the observed surface brightness distribution of the disc remains fixed with respect to the binary.

The method thus allows deconvolution of the eclipse profile. This is achieved by comparing, using maximum entropy methods, the observed intensity distribution with a default distribution specified by the above items and the parameters of the system. The brightness of the observed disc is then determined, subject to two constraints:

- (i) agreement between the calculated and observed light curves is achieved by the use of the χ^2 statistic, and
- (ii) to allow a choice of one of the many possible disc light distributions, the disc template map and light curve must be as close to axisymmetric as possible.

The eclipse mapping program used in our analysis is an extension of Horne's original code that allows a flared disc, i.e., one that increases in thickness outward from the centre, but is not concave. For this section and the remainder of the paper, we will use α to denote the opening angle of the disc. Thus $\alpha/2$ is the flare half-angle. That the line of sight must intercept the disc surface

constrains the allowed flare angles to $\alpha/2 < 90 - i$, which in our case is $< 7^\circ$.

4.2.2 Method

The disc dominates the flux at the optical bandpass used, thus the contribution from the secondary will be negligible. In choosing which light curves to map, we avoided those in which eclipses were contaminated with superhump light, as the presence of this excess light can affect the disc light distribution and cause spurious artefacts, especially if near phase zero. For our data set, it is clear that the light curves of 1994 February 8, 10, 11, 13, and 15 exhibit signs of superhump light contamination of the eclipse phase. These light curves also show dips, discussed above; these would render our eclipse mapping program invalid, as in this case $\alpha/2 > 90 - i$. We thus chose to map the light curves of 1994 February 9 and 12. We also attempted to map the light curve of February 14, but the poor signal-to-noise ratio of the observation made this difficult and introduced too much uncertainty for a realistic disc map.

The February 9 and 12 data were each divided into 40 bins for orbital phase $-0.2 \leq \phi \leq 0.2$. We found that simple Poissonian statistics produced uncertainties that were small when compared to the intrinsic flickering of the data, so we adopted a constant percentage error derived from the ratio of the flickering to the average flux out of eclipse, thus giving what we regard as a more realistic measure of the errors. This constant percentage error was different for each data set, as the mean out-of-eclipse flux has dropped by a factor ~ 40 per cent in the three-day period between the light curves. We used a mass ratio $q = 0.102$, a distance $D = 82$ pc, and inclination $i = 83.3^\circ$ as standard parameters, all from Wood et al. (1989), and a Cartesian grid of 69×69 pixels, with the white dwarf at the centre, to cover the accretion disc plane.

We initially started mapping the light curves with a flat disc. This produced maps with a pronounced front-back asymmetry and a high value of χ^2 , as would be expected if the flare had been ignored (Wood 1994). We then began mapping the data with a flared disc, gradually incrementing the value of the disc opening angle, α , from the flat case. This produced an immediate improvement in the front-back asymmetry and reduced the value of χ^2 . By using a combination of the front-back asymmetry and χ^2 diagnostics, we arrived at acceptable fits to each light curve. The corresponding disc opening angles were $\alpha = 11^\circ$ for the 1994 February 9 light curve, and $\alpha = 10^\circ$ for the February 12 light curve, respectively. The resulting contour maps and associated radial brightness temperature distribution in the discs of February 9 and February 12 can be seen in Figs 8, 9, 10, and 11, respectively. For comparison, the disc map and temperature distribution obtained when the light curve of February 12 is fitted with a flat disc are shown in Figs 12 and 13. Fig. 14 shows the light curves calculated from the flat and flared disc maps, plotted with the actual data. It is obvious that the flared disc is a far better fit to the data.

5 DISCUSSION

5.1 OY Car and VW Hyi in the EUV and X-ray

In this section, we discuss X-ray and EUV observations of VW Hyi and OY Car in order to address the question of whether or not the behaviour of OY Car in this wavelength range is typical for an

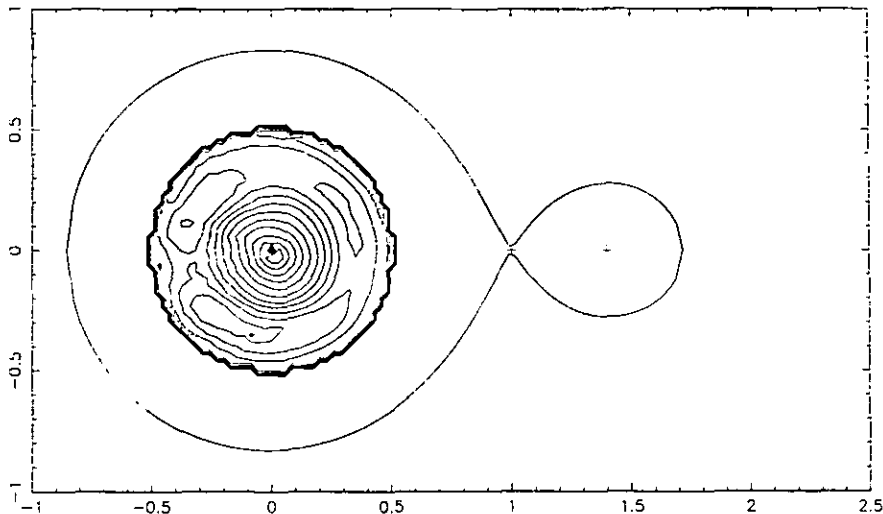


Figure 8. The reconstructed surface brightness in the disc of February 9. The flare angle is $\theta = 11^\circ$. The contour scale is logarithmic, with a contour interval of 0.2 decades.

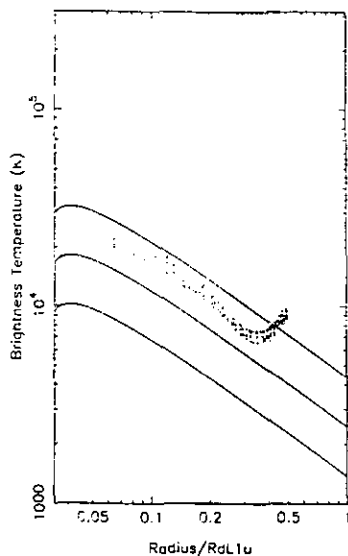


Figure 9. The brightness temperature distribution in the February 9 disc. Models of steady state optically thick for, from top to bottom: $\dot{M} = 10^{-9}$, 10^{-10} , and $10^{-11} M_\odot \text{yr}^{-1}$, are also shown.

SU UMa-type dwarf nova. Interpretation of the X-ray data from these two systems involves the consideration of several important interconnected factors.

(i) First, OY Car is an eclipsing system, whereas VW Hyi is not.

(ii) Secondly, the absorption to the X-ray source must be taken into account. The absorption can have a maximum of three possible components. First and foremost there is the *interstellar absorption*, which for VW Hyi is the lowest of all dwarf novae, at $n_{\text{H}} \sim 6 \times 10^{17} \text{cm}^{-2}$ (Belloni et al. 1991), but which is unknown in the case of OY Car. Secondly, there is the *local absorption* arising from the presence of the 'iron curtain' of material which veils the white dwarf in quiescence (Horne et al. 1994) and possibly outburst. Finally, in the case of high-inclination systems in outburst and superoutburst, there is the effect of *disc edge absorption*, a consequence of the material of the disc edge obscuring the central regions while flared. This last effect can be

seen in the dips of the optical light curves in this paper, while Billington et al. (1996) find dips in *HST* light curves of OY Car in superoutburst that are coincident with the optical superhump maximum. It is not known whether the 'iron curtain' phenomenon is connected to the disc, although the fact that to date, the 'iron curtain' has only been seen in high-inclination systems certainly suggests that this is so. There is no known way of disentangling the effect of absorption arising from the material of an 'iron curtain' from that of a disc seen nearly edge-on.

(iii) Lastly, the spectral responses of the various X-ray satellites are all different – the responses depend on the instrument and detector used aboard the observing satellite. Table 5 summarizes the instruments (and their respective spectral ranges) aboard the EUV/X-ray satellites relevant to this discussion, i.e. *EUVE*, *EXOSAT*, *ROSAT* and *GINGA*. A comparative illustration of the effective areas and spectral responses of the instruments aboard *EXOSAT* and *ROSAT* can be found in fig. 9 of Wheatley et al. (1996).

VW Hyi is perhaps the best-studied low-inclination SU UMa dwarf nova, bright in the optical [$m_v(\text{max}) \sim 9.5$, $m_v(\text{min}) \sim 13.3$], and observed to undergo regular outbursts ($T_n \sim 30\text{d}$; Ritter & Kolb 1998), and superoutbursts ($T_s \sim 180\text{d}$; Ritter 1997). Its brightness is to some extent a result of the low interstellar absorption of the system; it has thus been well studied in all wavelengths, including the X-ray.

5.1.1 Summary of observations to date

EUV data. VW Hyi is the only dwarf nova to be detected in quiescence by the *ROSAT* WFC, probably a consequence of the low interstellar column in this direction. VW Hyi was not observed above background in quiescence by either of the detectors aboard *EUVE* during the all-sky survey phase.

VW Hyi has also been detected in outburst with the *ROSAT* WFC, although this was during the all-sky survey phase. VW Hyi has been detected in superoutburst with the *EUVE*. Mauche (1996) shows different count rates depending on the spectrometer, with the count rate rising for the duration of the observation across all three detectors. The corresponding EUV spectrum of VW Hyi is

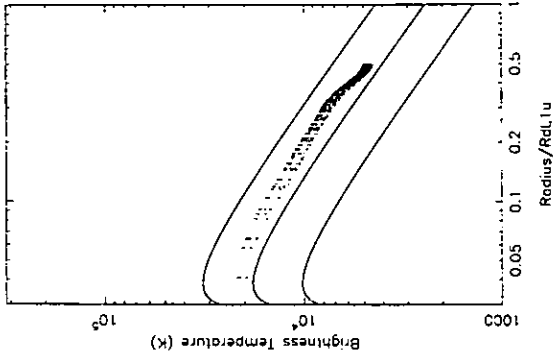


Figure 11. The brightness temperature distribution in the February 12 disc. Models of steady state optically thick fit, from top to bottom: $\dot{M} = 10^{-9}$, 10^{-10} , and $10^{-11} M_{\odot} \text{yr}^{-1}$, are also shown.

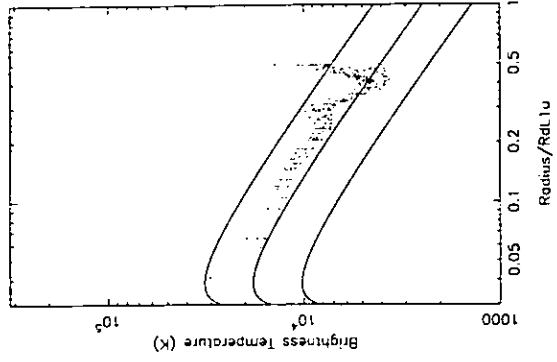


Figure 13. The corresponding brightness temperature distribution in the February 12 disc when fitted with a flat disc model. Models of steady state optically thick fit, from top to bottom: $\dot{M} = 10^{-9}$, 10^{-10} , and $10^{-11} M_{\odot} \text{yr}^{-1}$, are also shown.

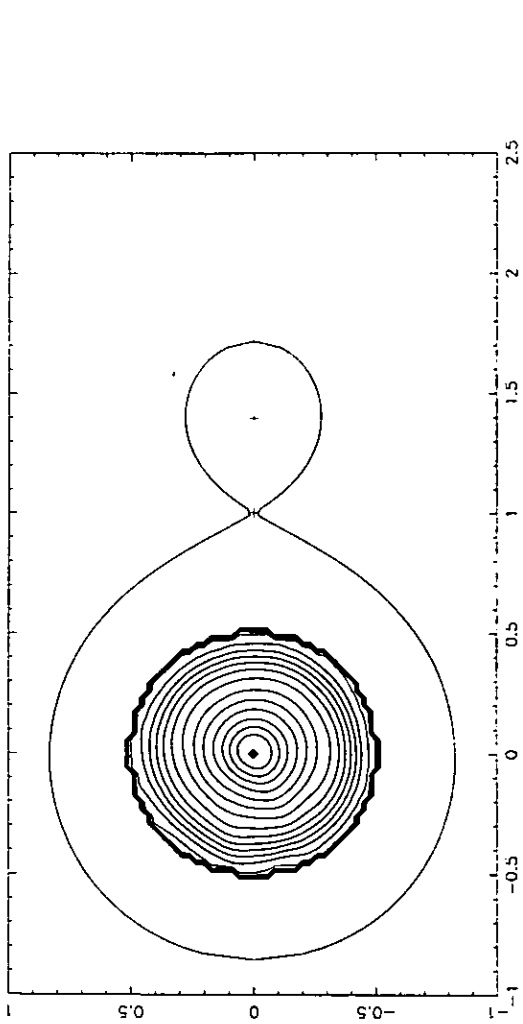


Figure 10. The reconstructed surface brightness in the disc of February 12. The flare angle is $\theta = 10^{\circ}$. The contour scale is logarithmic, with a contour interval of 0.2 decades.

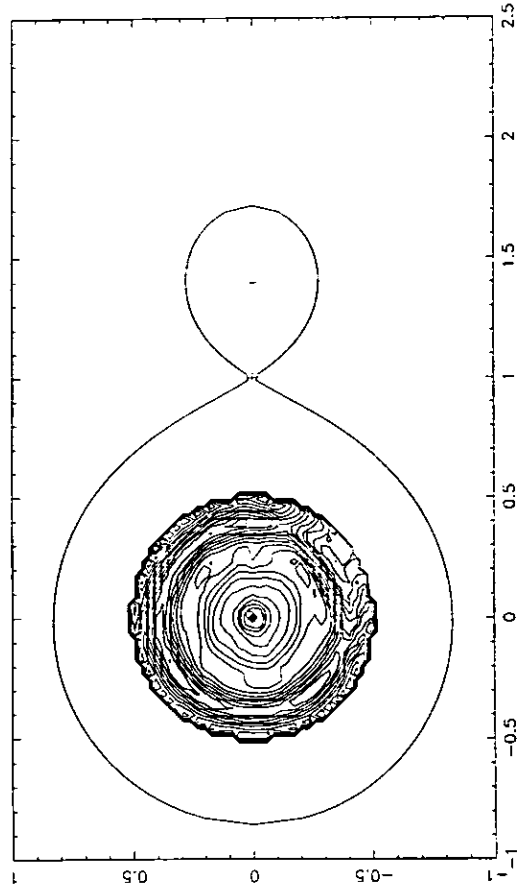


Figure 12. For comparison, this is the reconstructed surface brightness in the disc of February 12 using a flat disc model. The contour scale is logarithmic, with a contour interval of 0.2 decades.

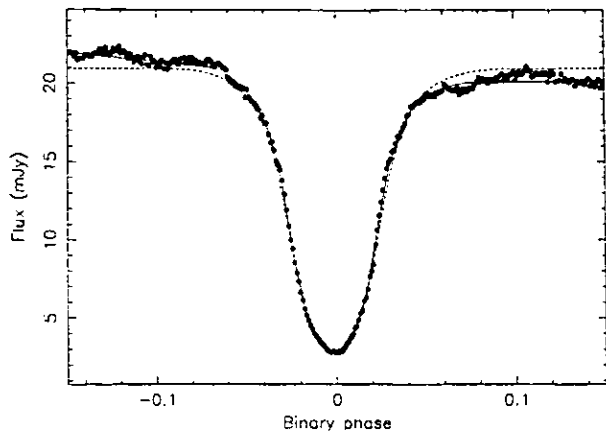


Figure 14. A comparison of the light curves calculated from the reconstructed disc map of February 12 when modelled with a flat disc (dashed) and a flared disc of opening angle $\alpha/2 = 5^\circ$ (solid).

Table 5. Instruments, filters, and spectral energy ranges of recent EUV and X-ray satellites.

Satellite	Instrument name	Range (keV)
EUVE	Lex/B scanner	0.07–0.25
	Al/Ti/C scanner	0.05–0.08
	SW spectrometer	0.07–0.18
	MW spectrometer	0.03–0.09
	LW spectrometer	0.02–0.04
EXOSAT	Low Energy (LE)	
	3000-Lexan	0.05–1.77
	4000-Lexan	0.07–1.77
	Al-Par	0.04–1.77
	Medium energy (ME)	1–20 5–50
ROSAT	WFC	
	S1a	0.09–0.21
	S2a	0.06–0.11
	PSPC/HRI	0.1–2.5
GINGA	Large Area Counter	2–30

shown to peak longward of 0.07 keV, and does not extend shortward of 0.12 keV. In Section 2 we show that OY Car was not detected by the ROSAT WFC during the 1994 January superoutburst.

X-ray data. Fits to the quiescent X-ray spectrum of VW Hyi have produced various values for the temperature of the emitting gas, typically yielding $kT < 10$ keV, depending on the spectral response of the satellite involved. Belloni et al. (1991) produced a quiescent temperature of $kT = 2.17 \pm 0.15$ keV when the ROSAT PSPC observation was fitted with a single-component Raymond–Smith optically thin thermal plasma with line emission at ~ 1 keV. Wheatley et al. (1996) extended the analysis further by combining the ROSAT PSPC observation of Belloni et al. with ROSAT WFC EUV data at the low end and GINGA hard X-ray data at the high end, giving unprecedented wavelength coverage of the high-energy spectrum of VW Hyi. Wheatley et al. fitted this combined spectrum with single and two-temperature Mewe optically thin plasma models, with and without line emission. They found that the dominant continuum temperature is ~ 6 keV for both model types, although they were unable to use the data to

distinguish between model types. For the two-temperature case, the components are at temperatures of ~ 6.0 and ~ 0.7 keV.

Our ROSAT observation of OY Car in quiescence does not contain enough information to do more than constrain the X-ray spectrum and the absorption to the X-ray source. We can, however, conclude that the quiescent spectrum of OY Car is produced by a boundary layer at a typical temperature for this type of object: i.e., $kT < 10$ keV.

OY Car and VW Hyi have been observed in an outburst state by both EXOSAT and ROSAT, although in the case of OY Car a normal outburst has never been observed. There is an increase in the soft X-ray flux from both systems during superoutburst (e.g., van der Woerd, Heise & Bateson 1986; Naylor et al. 1988), but the actual scale of the increase differs – the increase is a factor of ~ 100 for VW Hyi, whereas for OY Car it rises only by a factor of ~ 3 .

According to van Teeseling, Verbunt & Heise (1993), the EXOSAT-observed superoutburst X-ray spectrum of VW Hyi can be modelled in terms of either a single component optically thin spectrum with $0.043 \leq kT \leq 0.43$ keV, or a combination of a hot, optically thin component at $kT > 0.43$ keV (which they tentatively identify with the 2.17-keV quiescent spectrum found by Belloni et al. 1991) and a cooler, optically thick component at $0.034 < kT < 0.042$ keV. Wheatley et al. (1996) prefer the optically thin plus blackbody component interpretation for the spectrum of VW Hyi in both outburst and superoutburst. They suggest the superoutburst spectrum is a result of a drop of a factor ~ 3 –4 in the hot quiescent optically thin component and the rise of a very soft blackbody component that is easily detected by the EXOSAT filters but not by the ROSAT instruments. In other words, the quiescent and outburst spectra can both be explained in the context of a variation in the relative strengths of just the two components. They find no evidence for spectral change (from thermal Bremsstrahlung to blackbody, for example) during outburst observations.

OY Car has now been observed by both EXOSAT and ROSAT in superoutburst. The EXOSAT observation by Naylor et al. (1988) suggested that the X-rays in the 1985 May superoutburst came from a large optically thin corona at $kT \sim 0.43$ keV, producing a luminosity of $L_{X_{\text{soft}}} \sim 10^{31}$ – 10^{32} erg s $^{-1}$. Our ROSAT superoutburst observation of OY Car has a count rate comparable to the quiescent count rate, taking into account the fact that different detectors were used. This suggests that the ROSAT instruments are detecting a greater part of the hard, optically thin component than the corresponding detectors aboard EXOSAT.

Table 6 summarizes the EUV and X-ray observations of OY Car and VW Hyi to date.

5.1.2 So, how similar are OY Car and VW Hyi?

The approximate X-ray luminosity of each system in each state is shown in Table 7, from which it can be seen that the luminosity of OY Car is consistently the lower of the two. This could, however, be explained qualitatively in terms of the three differentiating factors, namely the satellite spectral responses, the inclination and the absorption.

Satellite spectral responses can and do confuse the issue. Wheatley et al. (1996) describe the evolution of the X-ray spectrum of VW Hyi from quiescence to outburst as the appearance of a very soft blackbody component accompanied by a change in the relative strengths of two optically thin

Table 6. Comparison of the EUV observations of OY Car and VW Hyi.

	OY Car	VW Hyi
<i>ROSAT</i> WFC		
Quiescence	No detection ^a	$18.7 \pm 2.7 \text{ count s}^{-1}$
Outburst	Unobserved	$0.08 \pm 0.04 \text{ count s}^{-1}$
Superoutburst	No detection ^b	Unobserved
<i>EUVE</i>		
Quiescence	Unobserved	No detection
Outburst	Unobserved	$\sim 0.09 \text{ count s}^{-1}$
Superoutburst	Unobserved	$\sim 1.0 \text{ count s}^{-1}$ (SW) $\sim 4.0 \text{ count s}^{-1}$ (MW) $\sim 2.0 \text{ count s}^{-1}$ (LW)

^a $1.5 \times 10^{-3} \text{ count s}^{-1}$ upper limit.

^b $1.2 \times 10^{-3} \text{ count s}^{-1}$ upper limit.

^cIn the ALTi/C detector during the all-sky survey phase.

components. In quiescence the optically thin components dominate, while in outburst, the very soft blackbody component rises to contribute most of the flux outside the *ROSAT* bandpass. This component has disappeared by the end of the outburst. Assuming that the same components occur in OY Car, we must bear in mind that only the optically thin components can contribute to the *ROSAT* bandpass. This suggests that we are underestimating the total high-energy output of OY Car because neither the *ROSAT* HRI nor the PSPC are sensitive to the lower energy ranges.

Additionally, the inclination of the system is crucial. The inclination of VW Hyi simply allows more of the X-ray and EUV-emitting boundary layer to be seen directly. For OY Car however, although the boundary layer can be seen in quiescence, during outburst/superoutburst there is no direct line of sight because the disc has flared up and the inclination is such that it blocks our view. There is increased absorption seen in OY Car as there is far more material in the orbital plane than there is in VW Hyi. The lack of X-ray eclipse, together with the evidence of a disc with an opening angle of 10° three days after the end of the superoutburst, illustrate this effect. The significantly lower X-ray luminosity in OY Car during superoutburst is another consequence of this increased absorption.

5.2 Superoutburst: flared discs and the lack of X-ray eclipse

5.2.1 Flare angles and temperature distributions

In the context of accretion disc mapping, the motivation for considering flared discs has arisen from the poor fitting, and the occurrence of spurious structure, that have resulted from flat disc model fits to outburst and superoutburst light curves. During outbursts of Z Cha (Warner & O'Donoghue 1988; Robinson et al. 1995) and OY Car (Rutten et al. 1992), bright rings around the outer edge of the disc and/or front-back asymmetries were present in the reconstructed disc when the light curve was mapped with a flat disc. There are two interpretations for this phenomenon: either the observed features are the result of an unclipped light source (e.g., the secondary star, or a large disc), or the disc is exhibiting a physical flare. See the review by Wood (1994) for further discussion.

Mapping light curves with flared discs has been attempted at normal outburst maximum for both OY Car and Z Cha. Rutten et al. (1992) briefly considered a flared disc in their optical examination of OY Car at normal outburst peak. They used small

opening angles and did obtain a satisfactory fit to the light curve, but this caused a front-back asymmetry to develop. Rutten et al. (1992) prefer the unclipped light source interpretation, finally eliminating the spurious features by subtracting 15 per cent of the flux before mapping.

However, the *HST* light curve of Z Cha at normal outburst maximum was mapped with a disc of opening angle $\alpha = 16^\circ$ by Robinson et al. (1995). The fact that by mid-decline, the light curve could be modelled by an axisymmetric flat disc, lends weight to the interpretation of these data at outburst maximum as being the result of a flared disc.

We demonstrated in Section 4.2.2 that a disc with a substantial flare exists in OY Car three days into the decline from superoutburst. These are the first maps of a disc in the superoutburst state that clearly show such flaring.

By way of illustrating the differences between observations and theory, we can calculate the theoretical flare angles and compare these to the results from eclipse mapping.

The *steady state* theoretical flare angle is given by (Shakura & Sunyaev 1973; Frank, King & Raine 1985)

$$\frac{h_d}{r_d} = 1.72 \times 10^{-2} \alpha_v^{-1/10} M_{\text{WD}}^{3/8} (r_d \times 69.6)^{1/8} \dots \left(\frac{\dot{M}}{1.587 \times 10^{-10}} \right)^{3/20} \times \left[1 - \left(\frac{R_{\text{WD}}}{r_d} \right)^{1/2} \right]^{3/5}$$

Here the equation is normalized to solar values, and α_v is the viscosity. Assuming that the disc radius is approximately equal to the tidal radius ($r_d \sim r_t$), r_t is approximated by

$$r_t = r_d = \frac{0.6a}{1+q}$$

(Warner 1995; after Paczyński 1977), where a is the binary separation and q is the mass ratio.

Using $M_{\text{WD}} = 0.685 M_\odot$, $a = 0.608 R_\odot$, $q = 0.102$ (Wood et al. 1989), and assuming $\alpha_v \sim 1.0$, we find a *steady state* disc flare angle of $\alpha \approx 2^\circ 6$.

Alternatively, if we assume that the disc is in a *non-steady state*, and that the disc includes radiative and convective zones, then

$$\frac{h_d}{r_d} \sim 0.038 \left(\frac{\dot{M}}{1.587 \times 10^{-10}} \right)^{3/20}$$

(adapted from Smak 1992). Adopting $\dot{M} \sim 4 \times 10^{-10} M_\odot \text{ yr}^{-1}$ (from Fig. 11), gives $\alpha \approx 5^\circ$.

Thus the flare opening angle of OY Car on superoutburst decline is considerably larger than that predicted by either steady state or non-steady state theory.

We find a flare angle of $\alpha \approx 10^\circ$ for the disc of February 12; however, we note that limb darkening has not been taken into account. The first steps towards including limb darkening in eclipse mapping have recently been taken by Robinson and collaborators, using the *HST* light curve previously mapped with a flared disc of opening angle $\alpha/2 = 8^\circ$ (Robinson, Wood & Wade 1999). The net result of including the limb darkening in their analysis of this UV data set is to reduce the opening angle of the disc to $\alpha/2 = 6^\circ$, a value that is still between 2° and 3° larger than that given by disc model atmospheres. We note that limb darkening will have less of an effect on our *B* band optical data.

Fig. 9 shows that the slope of the disc brightness temperature distribution on February 9 appears only approximately compatible

Table 7. Intrinsic luminosity values for OY Car and VW Hyi (very approximate, uncorrected for inclination).

System	State	L_X (erg s^{-1})	L_{UV}^1 (erg s^{-1})	$L_{\text{opt}+UV}^2$ (erg s^{-1})	L_X/L_{UV}	$L_X/L_{\text{opt}+UV}$
OY Car	quiescent	$\sim 10^{30}$	1.7×10^{31}	2.5×10^{31}	0.06	0.04
	superoutburst	$\sim 2 \times 10^{32}$	1.4×10^{32}	3.5×10^{32}	0.07–1.43	0.03–0.57
VW Hyi	quiescent	$\sim 10^{31}$	9.1×10^{31}	1.4×10^{32}	0.11	0.07
	superoutburst	$\sim 10^{34}$	1.2×10^{34}	1.6×10^{34}	0.83	0.63

¹Calculated using $F_{UV} = 718f_{1460} + 340f_{1800} + 540f_{2140} + 490f_{2880}$.

²Calculated using $F_{\text{opt}+UV} = 718f_{1460} + 340f_{1800} + 540f_{2140} + 1680f_{2880} + 2620f_{5500}$; Method used by van Teeseling et al. (1996), consisting of summing the average fluxes at 1460Å, 1800Å, 2140Å, 2880Å, and 5500Å, in $\text{erg s}^{-1}\text{Å}^{-1}$, multiplied by their weights.

with the theoretical steady state solutions. The overall mass flow rate is slightly larger than that for the disc of February 12.

The turn-up at the edge of the brightness temperature distribution on February 9 is similar to that seen in disc maps of Z Cha (Warner & O'Donoghue 1988). Physical explanation of this effect requires the presence of a ring at the outer edge. We would hesitate to invoke an explanation that requires a ring if the light curves were acquired in quiescence, but numerical simulations of superoutburst discs by Whitehurst (1988a,b) and Whitehurst & King (1991) suggest that rings exist at the outer edges of the disc in superoutburst, and indeed, are the most likely explanation for the superhump phenomenon. Unfortunately, in this case, we cannot say definitively whether the ring is real or an artefact from the modelling process.

In contrast, the observed slope of the disc brightness temperature distribution on February 12 (Fig. 11) is quite compatible with the overplotted theoretical curves of optically thick, steady state discs. The average rate of mass flow through the disc at this stage in the decline appears to be $\sim 4 \times 10^{-10} M_{\odot} \text{yr}^{-1}$. There is no evidence for a ring at the outer edge of the disc at this stage in the superoutburst decline.

This can be compared with a normal outburst peak mass flow rate of $\sim 1 \times 10^{-9} M_{\odot} \text{yr}^{-1}$ for OY Car, again with a relatively good fit to steady state theoretical disc curves (Rutten et al. 1992). We note the fact that our disc mass flow rate is lower than that found at normal outburst maximum. However, the data presented here were obtained well into the decline from superoutburst – the flux from the system is virtually at the quiescent level two days after the acquisition of these data.

5.2.2 Tying it all together

A self-consistent picture of OY Car in superoutburst emerges with the X-ray and optical data presented in this paper. The lack of X-ray eclipse affirms the conclusions of the *EXOSAT* observation of the 1985 May superoutburst by Naylor et al. (1988), suggesting that their extended, 'coronal' X-ray source may well be the rule and not the exception when superoutbursts occur in high-inclination systems. Our value for the X-ray luminosity in superoutburst is also in agreement with the value of $L_X \sim 10^{31} - 10^{32} \text{erg s}^{-1}$, found by Naylor et al. (1988). This is up to 100 times less luminous than VW Hyi in superoutburst.

Naylor et al. (1987, 1988) used contemporaneous observations in other wavelengths to suggest that the disc of OY Car had considerable vertical structure during the 1985 May superoutburst, and that the increased local absorption that resulted had the effect of shielding the boundary layer from view at all orbital phases. This also results in a decrease in the detected X-ray flux, leading

to false conclusions being drawn regarding the X-ray luminosity of the system and a very low $L_X/L_{\text{opt}+UV}$ ratio. The optical data presented here show for the first time how flared the disc is even three days into the superoutburst decline. It is not difficult to envision even larger opening angles during superoutburst maximum, but it is unclear whether the disc is thickened at the edge, or nearer the centre; even more perturbing is the lack of a simple mechanism to support this structure.

5.3 Quiescence: constraining the absorption

In terms of the emission measure and hardness ratio, OY Car is similar to the other high-inclination dwarf novae investigated in van Teeseling & Verbunt (1994) and van Teeseling et al. (1996); the volume of the X-ray emitting source is small compared to that in lower inclination systems.

The quiescent X-ray luminosity of OY Car appears comparable to both Z Cha (bolometric $L_{X_q} \sim 2.5 \times 10^{30} \text{erg s}^{-1}$; van Teeseling 1997) and HT Cas in its unusually low state (bolometric $L_{X_q} \sim 5 \times 10^{30} \text{erg s}^{-1}$; Wood et al. 1995a), but is an order of magnitude below the X-ray luminosity from the ASCA observation of HT Cas in the normal quiescent state ($L_{X_q} \sim 2.2 \times 10^{31} \text{erg s}^{-1}$; Mukai et al. 1997). Cordova & Mason (1984) quote typical CV X-ray luminosities of $\sim 10^{31} \text{erg s}^{-1}$ in quiescence, although it must be remembered that the proportion of eclipsing high-inclination CVs is small.

If the X-rays do come from the boundary layer, then assuming the steady state case, (i.e., $L_{\text{bl}} = \frac{1}{2} GM_{\text{WD}} \dot{M} / R_{\text{WD}}$); for the case of OY Car in quiescence, \dot{M} is $3 \times 10^{-13} M_{\odot} \text{yr}^{-1}$, an exceptionally low value. Wood et al (1995a) find a mass transfer rate on to the white dwarf of $\dot{M} \sim 1 \times 10^{-12} M_{\odot} \text{yr}^{-1}$ for the low state of HT Cas.

One possible explanation for such a low X-ray luminosity is that the white dwarf in these systems is spinning rapidly. This is not inconceivable, given that Sion et al. (1995), using high-resolution *HST* spectra, found that the white dwarf of VW Hyi was spinning at $v \sin i \sim 600 \text{km s}^{-1}$, although they subsequently show that even this rotation rate cannot account for the low $L_X/L_{\text{opt}+UV}$ ratio for this system. Further, Cheng et al. (1997) found that the white dwarf in WZ Sge is rotating at a $v \sin i \sim 1200 \text{km s}^{-1}$. Observations of U Gem show that the white dwarf in that system is rotating at $v \sin i \sim 100 \text{km s}^{-1}$ (Sion et al. 1994), while Mauche (1998) calculate a $v \sin i \sim 300 \text{km s}^{-1}$ for the white dwarf in SS Cyg. Of these systems, U Gem possesses the longest orbital period ($P_{\text{orb}} = 4.25 \text{h}$) and slowest white dwarf rotation, while WZ Sge has the shortest orbital period ($P_{\text{orb}} = 1.36 \text{h}$) and the fastest-spinning white dwarf. OY Car, Z Cha, and HT Cas all have orbital periods closer to that of WZ Sge than that of U Gem. On this

evidence, it could be that the white dwarf in OY Car is spinning relatively fast, and that this may have the effect of reducing the X-ray flux.

Alternatively, there may simply be a very low rate of mass transfer through the boundary layer on to the white dwarf. While this may be true for the two observations of HT Cas (it is observed to have occasional low states), it does not explain why the quiescent X-ray luminosities of both OY Car and Z Cha are an order of magnitude lower than typical values.

The real difficulty lies in constraining the value of the column density, n_{H} , and it is on this that the luminosity of the system is most dependent. It is perhaps premature to draw conclusions when this factor is such a relative unknown. Fig. 4 shows that a single component column density of 10^{22} cm^{-2} is not compatible with the data. Dual-absorption models featuring both neutral and ionized components fare no better because the relative contribution of each component is ill-constrained by the low-quality spectrum. The uncertainty in the value of the local absorption in OY Car may well raise some interesting implications, especially for the 'iron curtain' model of Horne et al. (1994). In that paper, *HST* observations of the quiescent system were decomposed into the individual contributions from the white dwarf, accretion disc, and bright spot. Horne et al. found that a fit to the white dwarf spectrum was only achieved when fitted not only with a white dwarf at $T_{\text{WD}} = 16.5 \times 10^3 \text{ K}$, but also with a veiling solar-abundance LTE gas of $T \approx 10^4 \text{ K}$ and $n_{\text{H}} \sim 10^{22} \text{ cm}^{-2}$. This veiling gas was found to have a velocity dispersion of $\Delta v \approx 60 \text{ km s}^{-1}$, suggesting a physical position at the edge of the disc. The analysis of the 'iron curtain' phenomenon has since been extended to Z Cha (Wade, Cheng & Hubeny 1994). It may be that the 'iron curtain' is not a permanent feature, and our observation happened to view the source at an epoch in which the veiling gas was absent. Both our observation and that of Horne et al. (1994) were obtained in the middle of the respective quiescent periods, which suggests that the source of the veiling gas is not directly connected to the outburst mechanism. It may also be that the 'iron curtain' is not azimuthally homogeneous, and that the observations obtained by Horne et al. (1994) happened to occur at an orbital phase during which the azimuthal distribution of the local absorption was strong.

6 CONCLUSIONS

We have used *ROSAT* observations of OY Car to confirm that there is no eclipse of the X-ray flux during superoutburst. Eclipse maps of contemporaneous optical light curves show that three days into the superoutburst decline, the disc was flared with an opening angle of $\alpha \approx 10^\circ$. Taken together with the multiwavelength observations of the 1985 May superoutburst of OY Car in Naylor et al. (1987, 1988), we can confirm that the disc becomes thick enough to obscure the central regions of the disc and boundary layer when in this state. While we now know that discs become physically thick in outburst, we do not yet know of a simple, plausible mechanism that can hold it in place for these considerable lengths of time.

We have difficulty reconciling the measurements of the absorption to the X-ray source in quiescence as derived from measurements in the X-ray and UV. Single-component absorption models with a column density of 10^{22} cm^{-2} , derived by Horne et al. (1994) from *HST* observations, are not compatible with the data; dual-component models do not allow any constraints to be

placed on the relative contribution of each component. A possible explanation, that the 'iron curtain' is variable, is one that is difficult to test observationally, in that it requires data acquired simultaneously in the UV and X-ray.

Future work includes further observations of OY Car in quiescence in order to tie down the spectrum of the X-ray source, its position, and the absorption to it. Pratt et al. (1999) use further *ROSAT* HRI observations of OY Car in quiescence to constrain the source of the X-ray emission, but detailed modelling of the spectrum and the absorption to the X-ray source requires spectrally resolved data such as are obtainable from *ASCA*. Looking further into the future, systems such as these will be ideal targets for *XMM*, and will make excellent use of the simultaneous optical monitoring.

ACKNOWLEDGMENTS

We thank K. Beuermann, F.V. Hessmann, B. Gänsicke and K. Reinsch for useful discussions. We acknowledge the data analysis facilities provided by the Starlink Project, which is run by the Space Science Department at Rutherford Appleton Laboratory, on behalf of the Particle Physics and Astronomy Research Council. GWP is in receipt of a University of Central Lancashire research studentship.

REFERENCES

- Belloni T. et al., 1991, *A&A*, 246, L44
- Billington I., Marsh T. R., Horne K., Cheng F.-H., Thomas G., Bruch A., O'Donoghue D., Eracleous M., 1996, *MNRAS*, 279, 1274
- Cheng F.-H., Sion E. M., Szkody P., Huang M., 1997, *ApJ*, 484, L149
- Cordova F. A., Mason K. O., 1984, *MNRAS*, 206, 879
- David L. P., Harnden F. R., Kearns K. E., Zombeck M. V., 1991, *ROSAT Mission Description*, Appendix F. Max-Planck-Institut, Garching
- Frank J., King A. R., Raine D. J., 1985, *Accretion Power in Astrophysics*, Cambridge Univ. Press, Cambridge
- Horne K., 1985, *MNRAS*, 213, 129
- Horne K., Marsh T. R., Cheng F. H., Hubeny I., Lanz T., 1994, *ApJ*, 426, 294
- Long K. S., Mauche C., Raymond J. C., Szkody P., Mattei J. A., 1996, *ApJ*, 469, 481
- Mauche C. W., 1996, *Cataclysmic Variables and Related Objects*, Kluwer, Dordrecht, p. 243
- Mauche C. W., 1998, in Howell S., Kuulkers E., Woodward C., eds. *ASP Conf. Ser. Vol. 137, Wild Stars in the Old West*. Astron. Soc. Pac., San Francisco
- Mewe R., Gronenschild E.H.B.M., van den Oord G. H. J., 1985, *A&AS*, 62, 197
- Mukai K., Wood J. H., Naylor T., Schlegel E. M., Swank J. H., 1997, *ApJ*, 475, 812
- Naylor T., la Dous C., 1997, *MNRAS*, 290, 160
- Naylor T., Charles P. A., Hassall B. J. M., Bath G. T., Berriman G., Warner B., Bailey J., Reinsch K., 1987, *MNRAS*, 229, 183
- Naylor T., Bath G. T., Charles P. A., Hassall B. J. M., Sonneborn G., van der Woerd H., van Paradijs J., 1988, *MNRAS*, 231, 237
- Oke J. B., 1974, *ApJS*, 27, 21
- Paczynsky B., 1977, *ApJ*, 216, 822
- Pfeffermann E., Briel U. G., 1986, *SPIE (Soft X-ray Optics and Technology)*, 97, 208
- Pratt G. W., Hassall B. J. M., Naylor T., Wood J. H., 1999, *MNRAS*, 307, 413
- Pringle J. E., 1977, *MNRAS*, 178, 195
- Pringle J. E., Savonije G. J., 1979, *MNRAS*, 187, 777
- Ritter H., Kolb U., 1998, *A&AS*, 129, 83
- Robinson E. L. et al., 1995, *ApJ*, 443, 295

- Robinson E. L., Wood J. H., Wade R. A., 1999, *ApJ*, 514, 952
- Rutten R. G. M., Kuulkers E., Vogt N., van Paradijs J., 1992, *A&A*, 265, 159
- Shakura N. I., Sunyaev R. A., 1973, *ApJ*, 24, 337
- Shore S. N., 1992, in Drissen L., Leitherer C., Nota A., eds. *ASP Conf. Ser. Vol. 22. Non-isotropic and Variable Outflows from Stars*. Astron. Soc. Pac., San Francisco
- Sims M. R., Barstow M. A., Pye J. P., Wells A., Willingale R., 1990, *Opt. Eng.*, 29, 649
- Sion E. M., Long K. S., Szkody P., Huang M., 1994, *ApJ*, 430, 53
- Sion E. M., Huang M., Szkody P., Cheng F.-H., 1995, *ApJ*, 445, L31
- Smak J., 1992, *Acta Astron.*, 42, 323
- van der Woerd H., Heise J., Bateson F. M., 1986, *A&A*, 156, 252
- van Teeseling A., 1997, *A&A*, 319, L25
- van Teeseling A., Verbunt F., 1994, *A&A*, 219, 519
- van Teeseling A., Verbunt F., Heise J., 1993, *A&A*, 270, 159
- van Teeseling A., Beuermann K., Verbunt F., 1996, *A&A*, 315, 467
- Wade R. A., Cheng F.-H., Hubeny I., 1994, *BAAS*, 184, 46.05
- Warner B., 1995, *Cataclysmic Variable Stars*. Cambridge Univ. Press, Cambridge
- Warner B., O'Donoghue D., 1988, *MNRAS*, 233, 705
- Wheatley P. J., Verbunt F., Belloni T., Watson M. G., Naylor T., Ishida M., Duck S. R., Pfeffermann E., 1996, *A&A*, 307, 137
- Whitehurst R., 1988a, *MNRAS*, 232, 53
- Whitehurst R., 1988b, *MNRAS*, 233, 529
- Whitehurst R., King A. R., 1991, *MNRAS*, 250, 512
- Wood J. H., 1994, in Shafter A. W., ed., *ASP Conf. Ser. 56. Interacting Binary Stars*. Astron. Soc. Pac., San Francisco, p. 48
- Wood J. H., Irwin M. J., Pringle J. E., 1985, *MNRAS*, 214, 475
- Wood J. H., Horne K., Berriman G., Wade R. A., 1989, *ApJ*, 341, 974
- Wood J. H., Naylor T., Hassall B. J. M., Ramseyer T. F., 1995a, *MNRAS*, 273, 772
- Wood J. H., Naylor T., Marsh T. R., 1995b, *MNRAS*, 274, 31

This paper has been typeset from a \TeX/L\TeX file prepared by the author.